Theoretical Study of Ozone Forming Recombination Reaction and Anomalous Isotope Effect Associated with It

Alexander Teplukhin
Marquette University

Recommended Citation

Teplukhin, Alexander, "Theoretical Study of Ozone Forming Recombination Reaction and Anomalous Isotope Effect Associated with It" (2017). *Dissertations (1934 -)*. 709.
https://epublications.marquette.edu/dissertations_mu/709

THEORETICAL STUDY OF OZONE FORMING RECOMBINATION REACTION AND ANOMALOUS ISOTOPE EFFECT ASSOCIATED WITH IT

by

Alexander Teplukhin, M.S.

A Dissertation submitted to the Faculty of the Graduate School,
Marquette University,
in Partial Fulfillment of the Requirements for
the Degree of Doctor of Philosophy

Milwaukee, Wisconsin

May 2017

ABSTRACT

THEORETICAL STUDY OF OZONE FORMING RECOMBINATION REACTION AND ANOMALOUS ISOTOPE EFFECT ASSOCIATED WITH IT

Alexander Teplukhin, M.S.

Marquette University, 2017

The ozone forming recombination reaction stands out among many chemical processes that take place in the atmosphere. This reaction is responsible for the reconstruction of ozone layer, which protects life on Earth from harmful ultra-violate radiation and is a source of so-called anomalous isotope effect in ozone. The reaction was intensively studied, but at a very basic level. There were only couple of papers where the recombination rate coefficient was computed and found to roughly agree with the experimental data.

In this dissertation, the recombination process in ozone is approached using new and efficient method, which includes several modern techniques. The rovibrational scattering resonances of O_3 are characterized by solving three-dimensional time-independent Schrödinger equation in symmetric-top approximation. The widths (or lifetimes) of scattering resonances are computed using complex absorbing potential. The high efficiency is achieved by using convenient vibrational coordinates, optimal grid for dissociative coordinate and construction of small Hamiltonian matrix in locally optimal basis. The symmetry of the problem is also utilized by implementing a symmetry-adapted basis for one of vibrational coordinates. Stabilization of scattering resonances is described approximately, using mixed quantum/classical theory, for which an efficient frozen rotor approximation is developed.

The rate coefficient of ozone recombination, predicted here for unsubstituted ozone, $^{48}O_3$, as well as its pressure and temperature dependencies, agrees very well with experimental data. The isotope effects, one related to zero-point energy and another to symmetry, are studied for a limited number of rotational excitations and for two isotopologues $^{50}O_3$ and $^{52}O_3$ (singly and doubly substituted with ^{18}O). Both effects were found to be in the right direction and of right order of magnitude. The width of scattering resonances control these isotope effects. The approach is universal and can be applied to any other similar system, for example, S_3.

ACKNOWLEDGMENTS

Alexander Teplukhin, M.S.

I would like to express my gratitude to my advisor, Prof. Dmitri Babikov, for his readiness to answer all my questions, helping me in overcoming obstacles in my research, professional mentoring, his never-ending enthusiasm and advice.

I want to thank my committee members for their suggestions and reviewing of my research, Prof. Scott Reid, Prof. Jier Huang, Prof. Chae Yi and Dr. Brian Kendrick. Their professional expertise allowed me to improve the quality of my work. Also, I would like to thank Alexander Semenov for thoughtful discussions of scientific topics and am also grateful to other group members I had a chance to work with, Mikhail Ivanov, Dmytro Shyshlov, Lei Wang, Igor Gayday and Bikram Mandal.

Special thanks to my parents and sister, who supported me on my way, by video calling or texting me from another side of the globe. I want also to acknowledge my close friends here, Maxim Ivanov, Elena Ivanova and Nikita Strelnikov and two close friends in my home country, Vasily Kolpakov and Pavel Kozlov.

I would also like to thank the Arthur J. Schmitt Foundation for the financial support granted through the fellowship for academic year 2015-2016 and for helping me in mastering my leadership skills.

Finally, a warm thank you to the whole Marquette community for a very positive atmosphere and always being ready to help.

TABLE OF CONTENTS

LIST OF TABLES

LIST OF FIGURES

Chapter 1. Introduction

1.1. Motivation to study ozone

Ozone (O_3) is one of the most important species in Earth's atmosphere. Perhaps, the most well-known global problem related to ozone is a depletion of ozone layer in the stratosphere (upper atmosphere). This layer absorbs ultra-violet (UV) radiation from the Sun, which in large amount could damage life on Earth. The scientists at NASA and around the world are closely monitoring the evolution of ozone holes in this layer with the help of satellites. The negative consequences for people include skin cancer, cataracts and reduction of immune system response.[1,2] As for Earth's flora and fauna, it could have even more complex and implicit impacts. For example, negatively affecting the oceanic plankton, the ozone depletion damages the ocean food chains and the carbon cycle.[3,4]

Another major problem with ozone is that O_3 is a dangerous pollutant in the troposphere (lower atmosphere). It forms in a smog from volatile organic compounds (VOCs) and is a problem for many industrial cities and cities close to the areas of possible wildfires. As a consequence, the ozone triggers asthma, irritates lungs and could exacerbate lung disease, like pneumonia and bronchitis. Besides, ozone may cause a crop damage and contributes to greenhouse effect, indirectly affecting Earth's temperature.

Thus, for quite a long time ozone has been worrying humanity with these two major problems, one in the upper atmosphere and another in the lower atmosphere, both requiring study and identifying the ways to resolve these problems.

In addition, there is one more reason to study ozone. An ozone molecule can be composed of different oxygen isotopes. The oxygen isotope fractionation has many applications in geo- and cosmochemistry, paleoclimatology, hydrology, and atmospheric chemistry. These applications include identification of chemical compounds, studying food webs in aquatic ecosystems, reconstruction of climate change and even extending our knowledge about solar system origin and its evolution. In 1981 the group of Mauersberger[5] discovered in a balloon flight measurement the phenomenon generally known as “anomalous isotope effect for ozone formation”, which will be discussed further. The current work continues the theoretical investigation of this phenomenon and, hopefully, will complete the full picture of anomalous isotope effect in ozone formation.

1.2. Anomalous isotope effect in ozone formation

The oxygen atom has three stable isotopes: ^{16}O, ^{17}O, and ^{18}O. The oxygen molecule (two oxygen atoms) mostly includes ^{16}O, because this isotope is dominant in atmosphere. As the magnitude of isotope mass ratio differs just a little, the isotope ratio has been measured relative to a standard in the following way:

$$\delta^{18}\mathrm{O(per\ mil)} = [({}^{18}\mathrm{O}/{}^{16}\mathrm{O})_{\mathrm{sample}} / ({}^{18}\mathrm{O}/{}^{16}\mathrm{O})_{\mathrm{standard}} - 1] \times 1{,}000$$

Here the standard is, by convention, the standard mean ocean water (SMOW). Figures 1.1 and 1.2 show the fractionation of ^{17}O and ^{18}O in ozone, taken from the three most recent reviews.[6–8] A normal, expected for thermodynamic or kinetic processes, mass-dependent isotope fractionation $\delta^{17}\mathrm{O} \approx 0.5\delta^{18}\mathrm{O}$ has been found in any terrestrial source, like water, rocks and air (see Figure 1.1).

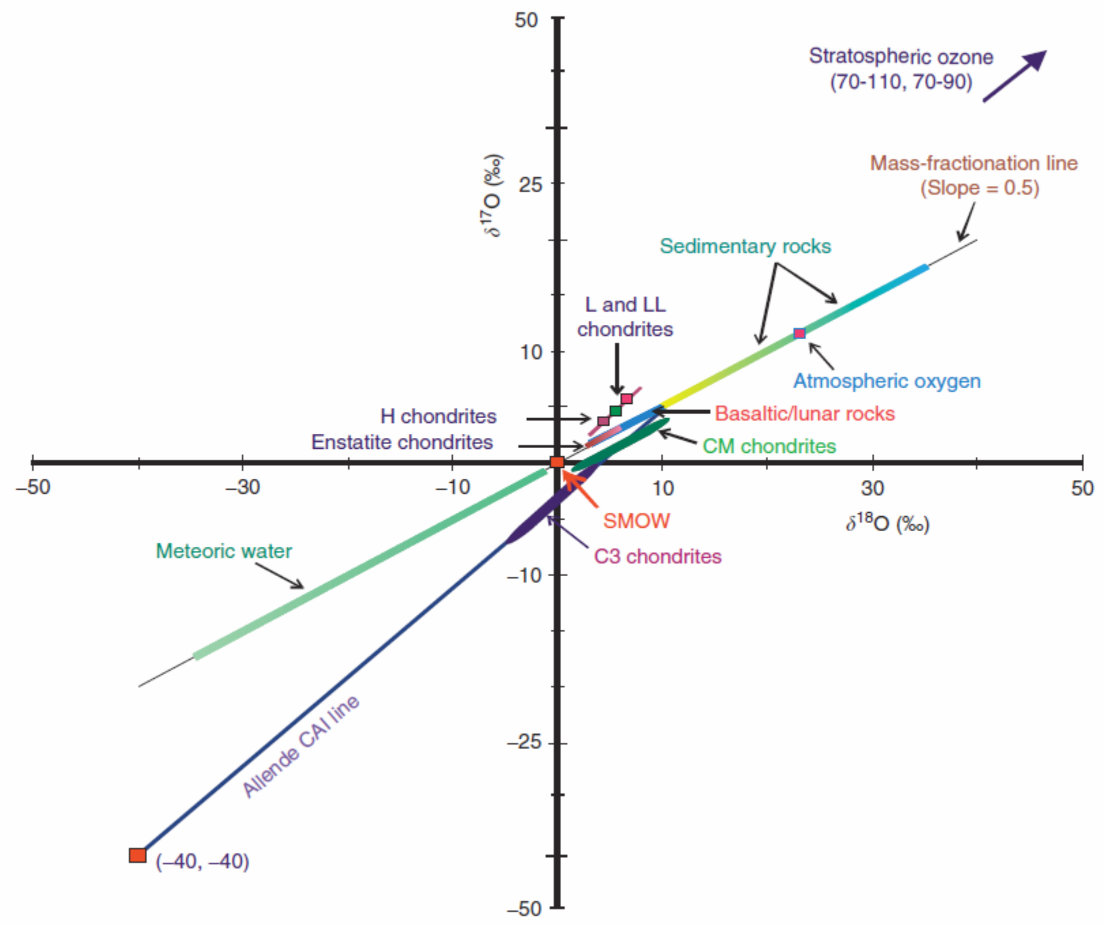

Figure 1.1. The ^{17}O and ^{18}O fractionation plot taken from different sources. All the terrestrial sources lie along mass-dependent fractionation line with the slope of 0.5. However, the isotope enrichments found in meteoritic sources and in stratospheric ozone draw up along mass-independent fractionation line with the slope of 1.0.[7]

Surprisingly, the ozone molecules in the stratosphere are heavily enriched in ^{17}O and ^{18}O, with respect to molecular oxygen,[5] (the arrow at the up-right corner of Figure 1.1). In addition to this already intriguing fact, the enrichments in ^{17}O and ^{18}O appeared to be nearly equal, as was shown in laboratory experiments of Thiemens and Heidenreich[9] in 1983. This phenomenon is called a mass-independent fractionation (MIF) of ozone. Initially, the anomalous isotope distribution $\delta^{17}O \approx \delta^{18}O$ has been found in meteorites, for example, in Allende meteorite, before Mauersberger has identified it in stratospheric ozone.[5] In fact, this inspired Thiemens to run laboratory experiments, where he obtained enormously enriched ozone from molecular oxygen. On the Figure 1.2, it is clearly seen that both formed ozone and residual O_2 in the reservoir follow the anomalous $\delta^{17}O \approx \delta^{18}O$ trend. This work proved that anomalous isotope effect in ozone comes from a chemical process, rather than nuclear reactions, as was thought previously.

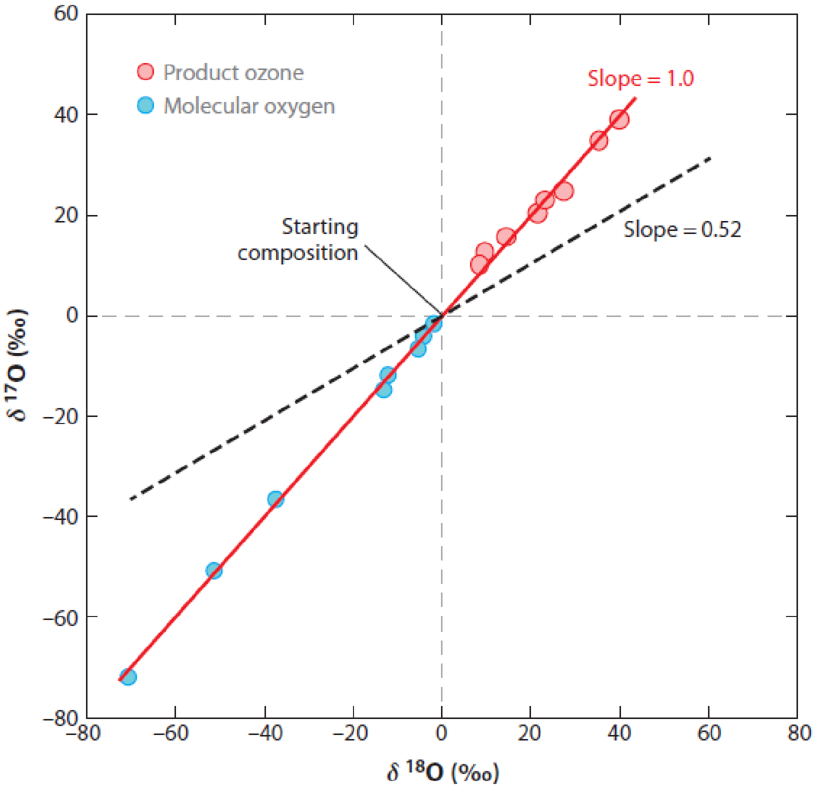

Figure 1.2. The oxygen isotope composition of ozone produced from molecular oxygen starting at (0, 0). The product ozone is equally ^{17}O- and ^{18}O-enriched, whereas the residual O_2 is by material balance, identically depleted.[8]

Interestingly, MIF takes place not only in ozone, but also in sulfur compounds.[7,10] Because the sulfur has four stable isotopes ^{32}S, ^{33}S, ^{34}S and ^{36}S, the fractionation plot becomes three-dimensional, $\delta^{33}S$ vs. $\delta^{34}S$ vs. $\delta^{36}S$ (see Figure 1.3). The sulfur fractionations measured in Archean sulfide follows a MIF trend, as seen by deviation of points from the mass-dependent line.

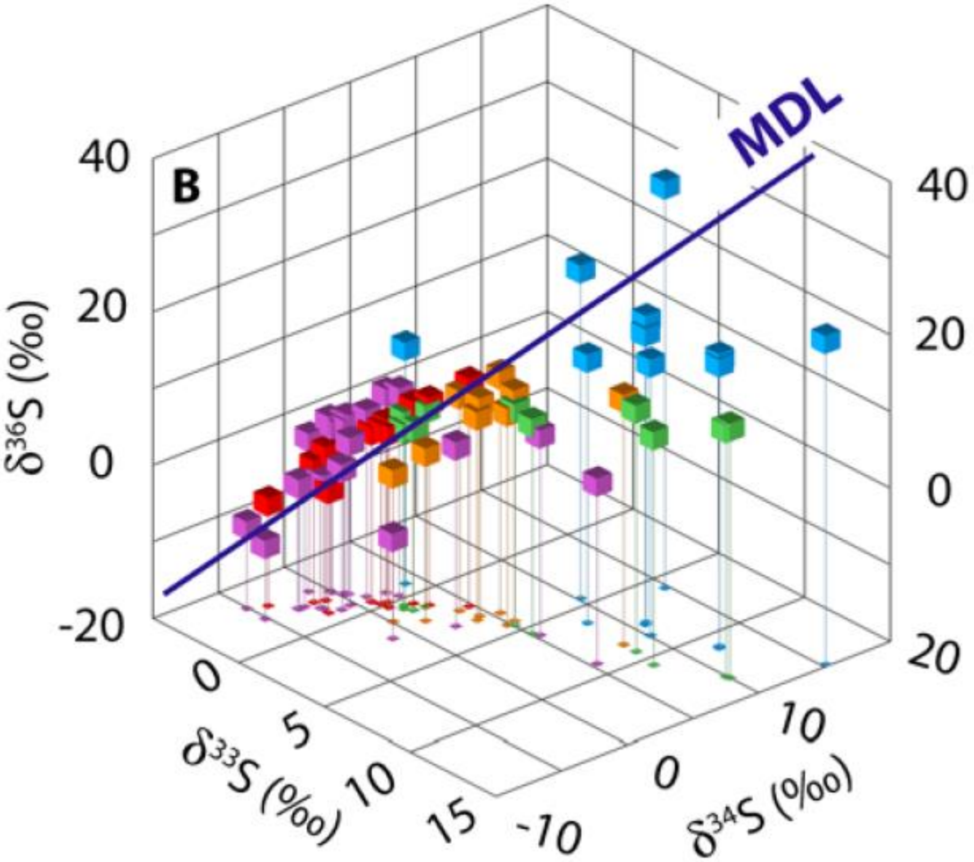

Figure 1.3. Anomalous sulfur fractionation in Archean sulfide (cubes). MDL is the mass-dependent line defined by $\delta^{33}S = 0.515\ \delta^{34}S$ and $\delta^{36}S = 1.90\ \delta^{34}S$.[10] Deviation of points from MDL is caused by MIF.

After Thiemens experiment[9] in 1983, it took about seven years for scientist to identify the reaction responsible for isotope selectivity in ozone chemistry. In 1990, the group of Mauersberger[11] experimentally showed that the ozone formation reaction is responsible for the discussed phenomena:

$$O_2 + O + M \rightarrow O_3 + M^* \tag{1.1}$$

Here an oxygen molecule O_2 recombines with oxygen atom (previously formed from another O_2 molecule broken by ultraviolet light) in a bath gas of atoms or molecules M (*e.g.* N_2, Ar). It was emphasized by many authors that in the low pressure regime (atmospheric pressure) the process (1.1) occurs in two consequent steps:

$$O_2 + O \rightarrow O_3^* \tag{1.2}$$

$$O_3^* + M \rightarrow O_3 + M^* \tag{1.3}$$

The first step is a formation of ozone molecule excited both rotationally and vibrationally. The second step is an energy transfer (ET) process, where the energy is transferred from excited zone molecule to the third body M (the quencher) that takes energy away.

The identity of M does not affect the isotope effect.[12,13] Figure 1.4 demonstrates that the absolute rate coefficient does depend on identity of the bath gas M, and the rate is higher for molecular quenchers. However, the relative rate coefficient does not. Both experimental groups continued regularly and concurrently reporting their progress in studying ozone formation, trying to measure in experiment the rates of different isotope combinations.[14,15]

In the reaction (1.1) any oxygen atom can be one of three stable isotopes ^{16}O, ^{17}O, and ^{18}O. This results in 36 different reactions. The most extensive experimental study of these reactions has been done by Janssen[16–19] in the Mauersberger group. Table 1.1 lists the measured rates of these reactions relative to the rate of $^{16}O + {}^{16}O^{16}O \rightarrow {}^{16}O^{16}O^{16}O$. From this table it becomes clear that the rates somehow depend on isotope combinations. Though differences in masses are quite small, the rates difference could reach 60%.

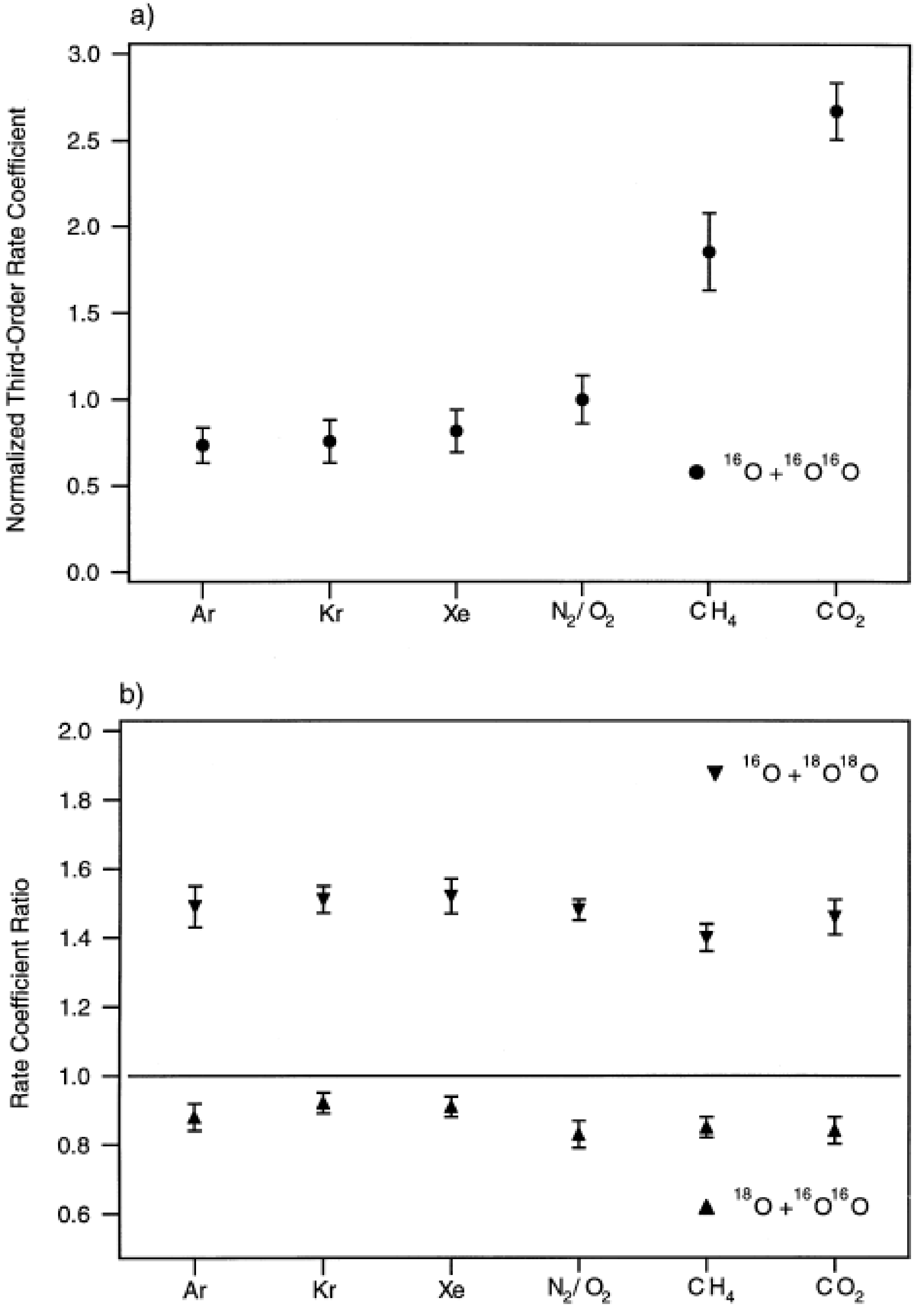

Figure 1.4. (a) Rate coefficient dependency on third body M, relative to N_2/O_2. (b) Rates coefficient ratios, $^{18}O^{16}O^{16}O$ are measured relative to $^{18}O^{18}O^{18}O$ and for $^{16}O^{18}O^{18}O$ relative to $^{16}O^{16}O^{16}O$.

Table 1.1. Measured rates for different isotope combinations, relative to the rate of $^{16}O + ^{16}O^{16}O \rightarrow ^{16}O^{16}O^{16}O$. Obtained at 267 hPa and room temperature.[16]

Mass	Reaction channel no.	Reaction	Relative rate coefficient
48	1	$^{16}O + ^{16}O^{16}O \rightarrow ^{16}O^{16}O^{16}O$	1.00
49	2	$^{16}O + ^{16}O^{17}O \rightarrow ^{16}O^{16}O^{17}O$	
	3	$\rightarrow ^{16}O^{17}O^{16}O$	
	4	$^{17}O + ^{16}O^{16}O \rightarrow ^{17}O^{16}O^{16}O$	1.03
	5	$\rightarrow ^{16}O^{17}O^{16}O$	
50	6	$^{16}O + ^{17}O^{17}O \rightarrow ^{16}O^{17}O^{17}O$	1.23
	7	$\rightarrow ^{17}O^{16}O^{17}O$	
	8	$^{17}O + ^{16}O^{17}O \rightarrow ^{17}O^{16}O^{17}O$	
	9	$\rightarrow ^{17}O^{17}O^{16}O$	
	10	$^{16}O + ^{16}O^{18}O \rightarrow ^{16}O^{16}O^{18}O$	1.45
	11	$\rightarrow ^{16}O^{18}O^{16}O$	1.08
	12	$^{18}O + ^{16}O^{16}O \rightarrow ^{18}O^{16}O^{16}O$	0.92
	13	$\rightarrow ^{16}O^{18}O^{16}O$	0.006
51	14	$^{17}O + ^{17}O^{17}O \rightarrow ^{17}O^{17}O^{17}O$	1.02
	15	$^{16}O + ^{17}O^{18}O \rightarrow ^{16}O^{17}O^{18}O$	
	16	$\rightarrow ^{16}O^{18}O^{17}O$	
	17	$\rightarrow ^{17}O^{16}O^{18}O$	
	18 to 23	six similar reactions	
52	24	$^{16}O + ^{18}O^{18}O \rightarrow ^{16}O^{18}O^{18}O$	1.50
	25	$\rightarrow ^{18}O^{16}O^{18}O$	0.029
	26	$^{18}O + ^{16}O^{18}O \rightarrow ^{18}O^{16}O^{18}O$	1.04
	27	$\rightarrow ^{18}O^{18}O^{16}O$	0.92
	28	$^{17}O + ^{17}O^{18}O \rightarrow ^{17}O^{17}O^{18}O$	
	29	$\rightarrow ^{18}O^{17}O^{18}O$	
	30	$^{18}O + ^{17}O^{17}O \rightarrow ^{18}O^{17}O^{17}O$	1.03
	31	$\rightarrow ^{17}O^{18}O^{17}O$	
53	32	$^{17}O + ^{18}O^{18}O \rightarrow ^{17}O^{18}O^{18}O$	1.31
	33	$\rightarrow ^{18}O^{17}O^{18}O$	
	34	$^{18}O + ^{17}O^{18}O \rightarrow ^{18}O^{17}O^{18}O$	
	35	$\rightarrow ^{18}O^{18}O^{17}O$	
54	36	$^{18}O + ^{18}O^{18}O \rightarrow ^{18}O^{18}O^{18}O$	1.03

[a] These rates may contain small contributions from the subsequent symmetric molecules.

[b] For reactions (10), (11) and (26), (27) involving heteronuclear oxygen molecules the relative reaction probability is shown while relative rate coefficients are obtained by dividing the quoted numbers by two.

1.3. Theoretical interpretation of anomalous isotope effect

There existed several hypotheses on correlation of measured reaction rate with some physical property or parameter that characterizes the recombination process. The rates do not correlate with masses of produced ozone isotopologues, neither with their symmetry, as it was thought previously.[12,20] The Mauersberger group discovered that the property the rates depend on is a change of O_2 zero-point energy (ΔZPE) in the atom-exchange version of step (1.3), for example for $^{16}O^{18}O^{18}O$:

$$^{16}O + {}^{18}O^{18}O \leftrightarrow ({}^{16}O\,{}^{18}O^{18}O)^{*} \leftrightarrow {}^{16}O^{18}O + {}^{18}O \qquad (1.4)$$

The oxygen molecules $^{18}O^{18}O$ and $^{16}O^{18}O$ on the left and right sides of Eq. (1.4) have different reduced masses μ, which the ZPE depends on it as seen in harmonic oscillator example:

$$\text{ZPE} = \frac{\hbar\omega}{2} = \frac{\hbar}{2}\sqrt{\frac{k}{\mu}} \qquad (1.5)$$

The ZPE difference of two possible channels of atom exchange reaction (1.4) is small, just within 22 cm^{-1}. This change makes the process (1.4) slightly endothermic or exothermic. However, it is insufficient to affect the rate and explain the isotope effect. The dependence on ΔZPE has been illustrated by Janssen[16] and is shown in Figure 1.5. Here the rates of the isotopically different reactions (Table 1.1) are plotted versus ΔZPE of atom-exchange step (4). The most pronounced feature in Figure 1.5 is a near-linear dependence on ΔZPE. Two pairs of points in corners of the plot, around $\Delta\text{ZPE} \approx \pm 22$ cm^{-1}, correspond to reactions with ^{16}O and ^{18}O. Two points at the lower left corner correspond to decrease of ZPE, specific to reactions $^{18}O + {}^{16}O^{16}O \rightarrow {}^{18}O^{16}O^{16}O$ and $^{18}O + {}^{18}O^{16}O \rightarrow {}^{18}O^{18}O^{16}O$. Two points in the upper right corner correspond to increase of

ZPE, specific to reactions $^{16}O + {}^{16}O^{18}O \rightarrow {}^{16}O^{16}O^{18}O$ and $^{16}O + {}^{18}O^{18}O \rightarrow {}^{16}O^{18}O^{18}O$. The rates of these two pairs differs by 60%, as it was mentioned earlier. Another set of four points around $\Delta ZPE \approx \pm 10$ cm^{-1} stands for the reactions that include only ^{16}O and ^{17}O. Together these two sets at $\Delta ZPE \neq 0$ set the main linear trend.

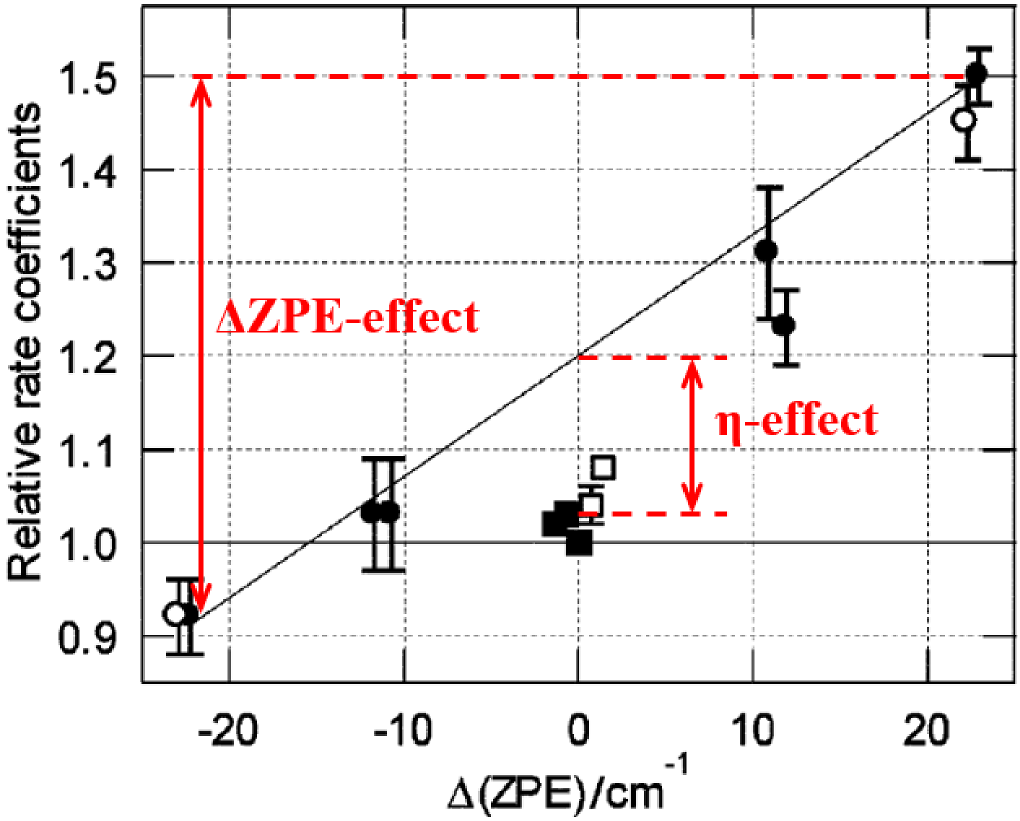

Figure 1.5. Relative rate coefficients vs. ZPE differences in oxygen molecules of the corresponding isotope exchange reactions. Exothermic or endothermic isotope exchange reactions (circles) can be distinguished from energetically neutral collisions (squares). Collisions with homonuclear diatom are shown with full symbols, while collisions with heteronuclear diatom are designated by open symbols.

The second pronounced feature in the Figure 1.5 is a deviation of five points at $\Delta ZPE = 0$ from the main trend. These points correspond to reactions forming symmetric ozone molecules, both heteronuclear, such as $^{16}O^{18}O^{16}O$ and $^{18}O^{16}O^{18}O$, and the homonuclear $^{16}O^{16}O^{16}O$, $^{17}O^{17}O^{17}O$ and $^{18}O^{18}O^{18}O$. The deviation from the trend is about 20%, which is also significant, even relative to the maximum difference 60%.

Marcus proposed[21–23] that these two features, near-linear dependence on ΔZPE and lowering of rates for points with ΔZPE = 0, result from two different phenomena. These phenomena have two distinctly different theoretical origins and may be revealed separately by the two types of experiments. The first phenomenon applies to *asymmetric* ozone molecules (as ΔZPE increases), so further we will call it ΔZPE-*effect*, while the second phenomenon is responsible for lowering the rates of formation of all *symmetric* ozone molecules. Marcus also suggested that the second effect is related to symmetry of the molecule produced in the recombination process and named it the η-*effect*.

Together all these experiments stimulated a series of theoretical studies to explain both qualitatively and quantitatively the main part of isotope effect: the ΔZPE-effect. The first study of this process was published by Marcus within framework of statistical mechanics.[21–23] He extended RRKM (Rice, Ramsperger, Kassel, Marcus) theory with several adjustable parameters in a statistical model for density of states in O_3. With this adjusted version he was able to reproduce the ΔZPE-effect in ozone quite well.

It is worth to mention, that the zero-point energy discussed here and everywhere in the related literature has nothing to do with stable O_3. Fundamental frequencies of O_3 are almost irrelevant to the recombination process, because stable O_3 is formed in the deep covalent well, more than 1 eV below the dissociation threshold. Only the zero-point energy of O_2 matters, since it defines the depth of a reaction channel. However, the proper explanation of the effect requires analysis of the metastable intermediate complexes O_3^* formed from O + O_2 collisions, which could not be obtained within a statistical theory. These complexes are quantum scattering resonances excited rotationally and vibrationally above the dissociation threshold. Their energies and lifetimes are essential to the process, and those can only be obtained from quantum dynamics theory, not from a statistical approach. Also, it should be stressed, that anomalous isotope effects in ozone should not be confused with conventional kinetic isotope effects (KIE), observed for reactions with activation barrier between the reactants and products and caused by tunneling through this barrier. The potential energy surface of ozone has no activation barrier.

1.4. The ΔZPE-effect

The first theoretical treatment of scattering resonances and analysis of their role in ΔZPE-effect has been done by Babikov *et al.* in 2003.[24–26] His work proves high importance of the resonance states in ozone chemistry. These calculated resonances exhibit very non-statistical distribution of lifetimes. Particularly, the calculated spectrum of scattering resonances appeared to be quite dense in ΔZPE energy band, relative to continuum, called “Background” in Figure 1.6.[25] Not only is the density of resonances in ΔZPE higher, but also they have more chances to be stabilized (than resonances in “Background”) as they are located much closer to bound states. Together these two factors, the density of resonances and their proximity to the bound spectrum cause a faster recombination of ^{16}O with $^{18}O^{18}O$, than ^{18}O with $^{16}O^{18}O$. Substitution of lifetimes in an ozone kinetic model, where different metastable O_3^* states are treated as different species, correctly reproduced the order of magnitude and direction of anomalous isotope effect.[26] As the study has been done on first-principal basis, it indicated the quantum mechanical origin of the anomalous isotope effect. However, calculations were done only for non-rotating ozone, i.e. for total angular momentum $J = 0$, so comparison with room temperature experiments should be done with caution. The reason was computational unaffordability. Nevertheless, the authors qualitatively showed[26] that inclusion of rotation in ozone quantum dynamics would improve the agreement with experiment. In 2009, Grebenshchikov *et al.*[27] incorporated the rotation by means of *K*-conserving approximation. Notably, the ΔZPE-effect obtained by Grebenshchikov was in excellent agreement with experiment.

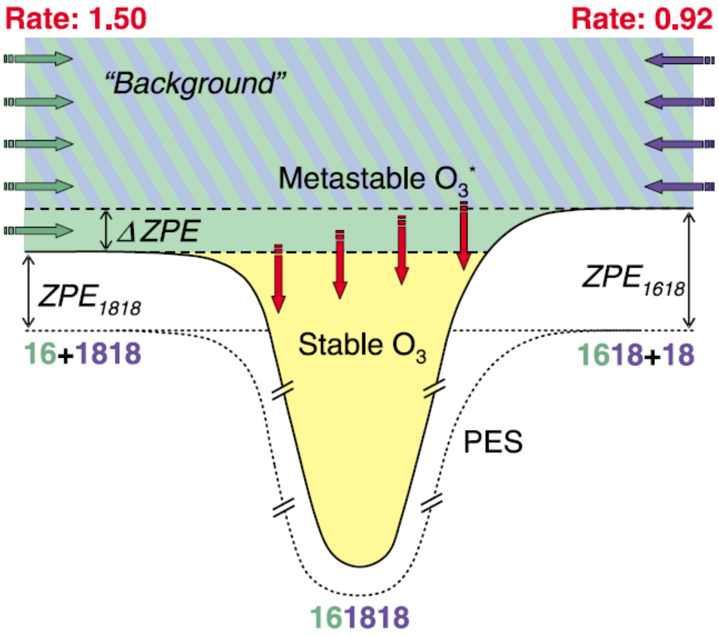

Figure 1.6. Energy diagram for $^{16}O + ^{18}O^{18}O \leftrightarrow ^{16}O^{18}O^{18}O \leftrightarrow ^{16}O^{18}O + ^{18}O$. Dotted line is PES. Solid line is PES+ZPE. Difference in reduced mass of O_2 results in ΔZPE>0. Yellow area contains stable bound states of O_3. Though some resonance states could form both channels in the "Background" area, the $^{16}O + ^{18}O^{18}O$ channel has an extra energy band ΔZPE, which contains the dense spectrum of most contributing resonances. The larger number of stabilizing states (red arrows) causes faster reaction (see experimental rates on the top).

Thus, the quantum origin of ΔZPE-effect has been justified by many authors using different theories and approaches. The near-linear dependence of recombination rates on ΔZPE has been attributed to lifetimes and energies of O_3^* and by now has been reproduced by statistical,[21–23] quantum mechanical,[24–27] semi-classical,[28–30] and even by the *ad-hoc* modified classical trajectory[31,32] models for the process (1.4).

1.5. The η-effect

The η-effect (lowering of rates for symmetric ozone formation by 20%) has not been explained within all theories enumerated above. Several attempts have been made to incorporate it. In order to reproduce experimental observations, Marcus[21–23] introduced this effect empirically, with the purpose to split oxygen isotopomers in two groups, so that the rate should be low for symmetric isotopomers, such as $^{16}O^{18}O^{16}O$ and $^{18}O^{16}O^{18}O$, and high for isotopomers, such as $^{16}O^{16}O^{18}O$ and $^{16}O^{18}O^{18}O$. In practice η-effect was just a multiplication of the rate constant by the η-factor, chosen to reproduce the experiment. The value close to $\eta = 1.2$ was obtained, which directly relates to the 20% deviation seen in the experimental results of Figure 1.5. Marcus formulated several possible sources of η-effect in his series of papers. One of suggestions[22] is that symmetry plays a role in ET reaction (1.3), where excited O_3^* is been stabilized in collision with a third-body M. Indeed, as applied to H + Ne_2 reaction[33] some state-to-state transitions are forbidden by symmetry in symmetric molecules. This in turn could lead to reduced stabilization cross section and lowered recombination rate.[34] However, such effects were not found in O_3 + Ar.[35] Another possible cause[22] is that in symmetric molecules the number of states dynamically active in the process (1.4) is lower, compared to asymmetric molecules (but these are hard to define). Also, he suggested several types of couplings that may be different in symmetric and asymmetric isotopomers of O_3 as alternative sources of η-effect, such as spin-orbit coupling[36] in the asymptotic region of the PES, resonance coupling effect,[37] chaotic behavior of trajectories at high energies[36] and, more recently, the Coriolis coupling effect.[38] Though all his ideas are of quite sound, no convincing prove has ever been given for any of these.

Other researchers influenced by Marcus' first suggestion attempted to find η-effect performing calculations of ozone stabilization step. Several attempts[39–42] have been done to treat process (1.3) using quantum mechanics. As it is a very challenging task, the inclusion of all degrees of freedom quantum mechanically was not affordable computationally. For this reason, all the models of this process proposed at that time involved significant approximations, in order to ease computational costs. For example, the first study by Charlo and Clary[39,40] used time independent coupled-channel formalism and included two approximations, the frozen-bending approximation for O_3^* and a sudden-collision assumption for O_3^* + Ar. Besides, they fixed the bending angle, so the calculations has been done in two dimensions. The next study has been done by Xie and Bowman.[41] They implemented full quantum treatment of O_3^*. However, increased computational costs resulted in a calculation of just a few number of trajectories (namely, three) with different combinations of Ar impact parameter and orientation of O_3^*. They implemented a sudden-collision assumption and did not compute resonance lifetimes. The third study has been done by Ivanov and Schinke,[42] also based the sudden-collision assumption. In addition, despite the fact that calculations converged with respect to the number of partial waves, their basis set included just the bound states of non-rotating O_3 (no scattering resonances). None of these studies revealed the origin of η-effect.

As mentioned above the exact quantum calculations are impossible for process (3) as seen on works done by the groups of Clary,[39,40] Bowman[41] and Schinke.[42] They all used the sudden collision approximation and carried out calculations for non-rotating ozone molecule ($J = 0$ only). In addition to these two approximation, they employed at least one more simplifying assumption, and none of them included lifetimes of O_3^* into their treatment of kinetics.

Five years ago, the group of Babikov[35,43–47] developed a more advanced theory to study ET process (1.3), namely – the mixed quantum/classical theory (MQCT) for collisional energy transfer and ro-vibrational energy flow. Although this theory is still approximate, it allows to improve the description of rotation and avoid the sudden collision approximation and treat the dynamics of O_3^* + Ar scattering in a time-dependent manner (classically, not quantum mechanically). This is a very reasonable way of approaching this problem, since a typical O_3^* + Ar collision is rather adiabatic than sudden. Second, they covered a large range of possible rotations, up to $J \sim 90$, and computed the rotational quenching of O_3^* in collisions with Ar. The classical treatment of rotation and translation is appropriate, since any quantum effects due to scattering of heavy Ar or due to rotation of heavy O_3^* are not expected here. At the same time, the vibrational motion of atoms within ozone molecule is treated quantum mechanically, so zero-point concept and vibrational symmetry are incorporated. The scattering resonances of O_3^* are accessible, including quantization of their energies, accurate calculations of their decay rates and the collision-induced dissociation. However, MQCT has been implemented for the dimensionally reduced model of ozone,[35,43,46] where bending angle is relaxed. This approximation resulted in “semiquantitative” agreement with experimentally observed ΔZPE- and η- effects. Namely, the both linear dependence on ΔZPE and lowering of rates for symmetric molecules was reproduced, but all absolute values of rate constants appeared to be 50 % smaller than experimental.[47] This is attributed to reduced density of states of dimensionally reduced O_3^*. Decreased density means larger energy spacing between levels in O_3^*, making state-to-state transitions harder to occur and the whole stabilization process slower. Therefore, the theoretical treatment of ozone needs to be improved by implementing full three-dimensional description of ozone molecule.

1.6. Objectives

Up to now, the MQCT[35,43–47] approach is the most successful and most accurate in description of both ΔZPE-effect and η-effect. However, the treatment of O_3 has two major problems.

First, the MQCT describes the ozone molecule using only two degrees of freedom, as the bending angle is relaxed. As explained above, to get a quantitative agreement with experiment the theory must incorporate full three-dimensional vibrational dynamics of ozone, i.e. no reduced dimensionality. Treating all three internal degrees of freedom of ozone on equal basis will give a rovibrational spectrum with proper density of states. We expect, that the substitution of this spectrum into the same kinetic model of ozone formation even without the recalculation of stabilization cross sections will significantly improve current rate constants.[47]

The extension of existing dimensionally reduced formalism[35,43–47] with a bending angle coordinate will considerably increase problem complexity, preventing calculations to be finished in reasonable time. Specifically, the computational time will scale as N^2 or N^3, where N is a number of points or basis function used to represent a new degree of freedom. Thus, we formulate the following goal:

1. **Develop an efficient theoretical method for calculations of energies and lifetimes, accurate and affordable for a broad range of rotational excitations and for all isotope compositions.**

The *efficient* calculation includes a convenient internal coordinate system, Hamiltonian expression in chosen coordinates, optimal distribution of grid points to cover the configuration space, usage of optimal bases set, efficient numerical calculation of derivatives, construction of small Hamiltonian matrix, solution for eigenvalues, efficient parallelization and load distribution scheme, the way to extract resonance lifetimes, and potential energy surface to perform calculations on.

Second, the scattering process within MQCT has one technical artifact (will be discussed later) and still has high computational cost. Both problems could be solved by simplifying the rotational description keeping the same accuracy. The formulated second goal is as follows:

2. **Develop an effective numerical approach to describe the stabilization of ozone molecule in collision with third body within MQCT.**

This required the development of frozen rotor approximation, where molecular orientation in space is fixed, however the energy exchange between rotational, vibrational, and translational digresses of freedom still occurs, allowing computing rovibrational excitation and quenching. Finally, the results of both steps 1 and 2 will be combined. We formulate the third goal as:

3. **Use computed energies and lifetimes of metastable states (goal 1) and computed stabilization cross sections (goal 2) in the kinetic model of ozone formation and calculate the rates of formation for different isotope combinations.**

This dissertation is structures as follows. Chapter 2 gives an extensive explanation of hyperspherical coordinates, used in calculations and important methodologically. The efficient numerical approach for calculations of energies and lifetimes of scattering resonances is described in Chapter 3 (Goal 1). In Chapter 4, the MQCT[35,43–47] is reviewed and a frozen rotor approximation is introduced to simplify and speedup the scattering calculations without losing much accuracy (Goal 2). The absolute rate coefficient of recombination reaction is computed in Chapter 5 and is applied to isotope problem in ozone in Chapter 6 (Goal 3). Finally, all important results and possible ways to improve the method are summarized in Chapter 7.

Chapter 2. Hyperspherical coordinates for description of ozone vibrations*

2.1. Coordinate systems for triatomic molecules

Quantum molecular dynamics in triatomic systems takes special place in the fundamental chemical theory and in the chemistry education as well, because it allows introducing and studying spectroscopy (three normal vibration modes for low-amplitude motion in ABC) and chemical reactions (large-amplitude motion leading to A + BC → AB + C), all using the smallest possible number of atoms.[48,49] Also, many important gas-phase molecules are triatomic, which makes this topic directly relevant to the real life problems in environmental chemistry,[50] atmospheric chemistry[24–26,51,52] and astrochemistry.[53,54]

Any theoretical description of a molecule starts with the choice of suitable coordinates to represent the arrangement of atoms in ABC, which gives the molecular shape or geometry. Three coordinates are needed in order to describe a shape of nonlinear triatomic molecule, which is the number of internal degrees of freedom, $3N - 6$, with N being the number of atoms. For example, familiar to every chemist are the *valence* coordinates $\{r_1, r_2, \gamma,\}$ which consist of two bond lengths in ABC and the angle between the two bonds. Another well-known coordinates are the *normal-mode* coordinates $\{\xi_1, \xi_2, \xi_3,\}$ which represent the collective motion of all three atoms leading to symmetric stretching, asymmetric stretching and bending of ABC. When the motion of atoms in a molecule is treated with quantum mechanics the vibrational wave function depends on

---

[*] Teplukhin A.; Babikov D., *Chem. Phys. Lett.*, 614, 99 (2014), *J. Chem. Educ.*, 92(2), 305 (2015)

these coordinates, $\psi(r_1, r_2, \gamma)$, and the vibrational Hamiltonian operator $\hat{H}$ in the Schrodinger equation acts on these coordinates, $\hat{H}\psi = E\psi$. It is important to note, however, that neither the valence nor the normal-mode coordinates are employed for accurate numerical studies of triatomics, because the simple valence coordinates result in the extremely complicated Hamiltonian operator,[55] while the normal-mode representation is an approximation which breaks down at higher levels of vibrational excitation and/or for anharmonic potentials.

Although a search for the best coordinates still continues,[56] several coordinates have been identified as convenient and have been used extensively in molecular calculations. Namely, the Jacobi coordinates $\{R, r, \Theta\}$ are probably the most popular, where r is the bond length of a diatomic fragment of the molecule, say BC, while R is the distance from A to the center-of-mass of BC, and Θ is the angle between them (see Figure 2.1). The Hamiltonian operator is rather simple in these coordinates and they work well in many cases, particularly for description of molecular vibrations in ABC (see Figure 2.2) or non-reactive elastic and inelastic scattering of A + BC.[57] However, there are situations when Jacobi coordinates are not the best choice. For example, if only the A + BC arrangement diatomic basis is used, and the ABC motion is floppy and anharmonic with vibrational character very different than that of BC, then the calculation of the ABC spectra may converge slowly or not at all. Besides the bound states, Jacobi coordinates are also used for description of chemical reactions like A + BC → AB + C[58] but in this case their intrinsic drawback shows up. It appears that a set of Jacoby coordinates introduced for the entrance channel of reaction, A + BC (see Figure 2.3a), becomes inappropriate for the exit channel of the reaction, AB + C. Indeed, at large AB + C separation the diatomic fragment AB is not described by any internal coordinate, but corresponds to numerically unstable geometry described by a very small value of angle $\Theta \rightarrow 0$ and large value of $r \rightarrow 2R$ (see Figure 2.3b). Asa consequence, the convergence of calculations could be very poor again.

This is inconvenient and it would often be beneficial to use some other coordinates that threat all the reaction channels on equal footing. Such coordinates were developed by Pack and Parker and are known as *adiabatically-adjusting principal-axes hyperspherical* (APH) coordinates.[59–61] They adjust smoothly from one arrangement of atoms to another arrangement and describe well not only the reagent channel A + BC, but also the product channel AB + C, and even the second product channel AC + B (in the cases when the second product channel is chemically relevant, see Figure 2.3c). Furthermore, the Hamiltonian operator is simple in the APH coordinates.[60]

Advantages of the APH coordinates for triatomic systems are known[60] and several examples can be drawn from the recent literature where molecular simulations successfully employ the APH coordinates. For example, spectroscopy of O_3, N_3, H_3, Ar_3, Ne_3,Ne_2H, HeNeH molecules,[26,51,62–66] molecular ions N_3^+, H_3^+, D_3^+,HCO^+, DCO^+, H_3^-, D_2H^-, H_2D^-,[48,53,54,67] and pseudo-triatomic Cl−CH3−Br,[68] have been studied using the APH coordinates. The exchange reactions $H + O_2 \leftrightarrow OH + O$, $O + H_2 \leftrightarrow OH + H$, $O + O_2 \leftrightarrow O_2 + O$, $H + H_2 \leftrightarrow H_2 + H$, $F + H_2 \leftrightarrow FH + H$, $D + H_2 \leftrightarrow DH + H$, $H + D_2 \leftrightarrow HD + D$, and $Cl^- + CH_3Br \rightarrow ClCH_3 + Br^-$ [26,49,50,61,68–72] have also been studied using the APH coordinates. Still, one should admit that the APH coordinates are much less popular, compared to the simpler but more limited Jacobi coordinates.

One reason for this is that the formalism of adiabatic adjustment is mathematically involved[60] which creates a barrier to understanding, particularly by students at the beginning of their computational research projects. In order to simplify introduction to the APH coordinates we created an interactive desktop application APHDemo that allows seeing a triatomic system on the screen, dragging atoms by mouse from one arrangement to another and watching how the APH coordinates adjust continuously, for example, from the reagent channel to the product channel, through the reaction intermediate. The Jacobi coordinates can also be made visible for comparison, which allows understanding better their drawbacks, and emphasizing advantages of the APH coordinates.

The major area of application of this program is, probably, in the educational process. We created several animations that illustrate typical examples of vibrational dynamics and can be used in the classroom presentation of the APH coordinates. However, this tool may also be rather handy to those who plan employing the APH coordinates in their research, particularly to graduate to students and postdocs.

2.2. APH coordinates

Pack and Parker[60] emphasized a link between the simple Jacobi coordinates and the APH coordinates, and described transformation from Jacobi to APH. It is convenient to introduce vector notation $\{\mathbf{R}, \mathbf{r}\}$ in addition to $\{R, r, \Theta\}$. Here $R = |\mathbf{R}|$, $r = |\mathbf{r}|$, while angle Θ can be easily determined from coordinates of vectors **R** and **r**. Next step is to introduce the *mass-scaled* Jacobi coordinates $\{S, s, \Theta\}$, or $\{\mathbf{S}, \mathbf{s}\}$ in matrix notation, as follows:

$$\mathbf{S} = d\,\mathbf{R}, \quad \mathbf{s} = d^{-1}\mathbf{r}\,. \tag{2.1}$$

Here

$$d = \left[\frac{m}{\mu}\left(1 - \frac{m}{M}\right)\right]^{1/2} \tag{2.2}$$

is a scaling factor, where *m* is the mass of atom that defines the arrangement (*e.g.*, atom A for arrangement A + BC), μ is a three-body reduced mass and *M* is a total mass:

$$\mu = \left[\frac{m_A m_B m_c}{M}\right]^{1/2}, \qquad M = m_A + m_B + m_C\,. \tag{2.3}$$

The mass-scaled Jacobi vectors {**S**, **s**} do not differ much from the original Jacobi vectors {**R**, **r**} because for natural triatomic molecules the value of scaling factor is always close to one, $d \approx 1$.

The next step is to define a set of new coordinates {**Q**, **q**} obtained by rotation of {**S**, **s**} as follows:

$$\begin{pmatrix}\mathbf{Q}\\ \mathbf{q}\end{pmatrix} = \mathbf{T}\begin{pmatrix}\mathbf{S}\\ \mathbf{s}\end{pmatrix}, \tag{2.4}$$

where **T** is a kinematic rotation matrix that depends on kinematic rotation angle χ, so, $\mathbf{T}(\chi)$. The value of χ is chosen such that vector **Q** would point along one of the *principal axes* of inertia for ABC, namely, the one with the smallest moment of inertia. Thus, in the reagent channel A + BC vector **Q** would approach vector **S**, but in the product channels AB + C or AC + B vector **Q** would significantly deviate from the Jacobi vector **S**. Pack and Parker showed analytically[60] that such value of χ maximizes the value of $Q = |\mathbf{Q}|$ and changes *adiabatically* (smoothly) between the various atom arrangements.

The last step is to convert a set of three coordinates $\{Q, q, \chi\}$ into a set of three *hyper-spherical* variables $\{\rho, \theta, \chi\}$ called APH coordinates, and to establish analytic transformation between Jacobi coordinates $\{S, s, \Theta\}$ and the APH coordinates $\{\rho, \theta, \chi\}$. Pack and Parker showed that:

$$\begin{aligned} \rho &= (S^2 + s^2)^{1/2} \\ \tan\theta &= \frac{[(S^2 - s^2)^2 + (2\mathbf{S}\cdot\mathbf{s})^2]^{1/2}}{2 S\, s \sin\Theta} \\ \tan(2\chi) &= \frac{2\mathbf{S}\cdot\mathbf{s}}{S^2 - s^2} \end{aligned} \tag{2.5}$$

The variable ρ, called hyperradius, represents the overall “size” of the ABC system, while two hyperangles θ and χ define “shape” of the ABC. For low-amplitude vibrational motion in a triatomic molecule the APH coordinates are similar to the normal-mode coordinates: ρ describes symmetric stretching, while θ and χ are responsible for the bending motion and asymmetric stretching, respectively. However, for large-amplitude vibrational motion ρ describes dissociation (*e.g.*, to A + BC), θ describes vibration of the diatomic product (*e.g.*, BC), while χ describes permutations of atoms or pseudo-rotation (*e.g.*, A–B–C to C–A–B and to B–C–A, see Ref. 48).

2.3. APHDemo application

APHDemo is a desktop Windows application developed to demonstrate the essence of APH coordinates. It shows how the adjustment of APH coordinates occurs in response to the motion of atoms in ABC. The window screenshot is shown in Figure 2.1. The original Jacobi vector pair {**R**, **r**} for the arrangement A + BC is shown in red. The APH vector pair {**Q**, **q**} is shown in blue. Solid lines correspond to **R** and **Q**, while dashed lines correspond to **r** and **q**. All vectors lie in the plane of the triatomic molecule. The values of APH variables $\{\rho, \theta, \chi\}$ are printed in the top-left corner. User can move atoms A, B or C with computer mouse and turn on and off the coordinate sets to show

(Jacoby or APH, or both) using checkboxes. In addition, a track bar is available to animate a pseudo-rotational collective motion of all three atoms.

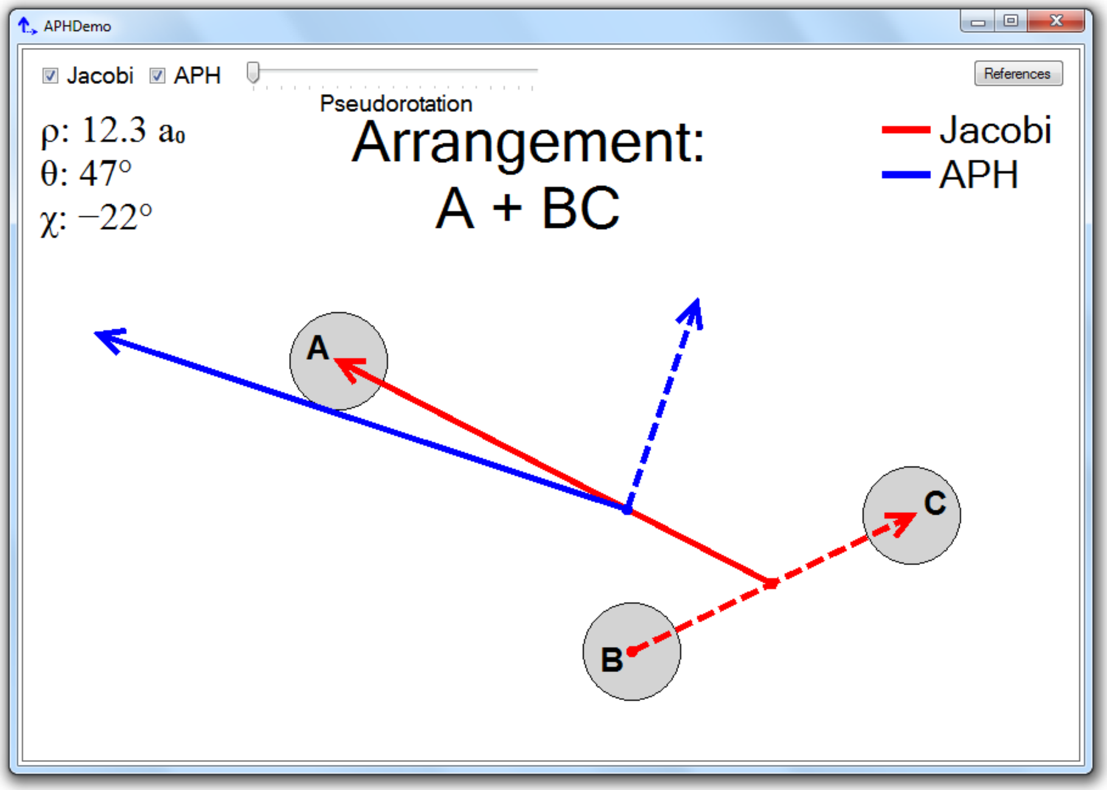

☑ Jacobi ☑ APH

ρ: 12.3 a_0
θ: 47°
χ: −22°

Arrangement:
A + BC

Figure 2.1. Screenshot of the APHDemo application. Checkboxes in the upper-left corner allow displaying Jacobi (red) or APH (blue) vectors, or both simultaneously. The values of hyperspherical variables $\{\rho, \theta, \chi\}$ are conveniently displayed. User can drag atoms with a mouse. Instantaneous arrangements of atoms are automatically labelled as “ABC”, in the case of a molecule or transient species, or “A + BC”, *etc.*, in the asymptotic case of chemical reagents/products.

Dragging atoms allows going through all possible configurations of ABC. Figure 2.2 illustrates the low-amplitude molecular vibrations, when three interatomic distances are all comparable. Three frames of the figure correspond to three possible cases of one atom (A, B or C) being slightly further from the other two atoms, for an arbitrary shape of ABC. We see that here the Jacobi coordinates (red) are quite appropriate for description of all three cases. However, the APH coordinates (blue) have one advantage. Notice that we intentionally chosen the three shapes in Figure 2.2 being congruent. Jacobi coordinates do not “see” this equivalence and describe three shapes by somewhat different values of $R = |\mathbf{R}|$ and $r = |\mathbf{r}|$. In contrast, the APH coordinates “recognize” the equivalence and describe all three arrangements by the same values of $Q = |\mathbf{Q}|$ and $q = |\mathbf{q}|$. This has important applications in spectroscopy, where symmetry is the factor determining the allowed state-to-state transitions.[48]

Figure 2.3 summarizes important concepts for the large-amplitude motion of atoms, when one atom is far from the other two (in the entrance/exit channel of a reaction). We see that in the reagent channel A + BC the APH vectors $\{\mathbf{Q}, \mathbf{q}\}$ are similar to Jacobi vectors $\{\mathbf{R}, \mathbf{r}\}$ and either coordinates describe the triatomic system well (see Figure 2.3a). Namely, both $\mathbf{q}$ and $\mathbf{r}$ describe vibration of diatomic reagent (the BC distance), while both $\mathbf{Q}$ and $\mathbf{R}$ describe collision of the two reagents (the A-BC separation). However, in the product channels neither of Jacoby vectors describes the diatomic product (see Figure 2.3 b and c). Indeed, in the product channels $|\mathbf{r}|$ becomes very large and describes separation of two products (AB–C or AC–B distances), while $R \rightarrow r/2$, so that asymptotically the vector $\mathbf{R}$ becomes obsolete. In contrast, the APH vectors $\{\mathbf{Q}, \mathbf{q}\}$ remain meaningful even in the product channels. From Figure 2.3 we see that vector $\mathbf{q}$ always remains small and always describes the diatomic fragment, either reagent or product, depending on the channel. At the same time, vector $\mathbf{Q}$ always remains large and plays a role of the universal reaction coordinate. This is a clear and significant advantage of the APH coordinates.

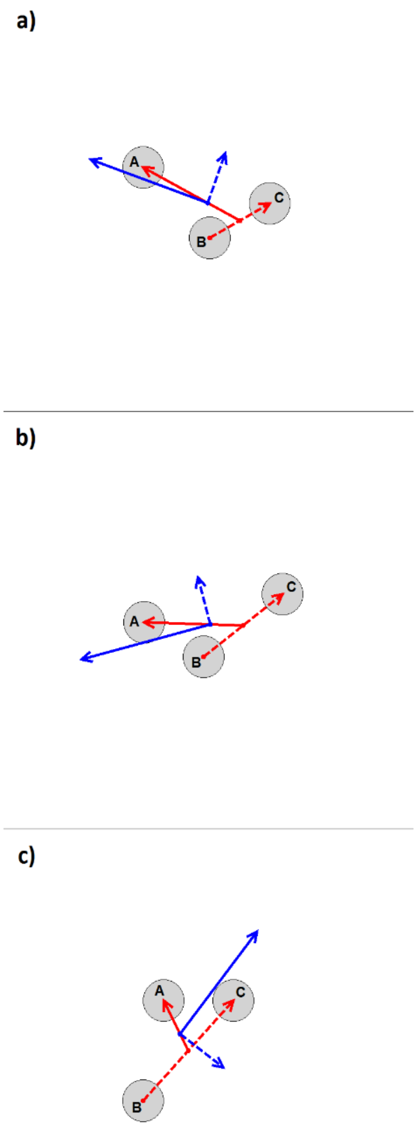

Figure 2.2. Examples of atom arrangements due to low-amplitude vibrational motion in the triatomic ABC system and their description using Jacobi (red) and APH (blue) vectors. Note that three physically different arrangements correspond to congruent triangles. Lengths of APH vectors remain the same, which emphasizes symmetry. Jacobi vectors do not have this advantage.

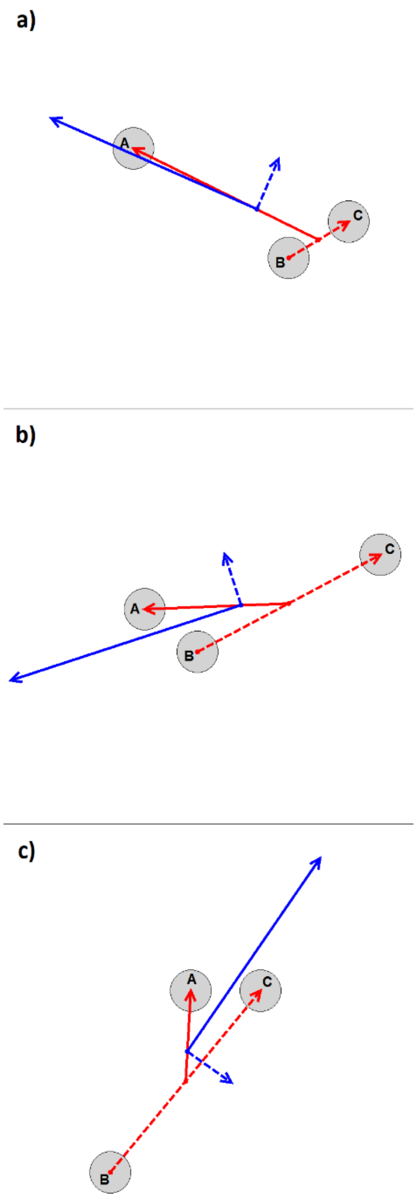

Figure 2.3. Examples of atom arrangements due to high-amplitude vibrational motion leading to A + BC, AB + C and AC + B reagents/products, and their description using Jacobi (red) and APH (blue) vectors. Note that in the product channels AB + C and AC + B the Jacobi vectors defined for the reactant channel A + BC become inappropriate. In contrast, the APH coordinates always adjust to the instantaneous arrangement of atoms.

One other capability of the APHDemo is to illustrate pseudo-rotational motion. During this process all three atoms in ABC move on circles of the same radius, but with phase shifts of 120° with respect to each other. Using the track-bar at the top of the APHDemo window (see Figure 2.1), user can initiate the trajectory of such collective motion. During pseudorotation the APH vectors {**Q**, **q**} simply rotate around the center of mass of ABC, which corresponds to the change of hyperangle χ only, with no changes of ρ and θ. One can see that it takes two full turns of the atoms in order for the APH vectors {**Q**, **q**} to return into their original position. This corresponds to the range of hyperangle $-180° < \chi < +180°$, which includes both roots of χ, as it was emphasized by Parker and Pack.[60] This last property has important implications in dynamics around the conical intersections and in theoretical treatment of the geometric phase effect.[62,73]

2.4. How this application can be used for research and in a classroom

The users of APHDemo are encouraged to try various arrangements of atoms in ABC. When the atoms are being moved, the set of blue vectors {**Q**, **q**} will stretch/compress but also rotate, while the set of red vectors {**R**, **r**} will primarily stretch/compress with little to no rotation. For some arrangements the APH vectors {**Q**, **q**} will become quite similar to Jacobi vectors {**R**, **r**}, but they will be very different for other arrangements, as discussed above. We created several representative animations that can be viewed and downloaded from the website of Chemical Physics Letters, where this chapter was published.[74] Those animations include trajectories for the local and normal mode vibration of ABC, for non-reactive scattering of A + BC, for reactive process A + BC → AB + C, and for pseudo-rotation in A–B–C. In addition, with

APHDemo it becomes easier to understand what shapes correspond to the limiting values of the APH hyperangles. For example, the equilateral configuration of ABC corresponds to $\theta = 0°$, while linear ABC is described by $\theta = 90°$. Isosceles shapes correspond to $\chi = 0°, \pm 60°, \pm 120°$. All these arrangements can be easily explored using our interactive tool, and the corresponding values of ρ, θ and χ can be read from the top-left corner of the screen (see Figure 2.1).

In addition to just visualization, the APHDemo can help in explaining, and potentially discovering new reaction mechanisms and pathways, such as roaming. It could be rather useful for mode assignment of vibrational states in both Jacobi and APH coordinates, as the user could simply drag back-and-forth any atom and observe corresponding changes of the coordinates.

The application was written in C# using Math.NET Numerics library[75] to perform vector operations. APHDemo requires Microsoft.NET Framework 4.5,[76] usually available in standard installation. The executable file is also available for download from the website of Chemical Physics Letters[74] and from my personal website.[77] It is sufficient to download this file (e.g., to a Desktop of a PC) and run it with double-click of the mouse.

2.5. Visualization of potential energy surface

The ansatz of computational chemistry is the Born-Oppenhimer approximation[78] that splits the overall molecular problem onto the electronic motion part and the nuclear motion part. The electronic part of the problem is solved first, for fixed positions of the nuclei, which provides the potential energy function V that governs the motion of nuclei. It is often said that electrons create the potential energy landscape on which for nuclei to move.[79] However, comparison of the potential energy function with a landscape is good only to a certain extent. When we say “landscape”, this usually means a two-dimensional potential energy surface, for example, $V(x, y)$. However, dimensionality of the potential energy function in molecules is usually higher than two; thus, the number of internal degrees of freedom for an N-atomic nonlinear molecule is $3N - 6$. Even for a triatomic molecule, for example, H_2O or O_3, the potential energy function is a function of three variables, $V(x, y, z)$, which is a hypersurface, rather than a surface.

A question of visualization of this hypersurface arises because in our three-dimensional world, one can plot, see, and comprehend a function of two variables at most, $V(x, y)$. One cannot plot a function of three or more variables. It is frustrating to realize that we are so limited in our abilities. Visualization of the potential energy function in its full dimensionality is impossible even for the smallest polyatomic molecules, the triatomics. This creates some barrier to understanding collective atomic motion in molecules, such as nonlocal vibrational modes, or trajectories of atoms in chemical reactions because all of these processes are driven by the potential energy hypersurface.

Several approaches are used to overcome this natural barrier. We can reduce the dimensionality of the potential energy function by freezing some internal degrees of freedom. This is equivalent to slicing the hypersurface and viewing one slice at a time. For example, in the case of O_3 described using valence coordinates,[80] the full dimensional potential energy function is a function of three variables, $V(R_1, R_2, \alpha)$, where R_1 and R_2 are bond lengths, and α is the bending angle. Freezing or fixing the value of R_1 (e.g., equal to the equilibrium bond length in O_3) yields a two-dimensional potential energy surface

$$V = V(R_2, \alpha)_{R_1 = R_{eq}} \tag{2.6}$$

that can be easily plotted and used for analysis of some processes, such as homolytic bond dissociation in ozone, $O_3 \rightarrow O_2 + O$, or inelastic scattering of oxygen atom by oxygen molecule, O_2 (j) +O → O_2 (j') + O. This works fine, but one should be aware of limitations of this approach. For example, such a dimensionally reduced potential energy surface would be useless for analysis of the atom exchange process in ozone, which is the simplest example of a reactive process: $O_2 + O \rightarrow O + O_2$. Indeed, in this reaction, both bond lengths change (e.g., the value of R_1 growth from R_{eq} to ∞, while the value of R_2 decreases from ∞ to R_{eq}), so freezing one of them is inappropriate.

Another known method of reducing dimensionality of the potential energy hypersurface is to relax some degrees of freedom. For example, in the case of ozone, one could relax the value of the bending angle α by minimizing energy for each pair of chosen values of R_1 and R_2, which produces a two dimensional potential energy surface:[35]

$$V = V(R_1, R_2)_{\alpha = f(R_1, R_2)} \tag{2.7}$$

Such surface can be easily plotted and used to visualize the reactive atom exchange process, $O_2 + O \rightarrow O + O_2$, but again, it is limited to the reaction path only, and some important information is missing. Namely, the zero-point energy of vibration is entirely lost.[35] The processes of O-atom permutation and pseudorotation[48,81] are also impossible to see on such a dimensionally reduced potential energy surface.

It would be beneficial to see all features of the global potential energy function at the same time, which can include deep covalent wells, transition states, shallow van der

Waals wells (usual in the channel regions), and the entrance/exit reaction channels themselves. It would be nice to have a method that allows visualization of the potential energy function in its full dimensionality, without reductions, at least for triatomic molecules. Seemingly simple, triatomic molecules still hold many puzzles, and their theoretical description is still challenging, particularly from standpoint of quantum molecular dynamics. Calculations of precise rotational−vibrational spectra, highly excited delocalized states near dissociation threshold, and scattering resonances above the threshold are just few examples. On the practical side, triatomic molecules play crucial roles in Earth’s atmosphere, environment, and interstellar medium.[50,51,53]

In this respect, the isoenergy approach introduced earlier by Babikov[82,83] that allows visualization of the potential energy function of a triatomic molecule in its full dimensionality in 3D space as a volume, not as a surface, provides an alternative method of presentation, addressing the above-mentioned concerns. With this approach, the potential energy wells look like “chambers”, while the transition state regions look like narrow “passages” between them, all in 3D space; reaction channels look like “tunnels”. Most importantly, we propose the use of 3D printing capabilities to create handy models of such isoenergy objects that can be taken into hands and inspected in detail from any perspective. Our own experience with such 3D models shows that they are rather useful in teaching and even in research.

2.6. Isoenergy approach applied to ozone

Isosurfaces are routinely used to visualize molecular orbitals or electronic densities. In those cases, a small, minimal value $\rho_{\min}$ of the electron density ρ is chosen, and a surface is built in 3D space (x, y, z) that connects all points in space with $\rho = \rho_{\min}$, the isosurface. Points with $\rho < \rho_{\min}$ are outside of the isosurface, and this part of space is made transparent to the observer. Points with $\rho > \rho_{\min}$ are inside of the isosurface, and they are invisible to the observer. They can be made visible by plotting another isosurface with a larger value of $\rho_{\min}$.

Our approach to visualizing the potential energy function of a triatomic molecule is very similar, but it is inverted in a sense. Namely, a large, maximum value of the potential energy $V_{\max}$ is chosen based on physical considerations. This can be a thermal energy of a chemical reaction, collision energy of a trajectory, or energy eigenvalue of a quantum state. Then, a 3D potential energy function $V(x, y, z)$ is visualized as follows: all points in 3D space with $V > V_{\max}$ are made transparent to the observer. This part of the configuration space is inaccessible to the motion of nuclei in a chemical process we consider (at least classically, neglecting the tunneling effects); thus, it is assumed to be unimportant (or less important), and that is why it is made transparent. In contrast, all points in 3D configuration space with $V < V_{\max}$ are made opaque because they are accessible to the motion of nuclei. The Cartesian variables (x, y, z) in physical 3D-space are used to represent some internal vibrational coordinates used for theoretical description of a molecule. For example, this may be the valence coordinates (R_1, R_2, α), the normal mode coordinates (ξ_1, ξ_2, ξ_3), or the hyperspherical coordinates (ρ, θ, φ) that we prefer for several reasons.[24,59,60,74]

By using this method, an observer can see the potential energy function as a continuous volume structure in 3D space, as shown in Figure 2.4, where we applied the isoenergy approach to the potential energy function of O_3 molecule expressed in the simplest valence coordinates, $V(R_1, R_2, \alpha)$. The bond lengths R_1 and R_2 of O_3 are plotted along x and y, while the value of the bending angle α is plotted along z. The ranges of coordinates in Figure 2.4 are $1.0 \leq R \leq 5.5\ a_0$ and $75° \leq \alpha \leq 180°$. This covers the deep covalent well region seen in the middle of Figure 2.4 as a "lobe", two transition states seen as the "bottlenecks", and two shallow van der Waals interaction regions – the "wings". If the vibrational energy of O_3 is low, the motion of its nuclei is restricted to the covalent well inside of the lobe only (the minimum energy point is at $R_1 = R_2 = 2.4\ a_0$ and $\alpha = 117°$). The transition state point, the bottleneck, can be reached by adding more vibrational energy to O_3 in order to stretch one of its bonds to $R = 3.5\ a_0$. Since two bonds in O_3 are equivalent, one can stretch either R_1 or R_2, which produces a symmetric structure in Figure 2.4 with two bottlenecks. Outside the transition state, when $R > 3.5\ a_0$, O_3 transforms into a van der Waals complex between O and O_3. Imagine that one could label the terminal atoms in O_3 using isotopes, which would produce $^{17}O^{16}O^{18}O$. Then, two possible van der Waals complexes would be $^{17}O\cdots{}^{16}O^{18}O$ and $^{17}O^{16}O\cdots{}^{18}O$, formed in the left and right wings in Figure 2.4, respectively. Note also that these wings cover a wide range of α, which means that the van der Waals complex is floppy, with large-amplitude bending motion allowed. In contrast, the lobe is compact along α, which means that bending the covalently bound O_3 results in significant energy increase (reflected by transparent areas below and above the lobe in Figure 2.4) and does not lead to any transition state. It is quite amazing that all of these features of the potential energy function can be seen in Figure 2.4.

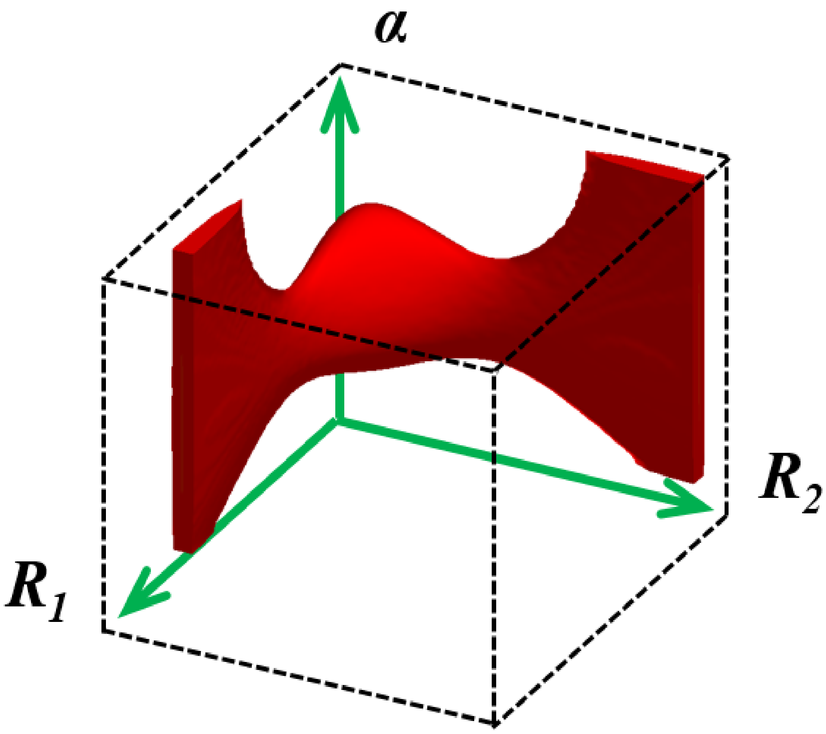

Figure 2.4. Isoenergy volume for O_3 molecule using valence coordinates. V_{max} is chosen at the dissociation threshold of O_3, which allows seeing the covalent well, the transition states and the van der Waals interaction regions.

It is also instructive to inspect the cut-outs of the volume structure in Figure 2.4. One example is shown in Figure 2.5, where the part of potential energy function with $\alpha >$ 117° is removed. The remaining piece exhibits a slice with a color map that corresponds to dimensionally reduced 2D potential energy surface $V(R_1, R_2)$ with the bending angle fixed at $\alpha = 117°$. Here, one can see a large gradient of potential, reflected by color change, with violet showing the minimum energy point of the covalent well. This slice is what is usually called the potential energy surface. Clearly, many features of the potential energy function discussed in the previous paragraph are missing if only this 2D slice is examined.

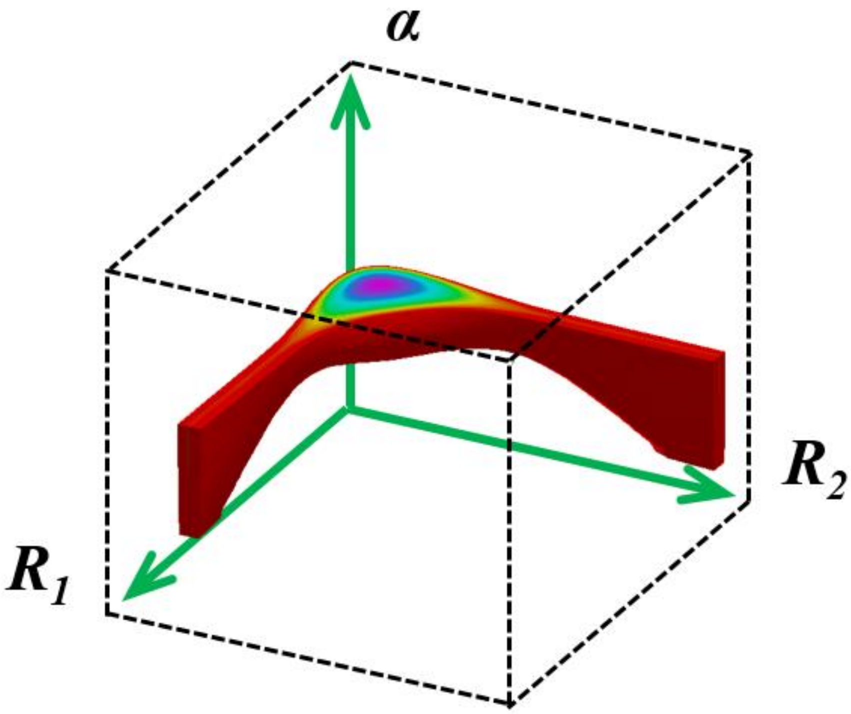

Figure 2.5. Slice through the covalent O_3 well of the isoenergy volume structure from Figure 2.4. Gradient of potential in the well is reflected by the color change. The minimum energy point is seen.

The shape of isoenergy volume for the potential energy function of O_3 expressed in the valence coordinates $V(R_1, R_2, \alpha)$ is relatively easy to understand (Figures 2.4 and 2.5) mainly because these coordinates are often used to represent the familiar molecular parameters, such as chemical bonds and bending angle. The isoenergy approach becomes even more useful in the cases when we have to deal with less intuitive coordinates such as hyperspherical coordinates discussed in the next section.

2.7. Global potential of ozone in the hyperspherical coordinates

Hyperspherical coordinates (ρ, θ, φ) have a number of advantages over other choices.[59,60,74] The most important is, perhaps, the simplicity of the rotational–vibrational Hamiltonian operator,[59,60] but this advanced topic is not covered here. Relevant to visualization of the potential energy function $V(\rho, \theta, \varphi)$ is the ability of the hyperspherical coordinates to describe, on equal footing, different arrangements of atoms in a triatomic molecule and different dissociation channels, emphasizing molecular symmetry globally, through the entire physical range of molecular shapes.[74]

For example, one must realize that the images of Figure 2.4 and Figure 2.5 represent only a small part of the global potential energy function. When the values of bond lengths are increased even further, beyond $R = 5.5\ a_0$, the dissociation channels of ozone $^{17}O^{16}O^{18}O$ onto ^{17}O + $^{16}O^{18}O$ and $^{17}O^{16}O$ + ^{18}O are observed. Furthermore, for the large-amplitude vibrational motion, the third dissociation channel, which gives $^{17}O^{16}O$ + ^{18}O, is also relevant as well as two ozone isomers (or isotopomers), $^{16}O^{17}O^{18}O$ and $^{16}O^{18}O^{17}O$, with isotopically substituted central atoms. The global potential energy function of O_3 describes all of these features (three wells connected to three dissociation channels through six transition states), and the question of its visualization is not a trivial one. This problem is emphasized here. A more detailed description of hyperspherical coordinates can be found elsewhere.[24,59,60,74]

Figure 2.6 illustrates the potential energy function of ozone molecule[82,84,85] using the hyperspherical coordinates, $V(\rho, \theta, \varphi)$,[24,59,60,74] and the isoenergy approach introduced in the previous section. The coordinates are assigned in a cylindrical style, with hyperradius ρ plotted along z and hyperangles θ and φ plotted in the (x, y) plane as shown in Figure 2.6. We can see that in the range of small ρ, the potential energy function exhibits three lobes that correspond to three possible isomers of O_3. At large values of ρ, we see three tunnels that describe three possible channels of dissociation to O_2 + O. The six bottlenecks (transition states) in the intermediate range of ρ interconnect all of these features into a single volume structure in 3D. Thus, the overall structure is rather complex, which makes a good case for 3D printing (discussed in the next section). Clearly, a plane figure cannot express all aspects of this object.

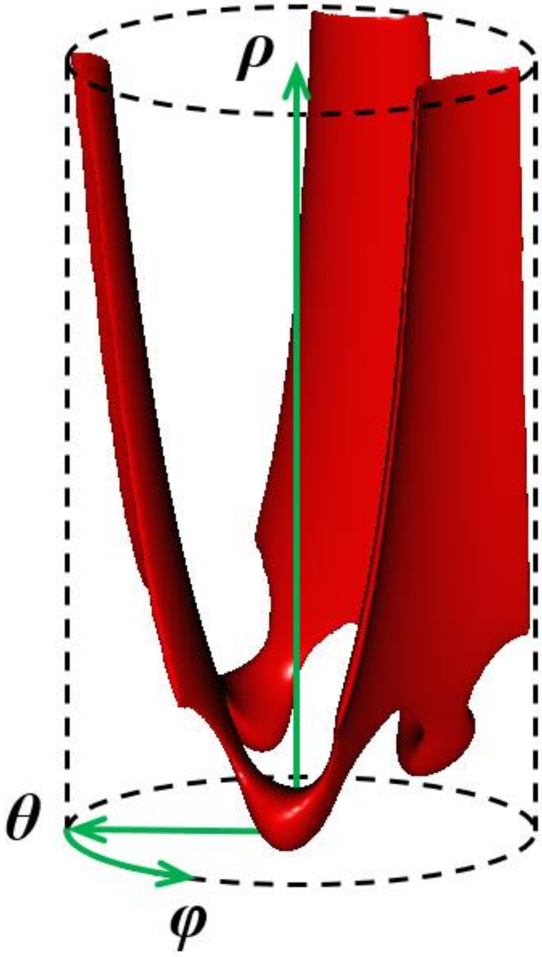

Figure 2.6. Global view of the isoenergy surface for $O_3 \rightarrow O_2 + O$. Hyperspherical coordinates are used. V_{max} is chosen at the quantum dissociation threshold of O_3, which allows seeing the dissociation channels. The range is $\rho < 15\ a_{0.}$

By analyzing Figure 2.6, it helps to keep in mind that hyperradius ρ reflects the overall size of a triatomic system, while hyperangles θ and φ determine its shape. For a triatomic molecule, for example, O_3, the low-amplitude vibrational motion along ρ, θ, and

φ corresponds to three familiar normal modes: symmetric-stretching, bending, and asymmetric-stretching, respectively. At the same time, the large-amplitude motion along φ leads to isomerization (permutation of O atoms within O_3), while the large-amplitude motion along ρ leads to dissociation of O_3 onto O_2 + O. As for numerical values of hyperspherical variables, it is useful to remember that $\theta = 0°$ corresponds to equilateral triangle configurations, and $\theta = 90°$ corresponds to collinear geometries; all isosceles triangle configurations are described by $\varphi = 0°$, 60°, 120°, etc. For example, in Figure 2.6, the three equivalent minima are at $\rho = 4.05\ a_0$, $\theta = 51.3°$, and $\varphi = 60°$, 180°, and 300°. Three dissociation channels lead to $\rho \rightarrow \infty$, $\theta \rightarrow 90°$, and $\varphi \rightarrow 0°$, 120°, and 240°. The six bottlenecks (transition states) are at $\rho = 5.63\ a_0$, $\theta = 68.8°$, and $\varphi = \pm 26°$, 120°±26°, and 240°±26°. The reader is encouraged to try our desktop application,[74] written with a goal of facilitating the understanding of connection between the APH coordinates and molecular geometry.

We stress one more time that no degrees of freedom are frozen or relaxed here. The surface is available for inspection in its full dimensionality. The only restriction is $V_{\max}$, but every chemical problem has some characteristic physical energy limit, so this cannot be regarded as a disadvantage. Quite opposite, this is an advantage that allows one to focus on chemically important parts of the potential energy function. For example, in Figures 2.4 - 2.6, the value of $V_{\max}$ is chosen at quantum dissociation threshold of ozone that corresponds to $O_3 \rightarrow O_2$ ($v = 0$) + O limit. This is equal to vibrational zero-point energy of O_2, which is set to 787.380 cm^{-1}.[86]

2.8. 3D printing of global potential energy

With inexpensive 3D prototyping (or additive manufacturing), it is possible to create a plastic model of the potential energy function. The 3D printing of a 2D potential energy surface was proposed by Lolur and Dawes.[87] For O_3, they fixed the diatomic bond distance R_1 and printed a 2D function $V(\underline{R}_2,\alpha)$ represented in a usual way, by a surface. We combined our isoenergy approach with 3D printing.

We wrote a Matlab[88] script to generate a stereolithography (STL) file ready to feed to a 3D printer. The script itself is rather short, about 20 lines, because there are free external functions available that make all the hard work automatic. Input for this script is a 1D potential energy data array of real numbers of the length $L \times M \times N$. Other inputs include the values of L, M, and N; the value of $V_{\max}$; and the names of input and output files. The script and examples of input and output files are provided as Supporting Information on Journal of Chemical Education website.

When this script is executed, the input array is first transformed by the “reshape” function into a 3D grid of dimensions $L \times M \times N$. Next, a Matlab subroutine “isosurface” creates a triangulated surface by interpolation. After that, the routine “smoothpatch” is called to make the isosurface even smoother. Finally, the routine “stlwrite” writes the triangulated mesh (see Figure 2.7) to the STL file. All of the third-party functions, the stlwrite, smoothpatch, etc., are available on MathWorks website.

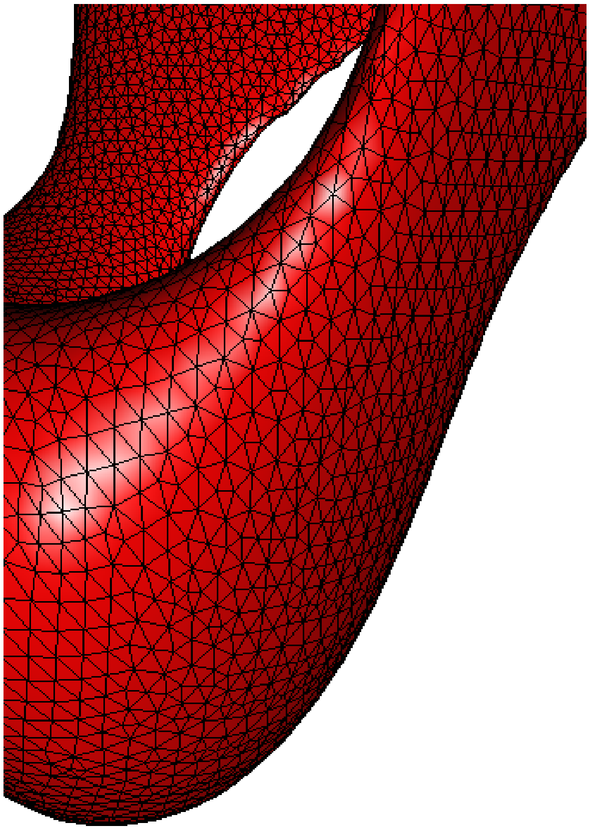

Figure 2.7. Triangulated mesh representing ozone isoenergy surface (the covalent well and the transition state region).

The resultant plastic model of 3D potential energy function of ozone is shown in Figure 2.8. It looks identical to the computer model of Figure 2.6, except for the color. Unfortunately, the 3D printing facility at Marquette University had only one color available, white. The actual size of the plastic model is 2 × 2 × 4 in. The cost of a model of this size was initially estimated at $80; however, since very little time and material were actually spent, we were not charged anything. This is because such a model contains a lot of empty space and little occupied space due to $V_{\max}$.

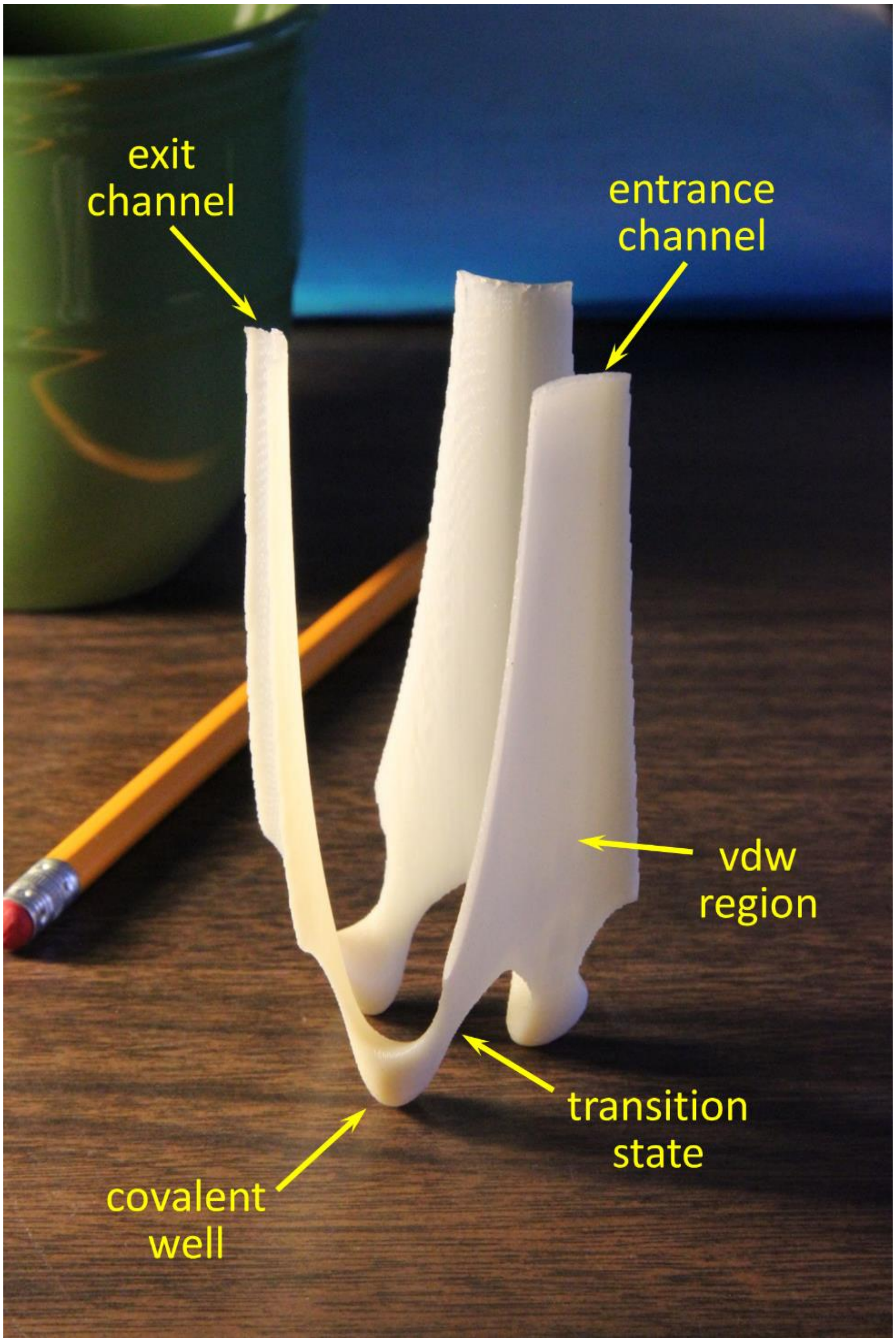

Figure 2.8. Photo of the prototyped potential energy function of ozone on a desktop. Chemically important features are subscribed for clarity.

2.9. Teaching interatomic interactions and reaction dynamics using 3D-printed isoenergy model

The plastic model of isosurface makes it straightforward to discuss various features of a complicated potential energy function (e.g., the one for ozone molecule) since all of them can be seen at the same time. For example, in Figure 2.8, one can easily discern a compact deep covalent well, a narrow transition state region, and a dissociation channel. A wide and shallow van der Waals interaction region is also indicated. Furthermore, the clear connection between these features allows easily visualization of many molecular processes. For example, one can talk about the ozone formation reaction, in which the reactant $O + O_2$ enter through one of the channels, pass through the van der Waals region where the intermediate species $O \cdots O_2$ are formed,[43] and then through the transition state, and end up in one of the covalent wells (see Figure 2.8), which correspond to formation of stable O_3. Or, one can talk about the atom exchange process, in which the reagent $O + O_2$ enter through one of the channels, passes through all the features discussed above, and exits in the other product channel (leading to $A + BC \rightarrow AB + C$). Also, in the case of ozone, the plastic model emphasizes permutation symmetry of the potential energy function: one can see the presence of three energetically equivalent covalent wells, different only by atom permutations (ABC, BCA, and CAB), and three dissociation channels (A + BC, B + CA, and C + AB). Even such intricate processes as pseudorotational motion are easily represented by the plastic model. During pseudorotation in O_3, the system moves from one covalent well to the next and the next, passing through transition states and the van der Waals regions between them.

The instructor can bring such plastic model (or models for several molecules) to the class and hand it out to students to take closer look during the discussion of potential energy functions, for example, the discussion outlined in the previous paragraph. This can be done simultaneously with projection of the 3D computer model of the structure on a screen. Even in the research we do on the ozone molecule,[35,43,89] we found it very useful to have a plastic model on the desktop. It showed to be handy in optimizing a process of grid generation for numerical representation of vibrational wave functions and computing the action of Hamiltonian operator on such wave functions.

2.10. Summary

The APHDemo application has been developed to visualize the process of adiabatic-adjustment of the APH coordinates to the shape of a triatomic system during molecular vibrations or chemical reaction. It helps to understand physical meaning of the APH coordinates without going into complicated math, and emphasizes their advantages over Jacobi coordinates. Simply by dragging atoms with a mouse the user can go through all possible arrangements of three particles, tracking orientations of the vectors and reading values of the adjusting coordinates. This demonstrational application will be very helpful for those who decided to use APH coordinates in their research, particularly for graduate students and postdocs. We plan implementing this interactive tool at Marquette University in the computational chemistry graduate course, a part of curriculum for the Physical Chemistry and/or Chemical Physics programs.

As for future prospects, this application can serve as a foundation for a software to visualize trajectories or wave functions in APH coordinates. Such software may help plotting time-independent vibrational wave functions, or visualizing motion of a wave packet from time-dependent calculations, or even showing trajectories from classical calculations. Addition of these features will make our application even more useful for computational research on triatomic molecules, including spectroscopy and dynamics. In principle, this application should work on Linux under the free and open source Wine software.[90] Such Linux version of APHDemo may also be developed in the future.

Our approach to visualize the potential energy function is quite different from the commonly used, which offers additional opportunities in teaching and research. It makes use of the computer graphics and 3D prototyping and reaches the purpose of visualizing all features of the potential energy function for triatomic molecules in full dimensionality, without freezing or relaxing any degrees of freedom. This is achieved by employing the isoenergy approach. Here, we considered the ozone molecule, but our approach is general and can be used to visualize any potential energy function. Our MATLAB code, available through the Supporting Information on Journal of Chemical Education website, can be used by students and postdocs to produce a plastic isoenergy model of the potential energy function they develop. Application to any triatomic molecule is straightforward, and we plan to prototype the potential energy functions of SO_2 and S_3.

Chapter 3. Efficient method for calculation of bound and resonance states of ozone[*]

3.1. Method background and overview

In recent years, a significant progress has been made in accurate *ab initio* calculations of global potential energy surfaces for small molecules that span the widest range of molecular geometries and energies, going from deep covalent wells (that accommodate stable molecular arrangements) toward the asymptotic range where much weaker van der Waals (vdW) forces dominate (and lead to formation of the weakly bound complexes or clusters) and all the way up to the formation/reaction channels (that describe reagents and products), and even above. Examples include surfaces for isomerization reactions of small polyatomic molecules,[91–93] for molecule-molecule interactions,[94,95] and very accurate surfaces for several triatomic and tetra-atomic molecules.[84,92] One example is a new and rather accurate potential energy surface (PES) of O_3 that has already been used recently to improve our understanding of the O atom exchange processes $O + O_2 \rightarrow O_2 + O$,[96–99] and of the ozone forming recombination reaction[100]

$$O + O_2 \;\Leftrightarrow\; O_3^* \xrightarrow{+\text{bath gas}} O_3.$$

Quantum mechanical description of molecular dynamics on such global potential energy surfaces is a very challenging task, since a broad range of molecular geometries is involved that calls for very large grids or basis sets in multiple dimensions, which translates into large matrices and very significant (often unaffordable) numerical cost of

---

[*] Teplukhin A.; Babikov D., *J. Chem. Phys.*, 145, 114106 (2016)

calculations. Relevant computational methodologies have been developed for molecular reaction dynamics in small polyatomic systems based on DVR techniques.[55,61,101] Those methods are able to cover a wide range of molecular geometries from reagents to products, but are focused exclusively on construction of a state-to-state transition matrix in the asymptotic region, bypassing calculations of the individual quantized states and their wave functions through the interaction region. In principle, such states and their wave functions could be determined using the FBR methods developed for calculations of bound rotational-vibrational states of the molecules,[62,102,103] but those methods become prohibitively expensive near the dissociation/reaction threshold where the PES “opens up” toward the entrance/exit channels. Therefore, a class of molecular dynamics problems that requires determination of energies and wave functions of ro-vibrational states close to dissociation threshold (and scattering resonances above it) represents a significant challenge.

One example of this sort is the above-mentioned recombination reaction that forms ozone. The process starts at energies *above* the dissociation threshold, where the thermal collisions of O and O_2 populate scattering resonances O_3^*. Those represent highly excited ro-vibrational states of O_3 and should be characterized by their energies, widths, and wave functions that determine the rates of their population, spontaneous decay, and quenching (by bath gas collisions) onto the bound states of O_3 somewhat *below* dissociation threshold. In order to treat these processes, we devised a method that combines some elements typical to the quantum reactive-dynamics calculations, with some other elements more typical to the multi-dimensional bound-states calculations. The resultant approach is efficient and fills the gap in computational methodology discussed above.

Namely, for description of vibrational motion in O_3 our approach employs the adiabatically adjusting principal axis hyper-spherical coordinates[60,74] that contain only one dissociative degree of freedom (hyperradius ρ) and two bound-like degrees of freedom (hyperangles θ and φ). In order to reproduce efficiently the delocalized wave functions at energies near dissociation threshold, we combine the sequential diagonalization-truncation procedure to construct FBR in θ and φ with a variable-step DVR grid along ρ, optimized based on the value of local de Broglie wavelength, that adjusts to the shape of the PES. Widths of resonances are obtained by introducing a complex absorbing potential along ρ in the asymptotic part of the PES. Symmetry of O_3 states is described by the coordinate φ, and is used to further simplify the calculations.

As Chapter 5 will show, the method was successfully applied to compute energies and widths of relevant scattering resonances O_3^* for rotationally excited ozone molecules up to $J = 60$ and, based on those data, we derived the recombination rate coefficient for ozone formation, as well as its temperature and pressure dependencies. Good comparison with the available experimental data was obtained. In current (more methodological) chapter all details of our approach are presented, since it is general and can be readily applied to several other important triatomic molecules, such as S_3,[104,105] SO_2,[106] NO_2,[107] and CO_2.[108] In order to conduct a rigorous benchmark study, we compute the spectrum of vibrational states in O_3 up to dissociation threshold using two different potential energy surfaces and compare our results against results available in the literature, computed by other groups for non-rotating molecule, $J = 0$. Then, we focus on an energy window of

600 cm^{-1} just below the threshold, since that this part of the vibrational spectrum plays the most important role in the recombination process that forms ozone, see Chapter 5. Properties of these highly excited and delocalized vibrational states are explored and reported in great detail, including analysis of three-dimensional wave functions and their assignments.

3.2. Theory

3.2.1. Hamiltonian operator in hyperspherical coordinates

As initially derived by Johnson,[109] the total rotational vibrational Hamiltonian operator for a triatomic system in hyper-spherical coordinates can be written in the form of $\hat{H} = \hat{T}_{vib} + \hat{V}_{rot} + \hat{T}_{cor} + \hat{V}_{pot}$, where the following notations are introduced:

$$\hat{T}_{vib} = -\frac{\hbar^2}{2\mu}\left\{\frac{1}{\rho^5}\frac{\partial}{\partial\rho}\rho^5\frac{\partial}{\partial\rho} + \frac{4}{\rho^2}\left[\frac{1}{\sin(2\theta)}\frac{\partial}{\partial\theta}\sin(2\theta)\frac{\partial}{\partial\theta} + \frac{1}{\sin^2\theta}\frac{\partial^2}{\partial\phi^2}\right]\right\}, \tag{3.1}$$

$$\hat{V}_{rot} = \frac{1}{\mu\rho^2}\left[\frac{\hat{J}_x^2}{1+\sin\theta} + \frac{\hat{J}_y^2}{2\sin^2\theta} + \frac{\hat{J}_z^2}{1-\sin\theta}\right], \tag{3.2}$$

$$\hat{T}_{cor} = \frac{4i\hbar\cos\theta\,\hat{J}_y}{2\mu\rho^2\sin^2\theta}\frac{\partial}{\partial\phi} \ . \tag{3.3}$$

Here $\hat{T}_{vib}$ is the kinetic energy operator for vibrational coordinates ρ, θ and φ, while $\hat{V}_{pot} = V_{pot}(\rho, \theta, \varphi)$ stands for the potential energy surface, $\hat{V}_{rot}$ represents centrifugal energy due to the overall rotation of the system, $\hat{T}_{cor}$ is the rotation-vibration (Coriolis) coupling term. Usual Euler angles α, β and γ are used to describe rotational motion of the molecule. The body-fixed reference frame is defined by three principal axes of inertia, with axis z chosen according to Pack: it is a symmetry axis of an associated prolate symmetric-top, which minimizes couplings between different components of total angular momentum.[60] The overall volume element is $d^6\upsilon = 1/8\ \rho^5 \sin\theta \cos\theta \sin\beta\ d\rho\ d\theta\ d\varphi\ d\alpha\ d\beta\ d\gamma$. Since the normalized Wigner functions are used for expansion of the rotational wave function, $\tilde{D}^J_{KM}(\alpha,\beta,\gamma) = \sqrt{(2J+1)/8\pi^2} \cdot D^J_{KM}(\alpha,\beta,\gamma)$, analytic integration over the rotational degrees of freedom leads to the volume element $d^6\upsilon = 1/8\ \rho^5 \sin\theta \cos\theta\ d\rho\ d\theta\ d\varphi$.

In this or very similar forms, the hyperspherical coordinates have been employed over the years by several groups, due to simplicity of the kinetic energy operator and ro-vibrational decoupling, and also due to convenience of describing molecular symmetry when identical atoms are involved. Most notable contributions were made by Parker, Pack and their co-workers,[60,61] by Kuppermann[110] and coworkers, more recently by Kendrick and co-workers,[24,62,103] by Kokoouline and Greene,[53,63,111] and also by several other independent followers.[66,112,113] The applications include both the reactive-scattering processes[60,61,103] and the bound-state calculations.[24,62,66,112,113]

In the past, several users made slight modifications to these hyper-spherical coordinates, in order to make them more suitable for their particular applications. Examples can be found in the work of Johnson,[109] Whitnell and Light,[114] Parker and Pack,[60] and Kendrick et al.[24,103] Some of those proposed transformations were intended to simplify the kinetic energy operator over ρ, others to deal with singularity over θ, or to enforce the desired symmetry properties over φ. Our goal was to obtain the simplest possible form of the kinetic energy operator with the simplest volume element. We found that this can be achieved by the following transformation of the "old" vibrational wave function, say $\bar{\Psi}(\rho, \theta, \varphi)$, to its new form $\Psi(\rho, \theta, \varphi)$, as follows:

$$\Psi(\rho,\theta,\phi) \leftarrow \tfrac{1}{4}\rho^{5/2}\sin^{1/2}(2\theta)\,\bar{\Psi}(\rho,\theta,\phi)\,. \tag{3.4}$$

Then, the Hamiltonian operator acting onto this transformed wave function can be written as $\hat{H} = \hat{T}_{vib} + \hat{V}_{rot} + \hat{T}_{cor} + \hat{V}_{pot} + \hat{V}_{ext}$ where, instead of Eq. (3.1), new expression is obtained for the vibrational kinetic energy operator:

$$\hat{T}_{vib} = -\frac{\hbar^2}{2\mu}\left[\frac{\partial^2}{\partial\rho^2} + \frac{4}{\rho^2}\left(\frac{\partial^2}{\partial\theta^2} + \frac{1}{\sin^2\theta}\frac{\partial^2}{\partial\phi^2}\right)\right], \tag{3.5}$$

and a new potential-like "extra" term is introduced:

$$\hat{V}_{ext} = -\frac{\hbar^2}{2\mu\rho^2}\left[\frac{1}{4} + \frac{4}{\sin^2 2\theta}\right]. \tag{3.6}$$

We see that now the kinetic energy operator has the simplest form, with only three second derivatives along each ρ, θ and φ. If the wave function is defined on a 3D-grid of points (direct-product DVR), the kinetic energy operator along each coordinate is trivially applied by Fourier-transforming the wave function to momentum representation, multiplying each point of it by $P^2/2\mu$, and Fourier-transforming it back to the coordinate representation (see, for example, Ref. 35). The additional potential term V_{ext} of Eq. (3.6) is simply added to the potential energy surface $V_{pot}(\rho, \theta, \varphi)$ and does not require any extra effort, since the potential energy operator is diagonal in the DVR representation. Furthermore, the volume element is now trivial: $d^3 v = d\rho\, d\theta\, d\varphi$.

Interestingly, that while this work was in progress, we learned that we were not the first to discover this way of simplifying the hyperspherical Hamiltonian operator. We found that this transformation was already discussed by Billing, in his book on the approximate quantum classical theory,[115] but was not applied to any real system.

3.2.2. Angular momentum decoupling approximation

In hyperspherical coordinates the coupling between vibrational and rotational coordinates (the Coriolis coupling) is described by one cross-term in the Hamiltonian operator, $\hat{T}_{cor}$, Eq. (3.3), which contains both the rotational operator $\hat{J}_y$ and the vibrational operator $\partial/\partial\varphi$. If needed, the action of this term onto wave function $\Psi(\rho, \theta, \varphi)$ can be rigorously evaluated.[60] Typically, the value of Coriolis coupling is small, but it leads to linear growth of the Hamiltonian matrix size for $J > 0$, and quadratic growth of the numerical effort. For this reason, it is practical (and is often justified) to neglect this cross-term. Parker and Pack named this simplification the centrifugal-sudden approximation.[60] It is equivalent to the symmetric-top rotor assumption, also known as K-conserving approximation, since Hamiltonian operator of the symmetric top rotor does not have such cross-term, and since projection K of angular momentum J onto symmetry axis of the rotor is conserved, making K a good quantum number.

Using this symmetric-top model, the Hamiltonian operator takes the simplest form $\hat{H} = \hat{T}_{vib} + V$, where all the potential terms are combined: $V = V_{pot} + V_{sym} + V_{ext}$, and the approximate centrifugal potential is given by:

$$V_{sym} = \bar{A}\hbar^2 J(J+1) + (C - \bar{A})\hbar^2 K^2 . \tag{3.7}$$

Here $\bar{A}$ and C are rotational constants of a symmetric top, with $\bar{A}$ being the approximate one, computed as average of two smaller rotational constants, A and B, of an asymmetric top: $\bar{A} = (A + B) / 2$. Exact instantaneous values of the rotational constants in the hyper-spherical coordinates, according to Eq. (3.3), are defined as: $A^{-1} = \mu\rho^2(1+\sin\theta)$, $B^{-1} = 2\mu\rho^2\sin^2\theta$ and $C^{-1} = \mu\rho^2(1-\sin^2\theta)$. Note that the centrifugal potential of Eq. (3.7) is obtained from the exact expression of Eq. (3.3) by neglecting a piece that corresponds to the asymmetric-top rotor centrifugal potential: $V_{asym} = (\hat{J}_x^2 - \hat{J}_y^2)(A - B) / 2$. As it was emphasized by Parker and Pack[60] this simplification, together with neglect of the Coriolis coupling term, constitute one single approximation, since both neglects are required in order to decouple the rotational and vibrational motions completely, in the hyperspherical coordinates. Also, these rotational constants are those of a so-called *fluid* rotor, because the expression for B constant of *rigid* rotor does not contain $\sin^2\theta$.[60]

For example, for an ozone molecule in its equilibrium configuration the values of rotational constants are $A\hbar^2 = 0.45$ cm^{-1}, $B\hbar^2 = 0.66$ cm^{-1} and $C\hbar^2 = 3.56$ cm^{-1}, which makes it very close to a prolate symmetric-top rotor. For this reason, the K-conserving approximation has been used in the past in several studies of ozone spectra and dynamics,[35,89] and was also adopted in Chapter 5. Within this approximation, calculations of vibrational states are carried out independently for different values of K, such that $K < J$, for each $J > 0$. In our study of recombination kinetics, see Chapter 5, we showed that significant contributions to the rate of ozone formation are made by states with moderate rotational excitations, in the range $8 \le J \le 38$, where this approximation is still expected to work reasonably well. The contribution of states with $J > 40$ was found to be small.

In the dissociation limit, when $\rho \rightarrow \infty$ and $\theta \rightarrow \pi / 2$, the rotational constants A, B, and $\bar{A}$ vanish, while $C^{-1} \rightarrow 2\mu_{O2}r^2\sin^2\Theta$, showing dependence on the reduced mass of O_2 and Jacobi coordinates r and Θ. For T-shape configuration $\Theta = \pi / 2$ and the equilibrium distance $r = r_e = 2.282\ a_0$, the value of C approaches the rotational constant of O_2, which is 1.44 cm^{-1}.

It should be stressed that in the hyperspherical coordinates, also called adiabatically adjusting principal-axis hyper-spherical (APH) coordinates, symmetry axis of the approximate symmetric-top rotor is always the principal-axis of inertia a (pointing along vector **Q** as defined by Parker and Pack[60]) for any instantaneous molecular configuration,[27,116] and *K* is always a projection of **J** onto this axis, $K = K_a$. This choice minimizes Coriolis coupling[116] and makes the symmetric-top rotor approximation most accurate.[117] Note, however, that this is not automatically the case in other coordinates. For example, using Jacobi coordinates with *R*-embedding,[116] *K* is a projection of **J** onto the Jacobi vector **R**, and the values of rotational constants *A*, *B*, and *C* are defined relative to **R**. Although **R** becomes close to the principal-axis of inertia *a* in the asymptotic range (as $R \to \infty$), it should be realized that **R** deviates from a quite substantially when molecular geometry is close to the equilibrium configuration, making Coriolis coupling significant. One known way to fix this problem is to use the adiabatic-rotation (AR) approximation of Bowman,[117] that expresses rotational energy through the principal axis of inertia, rather than Jacobi vectors.

3.2.3. Direct-product basis set

In quantum mechanics, two most frequently used mathematical representations of wave function are the finite basis representation (FBR) and the discrete variable representation (DVR).[118] In the FBR, wave function for the *i*th state is expanded over a basis set $\Phi_n(x)$, $1 \leq n \leq N$:

$$\Psi^{(i)}(x) = \sum_{n=1}^{N} a_n^{(i)} \Phi_n(x) \,. \tag{3.8}$$

In the DVR, in contrast, a wave function is numerically approximated by a set of values at the points x_n of the grid

$$\Psi_n^{(i)} = \Psi^{(i)}(x_n). \tag{3.9}$$

Despite this difference, DVR can be thought of as a special case of FBR, where basis functions $f_n(x)$ are localized at the points of the grid

$$\Psi^{(i)}(x) = \sum_{n=1}^{N} b_n^{(i)} f_n(x), \tag{3.10}$$

$$f_n(x) = \begin{cases} 1, & x = x_n; \\ 0, & x \neq x_n. \end{cases} \tag{3.11}$$

Now consider a two-dimensional problem, with Hamiltonian operator $\hat{H} = \hat{T}_x + \hat{T}_y + V(x,y)$ and wave function represented as a direct product (of DVR or FBR) basis function for each dimension

$$\Psi^{(i)}(x,y) = \sum_{n=1}^{N} \sum_{m=1}^{M} a_{nm}^{(i)} \Phi_n(x) \Lambda_m(y). \tag{3.12}$$

This representation has $S = N \times M$ two-dimensional basis functions and the same number of expansion coefficients $a_{nm}^{(i)}$. Size of the Hamiltonian matrix is $S \times S$. Structurally, it consists of N^2 square blocks (x-blocks) labeled by n. Each block contains $M \times M$ elements (y-elements).

The advantage of this direct-product approach is simplicity: the same basis set $\Lambda_m(y)$ for the coordinate y is used through the entire range of the coordinate x. Consequently, the same $M \times M$ matrix elements of the operator $\hat{T}_y$ are replicated over the entire matrix, in each x-block (see Figure 3.1, left panel):

$$H_{nm,n'm'} = \langle n m | \hat{H} | n'm' \rangle = \delta_{m,m'} (\hat{T}_x)_{nn'} + \delta_{n,n'} (\hat{T}_y)_{mm'} + V_{nm,n'm'}. \tag{3.13}$$

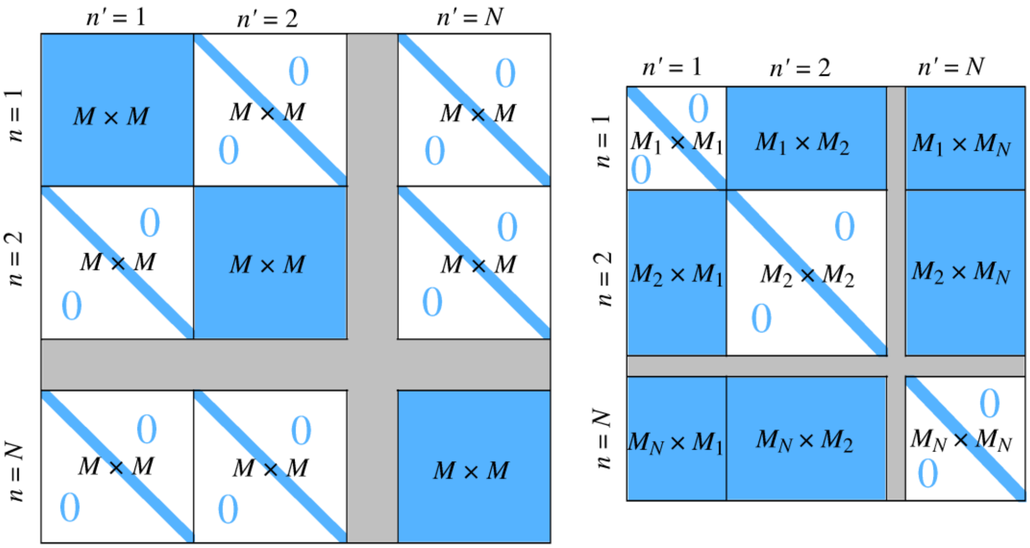

Figure 3.1. Structure of Hamiltonian matrices constructed using the direct-product basis (left panel) and the sequential diagonalization-truncation approach (right panel). All elements of blue blocks are non-zero, while white blocks are already diagonal, with non-zero elements shown by the blue stripe. Note that all blocks of the first matrix have the same size and are squared, while all blocks of the second matrix are different and are smaller, $M_n \leq M$, which results in a much smaller matrix size.

The disadvantage of the direct-product approach is the large size of the basis set. Indeed, since exactly the same basis set $\Lambda_m\,(y)$ is going to be used at all (different) values of the coordinate x, this basis set must be *globally* good, which in practice means rather large. A similar consideration applies to the basis set $\Phi_n(x)$, to be employed at all values of coordinate y. Thus, both N and M are expected to be large numbers, leading, in turn, to a large size of the resultant Hamiltonian matrix, which also increases rapidly with the addition of new coordinates. Namely, for a three-dimensional problem the size of the Hamiltonian matrix constructed using the direct-product FBR would be $S = N \times M \times L$, with L representing the number of basis functions for coordinate z (also large).

For example, we tried the direct-product DVR in hyperspherical coordinates ρ, θ and φ to compute vibrational states of ozone. We found that for the states localized in the main (covalent) well of ozone (not quite up to dissociation limit, just up to the van der

Walls plateau, see below), a grid of 64 × 64 × 64 equidistant points is sufficient for reasonably accurate results. This corresponds to the direct-product matrix size of almost $S = 3\cdot10^5$. But, such grid only covers a limited range of the hyperradius, $3.3 \leq \rho \leq 6.0\ a_0$.

Expanding this grid up to $\rho_{\max} = 15.0\ a_0$ (needed for calculations of all the bound states, including delocalized van der Waals states) would require $N = 280$ points along ρ, assuming the same step-size. This would lead to the matrix size of more than $S = 10^6$. Moreover, it appears that in the asymptotic range of the hyperradius the PES is very tight, which requires a much denser grid, compared to the covalent well. For example, we found that around $\rho_{\max} = 15.0\ a_0$ we need around $M = 280$ points for θ and $L = 400$ points for φ. Since the direct-product grid must be the same everywhere, one should use the 280 × 280 × 400 grid, with the matrix size on the order of $S = 3\cdot10^7$, which is computationally unaffordable.

3.2.4. Sequential diagonalization-truncation

The problems described above can be largely reduced by avoiding one universal basis set, and, instead, using different basis sets in different parts of the configuration space. Those could be optimized and made much smaller, *locally*, in order to reduce the size of the overall Hamiltonian matrix. In the literature this idea is called the sequential diagonalization truncation technique.[119–121] It is readily integrated into the hyperspherical coordinates using an efficient combined DVR/FBR approach, as described below.

Since the vibrational operator $\hat{T}_{vib}$ of the Hamiltonian can be naturally split onto two parts, $\hat{H} = \hat{T}_\rho + \hat{T}_{\theta\varphi} + V(\rho, \theta, \varphi)$, where

$$\hat{T}_{\theta\phi} = -\frac{2\hbar^2}{\mu\rho^2}\left(\frac{\partial^2}{\partial\theta^2} + \frac{1}{\sin^2\theta}\frac{\partial^2}{\partial\phi^2}\right) \tag{3.14}$$

It is possible to formulate and solve, first, a two-dimensional eigenvalue problem for the hyperangles θ and φ, at different values of the hyperradius ρ, keeping it fixed. For example, at $\rho = \rho_n$ the two-dimensional Hamiltonian operator is $\hat{h}_n = \hat{T}_{\theta\varphi} + V_n(\theta, \varphi)$ and the corresponding Schrödinger equation is

$$\hat{h}_n \Lambda_m^n(\theta,\phi) = \varepsilon_m^n \Lambda_m^n(\theta,\phi)\,. \tag{3.15}$$

Here $V_n(\theta, \varphi) = V_n(\theta, \varphi; \rho_n)$ represents a two-dimensional slice through θ and φ of the potential energy surface at $\rho = \rho_n$. Numerical solution of this equation gives a set of two dimensional eigenfunctions $\Lambda_m^n(\theta,\varphi)$ and a spectrum of the corresponding eigenvalues ε_m^n, labelled by index m, for each considered ρ_n. Note that since hyperangles θ and φ are "bound-like" degrees of freedom, the corresponding two dimensional slices $V_n(\theta, \varphi)$ of the PES are always localized to a relatively small range in the (θ, φ)-space, as illustrated by Figure 3.2 (upper frames). Thus, the eigenvalue problem is well defined and is relatively easy to solve. The corresponding eigenfunctions $\Lambda_m^n(\theta,\varphi)$ and eigenvalues ε_m^n are always real valued, even at high energies (above dissociation threshold) and at large ρ (in the asymptotic region). To illustrate this, we presented in Figure 3.2 five lowest-energy eigenfunctions $\Lambda_m^n(\theta,\varphi)$ for three representative values of ρ.

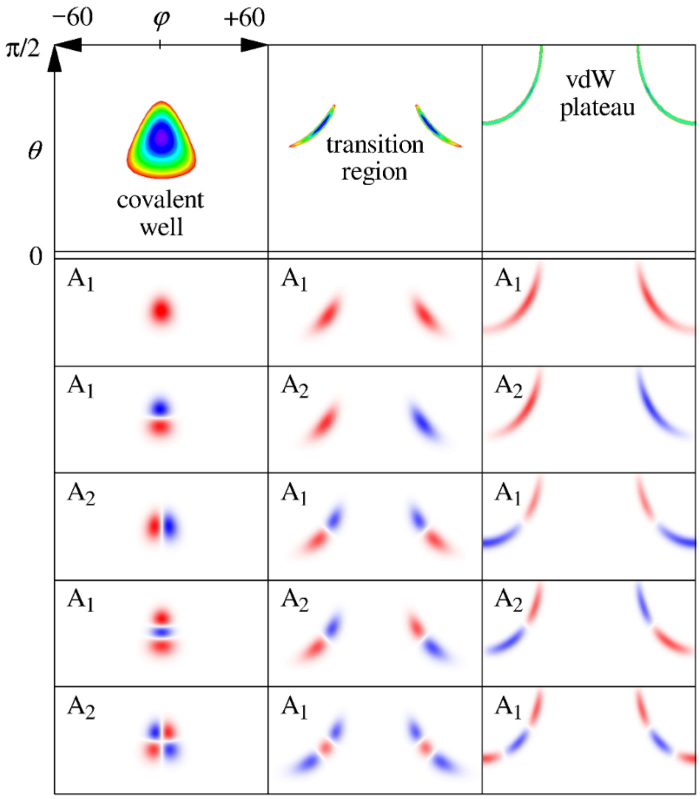

Figure 3.2. Top row gives three representative two-dimensional slices $V_n(\theta, \varphi)$ of the PES: through the deep covalent well, through the transition region, and through the vdW plateau. The ranges of θ and φ are indicated in the upper left frame. Under each slice, the corresponding two-dimensional local basis set $\Lambda_n(\theta, \varphi)$ is presented (five lower energy functions). Positive and negative lobes of wave functions are shown in red and blue, respectively. Their nodal structure reveals excitations of the normal or local vibration modes and changes significantly between the slices, following the PES shape. Since potential is symmetric with respect to hyperangle φ, the computed wave functions are either symmetric (A_1) or anti-symmetric (A_2).

Furthermore, Figure 3.3 shows energy eigenvalues ε_m^n as a function of slice number n along ρ. Each vertical “column” of points represents the energy spectrum of the two-dimensional Hamiltonian operator $\hat{h}_n$ for one slice. The minimum-energy path along ρ is also shown in Figure 3.3 (by red line), which reflects the shape of the PES and makes the local zero-point energy ε_0^n evident. The density of points in a given slice reflects properties of potential energy surface $V_n(\theta, \varphi)$ at ρ_n. For example, in the slice n = 33 the spectrum is sparser than in its vicinity, which corresponds to higher frequency, consistent with tight transition state in this slice. Slice $n = 17$ passes through the minimum of the covalent well, $D_e = 9275$ cm^{-1} relative to the bottom of the dissociation channel, that corresponds to classical dissociation limit. Finally, slice $n = 64$ (last slice in Figure 3.3) passes though the dissociation channel of the PES. Here we can see that quantum threshold is 794.51 cm^{-1} above the classical dissociation limit, which corresponds to zero-point of $^{16}O_2$ in the state $v = 0$ and $j = 1$. Asymptotic form of $\Lambda_m^n(\theta, \varphi)$, as $\rho \rightarrow \infty$, is discussed in Appendix A.

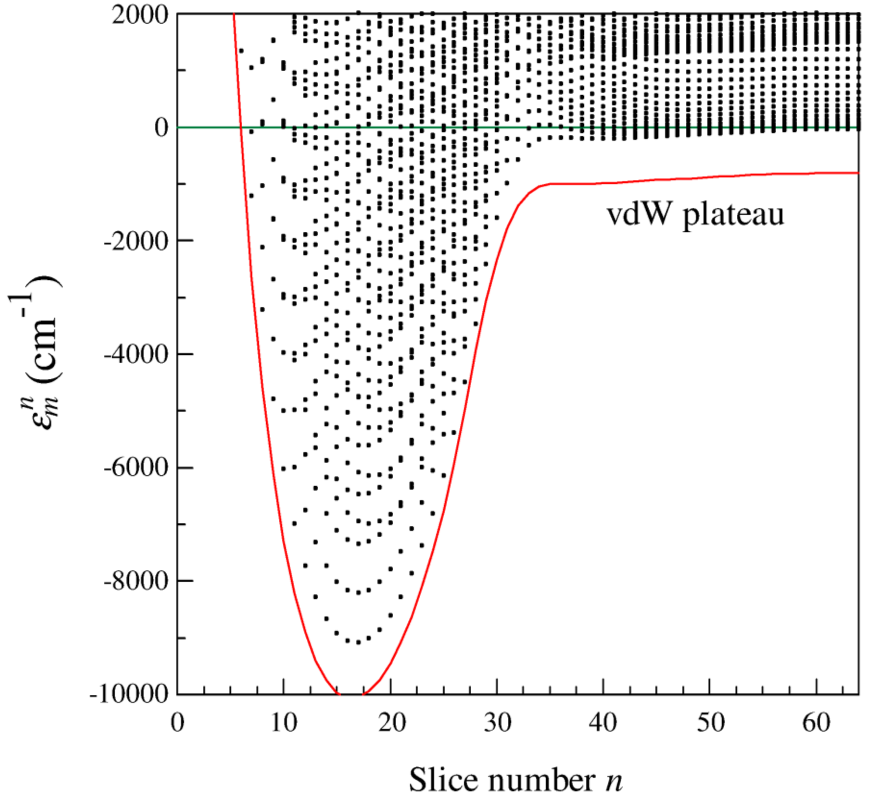

Figure 3.3. Energies $\varepsilon_m{}^n$ of two-dimensional eigenstates (black points) computed independently for each slice through the PES and plotted together as a function of slice number n. Only energies of A_1 states are shown, energies of A_2 states look similar. The minimum energy path for the PES is also shown for comparison (red line). Local vibrational zero-point energy is easily identified in each slice, as a distance between the lowest energy $\varepsilon_0{}^n$ and the minimum energy path. Asymptotically (to the right) the 2D-spectrum $\varepsilon_m{}^n$ turns into the ro-vibrational spectrum of the diatomic fragment O_2. Dissociation threshold (green line) includes ZPE of O_2.

The two-dimensional solutions $\Lambda_m^n(\theta,\varphi)$ will be employed as locally optimal basis functions (at the next step, see below). Note that although the eigenstates $\Lambda_m^n(\theta,\varphi)$ for a given ρ_n form an orthonormal set, the functions determined at different slices, say $\Lambda_m^n(\theta,\varphi)$, $1 \le m \le M_n$ and $\Lambda_{m'}^{n'}(\theta,\varphi)$, $1 \le m' \le M_{n'}$ are not mutually orthogonal. In this case one can define the *overlap* matrix[60,122,123]

$$O_{nm,n'm'} = \int \Lambda_m^n \Lambda_{m'}^{n'} d\theta d\varphi . \tag{3.16}$$

The size of this matrix is $S \times S$, where $S = \sum_{n=1}^{N} M_n$ is the total number of two-dimensional functions determined and employed for the range of ρ. Structurally, the overlap matrix O contains N^2 blocks (ρ-blocks). Only the diagonal blocks are squared, $M_n \times M_n$, and, by construction, are the identity matrixes. The off-diagonal blocks of the overlap matrix are rectangular, with dimensions $M_n \times M_{n'}$. They contain couplings between different values of ρ.

The second step is to combine the local FBRs in θ and φ, with the DVR in ρ, by expressing the overall three-dimensional wave function as:

$$\Psi^{(i)}(\rho,\theta,\phi) = \sum_{n=1}^{N} \sum_{m=1}^{M_n} a_{nm}^{(i)} f_n(\rho) \Lambda_m^n(\theta,\phi) \tag{3.17}$$

Importantly, size M_n of the local basis set $\Lambda_m^n(\theta,\varphi)$, $1 \le m \le M_n$, does not have to be the same for different values of ρ. Typically, it is minimal at $\rho \to 0$ (just a few functions in the repulsive region), is largest for the intermediate values of ρ (around 100 functions in the covalent well region), and is again small asymptotically as $\rho \to \infty$ (about a dozen functions in the channel region). In this representation, matrix elements of the total Hamiltonian operator $\hat{H}$ are computed as follows:

$$\begin{aligned} H_{nm,n'm'} &= \langle nm|\hat{H}|n'm'\rangle = \langle nm|\hat{T}_\rho|n'm'\rangle + \langle nm|\hat{T}_{\theta\phi} + V|n'm'\rangle = \\ &= \int \Lambda_m^n \Lambda_{m'}^{n'} d\theta d\varphi \times \int f_n \hat{T}_\rho f_{n'} d\rho + \int \Lambda_m^n \varepsilon_{m'}^{n'} \Lambda_{m'}^{n'} d\theta d\varphi \times \int f_n f_{n'} d\rho = \\ &= O_{nm,n'm'} \times (\hat{T}_\rho)_{n,n'} + \delta_{m,m'}\,\delta_{n,n'}\,\varepsilon_m^n \,. \end{aligned} \tag{3.18}$$

Here $(\hat{T}_\rho)_{n,n'}$ is a square matrix, $N \times N$, of the kinetic energy operator in ρ,

$$\hat{T}_\rho = -\frac{\hbar^2}{2\mu}\frac{\partial^2}{\partial\rho^2}\,, \tag{3.19}$$

in the DVR basis (a grid of N points ρ_n). Equation (3.18) shows that the overall Hamiltonian matrix $H_{nm,n'm'}$ is easily constructed from the overlap matrix $O_{nm,n'm'}$ by multiplying each its ρ-block by the corresponding element of the matrix $(\hat{T}_\rho)_{n,n'}$, and then adding to each diagonal element the corresponding value of two-dimensional energy ε_m^n. It is quite interesting that the PES $V(\rho, \theta, \varphi)$ does not show up in the final Eq. (3.18). All information about it, as well as the extra potential term V_{ext} and the rotational term V_{sym}, have already been encoded into the two-dimensional eigenvalues ε_m^n and the overlap matrix $O_{nm,n'm'}$ of two-dimensional eigenfunctions $\Lambda_m^n(\theta,\varphi)$.

The size of the Hamiltonian matrix is the same as that of the overlap matrix: $S \times S$, where $S = \sum_{n=1}^{N} M_n$. In practice, this means a significant reduction compared to the direct-product DVR in 3D. Local basis set $\Lambda_m^n(\theta,\varphi)$ at each ρ_n can be truncated based on a physical value of maximum energy in the problem, which gives one convenient convergence parameter for the entire problem: $\varepsilon_m^n \le E_{\text{cut}}$. In the ozone example considered in Sec. 3.2.3 above, where the covalent well is ~10^4 cm^{-1} deep, we found that E_{cut} = 7250 cm^{-1} above dissociation limit is sufficient to obtain reliable results for all bound states below dissociation threshold, and also for scattering resonances at energies up to 1000 cm^{-1} above dissociation threshold. This seemingly large value of E_{cut} truncates basis sets down to only M_n = 20 functions in the asymptotic range of ρ, and around M_n = 200 functions in the covalent well region (see Figure 3.3). At small ρ, in the repulsive range where all ε_m^n are above E_{cut}, we still keep 20 eigenvectors in the basis (10 of each symmetry, see below) as it was recommended by Carrington.[119–121]

A further increase in speed is obtained using symmetry of the vibrational states, as determined by the hyperangle φ. For this, after the two-dimensional eigenfunctions $\Lambda_m^n(\theta, \varphi)$ have been computed, they should be analyzed and labeled as symmetric (A_1) or anti-symmetric (A_2) with respect to φ. Since those have no net overlap (due to cancellation of the integral), one can split each local basis set onto two separate basis sets of given symmetry: A_1 and A_2. Each is used independently, according to Eqs. (3.16–3.18), which reduces the size of Hamiltonian matrix even further, roughly by a factor of two, and produces three-dimensional solutions of different symmetries through two independent calculations.

This approach (in conjunction with optimized grid DVR for ρ, see Sec. 3.2.5) leads to the total basis and matrix size of only $S = 7 \cdot 10^3$, for each symmetry. Recall that this is instead of the direct-product matrix with the size around 10^7 (see example in Sec. 3.2.3 above). Such a significant matrix reduction, by three orders of magnitude, is very appealing since the numerical cost of diagonalization algorithms scales as S^2 or S^3.

It is also instructive to mention the possibility of an adiabatic approximation, where the off-diagonal blocks of the overlap matrix $O_{nm,n'm'}$ are all neglected. This would lead, in the three-dimensional problem, to the Hamiltonian matrix that is automatically diagonal

$$H_{nm,n'm'} \approx \delta_{m,m'}\delta_{n,n'}\,(\hat{T}_\rho)_{n,n'} + \delta_{m,m'}\,\delta_{n,n'}\,\varepsilon_m^n\,. \tag{3.20}$$

Here, the diagonal elements of the kinetic energy operator in ρ are simply added to the values of two-dimensional energies in θ and φ. While useful in some cases, this approximation is expected to be rather rough in general. However, it should be recognized that a reasonably accurate approximation can be devised by neglecting not all, but some blocks of the overlap matrix. For example, those blocks that correspond to the values of ρ_n and $\rho_{n'}$ that are far apart may show negligible overlap anyway, and can be safely neglected.

The reason for efficiency of the sequential diagonalization-truncation approach discussed above is that each local basis set $\Lambda_m^n(\theta,\varphi)$ can be chosen relatively small, simply because its functions are perfectly suited to describe behavior of the overall wave-function near ρ_n. This is because $\Lambda_m^n(\theta,\varphi)$ are the local eigenfunctions, i.e., the best-possible functions, rather than some universal polynomials, or grids. Note, however, that this optimization concerns representation of a wave-function along θ and φ only, but not yet along ρ. Optimization of the grid $f(\rho_n)$ along ρ is discussed next.

3.2.5. Optimized grid DVR

Grid representation, or DVR, is a good choice for coordinate ρ, because this is a dissociative degree of freedom. When energy is high, the spectrum of states is continuous. Scattering resonances are important, that dissociate, exhibiting wave functions that expand far into the channels of the PES. In this regime, the grid should expand to large values of ρ, but it does not have to be equally dense everywhere. It is clear physically that the grid should be denser over the deep covalent well, where the wave-function oscillates rapidly. However, in the asymptotic range of large ρ, where the dissociation channels are shallow, wave function does not oscillate much (e.g., see Figure 3.9 below), and the grid does not have to be that dense.

Using this idea, the density of grid $f(\rho_n)$ along ρ can be optimized, locally, using the local value of de Broigle wavelength: $\lambda(\rho) = \pi \big/ \sqrt{2\mu[E_{\max} - E_{\min}(\rho)]}$. Here $E_{\max}$ is a constant number, one characteristic maximum energy of the problem. We recommend $E_{\max} \approx 2kT$ at room temperature. In contrast, $E_{\min}$ is a variable of ρ, and is a local minimum possible energy of the system. In one-dimensional problems (diatomic molecules) this is simply the value of the PES, e.g., $E_{\min} = V(r)$.[124] In the multi-dimensional problems one can define the envelope potential for each coordinate, e.g., $E_{\min} = V_{env}(r)$, for example, by computing the minimum energy path along ρ. But this method does not take into account local zero-point energy of the system that, in principle, can change significantly along the reaction coordinate. We realized that it is the best to define minimum energy as the ground state energy of the local two-dimensional eigenstates ε_m^n, which reflects the minimum energy path along ρ, but also takes the local zero-point energy into account (see Figure 3.3). So, we use $E_{\min}(\rho) = \varepsilon_0(\rho)$. In practice, it is constructed as a spline of the lowest energy values ε_0^n determined on a trial grid of points ρ_n (that can be uniform and rather sparse everywhere).

Using the local de Broglie wavelength $\lambda(\rho)$, the local step-size for the variable grid is defined as[35]

$$\Delta\rho = \alpha\lambda(\rho)\Delta\xi = J\Delta\xi\,. \tag{3.21}$$

In this formulation, sometimes called grid mapping,[124,125] the equidistant (working) grid ξ_n with $\Delta\xi = 1$ is defined along the auxiliary unit-less coordinate ξ. The Jacobian of transformation is $J(\rho) = \alpha\lambda(\rho)$, where α is a constant compression factor ($\alpha < 1$ is used to make the grid denser than the minimal requirement $\alpha = 1$). In order to generate the optimal grid ρ_n, the differential equation $d\rho \,/\, d\xi = J(\rho)$ is solved numerically (*e.g.*, by 4th-order Runge-Kutta method) with boundary condition $\rho = \rho_{\min}$ at $\xi = 0$, to determine the values of ρ_n at the points ξ_n. As it is often done, we place grid points in the middle of intervals, so, $\xi_1 = 0.5$ and ρ_1 is slightly larger than $\rho_{\min}$. Figure 3.4 gives example of such variable-step grid. One can see that the density of points is much lower in the range of shallow van der Waals (vdW) plateau, and in the dissociation channel, compared to the region of deep covalent well. Grid density changes smoothly through the range of ρ. In the final calculations, we used a denser grid, generated using $\alpha = 0.5$.

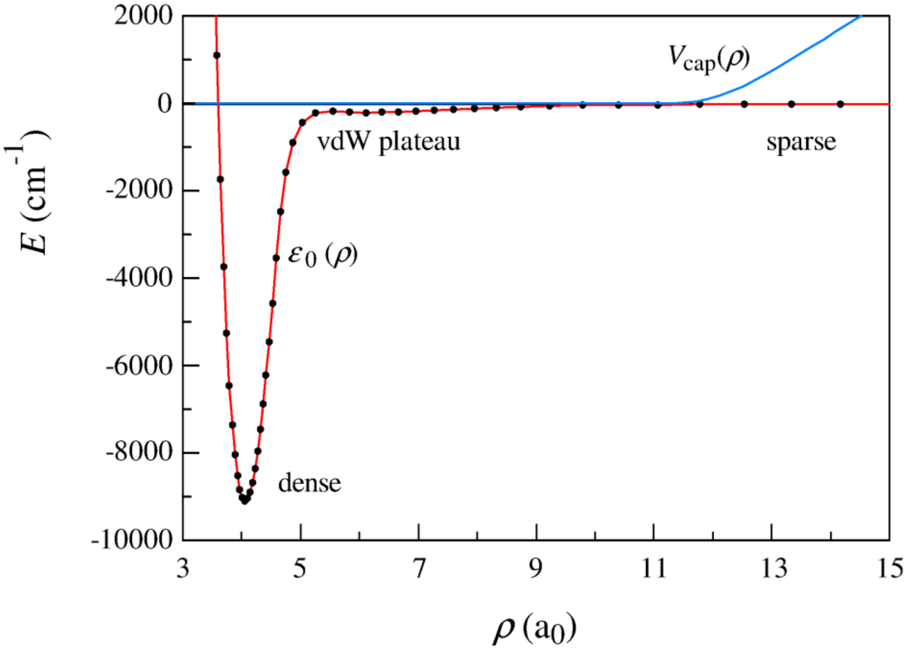

Figure 3.4. Variable-step grid generated for the dissociative coordinate ρ (black points). The grid is dense in the covalent well, is sparser in the vdW plateau region, and is even sparser in the asymptotic range. The ground state value of local 2D energy $\varepsilon_0(\rho)$, used to generate this grid, is also shown (red line). The complex absorbing potential $V_{\text{cap}}(\rho)$ is shown in the asymptotic region (blue line).

In fact, the physical optimized grid is only used for plotting the wave function (e.g. see Figure 3.6 below), for all other purposes the working grid ξ_n. is used. For example, applying the kinetic energy operator in ρ is done using the equidistant grid ξ_n, rather than a variable step-size grid ρ_n. The change of variable is taken into account using the Jacobian of transformation $J(\xi)$, not to confuse with total angular momentum

$$\hat{T}_\xi = -\frac{\hbar^2}{2\mu}\left(\frac{1}{J}\frac{\partial}{\partial\xi}\frac{1}{J}\frac{\partial}{\partial\xi}\right). \tag{3.22}$$

In order to keep the operator Hermitian and the matrix symmetric, a new wave function is introduced, with its corresponding operator

$$\tilde{\Psi}(\xi) = \sqrt{J(\xi)}\;\Psi(\rho), \tag{3.23}$$

$$\hat{T}_\xi = -\frac{\hbar^2}{2\mu}\left(\frac{1}{\sqrt{J}}\frac{\partial}{\partial\xi}\frac{1}{J}\frac{\partial}{\partial\xi}\frac{1}{\sqrt{J}}\right). \tag{3.24}$$

3.2.6. Calculations of resonance widths

Widths of scattering resonances, reported in Chapter 5, were computed by introducing into the range of large ρ values the complex absorbing potential in the analytic form suggested by Balint-Kurti,

$$V_{cap}(\rho) = -iA\exp\left(\frac{W}{\rho-\rho_c}\right), \tag{3.25}$$

with a set of parameters determined in our earlier paper:[35] $A = 10^4$ cm^{-1}, = 10.5 a_0 and W = 6.5 a_0. It is important to realize that $V_{cap}(\rho)$ depends on the value of hyperradius ρ only, and does not change through the two dimensional slice over θ and φ, which means that it does not affect two-dimensional solutions $\Lambda_m^n(\theta,\varphi)$ and the overlap matrix $O_{nm,n'm'}$, besides a constant shift $V_{cap}(\rho_n) = V_{cap}{}^n$. So, introduction of the complex potential only affects the last step of our method, by changing the Hamiltonian matrix:

$$H_{nm,n'm'} = O_{nm,n'm'} \times (\hat{T}_\xi)_{n,n'} + \delta_{m,m'}\, \delta_{n,n'}\, (\varepsilon_m^n + V_{\text{cap}}^n). \tag{3.26}$$

This matrix has the same size S as in the real-valued case of Eq. (3.18), but it is non-Hermitian and exhibits complex eigenvalues $E - i\Gamma/2$. Note, however, that the two-dimensional solutions $\Lambda_m^n(\theta, \varphi)$ stay real functions in this formalism; complexity comes solely from the third dimension of the problem – the dissociative coordinate ρ. Distribution of resonance energies E and widths Γ for calculations with $0 < J < 60$, $K < J$, and their role in the recombination process that forms O_3 will be discussed in detail in Chapter 5.

3.2.7. Notes

The approach we devised here has several things in common with previous studies where the hyperspherical coordinates were employed. For example, it resembles the methods of Pack,[60,61] Kendrick,[24,62,103] and Kokoouline and Greene[53,63,111] in what concerns the consecutive treatment of, first, the hyperangular degrees of freedom (θ, φ), and then, of the hyperradius ρ. However, the standard approach is to use the coupled-channel (scattering) formalism for the hyperradial coordinate, while we solve *the eigenvalue problem*. Typically, the goal of scattering calculations is to obtain the state-to-state transition matrix (e.g., for O + O_2 collisions), while our approach is better suited for calculations of the bound states and scattering resonances in O_3, using the *complex absorbing potential*. Traditionally, the CAP is used in conjunction with Jacobi coordinates, where a separate CAP has to be placed and tuned in each dissociation channel. In contrast, in the hyperspherical coordinates a single CAP defined along the hyperradius ρ takes care of all dissociative parts of the wave function, in all three channels. On the other hand, our formalism relies heavily on the idea of *sequential diagonalization truncation* proposed by Bačić and Light,[119–121] but this technique is normally applied to other types of coordinates (such as Jacobi), not the hyperspherical coordinates. Finally, we use the adaptive grid along the hyperradius ρ, and combine the DVR along ρ, with the FBR for (θ, φ), which is both practically convenient and numerically efficient.

We would like to note that during the editorial process, when this chapter was submitted for publication in Journal of Chemical Physics, it was brought to our attention that a very similar approach was recently developed by Kokoouline and co-workers.[67,123,126,127] They also use DVR in the hyperspherical coordinates, and solve the complex-eigenvalue problem using the CAP. They use the abbreviation SVD for their method, which stands for *slow variable discretization* (meaning the hyperradius ρ). Many components of our method are, indeed, the same. One methodological feature that we use, and they do not, is the sequential diagonalization-truncation technique, which makes calculations very efficient.

On the technical side we want to note that matrix diagonalizations were done in parallel using ScaLapack.[128] The kinetic energy operator is applied using FFT, which corresponds to periodic behavior for φ (Neumann boundary conditions), consistent with symmetries A_1 and A_2. For θ and ρ wave function vanishes at the ends of the grid, due to high potential energy. Two-dimensional eigenfunctions $\Lambda_m^n(\theta, \varphi)$ were obtained in two steps, using the same sequential diagonalization-truncation approach. Namely, we start with a 1D DVR in φ, which can be very dense, 400 points in the range $2\pi / 3 \leq \varphi \leq 4\pi / 3$, but causes no issues since 1D solutions are computationally cheap. Those are determined for each value of θ on the grid (280 points through $0.43 \leq \theta \leq \pi / 2$), and for each ρ slice (86 optimally spaced points in the range $3.3 \leq \rho \leq 15.0$ a_0). Those are truncated using E_{cut} (same value as reported above) retaining between 3 and 30 functions (of one symmetry), depending on the values of θ and ρ. These locally optimal and truncated 1D basis sets are used to set up the Hamiltonian matrix for 2D problem in θ and φ, diagonalization of which gives $\Lambda_m^n(\theta,\varphi)$. Since 1D and 2D calculations are (typically) very fast, we use simple equidistant grids, but in principle, grid optimization in θ and φ can also be implemented, similar to what was done for ρ. Further fine-tuning can be done by adjusting the ranges of the grids in θ and φ, and the grid density, individually for different slices in ρ. Figure 3.2 clearly shows that the grids in θ and φ do not have to be the same at different values of ρ.

We conducted careful convergence studies making sure that the values of energies for scattering resonances in the window 400 cm^{-1} above dissociation threshold are obtained with accuracy better than 1 cm^{-1} (energies of the bound states are converged better than this). To summarize, our convergence parameters, all tested individually, include the number of points for DVR in φ, the number of points for DVR in θ, the density of optimized grid in ρ determined by E_{max} and α, the extend of the grid [ρ_{min}, ρ_{max}], and the value of energy cutoff E_{cut} (used for truncation of 1D FBR basis in φ during solution of the 2D-problem, and for truncation of 2D FBR basis in hyperangles during solution of the 3D-problem). The final values of these parameters were given throughout the text above, and will not be repeated again here. Note that this procedure bypasses a common convergence studies of 2D energies ε_m^n, since only the final values of 3D energies matter. For scattering resonances, discussed in detail in the next chapter, we also checked the effect of absorbing potential (position, width and steepness) on resonance lifetimes, making sure that convergence of the recombination rate coefficient, determined by these lifetimes, is close to 5%.

3.3. Results and discussion

As mentioned above, application of our method to calculations of scattering resonances above dissociation threshold for a broad range of rotational excitations ($0 < J < 60$) is reported in the Chapter 5. Here, as a benchmark study of our method and new code, we compute the bound vibrational states of $^{16}O^{16}O^{16}O$ up to dissociation threshold for $J = 0$ and compare our results against results of another recently published paper,[129] where the standard approach (based on Jacobi coordinates) and a well-tested code were employed by another group. In the past similar calculations were carried out by several independent groups[51,52,130] using the older surface of ozone. The focus here is on the upper part of the spectrum, within 600 cm^{-1} below dissociation threshold, because we found that these vibrational states (bound in the $J = 0$ case) become scattering resonances when the rotational excitation $J > 0$ lifts them above the dissociation threshold, where these states can be populated from the continuum through $O + O_2 \rightarrow O_3^*$, and can contribute to the recombination process, O_3^* (+bas gas) $\rightarrow O_3$, as it will be shown in the next chapter. Thus, it is necessary to have all these states accurately computed, analyzed, and assigned, if only possible. Dissociation limit is defined as electronic energy of O + O_2 asymptote on the PES, plus the ro-vibrational energy of O_2 in the lowest-energy physically allowed state ($v = 0, j = 1$), which is 794.51 cm^{-1} for $^{16}O^{16}O$. This number was determined by 1D calculations for a slice through the asymptotic range of the PES, using a very dense grid of DVR points.

3.3.1. Lower part of vibrational spectrum in the well

For completeness, we also report the spectrum of vibrational states at energies lower than our "target" window of 600 cm^{-1} below dissociation threshold. This bound spectrum is given in Appendix B (Table B. 1) and includes 209 states, with the ground vibrational state at energy −8618.25 cm^{-1} below dissociation limit. The states are rigorously assigned by symmetry, A_1 for symmetric and A_2 for antisymmetric, and are also qualitatively assigned the normal mode quantum numbers (v_1, v_2, v_3) that correspond to symmetric stretch (breathing), bending, and asymmetric stretch, respectively. The normal mode assignment is done by visual inspection of the vibrational wave functions, and often is not entirely certain. One reason for this uncertainty is some *local-mode* character (due to the PES shape) mixed into the usually dominant normal-mode behavior. Such states are still assigned the normal mode quantum numbers in Table B. 1, but are labelled by "LM." Several lower energy examples are states (2,0,2), (2,1,2), and (2,0,3). At higher energies the local-mode behavior becomes the main reason for uncertainty of the normal mode assignments, as one can see from Table B.1. The second reason is similarity of the symmetric stretch and asymmetric stretch frequencies, v_1 and v_3, that lead to similar energies of the states (v_1, v_2, v_3) and (v_1+1, v_2, v_3-1). Such states have the same total number of quanta, but one quantum of asymmetric stretch is replaced by one quantum of symmetric stretch. In Table B.1 these pairs are labelled by "P#" where number indicates the corresponding pair state. Lowest energy example of this sort is the pair of states (0,0,4) and (1,0,3), followed by the pair of (0,1,4) and (1,1,3), and then by (0,0,5) and (1,0,4). Such pairs are more common at lower energies.

In order to have a quantitative picture of the vibrational spectrum in this energy range, we tried to fit our computed spectrum by the standard Dunham expansion formula, that has 10 fitting parameters: three harmonic frequencies (ω_1, ω_2, ω_3), three intra-mode anharmonicities (Δ_1, Δ_2, Δ_3), three inter-mode anharmonicities (Δ_{12}, Δ_{23}, Δ_{31}), and the well depth *D*. Results for four fits, using different number of computed states (60, 120, and 180 lower energy states) are summarized in Table 3.1. We see that the value of symmetric stretch frequency ω_1 and its corresponding anharmonicity Δ_1 are less sensitive to the number of states included (compared to other parameters), the values of ω_1 and ω_3 are different only by ~10 cm^{-1} (but are quite different from ω_2), and that the bending mode is the most harmonic (Δ_2 ~ 2cm^{-1}).

Table 3.1. Dunham expansion fitting coefficients (in cm^{-1}) for the vibrational spectrum of ozone

	Number of states fitted			
	60	120	180	248*
ω_1	1127.5	1126.3	1128.6	1141.6
ω_2	712.2	717.3	723.1	739.2
ω_3	1111.8	1119.1	1134.9	1157.4
Δ_1	3.4	3.2	3.4	4.1
Δ_2	1.7	2.0	2.2	2.9
Δ_3	16.6	18.2	20.5	22.2
Δ_{12}	8.8	10.3	11.2	13.8
Δ_{13}	34.6	30.8	30.1	32.2
Δ_{23}	16.7	18.6	20.6	24.6
D	-10075.9	-10086.3	-10107.9	-10159.7
Std. Dev.	10.0	18.7	30.8	52.1

* Including all states below vdW plateau of the PES.

Although these fits are reasonable, they are not particularly responsive to all properties of the spectra, showing rather large standard deviations (up to ~30 cm^{-1} in the case of 180 fitted states). Deviations of computed energies from the Dunham fit of 248 states (all the covalent well states, see below) are also given in Table B.1. We see that the bending mode states, even the highly excited ones, deviate little from the Dunham expansion. Examples are (0,10,0), (0,9,1), (1,9,0), (0,11,0), (0,10,1), and (1,10,0) that are within 10 cm^{-1} of the fit. Note that those are easily assignable states. In contrast, the largest deviations from the Dunham fit are observed for states that are hard-to-assign in terms of the normal mode quantum numbers (which makes sense, since the Dunham expansion assumes normal mode behavior). Thus, the states with the local mode character present, labelled "LM" in Table B. 1, often deviate from the Dunham fit by more than 100 cm^{-1}. They typically have fewer quanta of bending, but more stretching quanta, in particular the asymmetric stretching that asymptotically correlates with the local-mode (dissociative) motion. Examples are states (2,0,5), (1,1,6), (1,3,5), (2,1,5), (2,0,6), and (2,3,4).

Importantly, we found much better agreement between our computed energies and the energies reported by Ndengué *et al*.[129] Deviations are presented in Table B. 1 and we see that they increase from only -0.08 cm^{-1} for the ground state at −8618.25 cm^{-1}, to about −1 cm^{-1} for the states at energies near −1000 cm^{-1}, and stay at that level for the upper states in Table B. 1, up to energies −600 cm^{-1}. The difference is always negative and changes smoothly, which indicates some kind of a systematic, rather than random difference, more likely due to methodologies used, rather than the issue of convergence. Interestingly, the differences are slightly *smaller* for those hard to assign states (labeled by P# in Table B. 1), relative to the other states in their vicinity. Overall, taking into account the difference of methods, coordinates, basis sets, etc., this level of agreement can be characterized as good.

As for state assignments, Ndengué *et al.*[129] provided assignments for the lowest 120 states only. Our assignments go much higher in energy, although, as it was discussed above, some of them are not entirely certain. But, for the lowest 120 states our assignment fully agrees with those of Ndengué *et al*.[129]

We want to mention that we also carried out calculations of vibrational states using the older PES for O_3, developed by Schinke and co-workers,[131] and compared our results with their results. They reported 185 bound states and, for the most part, our energies and assignments agreed with their results, with mean deviation of only 0.6 cm^{-1} through the entire spectrum, except several upper states where the assignment of Schinke was uncertain, and some of the states were missing. Note that Schinke carried out a detailed comparison of his spectrum against experimental results from the literature. He reported mean deviation of only 4 cm^{-1} between his computed and experimental spectra. This gives us even more confidence in our method and new code.

3.3.2. Upper part of vibrational spectrum in the well

Overall, we found 288 bound vibrational states for $J = 0$ ozone on the PES of Dawes, out of which 163 are symmetric (A_1) and 125 are antisymmetric (A_2). This agrees well with results of Ref. 129 where 160 symmetric and 125 antisymmetric states were reported. Figure 3.5 shows energy of vibrational states (both symmetries) as a function of state number in the window 600 cm^{-1} below dissociation threshold, which gives information about density of states in this important part of the spectrum. We see that the density of states is roughly constant in the range of energies from −600 cm^{-1} to roughly −140 cm^{-1}, with average spacing between the states of about 11.7 cm^{-1}.

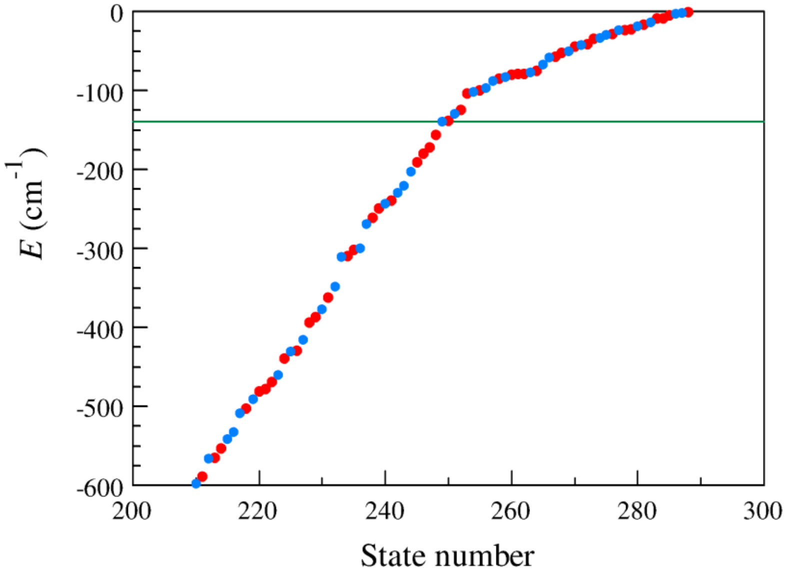

Figure 3.5. Computed vibrational spectrum of ozone (energy *vs*. state number) in the window 600 cm^{-1} below dissociation threshold. States of symmetry A_1 and A_2 are indicated by red and blue points, respectively. Energy of the lowest vdW state at −139.8 cm^{-1} is shown by solid line. Slightly above that point, near energy of the second vdW state at −103.5 cm^{-1} the density of states increases significantly, due to excitation of the local modes in the vdW plateau.

In the energy range from −140 cm^{-1} up to zero (dissociation threshold) the density is also constant, with average spacing of about 3.6 cm^{-1}. This pronounced transition occurs due to opening of the "shoulder" or "plateau" region of the PES that can accommodate additional vdW-type states. This region of the PES is seen on the minimum-energy path along ρ in Figure 3.3, but is also reflected by two-dimensional energies ε_m^n in Figure 3.3, and, in particular, by the ground state energy ε_0^n in Figure 3.4.

In this subsection we focus on the vibrational spectrum at energies between −600 cm^{-1} and −140 cm^{-1}, that has no vdW states. It contains states numbered 210 to 248, with properties summarized in Table 3.2. As before, assignments of states in terms of the normal mode quantum numbers (v_1, v_2, v_3) are given, but only one-third of states in this energy range are clearly assignable. The local-mode character is strongly mixed into wave functions of the remaining two-thirds of states. For such states, marked by a superscript c in Table 3.2, we give tentative assignments based on several factors, such as state energy and mode progression, in addition to visual analysis of vibrational wave function. The last column of Table 3.2 gives deviations of state energies from the Dunham expansion fit of all the covalent well states in the range from the ground vibrational state up to 140 cm^{-1} below dissociation threshold. Again, those states that are easily assignable show smaller deviations from the fit, while those that are hard to assign show larger deviations from the fit. Overall, based on absolute values of deviations from the fit, one can conclude the Dunham formula is not particularly useful in this energy range.

In this energy range the easily assignable states are those that have many quanta of bending and/or symmetric stretch, but no (or just a few) quanta of asymmetric stretch. This is easy to understand, since the large-amplitude asymmetric stretching motion correlates with dissociation of one bond, $O_3 \rightarrow O_2 + O$, that brings system to configuration space where the local-mode description of vibrations becomes appropriate. This leads to the appearance of the local-mode behavior in the vibrational wave functions and makes difficult (or even impossible) the assignment in terms of the normal modes. In contrast, neither bending nor symmetric stretching motion correlates with dissociation, which keeps even highly excited vibrations localized in the well region, and preserves the normal mode behavior.

Table 3.2. Vibrational spectrum of ozone from 600 cm^{-1} below dissociation threshold up to vdW plateau

#	E, cm^{-1}	Sym.	$(v_1,v_2,v_3)^a$	δ^b, cm^{-1}
210	-597.8	A_2	(1,4,5)*	133.9
211	-589.3	A_1	(5,4,0)	-61.4
212	-566.0	A_2	(2,5,3)	44.7
213	-565.1	A_1	(0,4,6)*	-29.2
214	-552.9	A_1	(1,8,2)*	101.6
215	-541.8	A_2	(5,0,3)	-15.4
216	-532.8	A_2	(1,1,7)*	-60.1
217	-508.9	A_2	(0,8,3)*	-79.3
218	-502.3	A_1	(1,0,8)*	123.0
219	-490.7	A_2	(0,0,9)*	-12.6
220	-480.6	A_1	(0,12,0)	-4.2
221	-478.0	A_1	(7,1,0)	30.6
222	-469.4	A_1	(3,2,4)*	-61.1
223	-459.7	A_2	(0,3,7)*	61.0
224	-439.7	A_1	(2,4,4)*	117.9
225	-430.6	A_2	(5,3,1)	2.5
226	-429.4	A_1	(2,9,0)	-57.2
227	-415.9	A_2	(1,7,3)*	145.9
228	-393.6	A_1	(3,5,2)*	24.7
229	-386.5	A_1	(6,0,2)	-0.6
230	-377.0	A_2	(3,6,1)*	-193.9
231	-361.8	A_1	(2,7,2)*	241.8
232	-348.1	A_2	(4,2,3)*	-26.2
233	-311.0	A_2	(2,8,1)*	8.2
234	-309.4	A_1	(4,6,0)	-99.0
235	-301.9	A_1	(2,1,6)*	-156.9
236	-299.6	A_2	(0,11,1)	-20.9
237	-268.7	A_2	(3,4,3)*	100.7
238	-261.5	A_1	(0,2,8)*	57.2
239	-249.5	A_1	(1,3,6)*	-17.5
240	-243.2	A_2	(3,1,5)*	-69.8
241	-239.5	A_1	(6,3,0)	-10.6
242	-229.5	A_2	(4,5,1)*	24.5
243	-220.9	A_2	(7,0,1)	15.7
244	-202.9	A_2	(2,3,5)*	79.5
245	-191.0	A_1	(0,10,2)	33.8
246	-180.1	A_1	(5,2,2)*	-26.5
247	-172.1	A_1	(0,7,4)*	-236.1
248	-156.1	A_1	(4,4,2)*	153.5

[a] Assignment using normal-vibration modes.

[b] Deviation from the fit by Dunham expansion.

[*] Wave function exhibits some local-mode character, the assignment is approximate.

Although it is clear that bending does not promote bond breaking, it may not be clear why the symmetric stretching motion does not lead to dissociation. This is so because stretching of two bonds simultaneously and in phase is not going to break one of them, while breaking two at the same time is impossible energetically.

So, among the easily assignable states in this energy range there are several dominantly symmetric stretching states, such as (8,0,0), (7,1,0), (7,0,1), (6,3,0), (6,0,2), and (5,0,3), there are several dominantly bending states, such as (0,12,0), (0,11,1), (0,10,2), (2,9,0), and (2,5,3), and there are several mixed states such as (5,4,0), (4,6,0), and (5,3,1). Figure 3.6 presents three-dimensional views of wave functions for all easily assignable states in this energy range. All of them are characterized by a relatively simple nodal structure and, although some of them show very significant spatial extent along the normal mode coordinate (e.g., very impressive bending progressions), neither of these functions extends into the dissociation channels.

In contrast to this behavior, Figure 3.7 gives examples of wave functions for four states that are hard to assign. All of them exhibit very significant excitation of the asymmetric stretching mode – five quanta and above. Their wave functions extend significantly into the dissociation channels, which is seen in Figure 3.7 at two “wings” of the wave function, reaching toward the upper left and right corners. In fact, in the case of state (1,0,8) the shape of wave function is dominated by the local, rather than normal mode behavior.

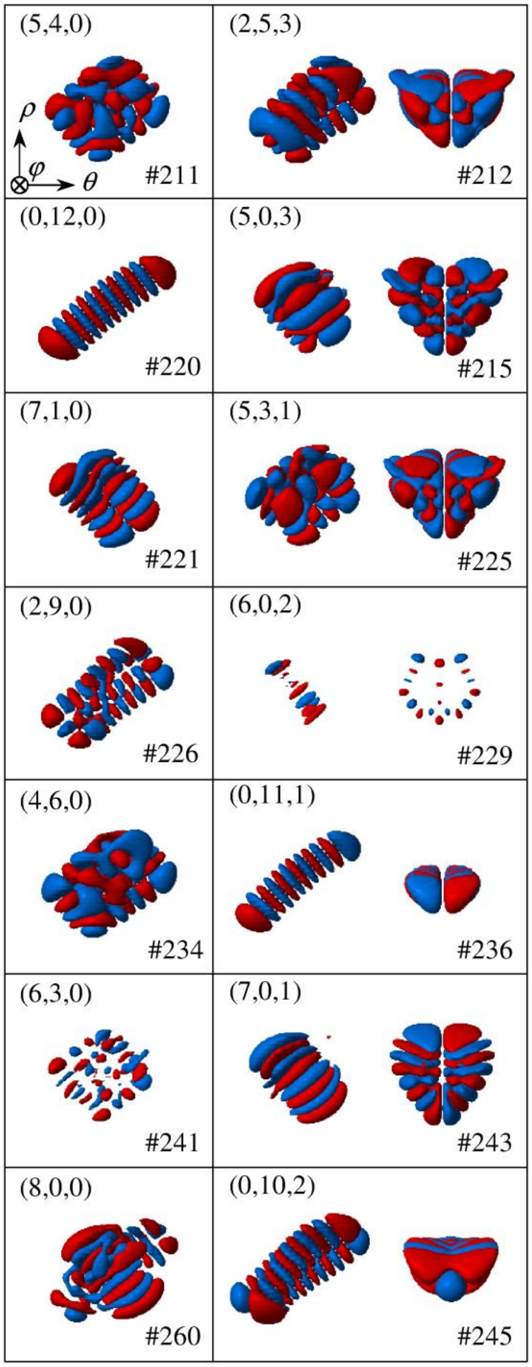

Figure 3.6. Examples of easily assignable wave functions of ozone in the energy range below the vdW plateau. Positive and negative lobes of wave functions are plotted in red and blue, respectively, using the isovalue of $|\Psi|=0.7$. Hyper-spherical system of coordinates is given in the upper left frame. Assignment by normal modes (v_1, v_2, v_3) and state number is given in the corners of each frame. Nodal structure of each wave function is readily identified, since these states are localized in the covalent well. States in the left column have no excitation in φ and thus only one (side) view is shown, while states in the right column have several excitation quanta in φ, so, in addition to the side view the second (front) view is presented.

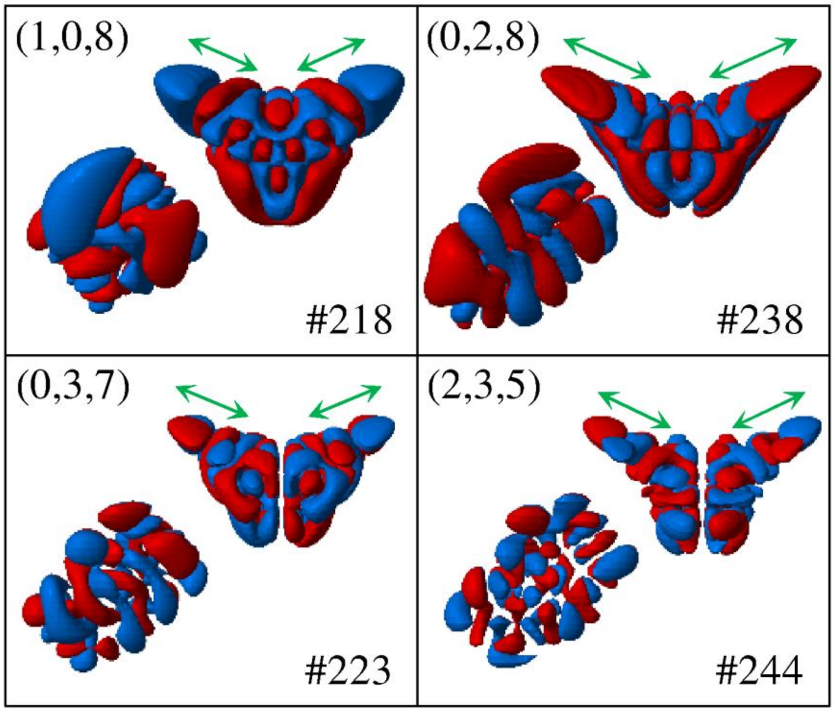

Figure 3.7. Examples of hard-to-assign wave functions of ozone in the energy range below the vdW plateau. Labels, colors, and positions are the same as in Figure 3.6. Due to significant excitation of asymmetric stretch ($v_3 > 5$) wave functions of these states extend significantly towards the dissociative channels of the PES, where the nodal structure reflects excitation of the local-mode vibrations (indicated by green arrows). Such states can be assigned only approximately, due to significant mixing of the normal and local vibration modes, in contrast to Figure 3.6, where the states are localized, simple, and easily assignable.

3.3.3. Vibrational spectrum in the vdW energy range

In the remaining part of the bound states spectrum, within 140 cm^{-1} below dissociation threshold, we found 40 states, listed in Table 3.3. Among these states only three are clearly assignable in terms of the normal mode quantum numbers: (8,0,0), (1,10,1), and (1,11,0). The first state is a highly excited symmetric stretch, while the two others are highly excited bending states, with little or no asymmetric stretch excitation, which explains their simplicity and localization, and is consistent with logics outlined in Sec. 3.3.2.

Table 3.3. Vibrational spectrum of ozone from energy of the vdW plateau up to dissociation threshold

#	E, cm^{-1}	Sym.	p_{w}[a], %	(v_1,v_2,v_3)[b]	$(v_{\mathrm{d}},v_{\mathrm{r}})$[c]
249	-139.8	A_2	29.9		(0,1)
250	-138.5	A_1	13.0		(0,0)
251	-129.9	A_2	67.7	(5,4,1)*	
252	-124.5	A_1	82.0	(5,5,0)*	
253	-103.5	A_1	57.6	(0,2,8)*	(1,0)
254	-102.2	A_2	15.2		(1,1)
255	-100.3	A_1	56.9	(4,1,4)*	(2,0)
256	-96.6	A_2	97.3	(4,5,1)*	
257	-88.0	A_2	99.6	(1,10,1)	
258	-85.0	A_1	90.1	(1,6,4)*	
259	-82.6	A_2	90.3	(2,0,7)*	
260	-79.9	A_1	99.8	(8,0,0)	
261	-79.1	A_1	78.9	(1,11,0)	
262	-78.7	A_1	23.9		(0,2)
263	-77.0	A_2	28.0		(2,1)
264	-74.6	A_1	25.4		(3,0)
265	-66.7	A_2	10.2		(0,3)
266	-58.7	A_2	44.3	(4,3,3)*	(3,1)
267	-57.0	A_1	34.3	(6,4,0)*	(3,0)
268	-52.1	A_1	9.2		(1,2)
269	-50.1	A_2	46.4	(5,1,3)*	(3,1)
270	-44.0	A_1	3.1		(0,4)
271	-42.2	A_2	19.7		(1,3)
272	-41.4	A_1	45.2	(3,3,4)*	(4,0)
273	-34.1	A_1	81.3	(1,1,8)*	
274	-33.9	A_2	40.9	(6,2,1)*	(4,1)
275	-29.8	A_2	78.6	(0,1,9)*	
276	-28.3	A_1	10.1		(2,2)
277	-23.5	A_2	4.3		(0,5)
278	-23.2	A_1	36.5	(3,8,0)*	(3,2)
279	-22.2	A_1	2.2		(1,4)
280	-18.8	A_2	12.3		(2,3)
281	-16.5	A_1	80.4	(0,8,4)*	
282	-14.0	A_2	13.2		(4,1)
283	-8.7	A_1	19.2		(5,0)
284	-8.3	A_1	1.6		(3,2)
285	-4.4	A_1	99.3	(3,0,6)*	
286	-2.6	A_2	10.1		(5,1)
287	-1.8	A_2	0.9		(1,5)
288	-0.4	A_1	4.1		(0,6)

[a] Probability in the covalent well.

[b] Assignment using normal-vibration modes.

[c] Assignment using vdW-type vibration modes (see text).

[*] The assignment is approximate.

All other well states in this energy range are assigned approximately. At these energies, the shallow vdW plateau becomes accessible to the vibrational motion of oxygen atoms in O_3. Topologically, this part of configuration space is reached by increasing the dissociative coordinate ρ (see Figures 3.3 and 3.4), which requires combination of asymmetric stretching and breathing motions of large-amplitudes. The usual normal modes cannot be used anymore but, for approximate assignment of the spectra, we can introduce two new effective vibration modes for the $O\cdots O_2$ complex, as shown in Figure 3.8.

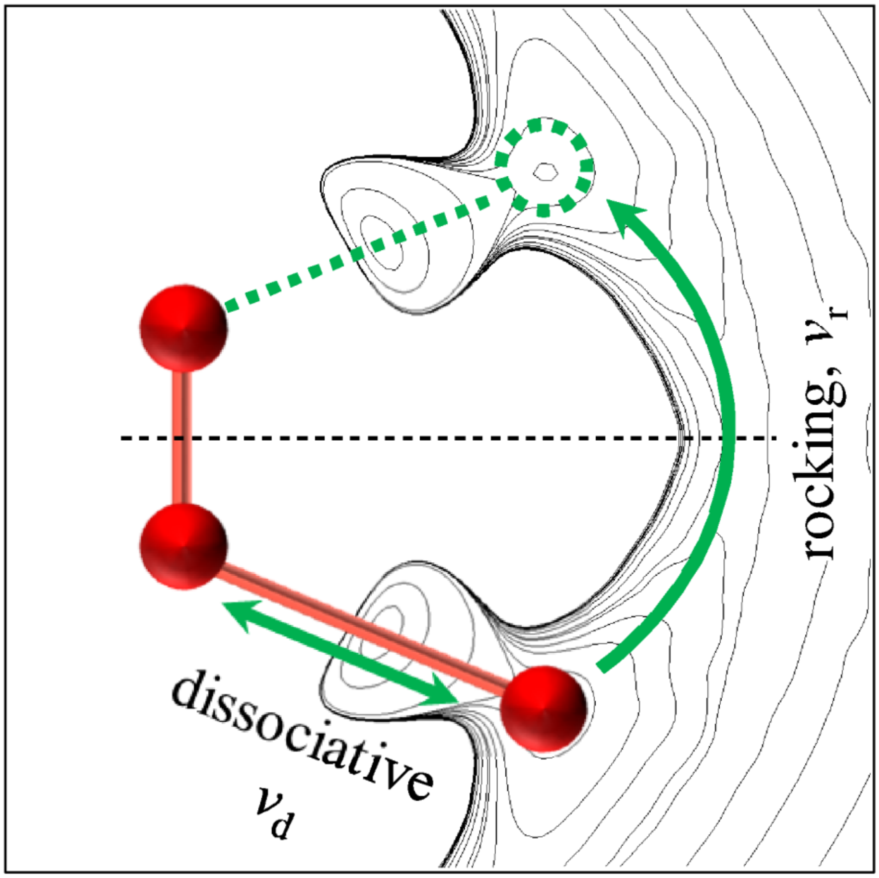

Figure 3.8. Explanation of the dissociative and rocking motion local modes over the vdW plateau of the PES in O_3.

These are *dissociative* stretching motion along ρ, described by the quantum number v_d, and "*rocking*" motion, described by the quantum number v_r. Many states listed in Table 3.3 show clear progressions of excitations of these two modes, up to $v_d = 5$ and $v_r = 5$. Note that large-amplitude rocking motion moves the system through T-shaped configuration and corresponds to highly delocalized states. The third vibration mode of the vdW complex $O \cdots O_2$ is stretching of the diatomic fragment O_2, but it remains in its ground state due to high excitation energy. So, the last column of Table 3.3 contains assignments of the vdW states in terms of (v_d, v_r).

However, since the vdW plateau is very shallow with no barrier to the covalent well, only a few vibrational states are entirely localized in the vdW range. Majority of wave functions in this energy range show non-negligible amplitudes in both the covalent well and over the vdW plateau. Figure 3.9 gives examples of wave functions for six states within 140 cm^{-1} below dissociation threshold. Three of them are almost pure vdW states, with very small amplitude in the covalent well. Three other states are mixed, showing significant amplitude everywhere. Indeed, the majority of states in this energy range are like this. To quantify this point we computed, for each state in this part of spectrum, the value of probability in the covalent well ($\rho_{\min} < \rho < \rho^{\ddagger}$) and included it in the fourth column of Table 3.3, as p_w. The value of probability over the vdW plateau ($\rho^{\ddagger} < \rho < \rho_{\max}$) is simply $1 - p_w$. From these data one can see that there are 20 bound states, 10 of each symmetry, with probability over the vdW plateau above 66%, but only 6 states with vdW probability over 95%. All those are found within 50 cm^{-1} below dissociation threshold, and include from four to six quanta of excitations: (0,4), (0,5), (1,4), (3,2), (1,5), and (0,6).

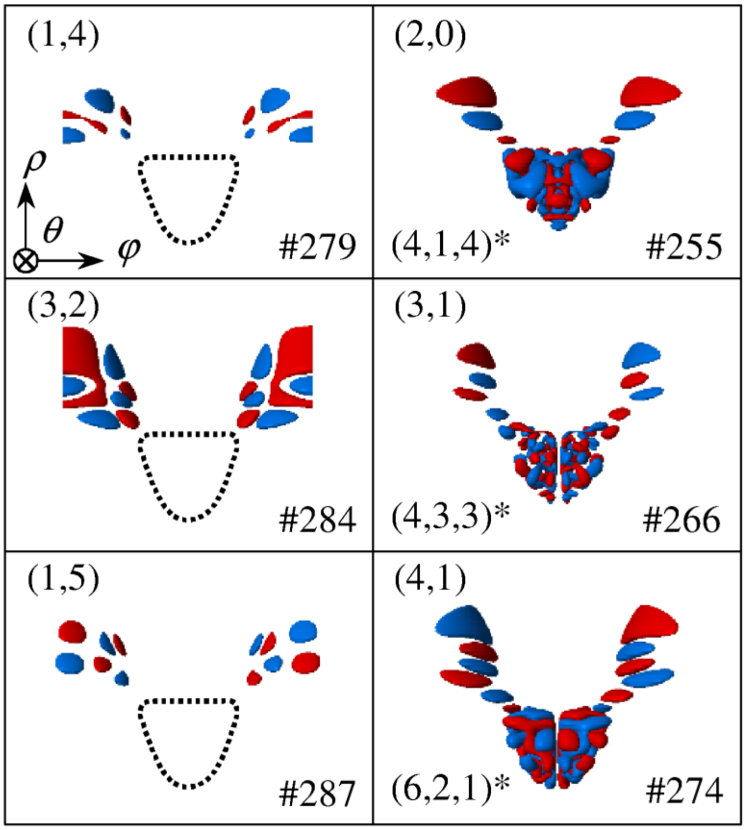

Figure 3.9. Wave functions of several pure vdW states localized entirely over the plateau (left column) and several mixed states delocalized between the covalent well and the vdW plateau (right column). Assignments are given only for the vdW parts of wave functions in terms of the dissociative and rocking modes. For pure vdW states the region of covalent well is indicated by dashed line, for clarity.

Also note that there are two vdW plateaus in the range $2\pi / 3 \leq \varphi \leq 4\pi / 3$ (see Figure 3.9), that correspond to dissociation of each bond in O_3, either O···OO or OO···O. If the covalent well would not be there, one would expect to see a spectrum of the double-well system (somewhat similar to the inversion states in NH_3), namely, two sets of the rocking states, symmetric and asymmetric (A_1 and A_2), nearly degenerate at low energy and non-degenerate at higher energy. Indeed, the data presented in Table 3.3 shows some of these features, but they are not particularly clear due to strong mixing with states of the deep covalent well. For example, the first two states of the (v_d, v_r) progression are (0,0) and (0,1) of symmetries A_1 and A_2. They are only 1.3 cm^{-1} apart, but this difference does not really reflect the splitting, because the state (0,1) appears at lower energy compared to (0,0), while the opposite is expected for the pure double-well system. The reason for this switch becomes obvious if one looks at the values of p_w for these (dominantly) vdW states. It appears that both have significant population in the covalent well, and more so for the state (0,1), which lowers its energy compared to the (0,0) state. As excitation of the rocking mode increases, the splitting increases. It is 12 cm^{-1} for states (0,2) and (0,3), and grows to 20.4 cm^{-1} for states (0,4) and (0,5). Similarly, this splitting is 1.3 cm^{-1} for states (1,0) and (1,1), grows to 9.9 cm^{-1} for states (1,2) and (1,3), and finally to 20.3 cm^{-1} for states (1,4) and (1,5). Also, the splitting is 9.4 cm^{-1} for states (2,2) and (2,3). These numbers seem to be consistent.

However, many splittings are off this order. Thus, states (2,0) and (2,1) are split by too much, and this is because (2,1) is an almost pure vdW state, while (2,0) is strongly mixed with (4,1,4) state in the covalent well. Similarly, states (3,0) and (3,1) are split by a lot, and this is again because (3,0) is an almost pure vdW state, while (3,1) is strongly mixed with (5,1,3) state in the covalent well. Finally, vdW states (4,0) and (4,1) are split by a lot, because both of them are strongly mixed with states in the covalent well, (3,3,4) and (6,2,1), respectively. However, states (5,0) and (5,1) are almost pure vdW states, and, as expected, are split by only 5 cm^{-1}.

One other complication is that some vdW states may show up several times in the spectrum, due to mixing with several different states of the covalent well. For example, we see from Table 3.3 that the vdW state (3,1) is found at -58.7 cm^{-1} mixed with the covalent state (4,3,3), and also at -50.1 cm^{-1} mixed with the covalent state (5,1,3). Similar behavior is found for states (3,0), (3,2), and (4,1).

Interestingly, many seemingly complicated features of the spectrum in the vdW plateau can be rationalized by analysis of two-dimensional energies ε_m^n as shown in Figure 3.10, separately for symmetries A_1 and A_2.

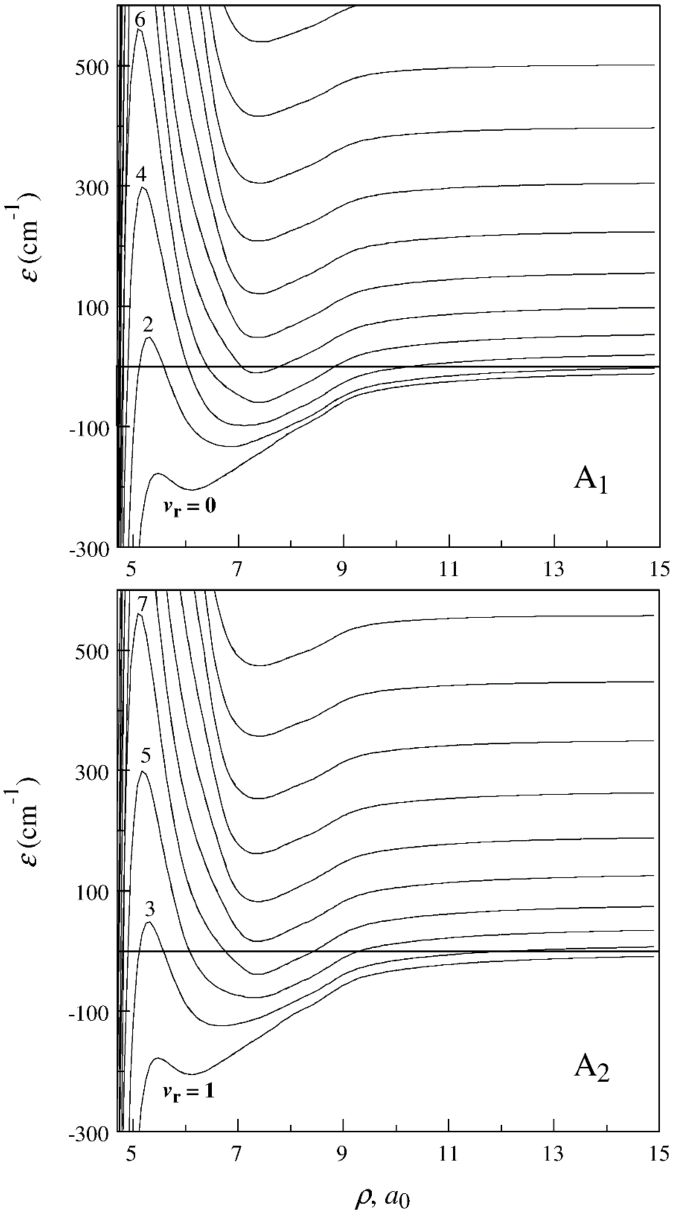

Figure 3.10. Energies $\varepsilon_m(\rho)$ of two-dimensional eigenstates in the region of vdW plateau for symmetric (upper frame) and anti-symmetric (lower frame) states. Four lower energy curves in each case are labelled by the number of rocking-mode quanta, since $v_r = m$ in the plateau region. Energies at stationary points of each curve are listed in Table 3.4.

Note that in the vdW plateau range, and asymptotically, the symmetric solutions correspond to $m = 0, 2, 4, 6$, etc., while asymmetric ones correspond to $m = 1, 3, 5, 7$, etc. Although the PES itself has no barrier between the covalent well and the vdW plateau, the $\varepsilon_m(\rho)$ dependencies all show some barrier-like features. In the case of the ground state (ε_0 for symmetric and ε_1 for asymmetric cases) we only see a tiny "reef" submerged below the dissociation asymptote, but for all upper states the top of the barrier is well above the dissociation limit. These properties are summarized in Table 3.4, and we see that in the cases of $m = 4$ and 5 the barrier is ~ 300 cm^{-1} above the dissociation limit.

Table 3.4. Properties of adiabatic 1D potentials for different channels in Figure 3.10

m	$\varepsilon_{\min}$[a], cm^{-1}	$\varepsilon^{\ddagger}$ [b], cm^{-1}	$\Delta\varepsilon$[c], cm^{-1}
0	-204.91	-175.29[d]	29.62
1	-204.89	-175.29[d]	29.60
2	-133.2	52.4	185.7
3	-123.9	52.4	176.4
4	-98.0	296.6	394.6
5	-77.8	296.6	374.4
6	-60.4	565.9	626.3
7	-39.4	565.9	605.3

[a] Energy of the vdW minimum for the channel.

[b] Energy of the barrier top for the channel.

[c] Height of barrier relative to the vdW minimum.

[d] Indicates a submerged reef.

It is important to understand that the value of m here is equivalent to the number of the rocking mode quanta $v_r = 6$, simply because ε_m is 2D energy, and in this part of configuration space one vibrational mode is unexcited (O_2 stretch in the O···OO complex), so, only one mode remains, which is the rocking motion. Thus, in the vdW range we can set $m = v_r$. To emphasize this point, in Figure 3.10 we labelled ε (ρ) dependencies using v, rather than m.

This, first of all, explains the appearance of the barriers in ε (ρ) dependencies of Figure 3.10. Indeed, even if there is no barrier along the minimum energy path on the PES, the transition state region is still very tight, and the rocking motion there (roughly normal to the dissociation coordinate) requires a lot of energy, but further in the vdW range less energy is required, which manifests as a barrier along the one-dimensional $\varepsilon_{v_r}(\rho)$ dependence.

Second, we can understand the spectrum of modes (v_d, v_r) over the vdW plateau using the adiabatic approximation discussed in Sec. 3.2. According to it, the dissociation-mode states v_d could be obtained by solving one-dimensional Schrödinger equation along ρ for each potential energy curve $\varepsilon_{v_r}(\rho)$, independently. Examining Figure 3.10 (say upper frame, the symmetric case), we see that the ground rocking state curve $v_r = 0$ has only a tiny well, separated from the covalent well by a tiny reef. This structure can support only one dissociation-mode state localized over the vdW plateau, $v_d = 0$, while all the excited states are forced to go over the reef and mix with states of the covalent well. However, the excited rocking state curve $v_r = 2$ exhibits a much more pronounced vdW well, better separated (by the barrier) from the covalent well. It can support three states of the dissociation-mode: $v_d = 0$, 1, and 2, that are localized dominantly over the vdW plateau. Similarly, the second excited rocking state curve $v_r = 4$ supports two bound states (below dissociation threshold): $v_d = 0$ and 1, while the third excited rocking state curve $v_r = 6$ supports one bound state $v_d = 0$. Overall, these considerations predict that the states (0,0), (0,2), (1,2), (2,2), (0,4), (1,4), and (0,6) are expected to be localized over the vdW plateau, while the states (1,0), (2,0), (3,0) etc. are expected to be delocalized over the vdW plateau and the covalent well (the mixed states). This simplified picture is very much consistent with exact results (and their qualitative assignments) presented in Table 3.3. The asymmetric case (lower frame in Figure 3.10) is analyzed in a similar way.

To derive some simple but quantitative measure of the vdW spectrum of ozone, we fitted some of the states of the two-dimensional progression (v_d, v_r) to a Dunham expansion. We did not include the ground rocking states, $v_r = 0$ or 1, because, when $v_d = 0$ they require parameters very different from the other states, whereas when $v_d > 0$ they mix with covalent well states. Roughly, we can say that for majority of the vdW states $\omega_d \approx \omega_r \approx 2$ cm^{-1}, with uncertainty within 2 cm^{-1}. However, for fundamental transition of the dissociative mode, the frequency is much higher, on the order of $\omega_d \approx 35 - 40$ cm^{-1}. This is clear from Figure 3.10, where we see that the ground state curve is much tighter, compared to the excited state curves.

Finally, it should be noted that analysis of vibrational states in the vdW plateau could employ Jacobi coordinates and the corresponding set of quantum numbers, as one alternative to the assignment we devised above. In such approach the rotation of a diatomic fragment with respect to the third oxygen atom in the O···OO complex (the internal or pseudo-rotation), described by the rotational quantum number j, would replace the “rocking” mode that we used above. The other two modes would be very similar. This way of wave function assignment would be ideal asymptotically, but the potential energy map in Figure 3.8 shows clearly that the PES of O_3 in the vdW region does not correspond to a free rotor (not yet). It has a shape along this delocalized vibration mode, and this shape is a double-well. For this reason, several pairs of lower energy vdW states are nearly degenerate (small splittings, as discussed above), which cannot be described by a rotational-like progression $Bj(j+1)$. However, if we only look at the upper vdW states (excluding $v_\mathrm{r} = 0$ or 1, just as in the previous paragraph), rename the v_r by j in Table 3.3, and try to fit the spectrum by

$$E(v_\mathrm{d}, j) = \omega_\mathrm{d}\,(v_\mathrm{d} + \tfrac{1}{2}) - \Delta\,(v_\mathrm{d} + \tfrac{1}{2})^2 + B\,j(j+1)\,, \tag{3.27}$$

we see a reasonable fit, with standard deviation of about 2 cm^{-1}. The values $\omega_\mathrm{d} \approx 25\ \mathrm{cm}^{-1}$ and $\mathrm{B} \approx 2.2\ \mathrm{cm}^{-1}$ are obtained. So, the free-rotor picture can probably be used for upper vdW states, while for lower vdW states the picture of rocking motion through the double-well potential is more appropriate.

3.4. Summary

In this chapter the method for calculation of rotational-vibrational states of triatomic molecules up to dissociation threshold (bound states) and even above (scattering resonances) was presented. The three major components of our approach are adiabatically adjusting hyper-spherical coordinates, the sequential diagonalization-truncation procedure (for the bound-like degrees of freedom), and the variable step-size grid (DVR, for the dissociative coordinate) optimized to the shape of the minimum-energy path on the potential energy surface. Calculations of resonance widths are possible by adding, at the last step of calculations, the complex absorbing potential to the asymptotic range of the PES. In this way the eigenvalue problem is solved for 3D-vibrations, without invoking the scattering formalism (such as coupled-channel). This approach is numerically efficient and allows rigorous incorporation of molecular symmetry.

New parallel code was written and used to compute energies and wave functions of the bound states of ozone, using two different potential energy surfaces: the older surface of Schinke and the newer surface of Dawes. In both cases very good agreement is obtained for all states assigned by these other authors in terms of the normal mode quantum numbers, which includes 185 lower energy states on the surface of Schinke, and 120 lower energy states on the surface of Dawes. Thus, we conclude that the theory is correct and the code is functional.

Our focus was on the upper part of vibrational spectrum, within 600 cm^{-1} below dissociation threshold (note that the covalent well of ozone is about 10 000 cm^{-1} deep). Interestingly, we found that progressions of the *symmetric-stretching* states (up to 8 quanta), and even more so of the *bending* states (up to 11 quanta), survive up to dissociation threshold and even above it, and are easy to recognize, assign, and fit reasonably well by a simple formula, such as Dunham’s expansion. In contrast to this behavior, excitations of the *asymmetric-stretching* overtones tend to explore more remote parts of the PES that correlate with dissociation channels. There, wave functions of O_3 are better described by the local vibration modes (rather than normal modes), which makes the assignments problematic and accurate fitting of energies impossible.

Finally, within 140 cm^{-1} below dissociation threshold, a broad plateau on the PES becomes accessible by large amplitude vibrations of a floppy van der Waals type complex $O\cdots O_2$. In this energy range the spectrum of ozone can be assigned quantum numbers using a two-dimensional progression of the vibration modes: the *rocking-motion* states, and the *dissociative-motion* states, up to 6 quanta in each, both with very low frequency on the order of 20 cm^{-1}. However, fundamental excitations of the ground rocking states require higher frequencies, about 35 and 40 cm^{-1} (depending on state symmetry), due to large anharmonicity brought about by the double-well character of the

PES near dissociation. Many of these (van der Waals plateau) states are mixed with the normal mode states of the main (covalent) well and, thus, are delocalized over a very large part of configuration space. Interestingly, we found that excitation of the rocking-motion helps to keep van der Waals states localized within the plateau region, by raising the *effective barrier*, even though the PES itself has no barrier between the covalent well and the van der Waals plateau.

Several improvements and further developments of the method are possible. First, the rigorous treatment of permutation group S_3 in calculations with $J > 0$ requires vibrational states of E-symmetry (doubly degenerate), in addition to symmetries A_1 and A_2 considered here. These states can be easily obtained by expanding the grid for hyper-angle φ onto its full physical range: $0 \leq \varphi \leq 2\pi$. See Chapter 6 for more details on this topic.

Another improvement could be a better treatment of singularity along the equator of the hypersphere, $\theta = \pi / 2$. Here we just checked and found that since this singularity is very narrow, and the DVR points are placed at the middle of the intervals (rather than at their borders), the effect of this singularity is minimal: it only affects, by ~ 2cm^{-1}, energies of the upper 17 most-delocalized states, which can be mediated by choosing carefully the value of $\theta_{\max}$ (slightly smaller than $\pi / 2$). More rigorous and automated treatments of singularities are known[72] and could be incorporated into our method.

Lastly, it should be admitted that the present formulation employs the centrifugal-sudden assumption, and thus is approximate for $J > 0$ states. More rigorous inclusion of the ro-vibrational coupling effect, due to the Coriolis term of Eq. (3.3), is desirable. In the future one can test the role of Coriolis effect in O_3 by including couplings between some (e.g., the nearest) K-blocks of the overall Hamiltonian matrix for $J > 0$, see Chapter 6.

Understanding the vibrational states of O_3 in the window 600 cm^{-1} below dissociation threshold is important because, as it will be shown in Chapter 5 this part of the vibrational spectrum plays the most important role in the recombination process that forms ozone. Due to rotation of O_3 molecules at thermal energies (up to $J \sim 40$), these bound states are lifted by the centrifugal potential to energies above dissociation threshold, which makes them *scattering resonances* O_3^* that can receive population from continuum through collisions, $O + O_2 \rightarrow O_3^*$, and can contribute to ozone formation. We think that a moderate centrifugal lift (say $J \sim 20 - 30$) causes only a slight change of wave functions for many of these states, due to their very significant vibrational content and distinct modal structure. Thus, understanding the highly excited vibrational states in non-rotating O_3 ($J = 0$) should be helpful in the future for analysis and assignment of wave functions of the rotationally excited states ($J > 0$).

Chapter 4. Theoretical treatment of ozone stabilization*

4.1. Collisional energy transfer

Collisional energy transfer (CET) plays crucial role during the second step of the recombination reaction that forms ozone in Earth's atmosphere:

$$O + O_2 \leftrightarrow O_3^*, \tag{4.1}$$

$$O_3^* + M \rightarrow O_3 + M^*. \tag{4.2}$$

Here, M can be any atmospheric molecule (or Ar atom in laboratory experiments[16]), whose role is to remove energy from the metastable O_3^* states (excited ro-vibrationally above the dissociation threshold) to produce stable ozone molecules, O_3. In order to provide complete theoretical treatment of ozone formation kinetics one should be able, ideally, to compute cross sections for all ro-vibrational state-to-state transitions that take place in O_3^* due to collisions with M, and incorporate those data into the master equation formalism.[34,132] While very easy to state, this is practically impossible to do. The density of vibrational states near dissociation threshold of ozone is close to one state per 3.6 cm^{-1}, and each of those vibrational states is accompanied by a dense spectrum of rotational states (rotational constant is ~ 0.5 cm^{-1}). Ozone is a heavy rotor and a broad distribution of rotational states (up to $J \sim 40$) is populated at room temperature. Thus, the rotational transitions between different J-values are impossible to rule out. Rotational energy transfer occurs simultaneously with vibrational stabilization and plays a very important role. Moreover, the collision-induced dissociation (CID) of O_3^* takes place simultaneously with its stabilization and should also be described theoretically.

---

[*] Teplukhin A.; Ivanov M.; Babikov D., *J. Chem. Phys.*, 139, 124301 (2013)

Recently, the group of Babikov implemented a conceptually different method for theoretical treatment of the ozone forming reaction – the mixed quantum/classical theory (MQCT) for collisional energy transfer and ro-vibrational energy flow.[35] This method is still approximate, but it overcomes many difficulties encountered earlier by other workers. Namely, the scattering of M and the rotational quenching of O_3^* are treated classically, which allows covering a broad range of rotational excitations, up to $J \sim 40$. These classical approximations are well justified because no quantum effects are expected to occur due to scattering of heavy M, or due to rotation of heavy O_3^*. The vibrational motion of ozone, however, is treated with time-dependent Schrödinger equation, which incorporates zero-point energy and vibrational symmetry. The scattering resonances of O_3^* are also accessible, including quantization of their energies, accurate calculations of their decay rates and CID.[44,47]

The MQCT is computationally feasible (in contrast to the full-quantum methods) but the high density of vibrational states, the broad range of rotational excitations in ozone and the diverse isotopic variability of the process (36 reaction, see Table 1.1) make even these calculations highly demanding. For these reasons, the calculations of Babikov’s group were carried out within the dimensionally reduced model of ozone,[35,46] where only two bond stretches were treated explicitly, while the bending motion was treated adiabatically (relaxed). In order to make such calculations even more computationally affordable one should think of some additional simplifications, within the framework of MQCT.

In this chapter the frozen-rotation (FR) approximation for MQCT is formulated and tested. Since MQCT is time dependent and involves classical as well as quantum degrees of freedom, the approximation we devise here is very different from the well-known sudden-rotation approximation used in the time-independent full-quantum calculations.[133–136] The main purpose of our FR approximation is to “freeze” the rotation of O_3^* during the M + O_3^* scattering event, *without* cutting off the energy exchange between translational, rotational, and vibrational degrees of freedom. Freezing the rotation of O_3^* gives significant computational advantages (discussed in this chapter), with relatively small intervention into the energy exchange process. Interestingly, it appears that rotational excitation and/or quenching of the molecule can be described without letting the molecule rotate in space during the collision with M.

The chapter is organized as follows. The MQCT method is briefly reviewed in Section 4.2. The formalism of FR approximation is introduced in Section 4.3. Numerical results that serve as a test of accuracy of the FR approximation are presented and discussed in Section 4.4. Section 4.5 summarizes all the work done.

4.2. The mixed quantum/classical theory

The idea of mixed quantum/classical treatment of collisional energy transfer is not entirely new.[137–141] A good review of methods and their applications was done by Billing.[115] In our implementation of MQCT[35] the vibrational motion of oxygen atoms in O_3 is treated quantum mechanically, while the rotational motion of O_3 and the translational (scattering) motion of Ar + O_3 are treated classically. All coordinates are divided into two groups: those describing quantum part of the system and those describing classical part. The former set is internal bond-angle coordinates $\mathbf{R}_Q = (R_1, R_2, \theta)$. The latter set $\mathbf{R}_C = (\mathbf{q}_{O_3}, \mathbf{q}_{Ar}, \alpha, \beta, \gamma)$ includes the Cartesian coordinates of ozone $\mathbf{q}_{O_3}$

and quencher $\mathbf{q}_{\mathrm{Ar}}$ in the laboratory-fixed frame and Euler angles (α, β, γ) for orientation of O_3 molecule in space.

Quantum description of vibrational motion involves propagation of wave function $\Psi(\mathbf{R}_{\mathrm{Q}}, t)$ using the time-dependent Schrödinger equation:

$$i\frac{\partial}{\partial t}\Psi(\mathbf{R}_{\mathrm{Q}},t) = \hat{H}(t)\Psi(\mathbf{R}_{\mathrm{Q}},t) \qquad (4.3)$$

$$\hat{H}(t) = \hat{T}_{J=0} + V(\mathbf{R}_{\mathrm{Q}};\mathbf{R}_{\mathrm{C}}(t)) + V_{\mathrm{rot}}(\mathbf{R}_{\mathrm{Q}};\mathbf{R}_{\mathrm{C}}(t)) \qquad (4.4)$$

Through the $V(\mathbf{R}_{\mathrm{Q}};\ \mathbf{R}_{\mathrm{C}}(t))$ dependence of the PES, the classical trajectory of motion $\mathbf{R}_{\mathrm{C}}(t)$ affects evolution of the quantum part of the system (vibration). The effect of rotational motion on vibration is included adiabatically[116,117,142–145], by introducing into the Hamiltonian of Eq. (4.4) the rotational potential V_{rot}, which is a smooth function of coordinates, computed numerically on a grid of points in $\mathbf{R}_{\mathrm{Q}}$ using:

$$V_{\mathrm{rot}}(\mathbf{R}_{\mathrm{Q}}) = \tfrac{1}{2}(\mathbf{J},\mathbf{I}^{-1}(\mathbf{R}_{\mathrm{Q}})\mathbf{J})\,. \qquad (4.5)$$

Here $\mathbf{I}(\mathbf{R}_{\mathrm{Q}})$ is the tensor of inertia on the grid and $\mathbf{J}(\mathrm{t})$ is the instantaneous vector of angular momentum of the molecule, both expressed in the lab reference frame. Rotational potential is a time dependent quantity.

The rotation itself is treated classically using the *fluid-rotor* equations of motion:[35]

$$\begin{pmatrix}\ddot{\alpha}\\ \ddot{\beta}\\ \ddot{\gamma}\end{pmatrix} = \mathbf{G}^{-1}\left[\tilde{\mathbf{I}}^{-1}\left[\tilde{\boldsymbol{\tau}} - \dot{\tilde{\mathbf{I}}}\mathbf{G}\begin{pmatrix}\dot{\alpha}\\ \dot{\beta}\\ \dot{\gamma}\end{pmatrix}\right] - \dot{\mathbf{G}}\begin{pmatrix}\dot{\alpha}\\ \dot{\beta}\\ \dot{\gamma}\end{pmatrix}\right]. \qquad (4.6)$$

Here $\tilde{\mathbf{I}}(t)$ is instantaneous mean tensor of inertia of the fluid rotor, while $\tilde{\boldsymbol{\tau}}(t)$ is mean torque on the molecule (caused by the quencher), defined as:

$$\tilde{\mathbf{I}} = \left\langle \Psi(\mathbf{R}_\mathrm{Q},t) \middle| \mathbf{I}^{-1}(\mathbf{R}_\mathrm{Q}) \middle| \Psi(\mathbf{R}_\mathrm{Q},t) \right\rangle^{-1}, \tag{4.7}$$

$$\tilde{\boldsymbol{\tau}} = -\left\langle \Psi(\mathbf{R}_\mathrm{Q}) \middle| \sum_i \mathbf{r}_i \times \nabla V \middle| \Psi(\mathbf{R}_\mathrm{Q}) \right\rangle, \tag{4.8}$$

where $\mathbf{r}_i = \{x_i, y_i, z_i\}$ is radius vector of i^{th} atom relative to molecular center of mass, $\mathbf{r}_i \times \nabla V$ represents the torque of the quencher on i^{th} atom in the molecule, the gradient ∇V is computed with respect to the Cartesian position of i^{th} atom. Summation in Eq. (4.8) is over three O atoms. Matrix **G** in Eq. (4.6) was introduced for convenience:

$$\mathbf{G} = \begin{pmatrix} 0 & \cos\alpha & \sin\beta\sin\alpha \\ 0 & \sin\alpha & -\sin\beta\cos\alpha \\ 1 & 0 & \cos\beta \end{pmatrix}. \tag{4.9}$$

Time derivative $\dot{\tilde{\mathbf{I}}}$ in Eq. (4.6) is computed as $\dot{\tilde{\mathbf{I}}} = \tilde{\mathbf{I}}\mathbf{A}\tilde{\mathbf{I}}$, where matrix **A** is:

$$\mathbf{A} = \left\langle \Psi \middle| \mathbf{I}^{-1}\left(\frac{d\mathbf{I}}{dt}\right)\mathbf{I}^{-1} \middle| \Psi \right\rangle - 2\,\mathrm{Re}\left\langle \Psi \middle| \mathbf{I}^{-1} \middle| \frac{d}{dt}\Psi \right\rangle. \tag{4.10}$$

Note that evolution of the vibrational state of the system affects its classical rotational motion, through vibrational wave function $\Psi(\mathbf{R}_\mathrm{Q}, t)$ in expressions for the mean values of $\tilde{\mathbf{I}}$, $\tilde{\boldsymbol{\tau}}$ and **A**.

Translational coordinates $\mathbf{q}_{\mathrm{O}_3}$ and $\mathbf{q}_{\mathrm{Ar}}$ are propagated using classical equations of motion: $\dot{\mathbf{q}} = \mathbf{p} / M$ and $\dot{\mathbf{p}} = -\nabla\tilde{V}$, where transcripts are omitted for simplicity, and the mean field potential is defined as:

$$\tilde{V}(\mathbf{R}_\mathrm{C},t) = \left\langle \Psi(\mathbf{R}_\mathrm{Q},t) \middle| V(\mathbf{R}_\mathrm{Q};\mathbf{R}_\mathrm{C}(t)) \middle| \Psi(\mathbf{R}_\mathrm{Q},t) \right\rangle. \tag{4.11}$$

Again, quantum vibrational state of the system $\Psi(\mathbf{R}_\mathrm{Q}, t)$ influences the classical trajectory for scattering, through $\tilde{V}$.

Overall, the energy is exchanged between translation, rotation and vibration, while the total energy is conserved.

4.3. Frozen rotor approximation

Let us start from the formal side of implementing the frozen-rotor approximation. Two terms in Eq. (4.10) have very transparent physical meaning. The first term is a rigid-rotor term, while the second term is a fluid-rotor term. The second term is zero if the vibrational wave function $\Psi(\mathbf{R}_\mathrm{Q})$ is constant over the time. Its effect on rotation becomes important only if the vibrational motion occurs and the wave function changes, which affects the tensor of inertia. We want to keep this term, because it describes ro-vibrational interaction. The first term in Eq. (4.10) is a simple rotation in 3D of the tensor of inertia of the rigid body. If the molecule does not rotate, this term is unnecessary. So, in the frozen-rotor case Eq. (4.10) simplifies to

$$\mathbf{A} = -2\,\mathrm{Re}\left\langle \Psi(\mathbf{R}_\mathrm{Q}) \middle| \mathbf{I}^{-1}(\mathbf{R}_\mathrm{Q}) \middle| \frac{d}{dt}\Psi(\mathbf{R}_\mathrm{Q}) \right\rangle . \qquad (4.12)$$

Note that our frozen rotor remains fluid, due to the time derivative in Eq. (4.12). Within its original orientation in space, the tensor of inertia is allowed to change over the time if $d\Psi / dt \neq 0$, for example, due to centrifugal effect or due to interaction with quencher.

Furthermore, if the molecule does not rotate, its orientation in space is constant and $\dot{\mathbf{G}} = 0$. So, the last term in Eq. (4.6) vanishes. Now it is convenient to introduce $\upsilon_\alpha = \dot{\alpha}$, $\upsilon_\beta = \dot{\beta}$ and $\upsilon_\gamma = \dot{\gamma}$. These moieties are related to angular velocity ω through

$$\boldsymbol{\omega} = \mathbf{G}\begin{pmatrix} \upsilon_\alpha \\ \upsilon_\beta \\ \upsilon_\gamma \end{pmatrix} . \qquad (4.13)$$

In these notations, Eq. (6.6) can be rewritten as follows:

$$\begin{pmatrix} \dot{\alpha} \\ \dot{\beta} \\ \dot{\gamma} \end{pmatrix} = \begin{pmatrix} \upsilon_\alpha \\ \upsilon_\beta \\ \upsilon_\gamma \end{pmatrix}, \tag{4.14}$$

$$\begin{pmatrix} \dot{\upsilon}_\alpha \\ \dot{\upsilon}_\beta \\ \dot{\upsilon}_\gamma \end{pmatrix} = \mathbf{G}^{-1} \left[\tilde{\mathbf{I}}^{-1} \left[\tilde{\boldsymbol{\tau}} - \frac{d\tilde{\mathbf{I}}}{dt} \mathbf{G} \begin{pmatrix} \upsilon_\alpha \\ \upsilon_\beta \\ \upsilon_\gamma \end{pmatrix} \right] \right]. \tag{4.15}$$

If the molecule does not rotate in space, we do not have to propagate Eq. (4.14) for angles at all, equivalent to saying that $\dot{\alpha} = 0$, $\dot{\beta} = 0$ and $\dot{\gamma} = 0$. Only Eq. (4.15) should be propagated. It captures the effect of rotational excitation and/or quenching and emphasizes that our frozen-rotor remains fluid, within its original orientation in space. If the mean tensor of inertia changes, $d\tilde{\mathbf{I}} / dt \neq 0$, its effect onto rotational excitation is included.

The existing computer code[35] can be very easily modified to propagate Eqs. (4.12) and (4.15), instead of Eqs. (4.6) and (4.10). Note, however, that Eq. (4.15) can be conveniently rewritten using Eq. (4.13) as follows:

$$\dot{\boldsymbol{\omega}} = \tilde{\mathbf{I}}^{-1} \left[\tilde{\boldsymbol{\tau}} - \frac{d\tilde{\mathbf{I}}}{dt} \boldsymbol{\omega} \right]. \tag{4.16}$$

Rearranging terms, using chain rule and introducing angular momentum $\mathbf{J} = \tilde{\mathbf{I}}\omega$ we obtain:

$$\frac{d\mathbf{J}}{dt} = \tilde{\boldsymbol{\tau}}. \tag{4.17}$$

Indeed, if the molecule is forcedly fixed in space, no equations for rotational coordinates are necessary at all. All we have to do is to integrate torque $\tilde{\boldsymbol{\tau}}(t)$ due to quencher along the trajectory to determine the change of **J** (i.e., rotational excitation or quenching). The time dependent value of $\mathbf{J}(t)$ goes directly into Eq. (4.5) to give evolution of rotational potential $V_{\mathrm{rot}}(\mathbf{R}_{\mathrm{Q}})$ along the trajectory $\mathbf{R}_{\mathrm{C}}(t)$ for inclusion into the Hamiltonian of Eq. (4.4). This is almost embarrassingly simple, but makes sense.

4.4. Results and discussion

We carried out preliminary calculations using both versions: either propagating Eqs. (4.12) and (4.15) or, alternatively, Eq. (4.17) alone. The results are entirely identical, however, Eq. (4.17) gives significant computational advantage, since calculations of the wave function derivative $d\Psi / dt$ (on the grid) in Eq. (4.12) are avoided, as well as numerous matrix operations in Eq. (4.15). The computational advantage of the FR method is substantial, speedup by a factor of ×3.8.

4.4.1. Examples of a single trajectory

Details of setting up the initial conditions for MQCT calculations have already been discussed in detail.[35] Initial wave function is one of vibrational eigenstates in the rotationally excited potential: $\Psi(\mathbf{R}_{\mathrm{Q}},t_0) = \Phi_n^{(i)}(\mathbf{R}_{\mathrm{Q}})$. Here, index i denotes initial rotational excitation (quantized semi-classically), while index n denotes a vibrational state in this rotationally excited potential. We always start at a scattering resonance, namely, the ro-vibrational state above the dissociation threshold, $E_n^{(i)} > 0$. The vibrational spectrum of $^{16}\mathrm{O}^{18}\mathrm{O}^{16}\mathrm{O}$ in the dimensionally reduced model is relatively sparse. The upper part of spectrum, within the energy range ~1000 cm^{-1} below the dissociation threshold, contains only 11 vibrational states (#41 to 51 in Table 4.1 and Table 4.2).

Table 4.1. Cross sections (a_0^2) for vibrational state-to-state transitions and stabilization of the normal mode state (#51)

Final vibrational state		Initial rotational state*							
		J=25, K=5 (73.4; 3.5×10^{-5})		J=35, K=0 (241.1; 1.1×10^{-4})		J=35, K=5 (309.0; 1.9×10^{-3})		J=35, K=12 (629.9; 1.5×10^{-3})	
#	Character	AR	FR	AR	FR	AR	FR	AR	FR
51	N	422.898	473.141	417.682	479.024	416.552	473.649	402.366	460.521
50	L2	0.100	0.085	0.139	0.057	0.120	0.079	0.202	0.376
49	L1	0.095	0.057	0.091	0.044	0.111	0.058	0.277	0.035
48	N	3.316	1.130	4.345	1.014	5.407	1.106	9.460	1.313
47	L2	0.030	0.034	0.046	0.018	0.036	0.032	0.174	0.074
46	L1	0.028	0.018	0.027	0.018	0.036	0.014	0.118	0.022
45	N	0.086	0.028	0.133	0.025	0.198	0.029	0.508	0.029
44	N	0.003	0.002	0.004	0.002	0.007	0.002	0.016	0.003
43	N	0.002	0.001	0.002	0.001	0.003	0.001	0.011	0.002
42	L2	0.003	0.000	0.000	0.000	0.000	0.000	0.001	0.002
41	L1	0.000	0.000	0.000	0.000	0.000	0.000	0.000	0.000
Ro-vibrational stabilization		99.969	47.206	51.375	26.318	45.481	14.620	10.430	3.439

* Each scattering resonance is characterized by J, K, energy and width (in parenthesis) in the units of wave number

Table 4.2. Cross sections (a_0^2) for vibrational state-to-state transitions and stabilization of the local mode state (#50)

Final vibrational state		Initial rotational state*							
		J=20, K=9 (26.1; 3.8×10^{-6})		J=35, K=−5 (133.6; 8.7×10^{-3})		J=35, K=9 (349.7; 2.5×10^{-6})		J=45, K=−5 (418.6; 2.5×10^{-1})	
#	Character	AR	FR	AR	FR	AR	FR	AR	FR
51	N	0.077	0.083	0.143	0.039	0.911	0.074	0.374	0.012
50	L2	400.088	434.582	365.551	359.478	360.393	427.081	360.987	244.492
49	L1	0.668	0.728	1.651	1.808	1.390	0.236	0.576	0.744
48	N	0.776	2.395	11.430	18.729	2.451	4.340	5.623	3.137
47	L2	29.544	16.832	41.678	8.661	33.814	15.381	41.652	5.309
46	L1	0.078	0.211	0.289	0.620	0.902	0.125	0.232	0.257
45	N	0.639	0.638	1.890	1.049	3.730	0.587	3.098	1.161
44	N	0.026	0.172	0.029	0.234	0.372	0.068	0.048	0.207
43	N	0.026	0.028	0.018	0.041	0.360	0.021	0.048	0.022
42	L2	0.016	0.070	0.017	0.020	0.332	0.077	0.040	0.016
41	L1	0.005	0.004	0.000	0.014	0.128	0.003	0.015	0.012
Ro-vibrational stabilization		127.245	94.858	104.177	52.552	45.906	14.148	48.544	18.438

* Each scattering resonance is characterized by J, K, energy and width (in parenthesis) in the units of wave number

Some of them belong to progression of the normal vibration modes (labeled by N), and some to the local-vibration mode progression associated with either channel 1 or 2 (namely, O···OO or OO···O, labeled L1 and L2). Typical rotational excitations of J ~ 20 – 30 bring these states up (the centrifugal effect) and converts them into scattering resonances trapped behind the centrifugal barrier at energies few hundred wavenumbers above the dissociation threshold. These are our initial states. Note that in rotationally excited ozone the vibrational motion is rather localized, due to sharp centrifugal barrier. We found that in such conditions all vibrational states can be easily assigned (in terms of quantum numbers) up to dissociation threshold and even above. This is very different from the non-rotating ozone, where the upper 20% of vibrational spectrum exhibit irregular behavior due to flattening of the PES near dissociation threshold.[131,146–148]

In Figure 4.1 we consider an example trajectory which starts at the scattering resonance with $J = 35$ and $K = –5$, $n = 50$ and $E_n^{(i)}$ =133.6 cm^{-1} (specifying semi-classical initial conditions for rotation we set $K_b = K_c$ and assume that $K = K_a$ is good quantum number, for simplicity). This is a local-mode state with 8 quanta of vibration along the O+O$_2$ dissociation channel and one quantum of vibration in O$_2$. Collision energy of Ar is $E_{\mathrm{coll}} = 217$ cm^{-1} and impact parameter is $b = 3.64\ a_0$. Plotted in Figure 4.1 are the values of rotational potential $V_{\mathrm{rot}}(\mathbf{R}_{\mathrm{Q}})$ at two important points on the PES: the bottom of covalent well (Figure 4.1a) and the top of centrifugal barrier in one of the dissociation channels (Figure 4.1b). We can see that in the original MQCT method, where the adiabatic-rotation (AR) is explicitly going on, the centrifugal potential V_{rot} evolves during the pre-collisional and post-collisional stages of the process, due to the ro-vibrational interaction in the fluid rotor model. In the frozen-rotor version of MQCT the rotational potential

$V_{\mathrm{rot}}(\mathbf{R}_{\mathrm{Q}})$ is constant over time (at every point of the $\mathbf{R}_{\mathrm{Q}}$ grid). Note that for description of the resonance stabilization, for CET, the focus is not really on the ro-vibrational interaction during the pre- and post-collisional stages, but more on the molecule-quencher interaction during the short collision event. Figure 4.1 demonstrates that this last effect is well described by the FR approximation.

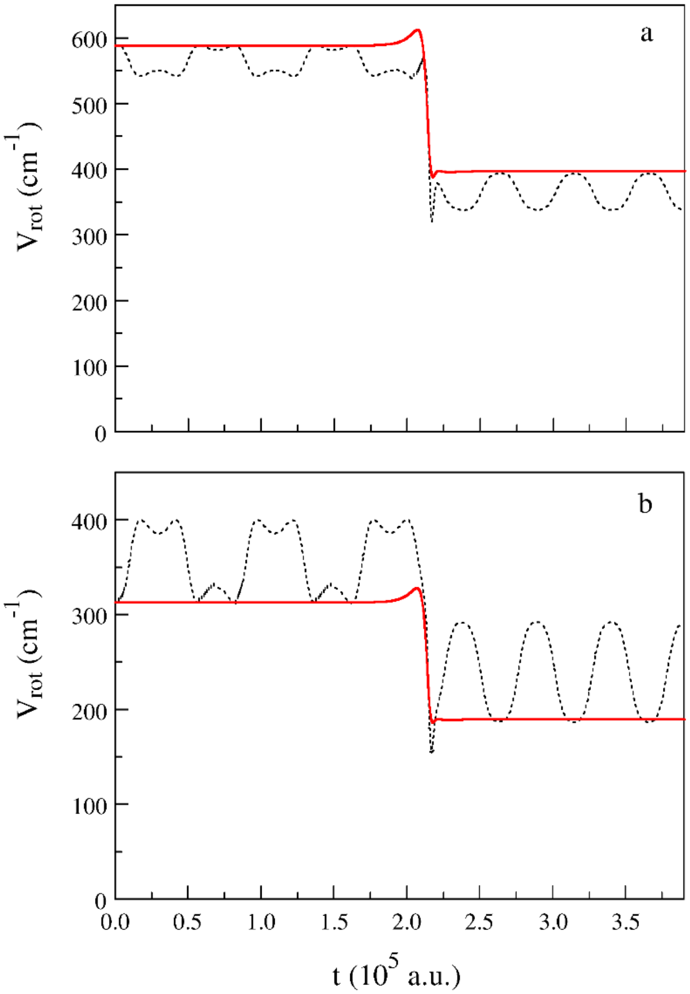

Figure 4.1. Time evolution of rotational potential along one trajectory at the point near a) bottom of covalent well on the PES of ozone $R_1 = R_2 = 2.4\ a_0$; b) top of centrifugal barrier $R_1 = 2.3\ a_0$, $R_2 = 3.8\ a_0$. Red solid line stands for FR-method, black dotted stands for AR-method. Initial (classical) rotational state is $J = 35$, $K = -5$, and the ro-vibrational energy is $E_n^{(i)} = 133.6$ cm^{-1}. See text for further details.

In the time-dependent mixed quantum/classical method we do not really have to make any assumptions about goodness of the rotational quantum number K, because we use classical trajectories for description of rotation, either as fluid-rotor or as rigid-rotor. In either case, three components of J evolve during the dynamics. Figure 4.2a shows an example of typical trajectory ($b = 2.55\ a_0$ and $E_{\mathrm{coll}} = 489\ \mathrm{cm}^{-1}$) for the initial vibrational state $n = 50$ and a quasi-classical initial state $J = 35$, $K = K_a = 12$, $|K_b| = |K_c| = 23$. One sees that the value of K_a is approximately conserved on the pre-collisional and post-collisional stages, in contrast to K_b and K_c that oscillate widely. This picture supports a well-known fact – ozone is very close to a symmetric top. Its rotational constants are only ~10% different. For simplicity, we sample the initial rotational states such that $|K_b| = |K_c|$, so that we can label these quasi-classical initial conditions by J and K only. As rotation start (on the pre-collisional stage) the memory of $|K_b| = |K_c|$ is immediately lost, while $K = K_a$ remains roughly the same. Figure 4.2b demonstrates that K remains good quantum number in the FR-method too.

One more advantage given by the FR approximation becomes obvious. On the post collisional stage the centrifugal potential is constant, so, one can start spectral analysis of the final vibrational wave packet $\Psi(\mathbf{R}_{\mathrm{Q}},t_{fin})$ at any moment of time, as soon as quencher leaves. This is not so straightforward in the AR version of the method, where rotational potential continues evolving due to ongoing rovibrational interaction. This continuing ro-vibrational energy exchange causes artificial ro-vibrational transitions at the post-collisional stage, which is a known deficiency of the mixed quantum/classical treatment.[35] In order to cancel its effect we usually use the forward-backward propagation technique,[45] but it doubles the computational effort. In the FR version of MQCT this problem does not exist, so that the backward propagation is unnecessary, which saves computational resources.

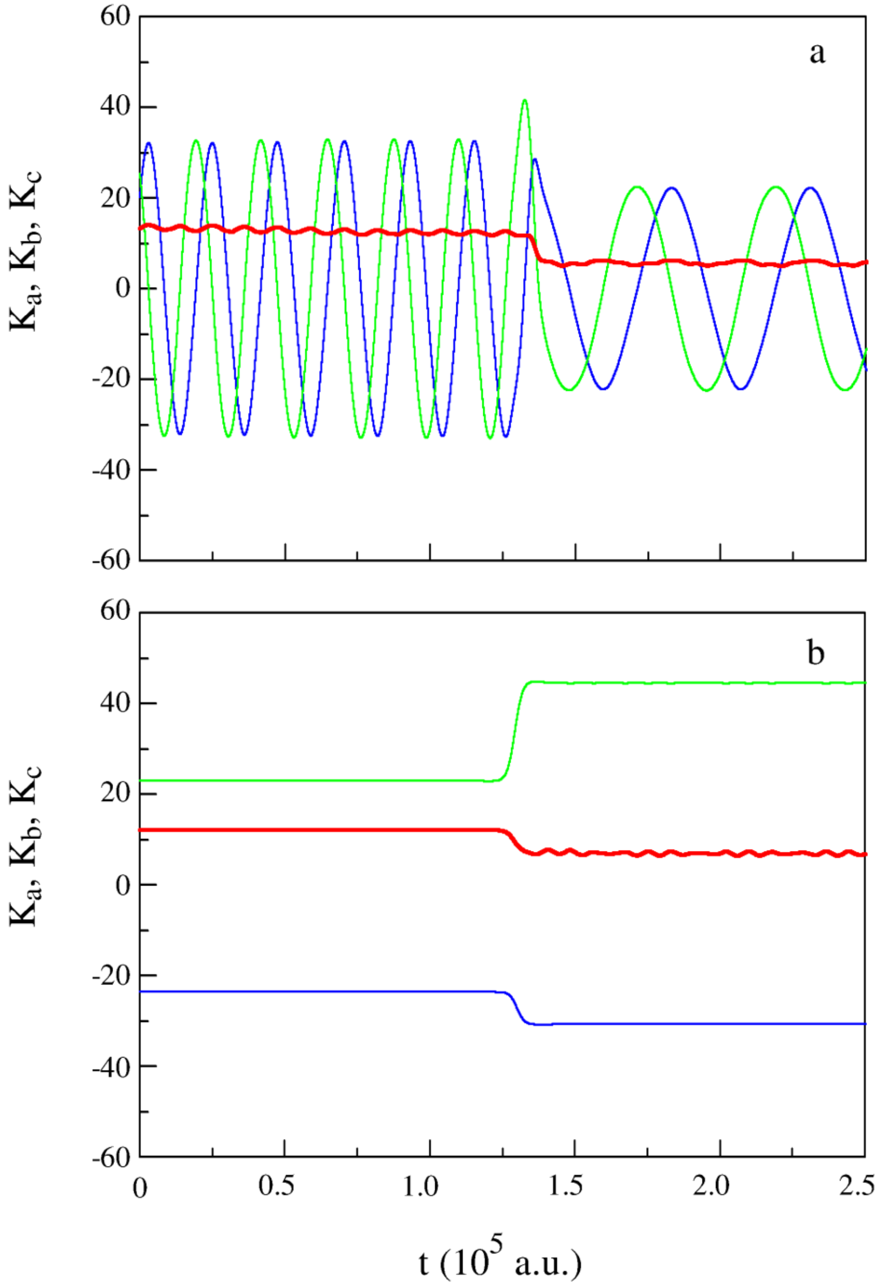

Figure 4.2. Time evolution of K_a (red), K_b and K_c (blue and green) along a typical trajectory for initial J = 35, K_a = 12, $|K_b|$ = $|K_c|$ = 23 and vibrational state n = 50. a) Original AR method; b) developed FR approach. One sees that K_a is approximately a good quantum number in both cases.

4.4.2. Energy transfer

Projection onto vibrational eigenstates of the final rotational potential permits to compute energy spectrum of the final wave packet, or the probabilities of state-to-state transitions:

$$p_{n,n'}^{(i)} = \left| \left\langle \Phi_{n'}^{(i')}(\mathbf{R}_{\mathrm{Q}}) \middle| \Psi(\mathbf{R}_{\mathrm{Q}}, t_{fin}) \right\rangle \right|^2 . \tag{4.18}$$

This information, together with magnitudes of the energy transfer $\Delta E = E_{n'}^{(i')} - E_n^{(i)}$, can be used to bin the data for a batch of trajectories into a 2D-hystogram, like those presented in Figure 4.3 (3000 trajectories for the same initial state as Figure 4.1). These plots visualize intensity of the excitation/quenching as a function of impact parameter $0 \leq b \leq 15\ a_0$ and the magnitude of energy transfer $-1000 \leq \Delta E \leq +1000$ cm^{-1}. Collision energy was sampled from thermal distribution at room temperature. Figure 4.3a describes the case of explicit adiabatic rotation (AR), while Figure 4.3b corresponds to our frozen-rotor approach (FR). Both methods show the elastic scattering peak ($\Delta E = 0$) at large impact parameters, and both indicate quenching ($\Delta E < 0$) as well as excitation ($\Delta E > 0$) going on at impact parameters less than $b \approx 8\ a_0$. We have to admit that in the FR case the excitation is clearly overestimated in the region of $\Delta E > +500$ cm^{-1}, compared to the AR case. This is understood as follows: when the rotational motion is frozen, the ability of the molecule to dodge the quencher is limited to the translational recoil only, which leads to more intense interaction with quencher and larger amount of energy transferred to the molecule. This is a negative consequence of FR approximation.

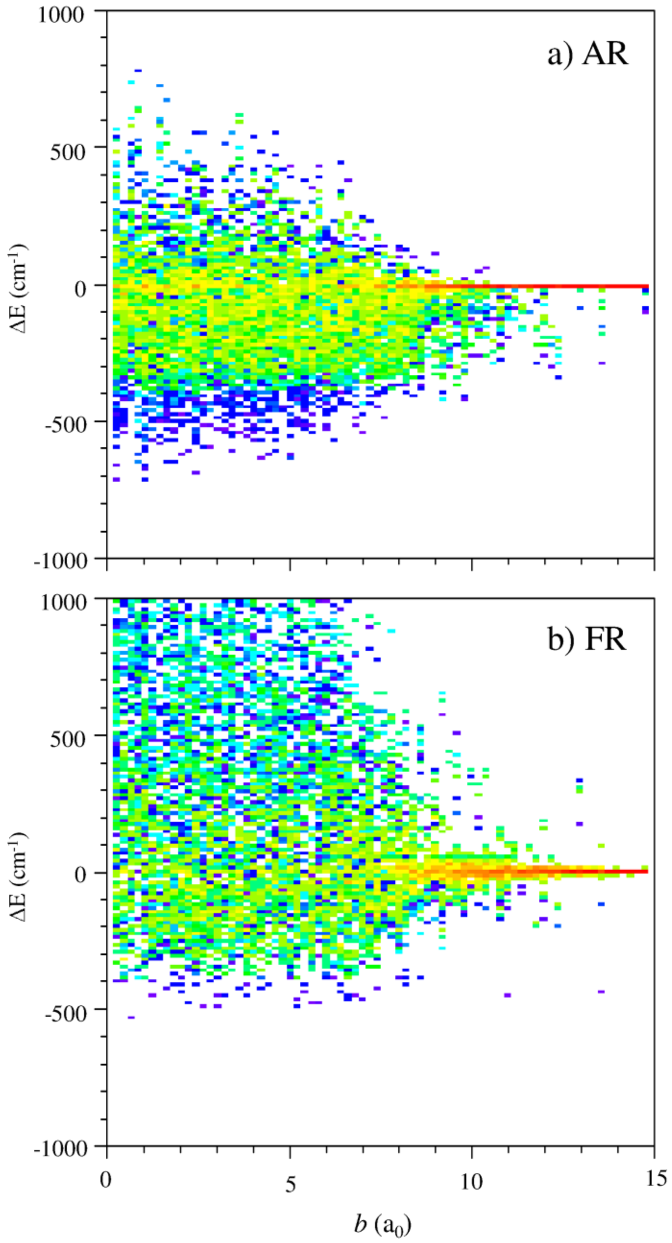

Figure 4.3. Intensity of the energy transfer as a function of impact parameter *b* and the magnitude of energy change Δ*E* for a batch of 3000 trajectories in the a) original AR method; b) developed FR approach. Red is for high intensity, blue is for low intensity. Excitation is at positive Δ*E*, quenching is at negative Δ*E*. Elastic peak is at Δ*E* = 0 and large impact parameter. Initial ro-vibrational state is the same as in Figure 4.1.

It should also be mentioned that the total energy in the FR method is not exactly conserved. We conducted a careful study of this issue and found that for some trajectories the total energy increases as a result of collision, while it decreases for others. Average over the batch of trajectories, with thermal distribution of collision energies at room temperature, leads to relatively small overall energy defect.

The weighted sum over b of the 2D-hystogram in Figure 4.3 produces a differential (over ΔE) cross section for energy transfer, plotted in Figure 4.4. Such dependence is used in analytic theories of CET[149–152] and is sometimes called the energy transfer function. Comparison of the AR *vs.* FR data (filled *vs.* empty symbols) shows that in the regime of moderate energy transfer, $-500 \leq \Delta E \leq +500$ cm^{-1}, the agreement between two methods is reasonably good. Furthermore, the overall trend of the differential cross section is reproduced well by FR-method through eight orders of magnitude range of values and in a broad range of ΔE. At large positive $\Delta E > +500$ cm^{-1} the FR-method overestimates cross section (as discussed above), while at large negative $\Delta E < +500$ cm^{-1} the FR-method somewhat underestimates the cross section. Note a sharp change of the slope at $\Delta E = -489$ cm^{-1}. This amount of energy corresponds to the initial rotational excitation of the molecule in this example, so, the point where the energy transfer function bends corresponds to transformation from the *ro-vibrational* quenching to purely *vibrational* quenching. Finally, note a discontinuity of cross section at $\Delta E = -590$ cm^{-1}. To the right of this dashed line the *normal-mode* state $n' = 47$ (which is ~ 101 cm^{-1} below the initial state) participates in the energy transfer, while to the left of this line the energy transfer is dominated by the local-mode state (much smaller cross section, see below). Interestingly, even these fine features of the energy transfer function are reproduced by the FR-method.

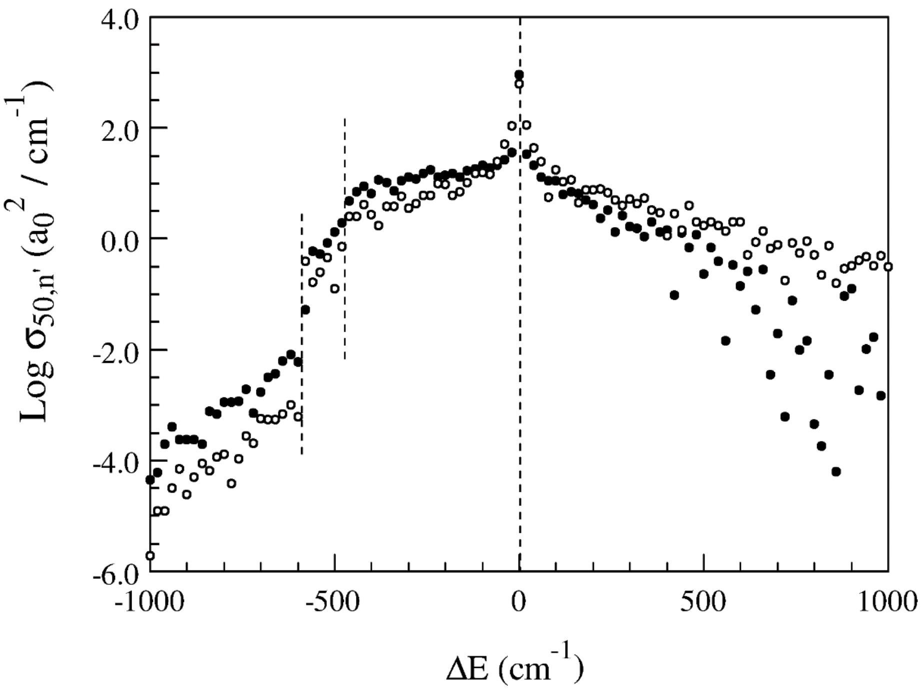

Figure 4.4. Energy transfer function obtained by the original AR (filled symbols) and the developed FR (empty symbols) methods. The long dashed line at $\Delta E = 0$ separates quenching (to the left) from excitation (to the right). Purely vibrational quenching is to the left of the short dashed line at $\Delta E = -489$ cm^{-1}. Discontinuity at $\Delta E = -590$ cm^{-1} is due to the vibrational mode character. Note that the FR method reproduces all these fine features. Initial ro-vibrational state is the same as in Figures 4.1 and 4.3.

4.4.3. Vibrational state-to-state transition cross sections

More detailed insight is provided by comparing cross sections for vibrational state-to-state transitions computed as:

$$\sigma_{n,n'}^{(i)} = \frac{2\pi b_{\max}}{N} \sum b p_{n,n'}^{(i)}(b) \,. \tag{4.19}$$

Here, the sum is over N trajectories in a batch and includes all the final (classical) rotational states. In this computational experiment we took, as initial states, four different rotational states of the normal-mode vibrational state $n = 51$, and four different rotational states of the local-mode vibrational state $n = 50$. Those are listed in Table 4.1 and Table 4.2. Total energies $E_n^{(i)}$ of these scattering resonances cover a broad range, from roughly

25 cm^{-1} to 630 cm^{-1} above dissociation threshold. Their widths $\Gamma_n^{(i)}$ (inversely proportional to lifetimes) also cover a broad range of values, 10^{-6} to 10^{-1} cm^{-1}. The final vibrational states are listed in the first column of Table 4.1 and Table 4.2.

The largest values in Table 4.1 and Table 4.2 correspond to elastic scattering cross sections. They are all reproduced accurately enough for the normal-mode initial states (deviations are 11-14%) and somewhat less accurately for the local-mode initial states (deviations are 2-17%). Only in one case the deviation is quite large (39%, last column of Table 4.2), but this is because this initial state is very close to the barrier top (large width of the resonance $\Gamma = 0.25$ cm^{-1}). It has short lifetime and, consequently, tends to dissociate. Small changes in the energy transfer lead to significant changes in the post-collisional behavior.

It is well known that the elastic scattering cross section, strictly speaking, diverges if the scattering motion is treated classically. Sometimes this problem is overcome by an appropriate choice of the maximum impact parameter, or by removing, in an *ad hoc* way,[43] the elastic scattering peak clearly seen at $\Delta E = 0$ in Figure 4.3(red) and Figure 4.4 (dashed line). We tried several of these methods and saw very similar results. The elastic scattering cross sections given in Table 4.1 and Table 4.2 were obtained by disregarding all trajectories with $|\Delta J| < 1$. This method allows removing selectively all points of the elastic scattering peak, without affecting the rest of data. Roughly, it corresponds to setting up the maximum impact parameter at ~ 9 a_0 (see Figure 4.3).

As for vibrationally inelastic processes, the largest cross sections are usually observed for transitions between states of same character. Normal-mode states tend to stabilize to the normal-mode states, while local-mode states tend to stabilize to proper local-mode states. For example, for the initial *normal-mode* state ($n = 51$) the largest inelastic cross section corresponds to the final state $n = 48$ (see Table 4.1), which is the closest *normal-mode* state. Similar, for the initial *local-mode* state ($n = 50$) the largest inelastic cross section corresponds to the final state $n = 47$ (see Table 4.2), which is the closest *local-mode* state in the same dissociation channel. This qualitative feature is reproduced well by the FR method, but the absolute values of cross sections are different in the AR and FR cases. For the initial states at lower energies $E_n^{(i)} < 350$ cm^{-1} the FR cross sections are factor of ×2 to ×5 smaller, compared to the AR cross sections. This difference increases to ×8 for states at higher energies $E_n^{(i)} \sim 420$ cm^{-1} and 630 cm^{-1} respectively (last columns in Table 4.1 and Table 4.2).

Other entries in Table 4.1 and Table 4.2 show similar differences of state-to-state cross sections obtained from AR and FR methods. Note that for smaller cross sections the statistical error is typically larger. In those cases when cross sections are reasonably large and statistical error is small (within ~ 25%) the typical difference between AR and FR results is ×4. This is similar to performance of the rotationally sudden approximation in the time-independent methods, known to produce cross sections that are factor of ×2 to ×4 smaller, compared to exact results.[153,154]

4.4.4. Stabilization cross sections

For approximate treatment of recombination kinetics at low and moderate pressure of M it is not really necessary to compute individual cross sections for all vibrational state-to-state transition. It is advantageous to introduce stabilization cross section for each scattering resonance:

$$\sigma_{n,stab}^{(i)} = \frac{2\pi b_{\max}}{N} \sum bP_{n,stab}^{(i)}(b) . \tag{4.20}$$

$$P_{n,stab}^{(i)} = \sum_{E<0} p_{n,n'}^{(i)} \tag{4.21}$$

The sum in Eq. (4.21) is over the final vibrational states below dissociation threshold, $E_n^{(i)} < 0$. Note that this energy includes the final rotational energy, so, the stabilization cross section characterizes the overall ro-vibrational quenching (within MQCT, where rotation is treated classically while vibration is treated with quantum mechanics). Stabilization cross sections are the most practically important moieties. Figure 4.5 shows convergence study of stabilization cross section for state n = 50 (same rotational state as before) in both AR and FR calculations. For a batch of 3000 trajectories the statistical error is rather small, typically close to 5%. Interestingly, Figure 4.5 demonstrates that with only as few as 100 trajectories one can obtain a reasonable estimate of stabilization cross section.

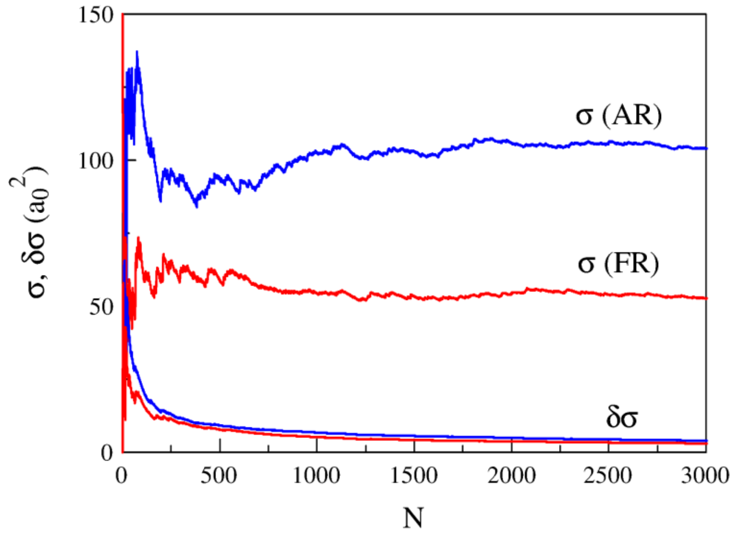

Figure 4.5. Convergence of stabilization cross sections in the original AR (blue) and the developed FR methods (red). Statistical errors for each method are given at the bottom of the figure. Initial ro-vibrational state is the same as in Figures 4.1, 4.3 and 4.4.

Last row in Table 4.1 and Table 4.2 lists the values of stabilization cross sections for eight scattering resonances considered here. The values obtained from FR method are only a factor of ×2 to ×3 smaller, compared to AR method, in the entire range of rotational excitations and for both normal and local vibration mode states. This is very encouraging, since such a difference is usually assumed quite acceptable in most kinetics models. In Figure 4.6 we plotted the ratio of cross sections $\Re = \sigma_{\mathrm{stab}}(\mathrm{AR}) / \sigma_{\mathrm{stab}}(\mathrm{FR})$ obtained from two methods, as a function of initial (total ro-vibrational) energy of the scattering resonance. Although the correlation is not particularly strong, these data suggest that a ratio of 2-to-3 is typical for the FR approach in the entire range of energies, when it is used to compute the ro-vibrational stabilization cross sections.

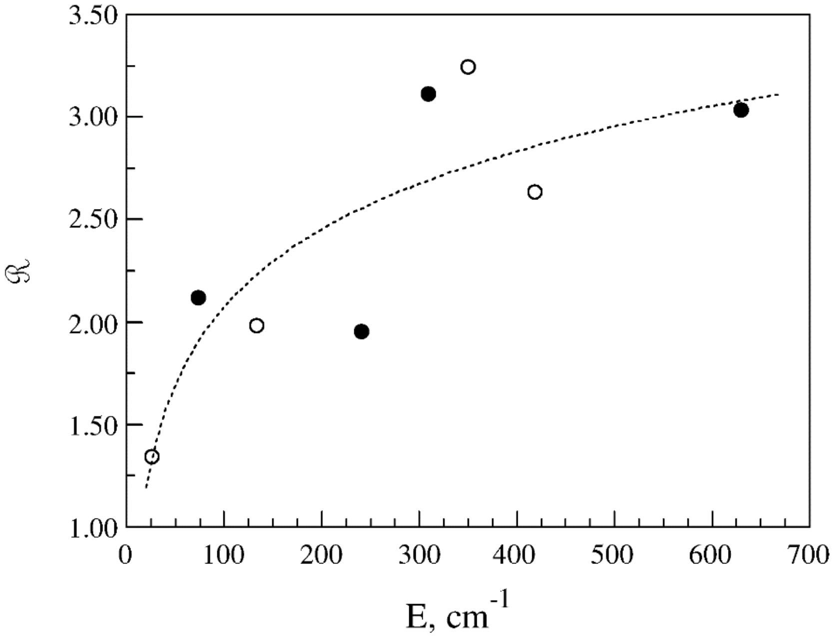

Figure 4.6. Ratio of stabilization cross sections computed from the original AR method and the developed FR method. The data are presented for eight scattering resonances: four different rotational states of the normal mode vibrational state (filled symbols, see Table 4.1) and four different rotational states of the local mode vibrational state (empty symbols, see Table 4.2). The fit is by a logarithmic function.

4.5. Summary

In this chapter the frozen-rotor approximation for MQCT was formulated and a thorough numerical test was conducted to assess its efficiency and accuracy, in comparison to the original version of MQCT where rotation of the molecule in space is treated explicitly and adiabatically. The FR treatment of rotation only requires propagating a simple Eq. (4.17) with mean torque defined by Eq. (4.8), and computing the centrifugal potential function in Eq. (4.5), to add to the quantum Hamiltonian. This approach permits to block the artificial and undesirable ro-vibrational transitions at the pre- and post-collisional stages of the process. As for computational costs, the FR method is 3.8 times faster (for the 2D-model of ozone) because the backward propagation is no more needed and because the equations for rotational excitation/quenching become much simpler. Computational advantage of the FR approximation is expected to be more important in the case of full-dimensional 3D calculations of ozone stabilization, planned in the near future.

Although molecular orientation is fixed in space, the energy exchange between rotational, vibrational, and translational degrees of freedom still occurs in the FR method, allowing to compute ro-vibrational excitation and quenching. Noteworthy, behavior of the energy transfer function through eight orders of magnitude range of values and in a broad range of ΔE is reproduced well by the developed FR-method, including some fine features. In the range of moderate $-500 \le \Delta E \le +500$ cm^{-1} the FR-method is rather accurate. The absolute values of stabilization cross sections for scattering resonances trapped behind the centrifugal threshold are a factor 2-to- 3 smaller (compared to the explicit-rotation approach). This performance is acceptable and is similar to the well-known sudden-rotation approximation in the time-independent inelastic scattering methods.

Chapter 5. Rate coefficient of ozone recombination reaction*

5.1. Two mechanisms

Atmospheric ozone, O_3, is formed as a product of recombination reaction of oxygen molecules, O_2, with oxygen atoms, O, but the mechanism of this process is not yet entirely understood. In the past, the energy-transfer mechanism, also known as Lindeman mechanism, was assumed almost exclusively,[155,156] according to which a metastable ozone molecule is formed at the first step of the process, and is stabilized at the second step by collision with an atom or a molecule of the bath gas (*e.g.*, Ar, N_2):

$$O_2 + O \rightarrow O_3^* \tag{5.1}$$

$$O_3^* + M \rightarrow O_3 + M^* \tag{5.2}$$

Here the role of M is to quench the metastable intermediate O_3^*, producing a stable ozone molecule. However, a more recent analysis of experimental data[157] indicates that this may not be the only and, in fact, not necessarily the dominant mechanism of ozone formation. It looks like simultaneously with the energy-transfer mechanism described above, the so-called chaperon mechanism, also known as radical-complex mechanism, may produce ozone *via*:

$$O + M \rightarrow OM^* \tag{5.3}$$

$$O_2 + OM^* \rightarrow O_3 + M \tag{5.4}$$

Here the roles of M are to (non-covalently) bind the oxygen atom, exchange it with O_2 and, finally, carry away the excess energy, leaving a stable ozone molecule behind. Experimentally it is not straightforward to tell the difference between these two

---

* Teplukhin A.; Babikov D., *Phys. Chem. Chem. Phys.*, 18, 19194 (2016)

mechanisms since, under the steady state conditions, each of them leads to the third-order kinetics overall, first order in each [O], [O_2] and [M]. But, based on the analysis of the temperature dependence of the recombination rate coefficient (in a broad range) Troe[157] was able to determine contributions of each mechanism. For example, at room temperature and atmospheric pressure, in the air bath, the contribution of energy-transfer is close to 40%, while the contribution of chaperon mechanism is close to 60% of the total recombination rate. At low temperatures chaperon dominates, while energy-transfer dominates at high temperatures.[157]

Using the method described in previous chapter the scattering resonances in full-dimensional model of ozone (including its bending motion) were computed and analyzed for a broad range of rotational excitations, up to $J = 64$, $K_a \leq J$. This information, together with the analytic formula for collisional energy-transfer and collision-induced dissociation derived earlier,[158] permitted building a more complete version of the energy-transfer mechanism of ozone recombination. When complemented by contribution of the chaperon mechanism (as suggested by Troe[157]) our results agree well with experimental data, including the absolute value of the recombination rate coefficient, its temperature and pressure dependencies.

In this chapter, the kinetic model of recombination reaction is presented in Section 5.2.1, the summary of the method used to compute resonances (Chapter 4) and its adaptation to rotationally-excited ozone is given in Section 5.2.2, while stabilization and dissociation models are described in Section 5.2.3. Properties of resonances has been analyzed separately using histograms and distributions and are discussed in Section 5.3.1. The value of absolute rate coefficient of ozone recombination reaction and its temperature and pressure dependencies are covered in Sections 5.3.2, 5.3.3 and 5.3.4, respectively. Section 5.3.5 discusses a validity of chaperon contribution to ozone recombination process.

5.2. Theoretical framework

5.2.1. Reaction mechanism

Kinetics of the processes (4.1 and 4.2) is described within the micro-canonical framework, where different scattering resonances of O_3^* are treated as different chemical species.[24,25,27] For each scattering resonance $O_3^{(i)}$ at energy E_i the processes affecting its population $[O_3^{(i)}]$ are considered and the corresponding rate constants are introduced. Those are:

i. Formation of $O_3^{(i)}$ from O_2 + O characterized by the second-order rate coefficient k_i^{form}:

$$O_2 + O \rightarrow O_3^{(i)} \tag{5.5}$$

ii. Spontaneous unimolecular decay of $O_3^{(i)}$ onto O_2 + O characterized by the first-order rate coefficient k_i^{dec} :

$$O_3^{(i)} \rightarrow O_2 + O \tag{5.6}$$

iii. Stabilization of $O_3^{(i)}$ by collision with a bath gas atom characterized by the second-order rate coefficient k_i^{stab}:

$$O_3^{(i)} + M \rightarrow O_3 + M^* \tag{5.7}$$

iv. Collision-induced dissociation $O_3^{(i)}$ onto O_2 + O characterized by the second-order rate coefficient k_i^{diss}:

$$O_3^{(i)} + M^* \rightarrow O_2 + O + M \tag{5.8}$$

The width Γ_i of quantum scattering resonance $O_3^{(i)}$, computed as explained in Sec. 4.2.2, gives us directly the value of its decay rate, $k_i^{\text{dec}} = \Gamma_i$. The coefficients k_i^{form} and k_i^{dec} for each scattering resonance are related to each other through micro-canonical equilibrium constant: $k_i^{\text{form}} = ½\, k_i^{\text{dec}} K_{\text{eq}}(E_i)$. Here the factor of ½ reflects the fact that while in a symmetric $^{48}O_3$ there are two equivalent channels for decay of resonances, the formation rate coefficient k_i^{form} is per one entrance channel, simply because O hits only one side of O_2 in a given encounter. The equilibrium constant $K_{\text{eq}}(E_i)$ for each scattering resonance is computed statistically using known formula,[44] and taking into account a symmetry number of ½ for the partition function of symmetric reagent $^{32}O_2$ (in denominator), where only odd rotational states are allowed. The values of k_i^{stab} and k_i^{diss} are computed based on the results of the mixed quantum/classical simulations for $O_3^{(i)}$ + Ar collision dynamics,[158] as explained in Sec. 4.2.3.

Assuming steady-state conditions for the concentration of each state $O_3^{(i)}$ allows deriving analytic expression for the third order recombination rate coefficient of the overall recombination reaction:

$$\kappa = \sum_i \frac{\frac{1}{2}\Gamma_i\ K_{\text{eq}}(E_i)}{\Gamma_i + (k_i^{\text{stab}} + k_i^{\text{diss}})[\text{M}]} k_i^{\text{stab}} \tag{5.9}$$

where the sum is over all scattering resonances $O_3^{(i)}$. As explained above, this recombination rate coefficient is per one formation channel.

Several processes, less important than (4.5–4.8), are neglected in our treatment of kinetics. Namely, we do not include the possibility of back excitations, $O_3 + \text{Ar} \rightarrow O_3^{(i)} + \text{Ar}$, assuming that concentration of the formed ozone $[O_3]$ is small. We also neglect the collision-induced transitions *between* different scattering resonances, $O_3^{(i)} + \text{Ar} \rightarrow O_3^{(j)} +$

Ar, assuming that their populations are entirely determined by equilibrium with reagents $O_2 + O$. These assumptions are reasonable at low and moderate pressures of the bath gas.

5.2.2. Energies, widths and wave functions of resonances

A numerical method used to determine the properties of scattering resonances was reported in detail in previous section. Here we give only a brief summary. Three vibrational degrees of freedom in O_3 are described using adiabatically-adjusting principal-axis hyperspherical coordinates ρ, θ and φ.[74] For low-amplitude vibrations near the equilibrium geometry of ozone ($\rho_{\mathrm{eq}} = 4.048\ a_0$) the motion along the hyperradius ρ corresponds to the breathing mode in O_3. For typical levels of rotational excitation the top of the centrifugal barrier occurs near $\rho^{\dagger} \approx 5.4\ a_0$. Wave functions of scattering resonances trapped behind the centrifugal barrier are localized mostly in the range $\rho < \rho^{\dagger}$. In the asymptotic (channel) region the motion along ρ describes dissociation of O_3 onto $O_2 + O$. Complex absorbing potential in the form suggested by Balint-Kurti[159] is placed in the range $10 < \rho < 15\ a_0$ in order to absorb the tails of resonant wave functions. Hyperangles θ and φ describe bending and asymmetric-stretching motions near the equilibrium point. The symmetry of the vibrational wave function is determined by reflection through $\varphi = 0$. For symmetric $^{48}O_3$ vibrational wave functions are either symmetric (A_1) or antisymmetric (A_2).

The potential energy surface of Dawes[84] was used in our calculations. Compared to the older surfaces of ozone,[24–26,80,82] this new surface has slightly better dissociation energy (compared to the most advanced experimental data), and slightly different behavior along the minimum energy path for dissociation (a flat ‘‘shoulder’’, rather than a small submerged ‘‘reef’’), which gives better agreement with experiment for the atom-exchange process.[96–99,101] Other than that, the older and new surfaces are very similar, and exhibit very similar densities of states near threshold.[129]

We found that it is impossible to come up with a 3D-grid that covers uniformly and efficiently the entire configuration space of the problem.[160] So, a straightforward diagonalization of the Hamiltonian matrix using a 3D-grid was found to be prohibitively expensive computationally. In order to make calculations feasible we employed the sequential diagonalization-truncation approach of Bačić and Light,[118,119] adapted to the hyperspherical coordinates. Namely, for each value of ρ on the grid, we determined solutions of a two-dimensional problem in θ and φ, and used those as locally optimal basis sets for efficient representation of the global 3D wave function (of the given symmetry, separately for A_1 and A_2). The grid along ρ was also optimized to reflect the shape of the potential energy surface, using a method based on the local value of de Broglie wave length.[124,125] We found that this combined FBR/DVR approach is very efficient, see previous chapter. Complex eigenvalues $E - i\,\Gamma/2$ and wave functions of the reduced matrix were computed using the ScaLAPACK package.[128] Instead of the scattering approach (coupled-channel, often used in conjunction with hyper-spherical coordinates), we solved a 3D-eigenvalue problem, with complex absorbing potential introduced in the asymptotic range of the PES.

Similar to the previous work by Grebenshchikov and Schinke,[27] we adopted the centrifugal-sudden approximation, known also as symmetric-top rotor approximation, or K-conserving approximation (where K is projection of total angular momentum J onto the first principal axis of inertia, i.e. $K = K_a$, for each instantaneous molecular configuration).

This is the only approximation used here. It involves neglecting the Coriolis coupling term in the Hamiltonian operator, but also neglecting the asymmetric-top term $(A - B)/2$ in the rotational potential. As was emphasized by Parker and Pack,[60] these two simplifications constitute one single approximation, and have to be made simultaneously in order to decouple rotational and vibrational degrees of freedom. Thus, our calculations were done independently for different values of $K_a \leq J$. Vibrational wave functions of both symmetries, A_1 and A_2, were retained, since they would contribute to solutions of different parities in the exact fully-coupled approach, except the case of $K_a = 0$, when only A_2 solutions were kept for $J = 0$, only A_1 solutions for $J = 1$, then, again, only A_2 solutions for $J = 2$, and so on (see for example, ref. 129). Note that states of symmetry E are not physically allowed for $^{16}O^{16}O^{16}O$, since in this case the wave function must be symmetric with respect to permutation of any two oxygen atoms. Thus, E-symmetry states were excluded from calculations, by restricting the range of hyperangle φ to one well only, $120° \leq \varphi \leq 240°$.

Typically, the Coriolis coupling is non-negligible in the ‘‘floppy’’ molecules only. In the ‘‘stiff’’ molecules, such as ozone, neglecting this coupling term is well justified and has been done in the past by other authors.[27] If needed, the action of this term onto wave function can be rigorously evaluated.[60,72] In the future we plan testing the effect of Coriolis coupling by including it, at least, for the states with small K values (e.g., $K < 7$), while neglecting it for larger K.

5.2.3. Stabilization and Dissociation Rates

Rate coefficients for stabilization k_i^{stab} of scattering resonances $O_3^{(i)}$ are obtained from the corresponding cross sections:

$$k_i^{\mathrm{stab}} = \sigma_i^{\mathrm{stab}} \left(\frac{8kT}{\pi \mu} \right)^{1/2} \tag{5.10}$$

where μ is O_3 + Ar reduced mass, and similar for the k_i^{stab} – rate coefficient for the dissociation of $O_3^{(i)}$. In our previous work we generated several sets of data that are used here to compute $\sigma_i^{\mathrm{stab}}(E_i)$ and $\sigma_i^{\mathrm{diss}}(E_i)$.

First of all, one can use the analytical formula obtained in ref. 158 to represent on average a large amount of data obtained for stabilization of various scattering resonances in four different isotopomers of ozone. In that case, for a resonance at energy E above dissociation threshold, the value of stabilization cross section is given by

$$\sigma^{\mathrm{stab}}(E) = \sigma_0^{\mathrm{stab}} \left(\exp\left\{ -\frac{E}{\gamma} \right\} + c \exp\left\{ -\frac{E}{d} \right\} \right) \tag{5.11}$$

The values of parameters σ_0^{stab}, c, γ and d for this model can be found in Table II of Ref. 158. A slightly different fit[158] of the same data uses two variables, E and E^{vib}:

$$\sigma^{\mathrm{stab}}(E, E^{\mathrm{vib}}) = \sigma_0^{\mathrm{stab}} \left(\exp\left\{ -\frac{E}{\gamma} \right\} + c \exp\left\{ -\frac{E}{d} \right\} \right) \left(1 - \frac{A_{\mathrm{v}}}{1 + (E^{\mathrm{vib}} / kT)^2} \right) \tag{5.12}$$

Here E^{vib} is vibrational energy of the resonance, which is total energy E less rotational energy, and A_{v} is one more fitting parameter.[158] This formula reflects observation that the stabilization process is influenced by the balance between vibrational and rotational content of the resonance. Namely, stabilization cross sections are larger for those states where rotational excitation is larger, because rotational energy is exchanged more readily in a typical $O_3^{(i)}$ + Ar collision. Eqs. (5.11) and (5.12) will be referred to as versions *a* and *b* of Stabilization Model 1, or SM1*a* and SM1*b*. The average dissociation cross section of a resonance at energy *E* is computed using the following formula:20

$$\sigma^{\text{diss}}(E) = \sigma_0^{\text{diss}}\left(1 + \tanh\left\{\frac{(E - E_0^{\text{diss}})}{\gamma^{\text{diss}}}\right\}\right) \tag{5.13}$$

and a set of parameters σ_0^{diss}, E_0^{diss} and γ^{diss} that can be found in Ref. 158.

Alternatively, one can use results of Ref. 158, where we determined the energy-transfer functions $\bar{\sigma}_i^{\text{tran}}(\Delta E)$ for several *individual* resonances (ten representative states) and fitted each separately by double-exponential analytic model (see Fig. 7 in Ref. 158 for examples of such energy-transfer functions and Table IV in Ref. 158 for the values of fitting parameters). Such energy-transfer functions $\bar{\sigma}^{\text{tran}}(\Delta E)$, measured in the units of a_0^2/cm^{-1}, can be analytically integrated through the range $(-\infty; -E]$ in order to obtain stabilization cross sections, in the units of a_0^2, for a resonance at energy *E* above dissociation threshold:

$$\sigma^{\text{stab}}(E) = \int_{-\infty}^{-E} \bar{\sigma}^{\text{tran}}(E')dE' \tag{5.14}$$

Employing the data for ten different resonances studied in Ref. 158 we introduce some range of typical values for stabilization cross section $\sigma^{\text{stab}}(E)$, rather than one definite number. This approach is further referred to as Stabilization Model 2, or SM2.

So, in this work the stabilization cross sections are not computed for each individual resonance (e.g., by solving the $O_3^{(i)}$ + Ar collision problem numerically), rather they are obtained approximately, by substituting resonance energy *E* (and E^{vib} for SM1b) computed in Sec. 4.2.2, into analytic expressions of Eqs. (5.11-5.13). Note, however, that parameters of Eqs. (5.11-5.13) were determined in the earlier work,[158] based on the mixed quantum/classical modeling of $O_3^{(i)}$ + Ar collisions.

5.3. Results and discussion

5.3.1. Properties of resonances

In this section we analyze the collective properties of resonances in O_3^* with emphasis on their contribution to the overall process of recombination, rather than the properties of individual resonances, simply because hundreds of resonances are involved. Thus, the histogram of Figure 5.1a represents contribution of resonances to the recombination rate coefficient κ, Eq. (5.9), as a function of resonance energy above the dissociation threshold of O_3 (which includes ro–vibrational zero-point energy of the O_2 product in the asymptotic/channel range). We see that the maximum of this distribution is close to E_i = 100 cm^{-1}. Lower energy resonances (closer to threshold) contribute less. The tail of distribution extends up to E_i = 800 cm^{-1}. Similarly, the histogram of Figure 5.1b represents the distribution of resonance widths, and we see that major contributions to the recombination rate coefficient κ come from resonances characterized by widths in the range $10^{-2} < \Gamma_i < 10$ cm^{-1}, with maximum of the distribution around $\Gamma_i = 1$ cm^{-1}.

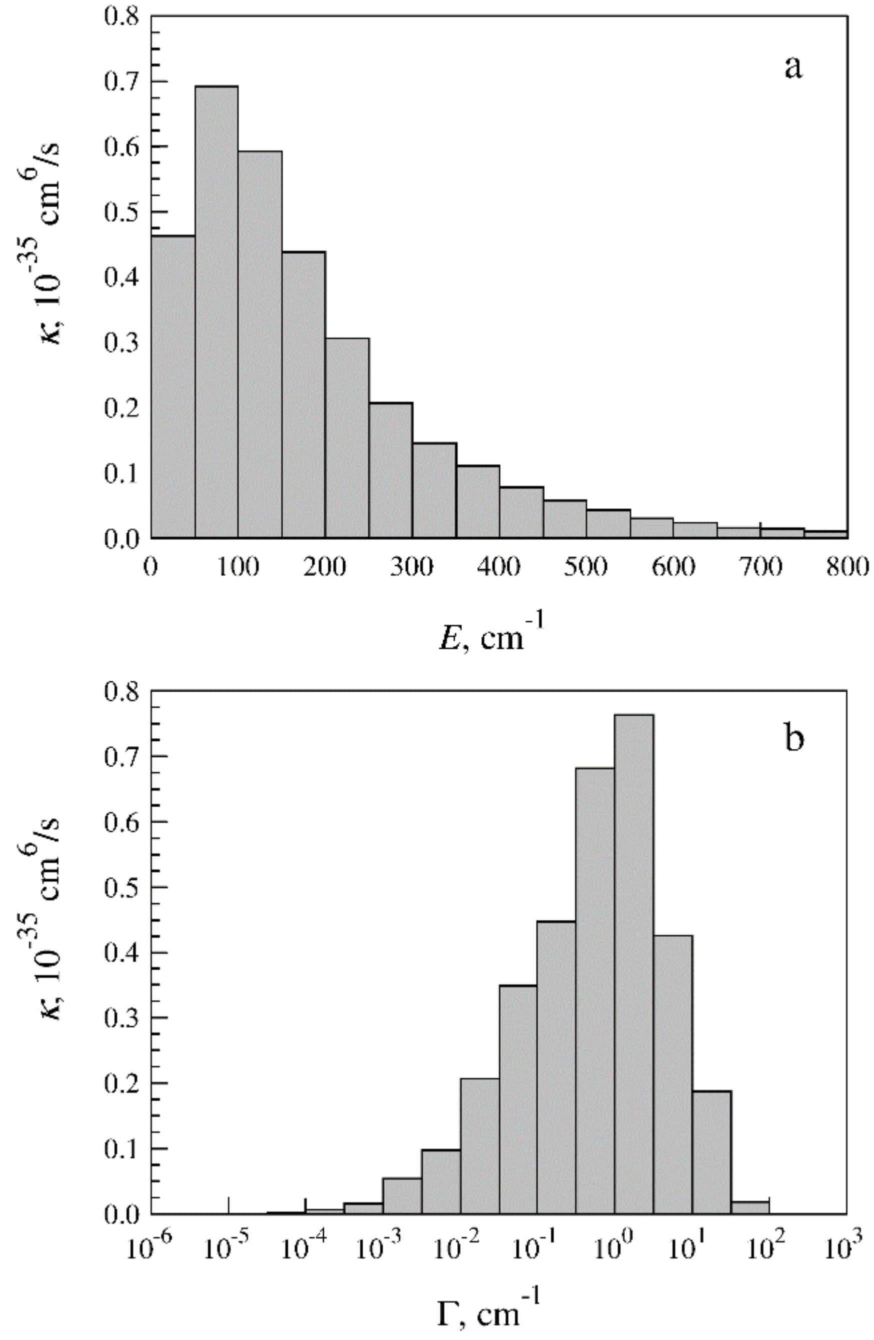

Figure 5.1. Contributions of scattering resonances to the recombination rate coefficient κ as a function of (a) resonance energy E_i above the dissociation threshold; and (b) resonance widths Γ_i.

Figure 5.2 shows a correlation between energy E_i and width Γ_i of resonances, again, with the focus on those states important for the recombination process. Color in Figure 5.2 indicates contribution to the recombination rate coefficient κ. Figure 5.1a and b are projections of the data in Figure 5.2 onto horizontal and vertical axes, E and Γ, respectively. Distribution of Figure 5.2 is not particularly broad: the most intense part of it spans only the 300 cm^{-1} range of resonance energies and three orders of magnitude range of resonance widths.

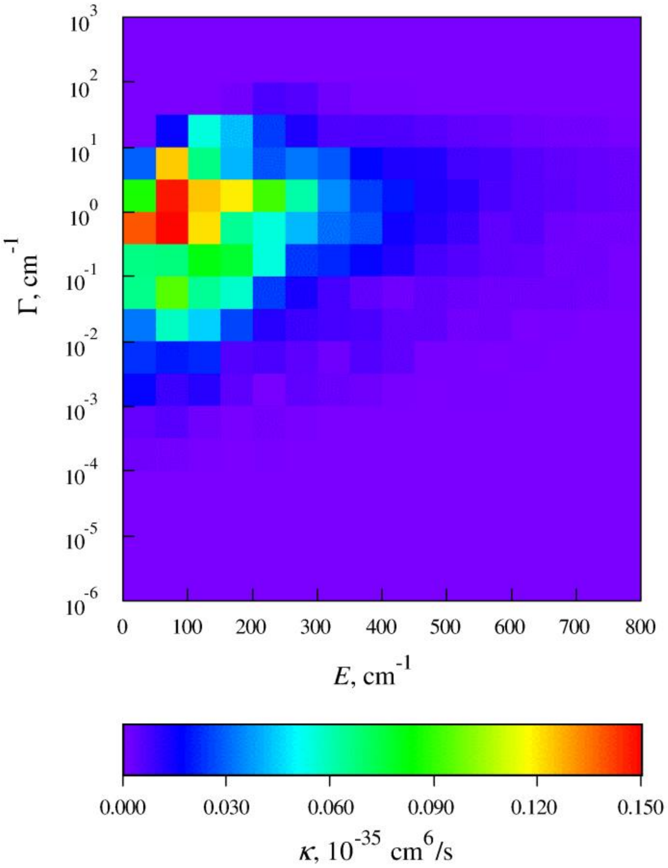

Figure 5.2. Contributions of scattering resonances to the recombination rate coefficient κ as a function of both resonance energy E_i and width Γ_i. Projections of this 2D distribution onto horizontal and vertical axis gives Figure 5.1 *a* and *b*, respectively.

Figure 5.3 represents contribution of different rotational excitations to the recombination process. Color indicates the value of κ (J, K_a) obtained using Eq. (5.9) where summation was carried out over the vibrational states only, within each rotational state characterized by J and K_a. The distribution in Figure 5.3 indicates that the most important contributions to the recombination process come from rotational excitations in the range $8 < J < 38$ and $K < 7$, which is close to the range studied by Grebenshchikov and Schinke.[27] Since many vibrational states are included, the distribution of Figure 5.3 is rather shapeless. Two (not particularly well pronounced) maxima barely seen in Figure 5.3 correspond to the states of symmetries A_1 and A_2 that exhibit slightly different properties.

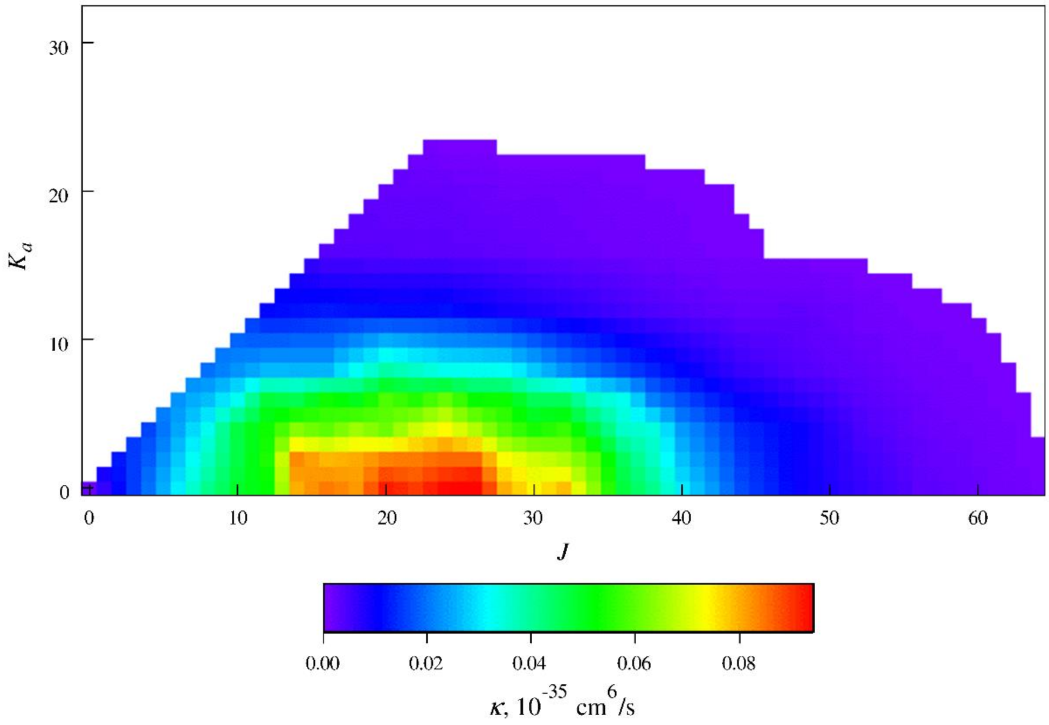

Figure 5.3. Contributions of scattering resonances to the recombination rate coefficient κ as a function of rotational excitation (J, K). Step size $\Delta J = \Delta K = 2$ was used in the range $12 \leq J \leq 36$ and $K \leq 4$; it was doubled in the range $J \leq 44$ and $K \leq 16$ and doubled again in the range $J \leq 64$ and $K \leq 32$. Contributions of all other rotational excitations were linearly interpolated between the computed points.

Note that low rotational excitations, say $J < 5$, make only a negligible contribution to the process. This means that any prediction or analysis based on calculations for $J = 0$ only (non-rotating O_3) is likely to be inaccurate, or may even be qualitatively wrong. Importantly, calculations with $J > 45$ are not really needed.

Vibrational content of resonances in O_3^* can be analyzed by determining the *state number* of the resonance within progression of vibrational states computed for given values of J and K_a, and by matching energy of the corresponding state in the spectrum of non-rotating ozone. This can be thought of as the vibrational energy of the resonance. The distribution of state numbers is given separately for symmetries A_1 and A_2 in two frames of Figure 5.4. We see that most significant contributions to the recombination process come from the state number 120-to-155 of symmetry A_1, and the state number 90-to-115 of symmetry A_2. Note that a nonrotating ozone molecule has 163 states of symmetry A_1, and 125 states of symmetry A_2 (using the PES of Dawes[84]). This means that upper vibrational states, closest to the dissociation threshold, are more important for the recombination process. In Figure 5.5 we gave a distribution of energies of these states, relative to the dissociation threshold, for both symmetries combined. This histogram shows that dominant contributions to recombination come from vibrational states in the range 600 cm^{-1} below the dissociation threshold. Such states contain 10 to 13 quanta of vibrational excitation distributed between three modes. Typical examples include 6 to 8 quanta of bending and/or asymmetric stretching, and 4 to 5 quanta of symmetric stretching. Some states have only two modes excited (e.g., 11 quanta of θ and 1 quanta of φ), or even a single mode (e.g., 12 quanta of bending). Properties of these vibrational states, including a detailed analysis of their wave functions, were reported in previous section.

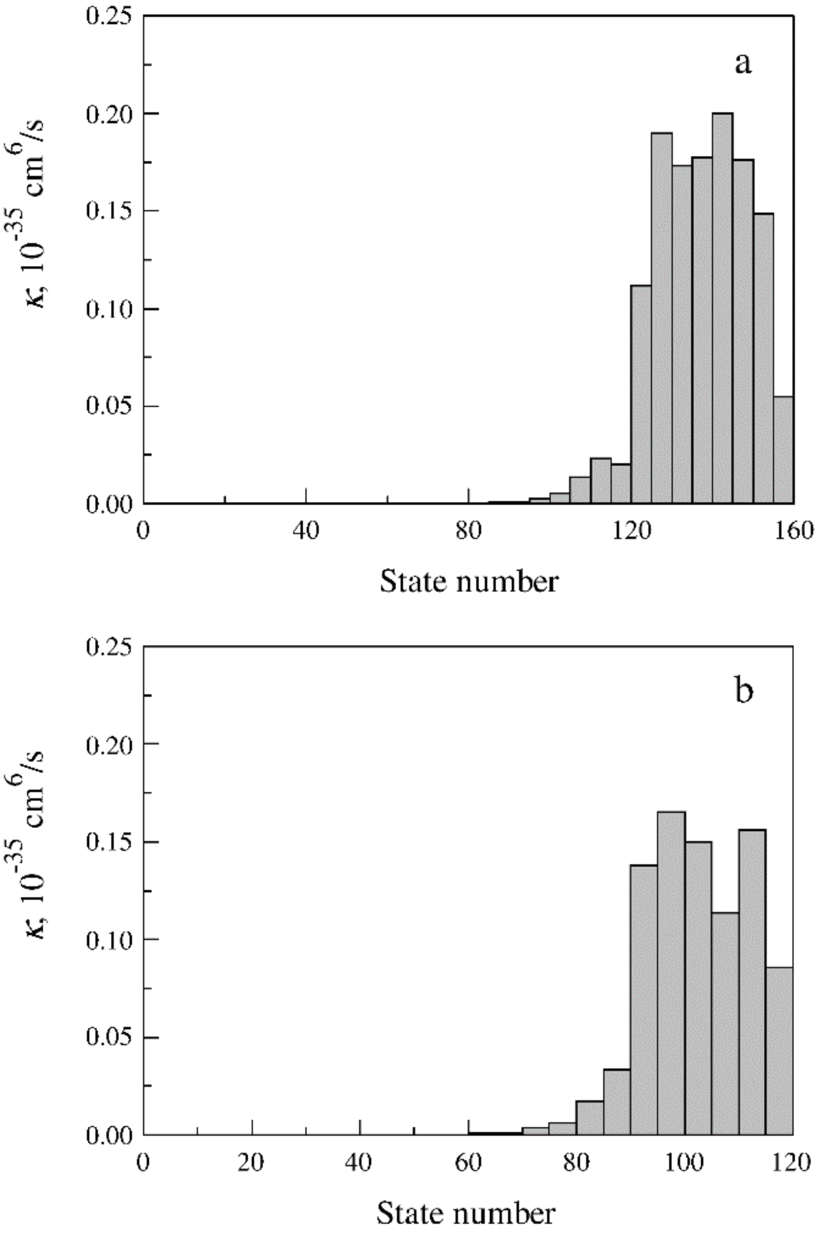

Figure 5.4. Contributions of scattering resonances to the recombination rate coefficient κ as a function of the state number in a progression of (a) symmetric and (b) anti-symmetric vibrational states. Only resonances localized in the well are included.

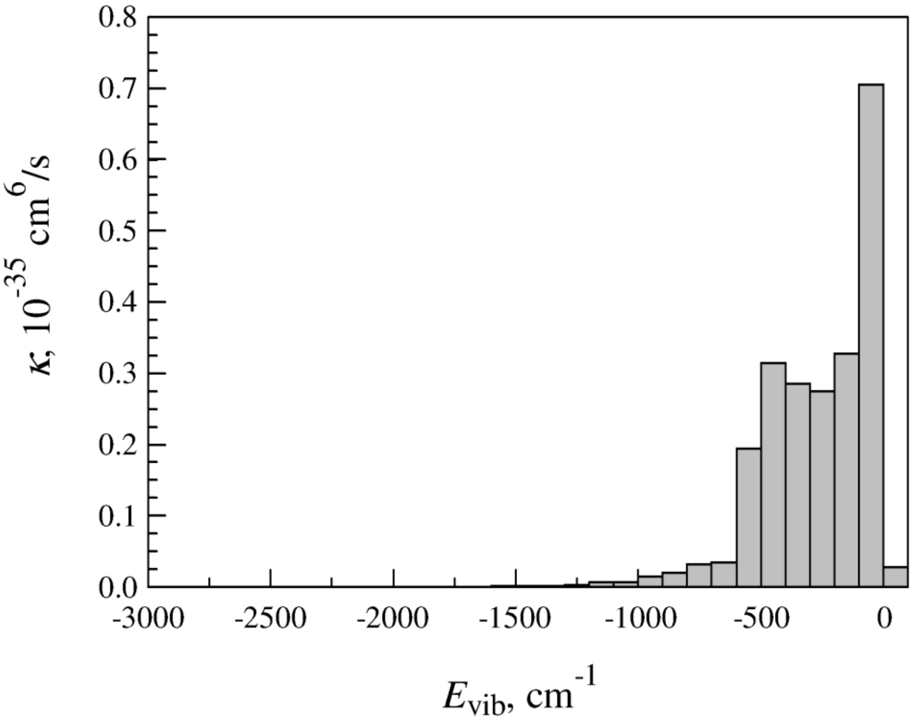

Figure 5.5. Contributions of scattering resonances to the recombination rate coefficient κ as a function of vibrational energy. Only resonances localized in the well are included. Both symmetries are combined.

Further insight comes from analyzing where these resonances are (in terms of their energy) relative to the top of the centrifugal barrier. The effective barrier $E^{\dagger}$ along the dissociative coordinate ρ can be defined for given J and K_a as maximum value of the ground vibrational state in the two-dimensional eigenvalue problem solved for non-dissociative coordinates θ and φ. Since the PES of ozone has no activation barrier for $O_2 + O \rightarrow O_3$, the value of $E^{\dagger}$ remains negative at lower levels of rotational excitation, forming a submerged "reef" rather than a barrier. At higher levels of rotational excitation $E^{\dagger}$ shows up above the dissociation threshold. (The borderline cases $E^{\dagger} = 0$ are found at $J = 25$, $K_a = 0$, or $J = 20$, $K_a = 6$, or $J = 12$, $K_a = 8$, etc. Exact position of this border is sensitive to the shape of the PES.[84]) Thus, Figure 5.6 gives correlation between the resonance lifetime Γ_i and the offset of resonance energy from this effective barrier top:

$\delta E_i = E_i - E^{\dagger}$. Color indicates contribution to the recombination rate coefficient κ. We see that some contribution, around 9%, comes from resonances at energies within 50 cm^{-1} below the barrier top. These can be populated by tunneling only and, consequently, exhibit narrower widths, on the order of $\Gamma_i \approx 10^{-2}$ cm^{-1}. Resonances at energies within 150 cm^{-1} above the barrier top make the largest contribution to recombination. They are broader, $10^{-2} < \Gamma_i < 10$ cm^{-1}, and can be populated by redistribution of vibrational energy within the three modes of O_3^*, rather than tunneling.

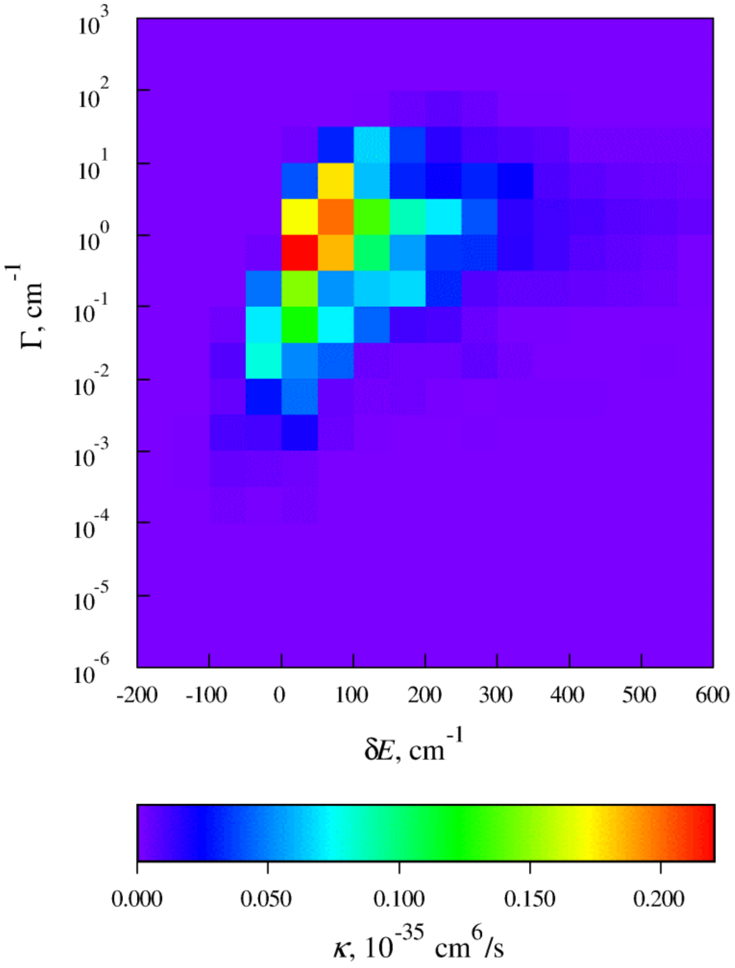

Figure 5.6. Contributions of scattering resonances to the recombination rate coefficient κ as a function of resonance energy relative to the top of centrifugal barrier (δE_i in the text) and the resonance width Γ_i.

Finally, Figure 5.7 presents correlation between δE_i and the probability of finding the system behind the centrifugal barrier, over the well region. This moiety, called here the well probability and denoted by p_w, is obtained by integrating the square modulus of wave function through the range $0 \le \rho \le \rho^\dagger$.

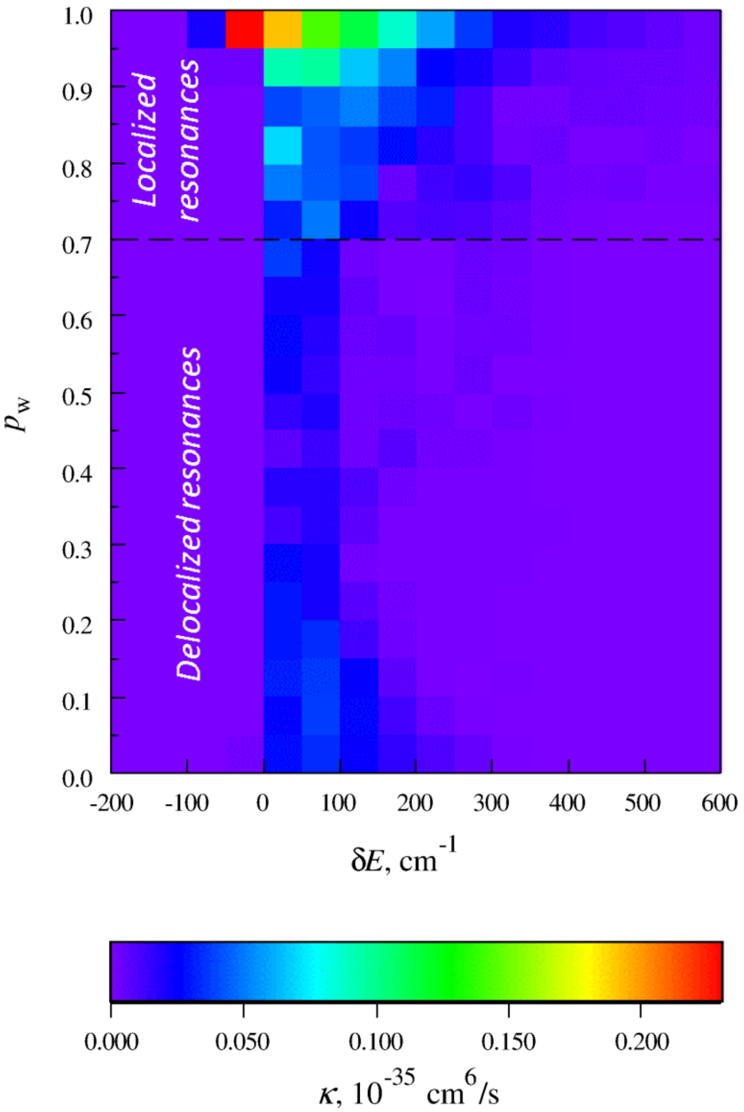

Figure 5.7. Contributions of scattering resonances to the recombination rate coefficient κ as a function of resonance energy relative to the top of centrifugal barrier (δE_i) and the probability of the corresponding wave function over the well region. The boundary between resonances localized in the well and delocalized resonances is depicted with a dashed line at $p_w = 0.7$.

In Figure 5.7 we see that for typical resonances at energies slightly below the top of the centrifugal barrier or somewhat above it, this probability exceeds $p_w = 0.7$. However, many higher energy resonances are more delocalized. Their contribution to the recombination process is not negligible, around 30%. A schematic in Figure 5.8 is used to demonstrate this concept. It shows examples of wave functions for three resonances: one sitting deep and behind the centrifugal barrier, one near the top of the barrier, and one significantly above the top of the barrier.

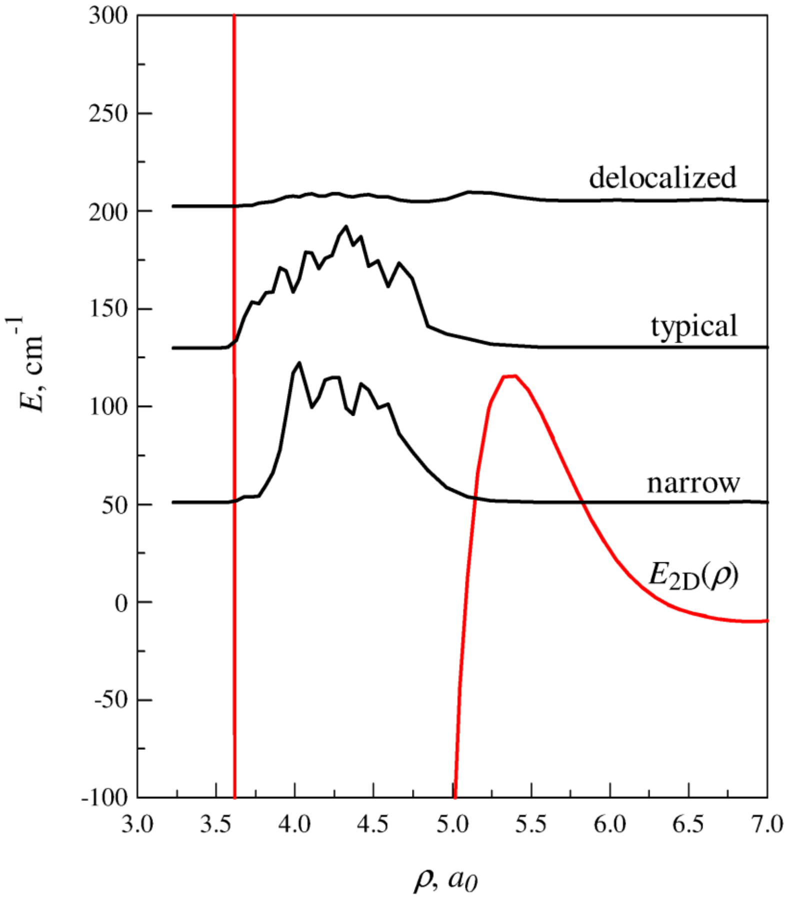

Figure 5.8. Three types of resonances observed in our calculations: narrow resonance trapped behind the centrifugal barrier (E = 51.1 cm^{-1}, $\Gamma = 3.6\times10^{-4}$ cm^{-1}), typical resonance slightly near the barrier top (E = 130.0 cm^{-1}, Γ = 0.16 cm^{-1}), and a highly delocalized state above the barrier (E = 202 cm^{-1}, Γ = 15.5 cm^{-1}). The barrier top is at 115.7 cm^{-1}, rotational excitation is J = 32, K = 0.

The data presented in Figures 5.1-5.7 can be summarized and interpreted in the following way: scattering resonances that participate in the recombination process represent upper bound states of non-rotating ozone (600 cm^{-1} below dissociation threshold) that are ‘‘lifted’’ by rotational excitation to energies above the dissociation threshold (around 100 cm^{-1}), where these states can be populated from O + O_2. Most important contributions to the recombination process come from resonances at energies just slightly below or somewhat above the top of the centrifugal barrier $-50 < \delta E_i < 150$ cm^{-1}) and at moderate levels of rotational excitation ($8 < J < 38$). Widths of such resonances are not too small ($10^{-2} < \Gamma_i < 10$ cm^{-1}), and their wave functions are localized dominantly over the covalent well, behind the centrifugal barrier ($p_w > 0.7$).

Indeed, on the lower energy side, resonances that sit too deep and behind the centrifugal barrier exhibit too narrow widths $\Gamma_i < 10^{-2}$ cm^{-1}, and contribute very little to recombination, according to Eq. (5.9). On the higher energy side, the resonances at energies too far above the centrifugal barrier, although may be rather broad (even exceeding $\Gamma \approx 10$ cm^{-1}), they exhibit smaller stabilization cross sections because they are delocalized over the large range of ρ, which reduces the probability of their stabilization into the covalent well ($p_w < 0.7$). Moreover, at lower levels of rotational excitation ($J <$ 25) the top of the effective centrifugal barrier is still submerged below the dissociation limit ($E^\dagger < 0$) which, again, makes resonances too delocalized. Finally, at higher levels of rotational excitation $J > 40$ the Boltzmann factor shuts off the recombination process. So, it appears that only at moderate levels of rotational excitation and only at energies near the top of the centrifugal barrier the resonances of O_3 are efficiently populated by O + O_2

collisions and are efficiently stabilized by Ar collisions. Widths of such resonances are neither too narrow nor too broad, as one can see from Figures 5.1b, 5.2 and 5.6.

5.3.2. Absolute value of recombination rate coefficient

The main (future, not immediate) goal of our efforts is to understand the anomalous isotope effect of ozone formation observed by Mauersberger group and reported in a series of papers (see, for example Refs. 15 and 16, review articles Refs. 131 and 132 and references therein). Majority of those studies were carried out at room temperature T = 296 K and the pressure P = 200 Torr, in the Ar bath gas, which translates into [M] = 6.53×10^{18} cm^{-3}. At these conditions the total rate coefficient for ozone recombination is $\kappa^{\text{TOT}} = 42 \times 10^{-35}$ cm^6/s.[13] According to analysis of Troe[157] the contribution of energy-transfer mechanism should be around $\kappa^{\text{ET}} = 23 \times 10^{-35}$ cm^6/s (close to 55% of the total rate). This is the value we are trying to reproduce by calculations.

The only other work, where the absolute value of the recombination rate coefficient obtained from quantum mechanics was reported, is the paper of Charlo and Clary.[40] Their calculations gave $\kappa = 13 \times 10^{-35}$ cm^6/s, although it is not entirely clear whether this value was taken directly from the dimensionally-reduced model, where the bending states are missing, or, it already includes a correction to account for the missing states (which would be a reasonable thing to do). Also, within a model based on classical trajectory simulations Schinke and Fleurat-Lessard[32] were able to reproduce the overall experimental value of κ^{TOT} but empirically, by adjustment of stabilization efficiency (coefficient $\Delta = 350$ cm^{-1} in their theory). To the best of our knowledge, these are the only two theoretical predictions of the recombination rate coefficient available in the literature. In all other papers on ozone the workers either were interested in the ratio of the recombination rates for different isotopomers, or looked at other processes, such as atom exchange or ro-vibrational energy transfer (so, did not report the absolute value of recombination arte coefficient).

In our case the less certain component of recombination theory is the stabilization step, or, more precisely, the values of σ_i^{stab}. Several models developed in our previous work (as explained in Section 5.2.3) are tested here by comparison vs. the experimental value of κ^{ET}. The results of these tests are presented in Table 5.1.

Table 5.1. Recombination rate constant κ (10^{-35} cm^6/s) for the energy transfer mechanism

Model	Localized resonances*	All resonances**
SM1a	13.4	19.1
SM1b	9.4	12.2
SM2	5.6 − 16.1	8.3 − 22.7
SM2'	8.1 − 19.4	11.6 – 27.0
Experiment		23

* Includes states with fraction in the well more than 70%

** Includes all states where contribution of delocalized states is multiplied by fraction

We see that all stabilization models give the recombination rate coefficient κ of correct order of magnitude. Namely, the first column in Table 5.1 shows that the values of κ obtained using SM1*a* and SM1*b* models fall between the minimum and maximum limits predicted by SM2. This makes sense, since SM1*a* and SM1*b* were constructed to represent stabilization cross sections on average, while SM2 represents the possible range. As for comparison with experiment we see that our predicted rate coefficients are somewhat smaller. Even the upper limit given by the SM2 model, $\kappa \approx 16.1 \times 10^{-35}$ cm^6/s, is only 70% of the experimental value of κ^{ET} (although it is very close to the result of Clary[40]).

Trying to find the missing piece we noticed that the lowest energy scattering resonances $O_3^{(i)}$ do not contribute to recombination. Qualitatively, they sit so deep and behind the centrifugal threshold that they can't be populated in a typical O_2 + O collision, just because heavy particles cannot tunnel through wide barriers (see Figure 5.8). Quantitatively, in the limit $\Gamma_i << (k_i^{\mathrm{stab}} + k_i^{\mathrm{diss}})[\mathrm{M}]$ the contribution of each resonance, according to Eq. (5.9), simplifies to the following expression: $\kappa_i \approx \frac{1}{2}\,\Gamma_i\, K_{eq}(E_i)/[\mathrm{M}]$. This shows clearly that resonances with negligible widths Γ_i make negligible contributions to recombination. Thus, they should be considered as bound states, rather than scattering resonances. Removing these states from the list of resonances does not reduce the value of the recombination rate coefficient much, but this modification ''lifts'' the bound state threshold, leading to more efficient stabilization of the remaining (higher energy) scattering resonances, since now the required energy-transfer ΔE is effectively reduced for them. We found that (at this pressure) the resonances with widths below $\Gamma_i \approx 10^{-2}$ cm^{-1} can be considered as effectively bound states. This adjustment, which represents an improved version of SM2, called SM2′ hereafter, permits increasing the maximum limit of the recombination rate coefficient to $\kappa \approx 19.4 \times 10^{-35}$ cm^6/s (bottom of the first column in Table 5.1), which is about 84% of the experimental value of $\kappa^{\mathrm{ET}} \approx 23 \times 10^{-35}$ cm^6/s, and is still not quite sufficient.

Searching for the still missing piece we realized that we took into consideration, so far, only resonances that are localized mostly over the covalent well, inside the centrifugal barrier, rather than outside (see Figure 5.8). As we showed in Section 5.3.1

above, for typical resonances at energies slightly below the top of the centrifugal barrier or slightly above it, the value of well probability p_w exceeds 0.7 or so. Consequently, the results given in the first column of Table 5.1 were obtained including only localized resonances, with $p_w > 0.7$. However, many higher energy resonances are more delocalized, characterized by $p_w < 0.7$. Although energies and lifetimes of these states are available from our calculations, it appears that including them into consideration of recombination kinetics is not straightforward, because our stabilization models (SM1 and SM2) were set up for the localized states only.[44,158] From ref. 43 we know that transitions from the outside of the centrifugal barrier into the states localized in the well are very weak. So, using SM1 and SM2 for delocalized states would be incorrect and would, certainly, overestimate the value of the recombination coefficient κ (we checked this by calculations).

It makes sense, however, to use SM1 and SM2 for only a portion of the delocalized resonance, namely, for that piece of it that sits inside of the centrifugal barrier. This is equivalent to multiplying stabilization cross section by the well probability p. So, for the localized states (characterized by $p_w > 0.7$) we use SM1 and SM2 straight, whereas for delocalized states ($p_w < 0.7$) we reduce the value of stabilization cross section proportionally to the well probability p. Recombination rate coefficients computed in this way, with delocalized states included, are given in the second column of Table 5.1. They are somewhat higher than those in the first column of Table 5.1. Predictions of SM1*a* and SM1*b* are still somewhat below the experimental value of κ^{ET}, but the upper limit of the SM2 model with delocalized states included is now $\kappa^{\mathrm{ET}} \approx 22.7 \times 10^{-35}$ cm^6/s, which almost reaches the experimental value of $\kappa^{\mathrm{ET}} \approx 23 \times$

10^{-35} cm^6/s. Finally, the upper limit of SM2′ is now $\kappa^{ET} \approx 27.0 \times 10^{-35}$ cm^6/s, which is above the experimental value of κ^{ET}. So, in this final form of our theory, the experimental value of κ^{ET} is within the ranges predicted by the SM2′ model.

The following conclusion can be drawn from the data presented in Table 5.1. In order to reproduce the experimental rate coefficient for ozone recombination we had to take delocalized resonances into consideration. It is also important to treat the low-energy resonances as bound states, but this is not sufficient by itself. Only when those two effects are both included, the experimental value of the recombination rate coefficient is recovered by the SM2′ model of stabilization. In what follows we will use this approach as the working model, but, for comparison, we will also present results obtained using the simplest SM1*a* model (with delocalized states included), which gives the rate coefficient just 17% below the experimental value of κ^{ET}. Note that in Figures 5.1-5.3, 5.6 and 5.7 were generated using SM1*a* with delocalized states included. Figures 5.4 and 5.5 were generated using SM1*a* without delocalized states (since it is harder to make connection between the highly excited delocalized scattering resonances and the bound states of a non-rotating ozone molecule).

5.3.3. Pressure dependence

Pressure dependence of the third-order rate coefficient for ozone formation is known to be weak. So, it is usual to plot, as a function of pressure, the product $\kappa \times [M]$, which represents the second-order rate coefficient for recombination of O_2 with O. Its pressure dependence is expected to be roughly linear. Figure 5.9 presents experimental data from Ref. 161 and 162 in a broad range of pressure values, for three representative temperatures. We focus on frame *b* of this figure, since that temperature, $T = 300$ K, is very close to the temperature in experiments of the Mauersberger group. For completeness, the value of the recombination rate coefficient given by Mauersberger and co-workers[13] is also shown in Figure 5.9*b*, at low pressure $P = 200$ Torr.

Our predictions of $\kappa^{\mathrm{ET}} \times [\mathrm{M}]$, computed using the SM1*a* and SM2′ models of stabilization, are shown on these figures too (yellow line and green range). As expected, the results of the SM1*a* model are within the range of the SM2′ model, and show the same pressure dependence. The dependence starts roughly linear, but it falls off at higher pressure. This behavior is typical to the energy-transfer (Lindeman) mechanism of recombination. It is explained by competition between two terms in the denominator of Eq. (5.9), namely, between the spontaneous decay of scattering resonances and their collision-induced stabilization. At high pressure one can neglect Γ_i in the denominator of Eq. (5.9), which leads to $\kappa_i \times [\mathrm{M}] \approx \frac{1}{2} \Gamma_i K_{eq}(E_i)$ for each resonance. This means that the value of $\kappa^{\mathrm{ET}} \times [\mathrm{M}]$ stops increasing with pressure, it decreases, just as shown in Figure 5.9. Such behavior was also observed by Marcus and co-workers in their model of ozone formation,[23] and by Pack et al.[132] in their studies of the $\mathrm{Ne} + \mathrm{Ne} + \mathrm{H} \rightarrow \mathrm{Ne}_2 + \mathrm{H}$ recombination process.

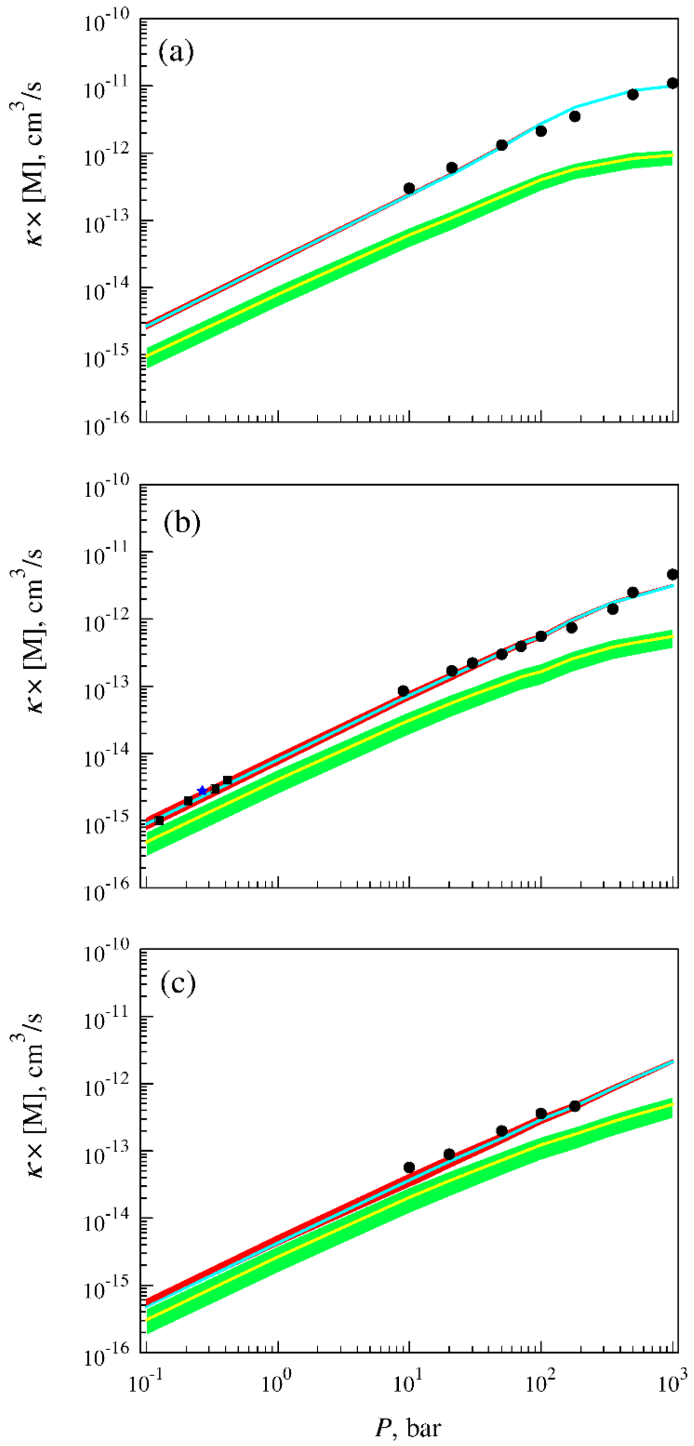

Figure 5.9. Pressure dependence of the second-order recombination rate coefficient $\kappa \times$ [M] for three temperatures: (a) 213 K, (b) 300 K and (c) 373 K. Yellow line with green range corresponds to the energy transfer mechanism alone, while blue line with red range represents the total rate coefficient, with chaperon contribution added. Black symbols depict experimental data: circles (Ref. 161), star (Ref. 13) and squares (Ref. 162).

Note, however, that the experimental data in Figure 5.9 hardly show any decrease. As discussed above, the analysis of Troe[157] indicates that in the experiment the recombination process involves both the energy-transfer and the radical-complex (chaperon) mechanisms. Therefore, in order to compare with experiment, we added to our $\kappa \times [\mathrm{M}]$, predicted here by calculations, the contribution of radical-complex $\kappa^{\mathrm{RC}} \times [\mathrm{M}]$, determined by Troe[157] from the analysis of experimental data. The total rate is shown by blue line with red range in Figure 5.9, and we see that it is in good agreement with experiment, both in terms of the absolute value and pressure dependence, in a broad range.

Moreover, our calculations show similarly good agreement with experimental data for pressure dependence at slightly elevated and slightly reduced temperatures: T = 373 K and T = 213 K, respectively. This is illustrated by Figure 5.9*a* and *c*. The fall off is more pronounced at lower temperature, and is barely visible at higher temperature. In either case, the total of energy-transfer and radical-complex contributions agree well with the experiment in a broad range of pressure values, and for all three values of temperature.

5.3.4. Temperature dependence

Initially, we did not plan to study temperature dependence of the recombination rate coefficient. For this, strictly speaking, one has to compute temperature dependence of stabilization cross sections, but we did not really do that. Our previous mixed quantum/classical calculations of energy-transfer[44,47,158] were carried out at room temperature only. However, reasonable agreement with experiment in all three frames of

Figure 5.9, that cover the temperature range $213 \leq T \leq 373$ K, indicates that we can try to explore the temperature dependence, at least in a narrow range of couple hundred degrees Kelvin. Furthermore, quantum calculations of temperature dependence of stabilization rate coefficients by Charlo and Clary[39] showed that those depend only weakly on temperature, even in a much broader temperature range. Similar conclusions were drawn by Ivanov and Schinke,[163,164] based on classical trajectory simulations.

So, we decided to check what temperature dependence is predicted by our calculations. Figure 5.10 shows experimental data available for the third-order recombination rate coefficient through a broad range of temperatures, as summarized by Troe.[157] Our predictions, obtained using SM1*a* and SM2′ models for stabilization, are also shown in Figure 5.10. Yellow line with green range is used for $\kappa(T)$ based on the energy-transfer mechanism alone, while blue line with red range is used for the total of our $\kappa(T)$ plus the $\kappa^{\mathrm{RC}}(T)$ contribution, as reported by Troe.[157] We see that temperature dependence of the total recombination rate is in very good agreement with experiments. The temperature dependence of the $\kappa^{\mathrm{ET}}(T)$ alone is not available from the experiment, but it can be estimated (extrapolated) from the high-temperature data, where the contribution of the radical-complex mechanism is expected to vanish. This extrapolation is shown by black line in Figure 5.10. We see that our prediction of temperature dependence for the energy-transfer mechanism alone is also in reasonable agreement with experimental information. Better agreement is hard to achieve, due to the nature of extrapolation, but also due to a significant spread of experimental data in the high temperature range, as one can see in Figure 5.10.

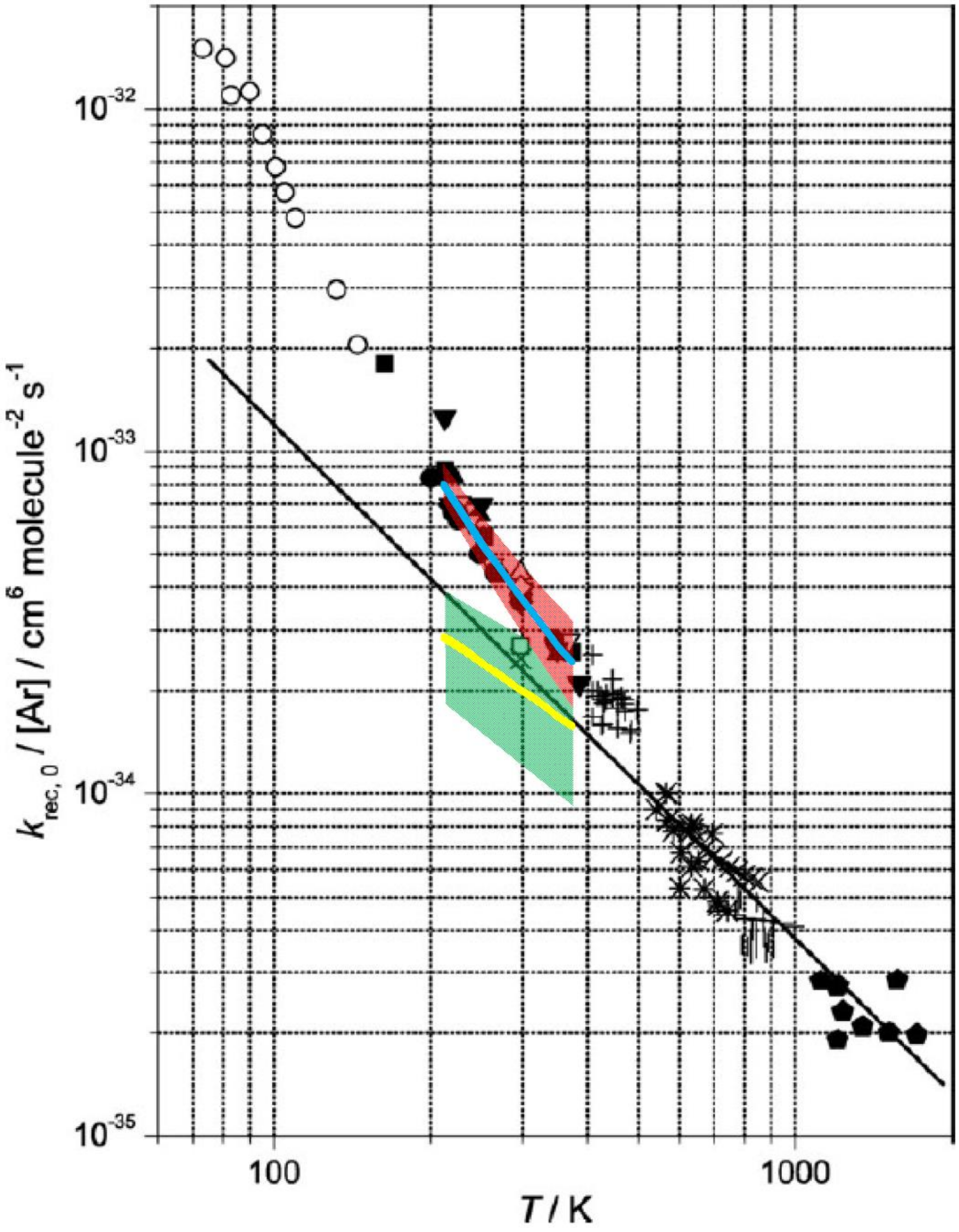

Figure 5.10. Temperature dependence of the recombination rate coefficient κ at P = 0.1 bar. Yellow line with green range corresponds to the energy transfer mechanism alone, while blue line with red range represents the total rate coefficient, with chaperon contribution added. The original figure, containing combined experimental data, was taken from the paper by Troe, Ref. 157. The long black line is an experiment-based estimation of ET rate coefficient.

It is usual to fit experimental or theoretical data for temperature dependencies by T^{-n} functions. We also did this, using different models for the stabilization process. Our results are summarized in Table 5.2, together with other theoretical predictions from the literature, and available experimental data. The first column of Table 5.2 gives the values of n for the energy-transfer mechanism alone. Predictions of SM1*a* and SM2′ models are slightly below the experimental value of $n = 1.5$, while prediction of SM1*b* is slightly above it. A larger deviation from the experimental value of n was observed in the work of Grebenshchikov and Shinke[27] where $n = 2.1$ was reported, which is close to the temperature dependence of the total recombination rate coefficient. Charlo and Clary[40] had negative temperature dependence, $n = -0.64$, due to the artifact of the older potential energy surface. Schinke and Fleurat-Lessard[32] obtained $n = 1.5$, but only after empirical adjustment of the damping coefficient in their classical (trajectory based) approach.

Table 5.2. Temperature dependence T^{-n} of the recombination rate constant

Model	ET mechanism		ET + RC mechanisms	
	Localized resonances*	All resonances**	Localized resonances*	All resonances**
SM1a	0.96	1.09	2.16	2.10
SM1b	1.55	1.72	2.66	2.65
SM2	1.00 − 1.37	1.12 − 1.49	2.16 − 2.69	2.09 − 2.62
SM2'	0.86 − 1.15	0.98 − 1.28	2.01 − 2.48	1.95 − 2.42
Experiment		1.5		2.22 (2.7)
Ref. 27		2.1		
Ref. 32		1.5		
Ref. 40		−0.64		

* Includes states with fraction in the well more than 70%

** Includes all states where contribution of delocalized states is multiplied by fraction

The second column in Table 5.2 reports the values of n obtained for temperature dependence of the *total* recombination rate coefficient which, again, includes our computed contribution of the energy-transfer mechanism, plus the contribution $\kappa^{\mathrm{RC}}(T)$ of the radical-complex mechanism as reported by Troe.[157] The experimental value of $n = 2.2$ is in the ranges predicted by SM2 and SM2′. The prediction of SM1a is somewhat lower than the experimental value, while prediction of SM1b is somewhat above it. The experimental value of $n = 2.7$ reported in the earlier work[165] is closer to the prediction of SM1b and the upper limit of SM2.

5.3.5. Discussion

Comparison of our results vs. experimental data is very good. We should admit, however, that the less certain component of our theory, the stabilization step, is still described approximately, by a simple analytic energy transfer model (several variations of which have been tested above). Alternatively, one may wish to use accurately computed stabilization and dissociation cross sections for each individual resonance, which could be regarded as the exact approach to the problem. In fact, we did such calculations in our earlier work, but only for the dimensionally-reduced model of an ozone molecule (with bending states omitted) and within the framework of the mixed quantum/classical theory. Similar quantum/classical calculations for stabilization of individual ro–vibrational states within the full-dimensional description of the ozone molecule would be extremely demanding, while the full-quantum scattering calculations would be computationally unaffordable. So, for now, we decided to explore what can be learned using those simpler models for the stabilization step.

Although in this work we tested several models of the energy transfer, note that we did not tune any parameters in these models (e.g., trying to reproduce experimental data). Instead, we explored all possible sources of contributions to the recombination process. But, in principle, someone may want to ask a question: *could it be that slight variation of model parameters would permit reproducing the total experimental rate coefficient by the energy-transfer mechanism alone*, *without any involvement of the chaperon mechanism*? Well, in order to reach the value of $\kappa^{\mathrm{TOT}} \approx 42 \times 10^{-35}$ cm^6/s within the current approach and using SM1*a* (with delocalized states included) we would have to increase the value of σ_0^{stab} in Eq. (5.11) by a factor of 2.5, and, it would be problematic to find a justification for this. In fact, our stabilization cross sections are already rather large. Comparisons can be made with the thermal stabilization rate coefficient reported by Clary,[39] 4.92×10^{-11} cm^3/s, and with the energy transfer function reported by Schinke (see Fig. 2 in Ref. 164). We checked and found that the corresponding numbers in our calculations are larger than those of Clary by a factor of three, and, larger by a factor of four than those of Schinke. So, we would be very hesitant to ‘‘tune’’ stabilization cross section without any justification, just in order to fit the experimental value of κ^{TOT}. Inclusion of delocalized resonances, and treating narrow resonances as bound states, permitted us to reach the level of experimental κ^{ET}, but not the level of experimental κ^{TOT}. We conclude that within the energy-transfer mechanism, we cannot find any other possible source of additional contribution to recombination.

Moreover, we checked and found that a straightforward increase of σ_0^{stab} by a factor of 2.5 does not resolve all problems, because it leads to incorrect pressure and temperature dependencies. We tried this, and it appears that the resultant pressure dependence would exhibit a pronounced fall-off in the high pressure regime, which contradicts with experiments. Quantitatively, at pressure $P = 10^3$ bar the rate coefficient would be 3.1 times smaller than the experimental value. The temperature dependence would also be way too weak, with $n = 1.06$.

Furthermore, recall that as we explained above, in the high pressure limit Eq. (5.9) simplifies, giving $\kappa_i \times [\mathrm{M}] \approx \frac{1}{2}\,\Gamma_i\, K_{eq}(E_i)$ which is independent of k_i^{stab} at all! So, it does not matter which stabilization model is used, and how accurate it is. If the resonances (number of states, their energies and lifetimes) are computed using accurate treatment of O_3, then this information alone sets up the high-pressure limit of the recombination rate, and there is no need to consider the Ar + O_3 collision process. Since here the treatment of resonances in O_3 is rather accurate, but the high-pressure rate coefficient is still 3.1 times smaller than the experiment, it means that there must be some additional contribution to recombination, other than the energy transfer mechanism. From our point of view this is the strongest argument in support of the chaperon mechanism.

So, it appears that in order to reproduce experimental data one must involve the chaperon mechanism, as we did here, using the fitting parameters of Troe.

5.4. Summary

This chapter has covered rigorous calculations and a detailed analysis of scattering resonances in ozone, for a broad range of rotational excitations. We adopted a recently developed accurate potential energy surface,[84] and developed an efficient method for calculations of ro–vibrational energies, wave functions and resonance lifetimes (using hyper-spherical coordinates, the sequential diagonalization/truncation approach, grid optimization and complex absorbing potential, see previous chapter). The distribution of resonance energies and lifetimes was discussed, as well as their rotational and vibrational content, and even other interesting features, such as positions of resonances with respect to the centrifugal barrier (both energetically and in terms of the probability distribution). Correlations between many of these properties were visualized with emphasis on the contribution of resonances into the recombination process.

This accurate information was augmented by the energy-transfer models derived earlier for stabilization and dissociation of scattering resonances,[44,158] in order to predict the absolute value of the recombination rate coefficient and determine its pressure and temperature dependencies. Our results offer strong support for the work of Troe,[157] who argued that the energy transfer mechanism of recombination, the Lindeman mechanism, is just one of two mechanisms forming ozone. The recombination rate coefficient that we obtained for the energy-transfer mechanism at room temperature in Ar bath gas (using the simplest stabilization model SM1*a*) is about 45% of the total rate coefficient measured in the experiment. An alternative version of the stabilization model, SM2′, gives the range of values 30–63%. These match nicely with the conclusion of Troe, who derived that it should be close to 55%. Furthermore, both experimentally determined pressure dependence of the rate coefficient (in a broad range) and its temperature dependence (in the narrower range) are reproduced well, if we add to our data the contribution of the chaperon mechanism, as derived by Troe.

In our calculations, we found that it is important to include broader delocalized resonances at higher energies into consideration, since their contribution is not negligible. In the future, a model for the stabilization of such resonances, more accurate than the one adopted here, is desirable. It was also important to treat the low-energy narrow resonances (trapped deep and behind the centrifugal barrier) as bound states, which increases stabilization rates for the most important resonances at energies near the top of the barrier. In the future, one could try to implement solution of the master equation, in order to have these effects included automatically and more rigorously.

The accurate description of the energy-transfer mechanism of ozone formation is important for understanding anomalous enrichments of various isotopomers of ozone (there are 36 isotopically distinct variants of this reaction, see Table 1.1). Our next step is to repeat, for several isotope substitutions, all the calculations reported in this chapter, hoping that the isotope effects will emerge in calculations, which would help understand its origin.

Chapter 6. Application to isotope problem in ozone

To study isotope effects in ozone, the method, described in Chapter 3, must be modified. The modifications include the transition from DVR to FBR in hyperangle φ and the extension of configuration space to include two other covalent wells of ozone on global PES. Then, selection rules are derived for wave functions that span configuration space over three wells on the PES. Two choices of axes orientation and preliminary results for two isotope effects are presented and discussed. Primarily, we consider singly and doubly substituted ozone isotopologues, 686 ($^{50}O_3$) and 868 ($^{52}O_3$). By convention, labels 6, 7 and 8 stand for oxygen isotopes ^{16}O, ^{17}O and ^{18}O, correspondingly. The isotopologue 686 includes three covalent wells, 686, 668 and 866. The covalent well 686 represents one isotopomer, while the wells 668 and 866 represent another isotopomer. At the same time, the isotopologue has three channels for dissociation, one with homonuclear oxygen molecule, $^{16}O^{16}O$, and two with heteronuclear oxygen, $^{16}O^{18}O$. The same classification is applied to isotopologue 868. It has one covalent well, or isotopomer, that stands out, 868 and two covalent equivalent wells 688 and 886, that represent another isotopomer. Three dissociation channels are $^{16}O + {}^{18}O^{18}O$, $^{18}O + {}^{16}O^{18}O$ and $^{18}O^{16}O + {}^{18}O$, in the last two the same heteronuclear O_2 is formed. In this way, when we refer to isotopologues, we imply the calculation with all three covalent wells, $0 \leq \varphi \leq 2\pi$, but when we consider only one covalent well, we call it isotopomer or molecule. Finally, the last section of this chapter explains how the couplings between rotation and vibration, due to (i) Coriolis term and (ii) the asymmetric part of the rotational potential, may be incorporated into calculations in future.

6.1. Advantage of basis set representation for rigorous treatment of symmetry

In the previous chapters, the grid representation, or DVR, was used to describe motion along each degree of freedom. However, for rigorous treatment of symmetry, basis set representation, or FBR, can be more favorable, than grid representation. In this section we will focus on advantages of FBR and apply it to hyperangle φ, because it is the only vibrational coordinate which is responsible for symmetry in ozone.

First of all, there are at least two ways to handle symmetry in the calculation of the rovibrational spectrum of ozone. One way is to construct a two-dimensional basis set $\Lambda_m^n(\theta,\varphi)$, split it by symmetry and then solve three-dimensional problem separately for each symmetry, as was shown in Chapter 3. But even better is to separate symmetries on earlier stage, right after one-dimensional eigenvectors are computed. This can be easily achieved by implementing FBR for hyperangle φ. Instead of the grid, a finite expansion with trigonometric basis, $f \sim \cos(\varphi)$ or $\sin(\varphi)$, can be utilized. Then, the basis of cosine functions will give exactly symmetric states (and only these), while the basis of sine functions will give the remaining exactly asymmetric states. This is a significant advantage of symmetry-adapted FBR.

Second, as follows from previous discussion, FBR allows to split Hamiltonian matrix into two independent matrix blocks, one for symmetric states and another for asymmetric states. In general, the eigenvalue decomposition of two twice-smaller matrices is numerically cheaper, than that of one total matrix: $2N^2$ vs. $4N^2$ for quadratic scaling, or $2N^3$ vs. $8N^3$ for cubic scaling (factor of 2 to 4).

Third, when configuration space is expanded, for example, to include two other covalent wells of ozone, as explained in the next section, the number of grid points in DVR must be tripled to cover added areas, $0 \leq \varphi \leq 2\pi/3$ and $4\pi/3 \leq \varphi \leq 2\pi$, while there is no change in number of basis functions in FBR, because the existing basis function are simply continued to fill in the extended range.

In our calculations, we implemented a symmetry-adapted FBR for hyperangle φ. When all three covalent wells are included, then $0 \leq \varphi \leq 2\pi$ and the basis is

$$f_0^{sym}(\varphi) = \frac{1}{\sqrt{2\pi}}; \quad f_n^{sym}(\varphi) = \frac{1}{\sqrt{\pi}}\cos(n\varphi); \quad n = 1 \ldots N-1 \tag{6.1}$$

$$f_n^{asym}(\varphi) = \frac{1}{\sqrt{\pi}}\sin(n\varphi); \quad n = 1 \ldots N \tag{6.2}$$

When only one central well is included, then $2\pi/3 \leq \varphi \leq 4\pi/3$, the frequency in the equations above must be tripled and $f_0^{sym}(\varphi) = \sqrt{3/2\pi}$. In FBR, the matrix elements of the kinetic energy operator $\hat{K}$ are calculated analytically and the matrix itself is diagonal. For the basis of sine function:

$$K^{asym} = \int f_i^{asym}(\varphi)\,\hat{K}\; f_i^{asym}(\varphi)d\varphi = \left(-\frac{\hbar^2}{2\mu}\right)\frac{4}{\rho^2\sin^2\theta}\begin{bmatrix} 1^2 & 0 & \cdots & 0 \\ 0 & 2^2 & \cdots & 0 \\ \vdots & \vdots & \ddots & \vdots \\ 0 & 0 & \cdots & N^2 \end{bmatrix} \tag{6.3}$$

For the basis of cosine functions (where f_0^{sym} function is constant):

$$K^{sym} = \int f_i^{sym}(\varphi)\,\hat{K}\; f_i^{sym}(\varphi)d\varphi = \left(-\frac{\hbar^2}{2\mu}\right)\frac{4}{\rho^2\sin^2\theta}\begin{bmatrix} 0^2 & 0 & \cdots & 0 \\ 0 & 1^2 & \cdots & 0 \\ \vdots & \vdots & \ddots & \vdots \\ 0 & 0 & \cdots & (N-1)^2 \end{bmatrix} \tag{6.4}$$

The matrix of potential energy operator $\hat{V}$ is defined in a similar fashion:

$$V_{ij}(\rho,\theta)=\int f_i(\varphi)V(\rho,\theta,\varphi)\,f_j(\varphi)d\varphi \tag{6.5}$$

When an equidistant grid for φ is still used, these matrix elements of potential energy operator $\hat{V}$ can be estimated numerically:

$$V_{ij}(\rho,\theta)=\Delta\varphi\cdot\sum_k f_i(\varphi_k)V(\rho,\theta,\varphi_k)\,f_j(\varphi_k) \tag{6.6}$$

Here $\Delta\varphi$ is a grid step size, while k is a grid point number. Therefore, in terms of matrix structures, FBR contrasts with DVR. In FBR approach, the kinetic energy operator is diagonal, while potential energy operator is not. In contrast, in DVR the potential energy operator is diagonal, while kinetic energy operator is not diagonal. The construction of Hamiltonian matrices for one-dimensional problems is always very fast, does not matter which representation is used.

6.2. Inclusion of all three equilibrium configurations of isotopically substituted ozone

In Chapters 2-5, we computed bound and resonance states of unsubstituted isotopologue $^{48}O_3$ over one covalent well, i.e. the hyperangle φ was confined in [2π/3, 4π/3]. In this isotopologue all three covalent wells are equivalent. However, as soon as one of oxygen atoms ^{16}O is replaced with another isotope, for example ^{18}O, then one covalent well becomes different from the other two. Obviously, the potential energy surface does not depend on oxygen masses, but Hamiltonian and APH coordinates are mass-dependent. In Hamiltonian operator, the masses of three atoms enter through one three-body reduced mass μ Eq. (2.3), while APH coordinates include mass coefficients d, Eq. (2.2). Figure 6.1 demonstrates this change with respect to unsubstituted ozone, 666.

For unsubstituted ozone, the potential energy surface in the range $2\pi/3 \le \varphi \le 4\pi/3$ is identical to those in the ranges $0 \le \varphi \le 2\pi/3$ and $4\pi/3 \le \varphi \le 2\pi$. For substituted ozone, the shape of PES is slightly changed: for singly substituted ozone all features of PES (well, transition states and dissociation channels) change their sizes a little and move away from $\varphi = \pi$ towards the edges of the plot, for double substituted ozone, features also change size, but move closer to the middle. The symmetry of the system being degraded: number of symmetry planes is reduced from three in $^{48}O_3$ to only one in $^{50}O_3$ and $^{52}O_3$.

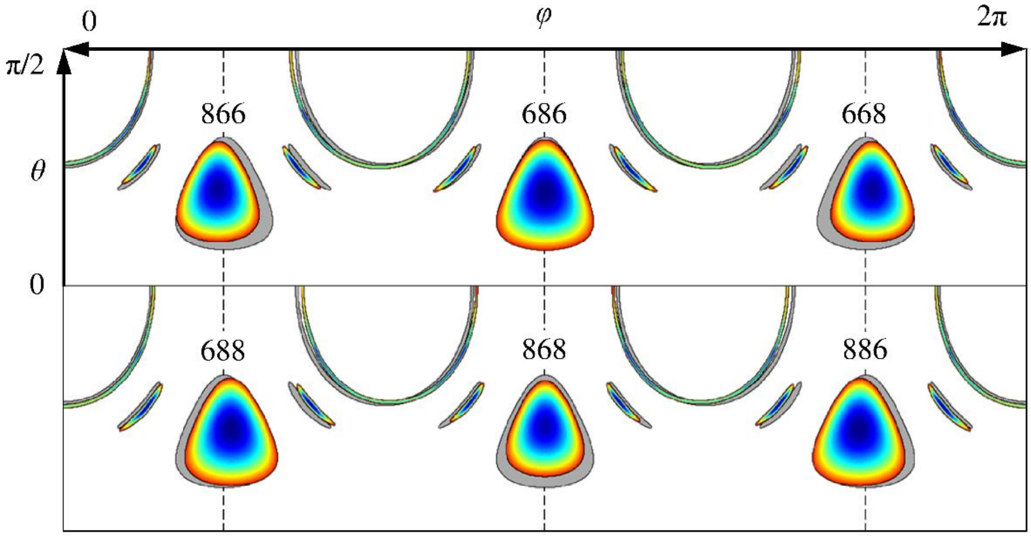

Figure 6.1. Structure of the PES in APH coordinates for singly (top panel) and doubly (bottom panel) substituted ozone. Three slices are merged together on each panel: through the deep covalent well, through the transition region, and through the vdW plateau, similar to the top panel of Figure 3.2. Structure of PES for unsubstituted ozone $^{48}O_3$ is shown with grayed areas and exhibits a threefold symmetry with symmetry planes at $\varphi = \pi/3$, π and $5\pi/3$. When at least one oxygen is substituted, all features change their sizes and are shifted a little, resulting only in one remaining symmetry plane at $\varphi = \pi$. Label "6" stands for ^{16}O, while "8" for ^{18}O.

The two-dimensional wave functions $\Lambda_m^n(\theta,\phi)$, used as a basis in Sequential Diagonalization Truncation, follow the PES changes in a similar way when two other covalent wells are added. For unsubstituted ozone, they consist of three identical replica of one-well wave functions from Figure 3.2 over the extended range of φ. For substituted ozone, the central covalent well is no more degenerate with left and right wells, which results in $\Lambda_m^n(\theta,\phi)$ functions of two types: functions localized in two central well and functions localized in both side wells simultaneously, as shown in Figure 6.2. The functions form two groups, which may be called the functions of single well and the functions of double well. They are exactly symmetric, because were computed with cosine FBR. Asymmetric functions, computed with sine FBR, are shown in Figure 6.3 and are distributed between the wells in a way similar to the symmetric case. Since all states are normalized, but are localized in different number of wells (one or two), the intensity of single well states in these figures is higher, than that of the double well states.

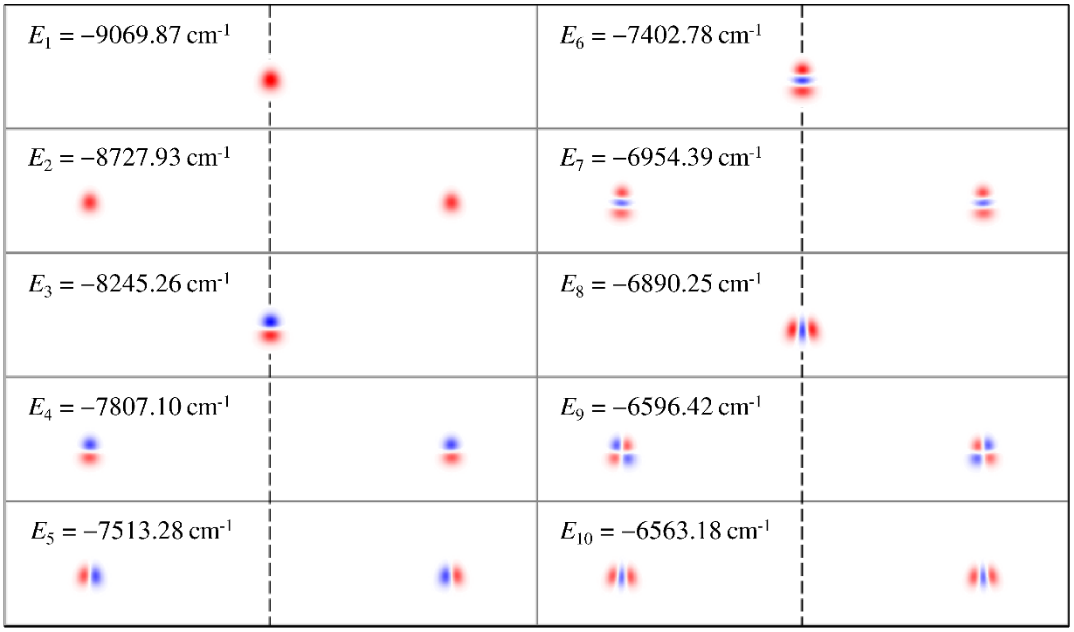

Figure 6.2. First ten symmetric 2D wave functions $\Lambda(\theta, \varphi)$ in a full range of hyperangle φ for singly substituted ozone $^{50}O_3$. The slice is made though covalent region. Wave functions are listed in ascending order of state energy, shown in top-left corner of each panel. The states form two groups, one includes states of the single (central) well, or molecule 686, while another includes states of the double (side) well, or molecules 866 and 668.

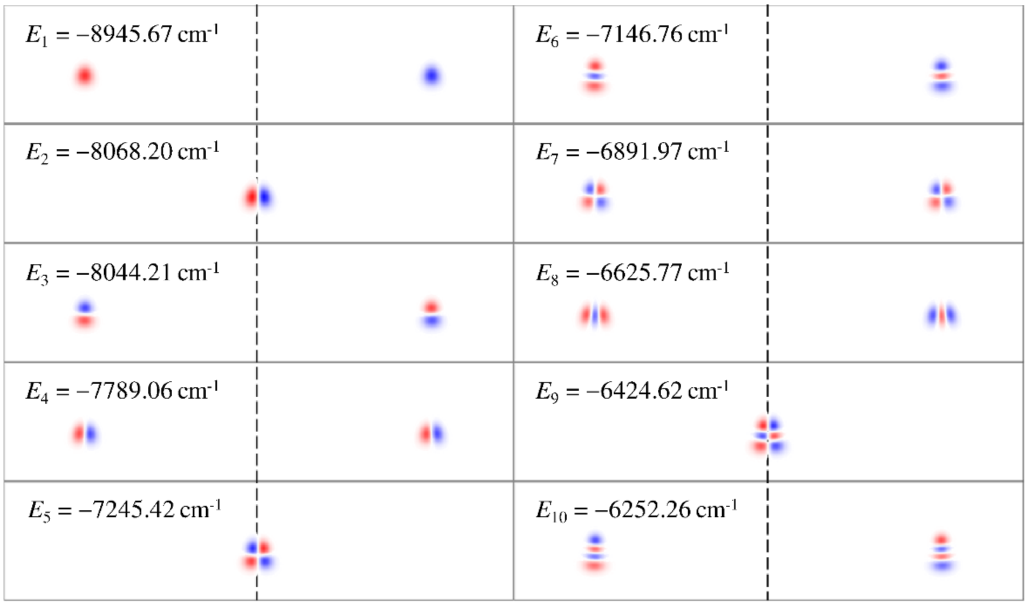

Figure 6.3. First ten asymmetric 2D wave functions $\Lambda(\theta, \varphi)$ in a full range of hyperangle φ for singly substituted ozone $^{50}O_3$, similar to Figure 6.2.

In fact, these single and double well wave function $\Lambda_m^n(\theta,\phi)$ can be approximated using one-well solutions for molecules 686 $(2\pi/3 \le \varphi \le 4\pi/3)$ and 668 $(0 \le \varphi \le 2\pi/3)$. Then, the single well functions are the states of molecule 686, while the double well states are the positive and negative linear combinations of the two states of the molecule 668. The positive linear combinations end up in the group of symmetric functions, and the negative linear combinations appear in the group of asymmetric states. The single well states appear in both groups, depending on evenness or oddness of the number of quanta along hyperangle φ. But, such approach would be approximate and may not work for some highly-excited states, where the wave functions can show delocalization over all three wells.

It is also worth mentioning, that the solution for unsubstituted ozone, $^{48}O_3$, can be obtained in two ways. One way is to use FBR, Eqs. (6.1) and (6.2), with tripled frequency, which will give $\Lambda_m^n(\theta,\phi)$ with a three-fold symmetry, the wave functions will be equivalently distributed between all three wells. In contrast, one can use FBR without frequency tripling, i.e. exactly the same FBR used for substituted ozone. In this approach, two-dimensional states of $^{48}O_3$ will look the same as in Figures 6.2 and 6.3, but corresponding single well and two double well states will be nearly degenerate, the lower is the state the higher is degeneracy.

The extension of configuration space along φ also means addition of many other features of PES, besides three covalent wells. Total, there are three covalent wells, six transition states, six van-der-Walls wells and three dissociation channels. In all these chemically important regions of the PES, the two-dimensional basis $\Lambda_m^n(\theta,\phi)$ behave symmetrically similar, as was discussed for covalent wells. For example, in case of singly and doubly substituted isotopologues, for large hyperradius ρ two dissociation channels are identical, but different from the third one. The computed functions $\Lambda_m^n(\theta,\phi)$ reflect equivalence of two channels, as is seen in Figures 6.4 and 6.5.

Again, symmetric states are either the positive linear combinations of states in two identical channels (double channel states, similar to double well states above) or the states in the different channel with even number of quanta. Similarly, asymmetric states are either the negative combinations or the states in the different channel with odd number of quanta. Since for isotopologue 686 the dissociation threshold associated with the single channel, where $^{32}O_2$ is formed, is larger, then in double channel, where $^{34}O_2$ is formed, the states in single channels appear higher in energy (as seen in Figure 6.4, four states of double channel precede the ground state of the single channel). Note, that this is opposite for doubly substituted isotopologue 868 (not shown here): the heavy $^{36}O_2$ is formed in the single channel, so two-dimensional states of the single channel will precede the states in $^{34}O_2$ channels.

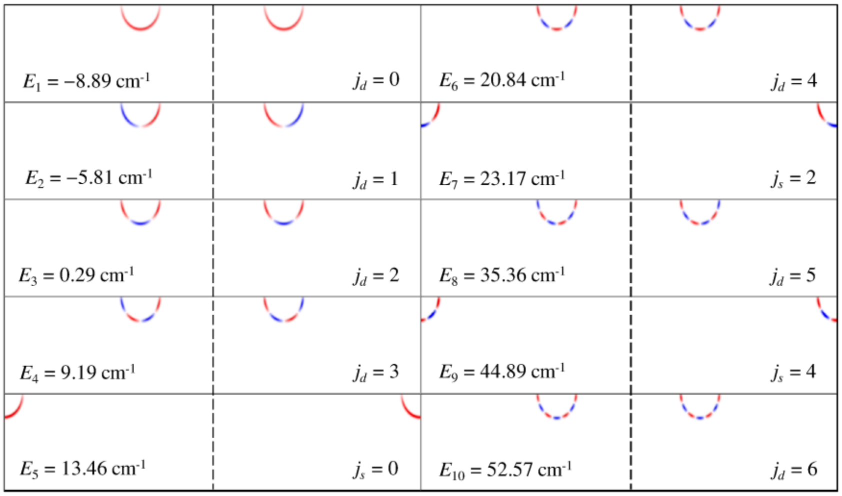

Figure 6.4. First ten symmetric 2D wave functions $\Lambda(\theta, \varphi)$ in a full range of hyperangle φ for singly substituted ozone $^{50}O_3$. The slice is made though dissociation channels. Wave functions are listed in ascending order of state energy, shown in bottom-left corner of each panel. Quantum number j is a number of rotational quanta in O_2, for single channel states of $^{16}O^{16}O$ (j_s) and double channel states of $^{16}O^{18}O$ (j_d).

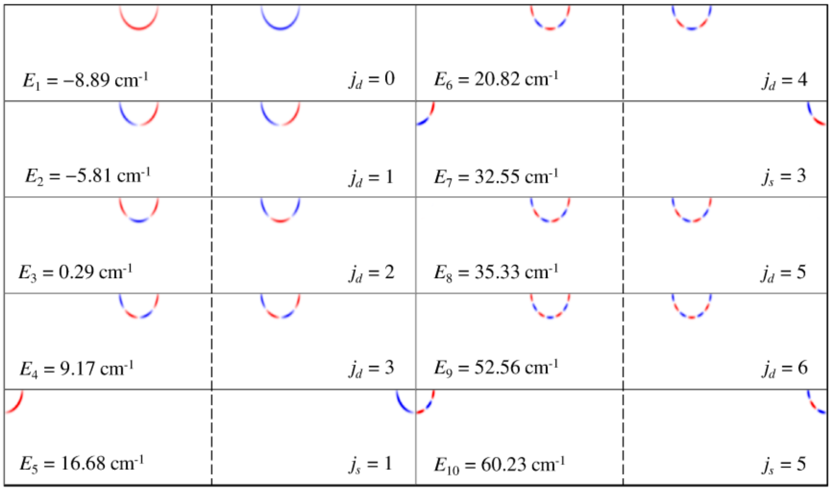

Figure 6.5. First ten asymmetric 2D wave functions $\Lambda(\theta, \varphi)$ in a full range of hyperangle φ for singly substituted ozone $^{50}O_3$, similar to Figure 6.4.

6.3. Symmetry of rotational and vibrational wave functions in ozone

In this section, the symmetry of allowed rotational and vibrational wave functions is discussed in more detail than in Chapter 3. These rules define the vibrational wave functions, or metastable resonance states, to be included into the recombination kinetics formalism to determine the rate coefficient, Eq. (5.8). We will show, how the selection rules could be derived for two orientations of the *z* axis, see Figure 6.6. According to the first choice, the *z* axis, which total angular momentum is projected on, lies in the molecule plane. According to the second choice, the *z* axis is perpendicular to the molecule plane. Also it will be shown how selection rules can be applied to isotopologues $^{50}O_3$ and $^{52}O_3$ that include all the covalent wells, $0 \leq \varphi \leq 2\pi$. These isotopologues are described using C_{2v} point group, because it is the molecular symmetry group of the ozone molecules 686 and 868, similar to the water molecule. For consistency, we will also briefly explain how everything is simplified for the isotopologues with no symmetry, such as 678, that obey C_s symmetry group. The unsubstituted isotopologue, 666, could also be considered using C_{2v}, or using a group with more symmetry constrains, D_{3h}.

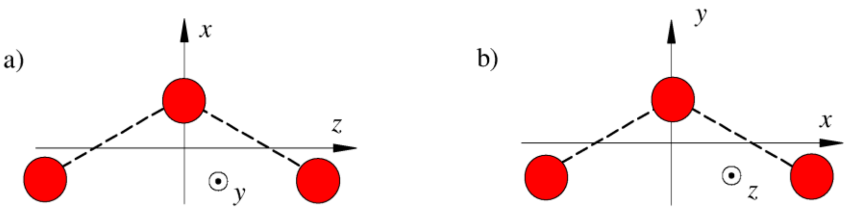

Figure 6.6. Two choices of the body-fixed coordinate systems: a) the *z* axis lies in the molecule plane, b) the *z* axis is perpendicular to the molecule plane.

6.3.1. Symmetry of ozone in C_{2v} group

Similar to water molecule, ozone, in its equilibrium configuration, can be described with C_{2v} symmetry group, see character Table 6.1. It has one two-fold symmetry axis (C_{2b}) and two reflection plans (σ_{ab} and σ_{bc}).

Table 6.1. Character table of C_{2v} point group.

	E	C_{2b}	σ_{ab}	σ_{bc}
A_1	1	1	1	1
A_2	1	1	-1	-1
B_1	1	-1	1	-1
B_2	1	-1	-1	1

The *b* axis is the symmetry axis of the molecule.
The *c* axis is perpendicular to the molecule plane.
The *a* is perpendicular to both *b* and *c*.

The total wave function of the molecule can be expressed as a product of the nuclear spin, electronic, rotational and vibrational components:

$$\Psi = \Psi_s \Psi_{el} \Psi_{rot} \Psi_{vib} \tag{6.7}$$

The same is true for the symmetry of the wave functions:

$$\Gamma = \Gamma_s \Gamma_{el} \Gamma_{rot} \Gamma_{vib} \tag{6.8}$$

Since isotopes ^{16}O and ^{18}O are bosons, then the total wave function Ψ must be symmetric under exchange of any two oxygens, $\Gamma = A_1 \oplus A_2$. The isotopes ^{16}O and ^{18}O are spineless, so the nuclear spin wave function is symmetric: $\Gamma_s = A_1$. The ground electronic state of ozone is also symmetric, so $\Gamma_{el} = A_1$. For ozone molecule, the symmetry of vibrational wave functions is the same as for water molecule, $\Gamma_{vib} = 2A_1 \oplus B_1$. The vibrational states in Figures 6.2 and 6.4 have A_1 symmetry, the states in Figures 6.3 and 6.5 have B_1

symmetry. Consequently, the symmetry of the rotational states could be either A_1 or A_2, see multiplication Table 6.2.

Table 6.2. Multiplication table for C_{2v} point group.

	A_1	**A_2**	**B_1**	**B_2**
A_1	A_1	A_2	B_1	B_2
A_2	A_2	A_1	B_2	B_1
B_1	B_1	B_2	A_1	A_2
B_2	B_2	B_1	A_2	A_1

In our approach, we compute the vibrational states for each rotational state (*J*, *K*) individually. To satisfy selection rules, some of computed vibrational states must be excluded. So, further we will derive how the symmetry of rotational states depends on particular *J* and *K*, and will see which vibrational states must be kept to result in the total wave function of correct symmetry. Here, according to Bunker and Jensen,[166] the transformation of rotational states is convenient to treat using *equivalent rotations R*, which basically represent how the body-fixed molecular axis are rotated under the operations of molecular symmetry group. The equivalent rotation are listed in Table 6.3 for two conventions of axes orientation, shown in Figure 6.6.

Table 6.3. Equivalent rotations for two axis orientations in ozone

	E	C_{2b}	σ_{ab}	σ_{bc}
	E	(12)	E^*	(12)*
z in plane	R^0	R_x^π	R_y^π	R_z^π
z ⊥ plane	R^0	R_y^π	R_z^π	R_x^π

See text for details.

The rotations in Table 6.3 are of two types: a rotation through angle $\delta = \pi$ about *z* axis, R_z^δ, and rotations R_α^π about the axis, which is perpendicular to *z* and forms the angle α with the *x* axis. Both δ and α are measured in a right-handed sense about the *z* axis. Then,

$R_x^\pi = R_0^\pi$ and $R_y^\pi = R_{\pi/2}^\pi$. The corresponding operations of the complete nuclear permutation inversion (CNPI) group are given in a second header row for reference.[166] Those are identity operation E, permutation of identical nuclei (12), the inversion of spatial coordinates of all nuclei and electrons E^* and the product of E^* with (12).

The rotational states are eigenstates of the symmetric top rotor, $| J, k, m\rangle$, proportional to pure Winger functions $D_{KM}{}^J(\alpha, \beta, \gamma)$. Under two operations R_z^δ and R_α^π discussed above, $| J, k, m\rangle$ transforms to either $| J, k, m\rangle$ or either $| J, -k, m\rangle$:[166]

$$R_z^\delta \left| J,k,m \right\rangle = e^{ik\delta} \left| J,k,m \right\rangle , \tag{6.9}$$

$$R_\alpha^\pi \left| J,k,m \right\rangle = (-1)^J e^{-2ik\alpha} \left| J,-k,m \right\rangle . \tag{6.10}$$

Under symmetry operations from Table 6.3 the transformations are

$$R_x^\pi \left| J,k,m \right\rangle = (-1)^J \left| J,-k,m \right\rangle , \tag{6.11}$$

$$R_y^\pi \left| J,k,m \right\rangle = (-1)^{J+k} \left| J,-k,m \right\rangle . \tag{6.12}$$

$$R_z^\pi \left| J,k,m \right\rangle = (-1)^k \left| J,k,m \right\rangle \tag{6.13}$$

Two rotational states $\varphi_1 = | J, K, M\rangle$ and $\varphi_2 = | J, -K, M\rangle$, where $K = |k|$, comprise a two-dimensional reducible representation. The transformation matrices of representation Γ_{rot} generated by φ_1 and φ_2, written as a column vector, are as follows:

$$\begin{gathered} M(R^0) = \begin{bmatrix} 1 & 0 \\ 0 & 1 \end{bmatrix} \qquad M(R_x^\pi) = \begin{bmatrix} 0 & (-1)^J \\ (-1)^J & 0 \end{bmatrix} \\ M(R_y^\pi) = \begin{bmatrix} 0 & (-1)^{J+K} \\ (-1)^{J+K} & 0 \end{bmatrix} \quad M(R_z^\pi) = \begin{bmatrix} (-1)^K & 0 \\ 0 & (-1)^K \end{bmatrix} \end{gathered} \tag{6.14}$$

Table 6.4 summaries the characters of reducible representation Γ_{rot} generated by φ_1 and φ_2 for two choices of axes orientation.

Table 6.4. Characters of the reducible representation Γ_{rot}.

	E	(12)	E*	(12)*
z in plane	2	0	0	$2(-1)^K$
z ⊥ plane	2	0	$2(-1)^K$	0

See text for details.

Quite often it is much more convenient to treat φ_1 and φ_2 together as a positive or negative linear combinations. With such combinations the two-dimensional representation Γ_{rot} can be reduces down to two irreducible representations. There are several ways to define these combinations. The simple normalized sum and difference of φ_1 and φ_2 was used by Bunker and Jensen[166] and is considered in Appendix C. Alternatively, one can add the factor $(-1)^{J+K}$ before function φ_2, as did Pack and Parker in their paper.[60] Here, we will follow the definition by Pack and Parker, at least because the derived selection rules (see further) do not depend on J at all. Therefore, we introduce the following linear combinations:

$$\varphi_\pm = (|\, J, K, M\rangle \pm (-1)^{J+K}\, |\, J, -K, M\rangle) \,/\, (2 \cdot (1 + \delta_{K0}))^{1/2}, \qquad (6.15)$$

The Kronecker delta in denominator is used to have a proper normalization for the case of $K = 0$, so that $\varphi_0 = \varphi_+ = |\, J, 0, M\rangle$. Written as a column vector, functions $\varphi_\pm$ generate the diagonal transformation matrices:

$$\begin{aligned} M(R^0) &= \begin{bmatrix} 1 & 0 \\ 0 & 1 \end{bmatrix} & M(R_x^\pi) &= \begin{bmatrix} (-1)^K & 0 \\ 0 & (-1)^{K+1} \end{bmatrix} \\ M(R_y^\pi) &= \begin{bmatrix} 1 & 0 \\ 0 & -1 \end{bmatrix} & M(R_z^\pi) &= \begin{bmatrix} (-1)^{-K} & 0 \\ 0 & (-1)^{-K} \end{bmatrix} \end{aligned} \qquad (6.16)$$

Obviously, the character of Γ_{rot} is the same as in Table 6.4, as any other linear combinations of functions φ_1 and φ_2, but now each of them can be treated separately and assigned a one-dimensional irreducible representations from Table 6.1. In total, there are

$2J + 1$ rotational wave functions: J positive combinations (φ_+), J negative combinations (φ_-) and one function for $K = 0$ on its own (φ_0).

The symmetry of rotational wave functions depends on K and on the coordinate system, i.e. the orientation of coordinate axes. The characters and symmetries of the rotational wave functions for the z axis chosen to lie in the plane of the molecule are summarized in Tables 6.5 and 6.6. In this tables, label "e" stands for the even values of rotational quantum number K, whereas label "o" for the odd values.

Table 6.5. Characters and symmetries of the positive combination φ_+ and φ_0 of the symmetric top wave functions in C_{2v} for the z axis lying in the molecule plane.

K	E	(12)	E^*	$(12)^*$	Γ
	R^0	R_x^π	R_y^π	R_z^π	
e	1	1	1	1	A_1
o	1	-1	1	-1	B_1

Table 6.6. Characters and symmetries of the negative combination φ_- of the symmetric top wave functions in C_{2v} for the z axis lying in the molecule plane.

K	E	(12)	E^*	$(12)^*$	Γ
	R^0	R_x^π	R_y^π	R_z^π	
e	1	-1	-1	1	B_2
o	1	1	-1	-1	A_2

Another choice of coordinates system, where the z axis is perpendicular to the molecule plane, differs in the rearrangement of the rotational operators R_x^π, R_y^π and R_z^π, and, consequently, in character and symmetries, see Tables 6.7 and 6.8.

Table 6.7. Characters and symmetries of the positive combination φ_+ and φ_0 of the symmetric top wave functions in C_{2v} for the z axis perpendicular to the molecule plane.

K	E	(12)	E^*	$(12)^*$	Γ
	R^0	R_y^π	R_z^π	R_x^π	
e	1	1	1	1	A_1
o	1	1	-1	-1	A_2

Table 6.8. Characters and symmetries of the negative combination φ_- of the symmetric top wave functions in C_{2v} for the z axis perpendicular to the molecule plane.

K	E	(12)	E^*	(12)*	Γ
	R^0	R_y^π	R_z^π	R_x^π	
e	1	-1	1	-1	B_1
o	1	-1	-1	1	B_2

Once the symmetries of the rotational wave functions are known, one can determine the symmetry of the matching vibrational wave functions, so that symmetry constrain imposed on the total wave function by boson statistics is satisfied. The Tables 6.9 and 6.10 show the resultant selection rules. For example, for the calculation with *z* axis lying in plane and odd *K*, the positive combination of the rotational wave functions φ_+ (columns with “+” in the table header) has symmetry B_1 and must be paired with the vibrational state of symmetry B_1 to obtain the allowed symmetry A_1 of the rovibrational wave function (which also coincides with the symmetry of the total wave functions).

Table 6.9. Selection rules in C_{2v} for the z axis lying in the molecule plane.

K	Γ_{rot}		Γ_{vib}		Γ_{rv}	
	+	−	+	−	+	−
e	A_1	B_2	A_1	B_1	A_1	A_2
o	B_1	A_2	B_1	A_1	A_1	A_2

Table 6.10. Selection rules in C_{2v} for the z axis perpendicular to the molecule plane.

K	Γ_{rot}		Γ_{vib}		Γ_{rv}	
	+	−	+	−	+	−
e	A_1	B_1	A_1	B_1	A_1	A_1
o	A_2	B_2	A_1	B_1	A_2	A_2

This information in these tables may be visualized in a more convenient way, if one plots the vibrational symmetry as a function of the total angular momentum *J*, modulus of the projection *K* and parity $p = +/-$, see Tables 6.11 and 6.12. In fact, there is no dependence on *J*, but we keep referring to it, because we do calculations for given pair (*J*, *K*), rather than solely for *K*.

Table 6.11. Symmetry of the allowed vibrational states as a function of total angular momentum *J*, projection *K* and parity *p* of the rotational state. The *z* axis is in the molecule plane.

$K^p \backslash J$	0	1	2	3	4	5
3^+				B_1	B_1	B_1
2^+			A_1	A_1	A_1	A_1
1^+		B_1	B_1	B_1	B_1	B_1
0^+	A_1	A_1	A_1	A_1	A_1	A_1
1^-		A_1	A_1	A_1	A_1	A_1
2^-			B_1	B_1	B_1	B_1
3^-				A_1	A_1	A_1

Table 6.12. Symmetry of the allowed vibrational states as a function of total angular momentum *J*, projection *K* and parity *p* of the rotational state. The *z* axis is perpendicular to the molecule plane.

$K^p \backslash J$	0	1	2	3	4	5
3^+				A_1	A_1	A_1
2^+			A_1	A_1	A_1	A_1
1^+		A_1	A_1	A_1	A_1	A_1
0^+	A_1	A_1	A_1	A_1	A_1	A_1
1^-		B_1	B_1	B_1	B_1	B_1
2^-			B_1	B_1	B_1	B_1
3^-				B_1	B_1	B_1

From these vibrational symmetry patterns it becomes obvious, that the vibrational states of both symmetries, A_1 and B_1, must be retained for a given pair of (*J*, *K*). Since there is no need to do a separate calculations for each value of parity *p*, it can be dropped. The only exception is $K = 0$. For that case, the states of A_1 symmetry must be retained, whereas B_1 states must be excluded. Also, the derived selection rules are applied to both types of calculations: including only one covalent well, or including all three covalent wells. In both cases, the vibrational states obey A_1 or B_1 symmetry, they are ether symmetric or asymmetric with respect to $\varphi = \pi$. The discussion in this section is true for the isotopomers which contain two different isotopes at maximum. When all three atoms are identical, for example molecules 666 or 888, then the same selection rules could be applied. Alternatively, such isotopologues could be considered in the symmetry group of higher order, for example D_{3h}. When all three atoms are different, than symmetry group of lower order, C_s, must be used.

6.3.2. Symmetry of ozone in C_s group

The isotopomer $^{16}O^{17}O^{18}O$ contains three different isotopes and therefore should be described with C_s point group, which is the subgroup of C_{2v}, see character Table 6.13 and multiplication Table 6.14.

Table 6.13. Character table of C_s point group.

	E	σ_h
A'	1	1
A''	1	-1

Table 6.14. Multiplication table for C_s point group.

	A'	A''
A'	A'	A''
A''	A''	A'

The symmetries of the wave functions are $\Gamma = A' \oplus A''$, $\Gamma_{vib} = A'$, $\Gamma_s = A'$, $\Gamma_{el} = A'$ and $\Gamma_{rot} = A' \oplus A''$. Basically, the total wave function has no symmetry constrains and only the rotational part determines its symmetry. When the z axis lies in the molecule plane, then the positive combination φ_+ and φ_0 transform as A', whereas φ_- obeys A''. The symmetry of rotational wave functions does not depend on rotational quantum numbers J and K and depends only on parity $p = +/-$.

For the z axis, perpendicular to the molecule plane, the symmetries of the rotational states depend on K and can be summarized in only one Table 6.15.

Table 6.15. Characters and symmetries of both positive and negative combinations $\varphi_\pm$ of the symmetric top wave functions in C_s for the z axis perpendicular to the molecule plane. K = 0 is also included.

K	E R^0	E^* R_z^π	Γ
e	1	1	A'
o	1	-1	A''

The fact that vibrational wave functions exhibit no symmetry, simply means that all computed vibrational states for a given pair of (J, K) and parity p must be retained.

6.4. Isotope effects

6.4.1. Numerical estimation of isotope effects in three well calculations

To study isotope effects in ozone, the rate coefficients for four versions of recombination reactions may be introduced:

$$6 + 66 \xrightarrow{k} 666 \tag{6.17}$$

$$6 + 86 \xrightarrow{k_{sym}} 686 \tag{6.18}$$

$$6 + 68 \xrightarrow{k_A} 668 \tag{6.19}$$

$$66 + 8 \xrightarrow{k_B} 668 \tag{6.20}$$

The rate coefficients could be computed with slightly different versions of Eq. (5.9):

$$k_{sym}(\text{or}\, k) = \sum_i \frac{\Gamma_i\, K_{eq}^A(E_i)}{\Gamma_i + (k_i^{\text{stab}} + k_i^{\text{diss}})[\text{M}]} k_i^{\text{stab}} \tag{6.21}$$

$$k_A = \sum_i \frac{\Gamma_i^A \, K_{eq}^A(E_i)}{\Gamma_i + (k_i^{\text{stab}} + k_i^{\text{diss}})[\text{M}]} k_i^{\text{stab}} \tag{6.22}$$

$$k_B = \sum_i \frac{\Gamma_i^B \, K_{eq}^B(E_i)}{\Gamma_i + (k_i^{\text{stab}} + k_i^{\text{diss}})[\text{M}]} k_i^{\text{stab}} \tag{6.23}$$

The denominators are the same, but numerators are different. The numerator for the symmetric ozone contains the full resonance width Γ_i, while two other equations include only corresponding portion of the resonance width, Γ_i^A or Γ_i^B, representing the partial decay rate constant, $\Gamma_i = \Gamma_i^A + \Gamma_i^B$.

In these equations, there are three hidden sources of factor of two, which we carefully discuss further. First of all, in the case of identical channels A and B, the widths Γ_i^A or Γ_i^B are equal, $\Gamma_i^A = \Gamma_i^B = \Gamma_i / 2$. This is one factor of two.

Next, we should mention that the sums in Eqs. (6.20) − (6.22) are over different types of states. As follows from Section 6.2, in the singly substituted ozone the two covalent wells 668 are equivalent and 686 is different. This is seen from PES slices, Figure 6.1, and also was observed in computed two-dimensional basis functions, Figures 6.2 and 6.3. The three-dimensional resonance states of ozone are not an exception and also form two groups of states: the resonances localized in the single well 686 and the resonances localized in the double well 668, see Figure 6.7.The single well states 686 contribute to the recombination rate coefficient k_{sym}, while the double well states 668 contribute to both k_A and k_B. Typically, the double well states decay into both channels, however, there are cases when double well state decays in only one channel, A or B, as shown on Figure 6.7.

The number of states contributing to recombination for typical rotational excitation $J = 24$ $K = 2$ is plotted in Figure 6.8. The figure clearly demonstrates an expected statistical fact: the number of states in asymmetric molecule is twice larger than in symmetric molecule. In practice, the factor is not exactly two and may depend on isotopomer and rotational excitation. This is second factor of two in our equations.

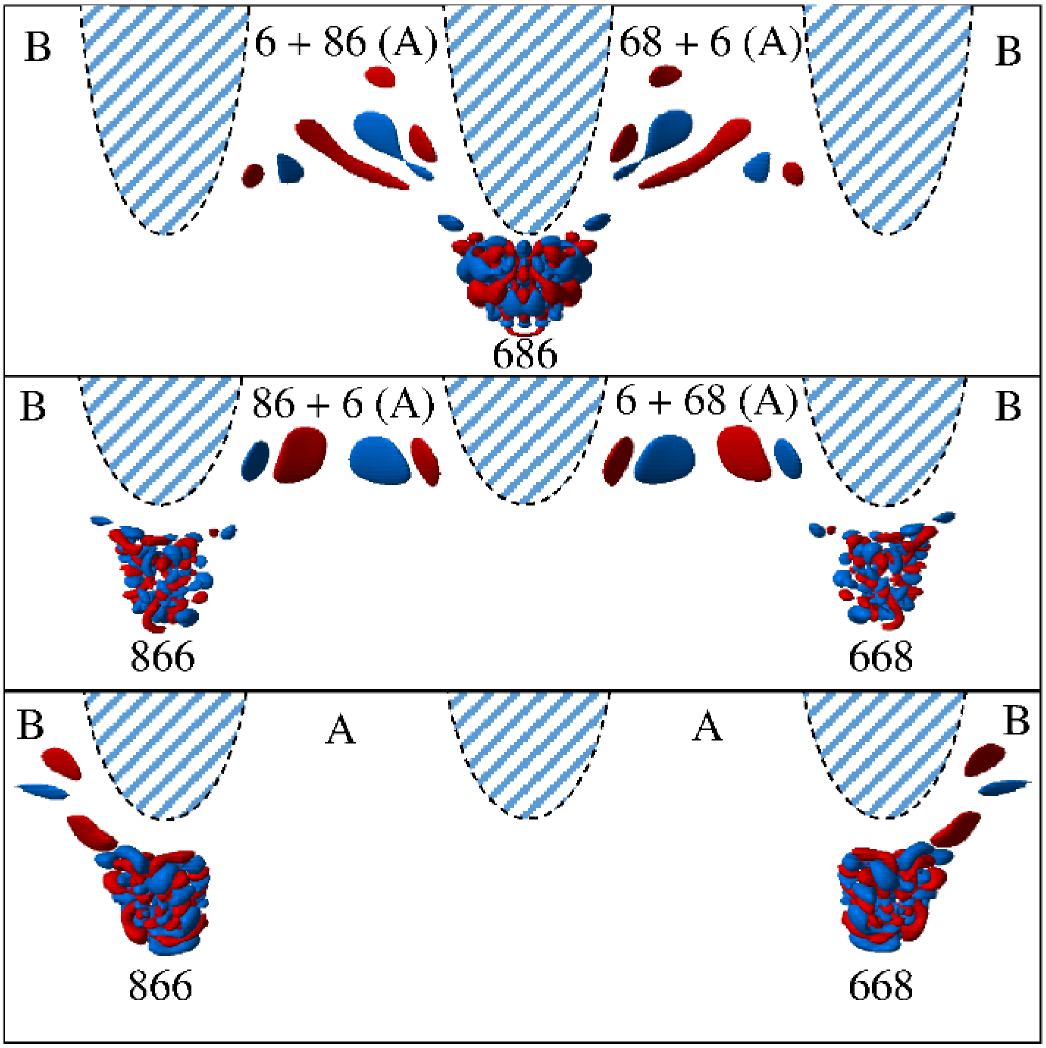

Figure 6.7. Two types of three-well resonance states in $^{50}O_3$ isotopologue: single well state (top panel) and double well state decaying into channel A, where O_2 is heteronuclear (middle panel), or into channel B, where O_2 is homonuclear (bottom panel).

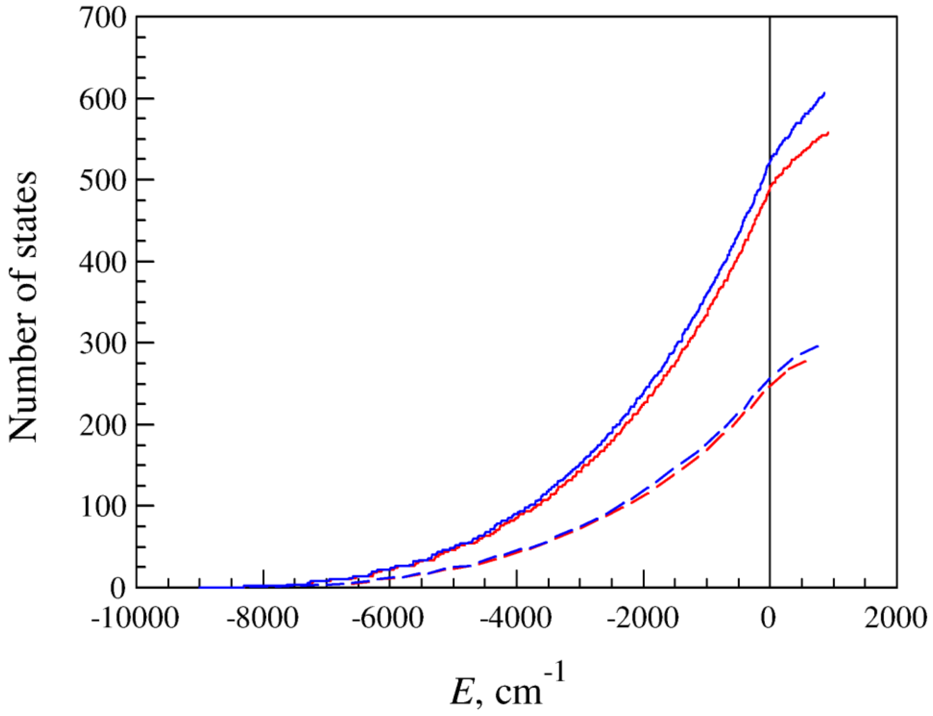

Figure 6.8. Number of states as a function of state energy for singly (red) and doubly (blue) substituted isotopologues, $^{50}O_3$ and $^{52}O_3$. Number of states in symmetric molecules 686 and 868, or single well states, is shown with dashed lines, number of states in asymmetric molecules 668 and 688, or double well states, is shown with solid lines. Rotational excitation is $J = 24$ $K = 2$.

Then, the equilibrium constants in Eqs. (6.21) − (6.23) K_{eq} are also different. The oxygen in channel A is heteronuclear, $^{16}O^{18}O$, while in channel B it is heteronuclear, $^{16}O^{16}O$. Because the rotational partition function of O_2 appears in the denominator of K_{eq}, the equilibrium constant for channels B is twice larger, then for channel A:

$$K_{eq}^{B} = 2K_{eq}^{A} \tag{6.24}$$

This is the third and last factor of two.

Based on these three factors of two, found in equations, the rate coefficients k, k_{sym}, k_A and k_B could be related. First, when k_{sym} is compared with k_A, the factor of two derived from partial widths is compensated by the factor in number of states, so $k_{sym} \approx k_A$. For rate constants k and k_B the factor of two due to the symmetry of reacting O_2 starts playing, making them twice larger then k_{sym} and k_A. All this can be summarized in the following relation:

$$k \approx 2k_{sym} \approx 2k_A \approx k_B \tag{6.25}$$

If there were no isotope effects in ozone, than this relation would be exact (the approximately equal signs would be replaced with the exactly equal signs). To compare the rate coefficients, it is convenient to introduce another set of rate coefficients with the factors of two being dropped

$$\begin{gathered} \varkappa_{sym} = 2k_{sym}; \quad \varkappa_A = 2k_A; \quad \varkappa_B = k_B \\ \varkappa \approx \varkappa_{sym} \approx \varkappa_A \approx \varkappa_B \end{gathered} \tag{6.26}$$

so that we see that, the rate coefficients $\varkappa_{sym}$, $\varkappa_A$ and $\varkappa_B$ are "normalized", with $\varkappa$ as a reference. To study the ΔZPE-effect, these coefficients $\varkappa$ can be plotted in the same fashion as in Figure 1.5 and the ratio $R = \varkappa_A / \varkappa_B$ can be introduced. To quantify the η-effect, the average rate coefficient for asymmetric ozone must be defined:

$$\varkappa_{asym} = (\varkappa_A + \varkappa_B) / 2 \tag{6.27}$$

The value of η is simply the ratio between $\varkappa_{asym}$ and $\varkappa_{sym}$:

$$\eta = \varkappa_{asym} / \varkappa_{sym} \tag{6.28}$$

Recall that, the experimentally observed deviation is $\eta = 1.2$.

To obtain an insight on isotope effects, the rate coefficients $\varkappa_{sym}$, $\varkappa_A$ and $\varkappa_B$ were computed only for a limited number of typical rotational excitations. In total 13 rotational states were chosen based on the rotational distribution, see Figure 6.9. Both isotope effects were analyzed on this small subset of rotational states, so the results discussed below are preliminary.

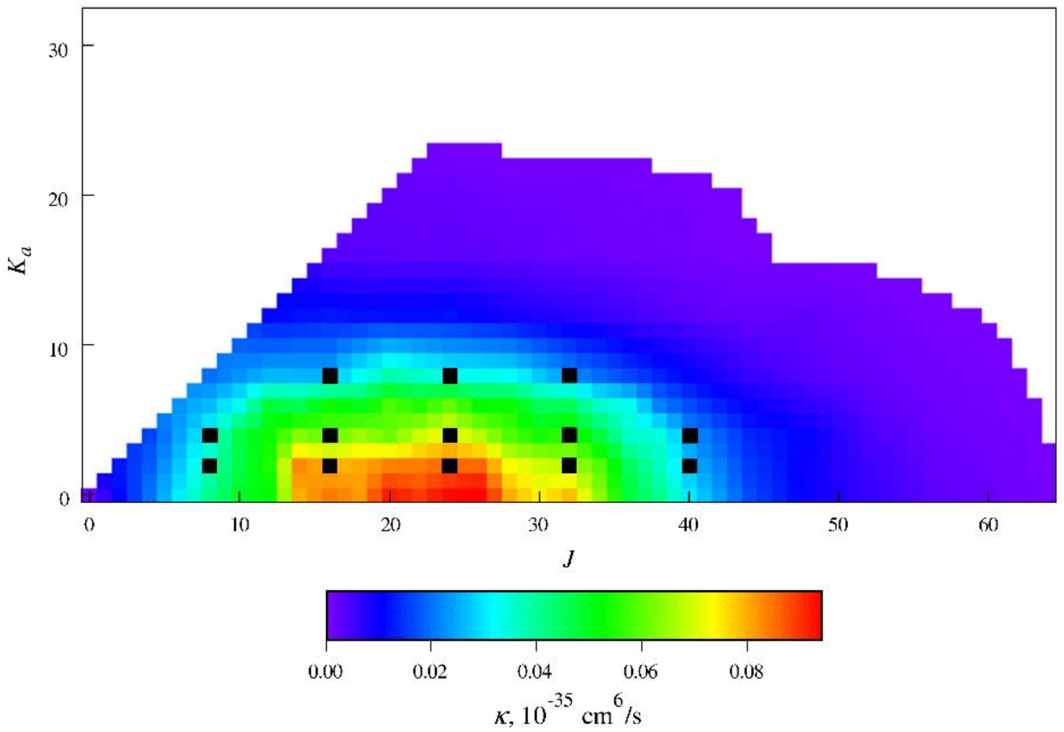

Figure 6.9. Typical rotational excitations (black squares) to study isotope effects on.

6.4.2. Results

To study isotope effects and compare them with available experimental data, the rate coefficients $\varkappa_{sym}$, $\varkappa_A$ and $\varkappa_B$ must be computed, normalized using some reference and plotted as a function of ΔZPE. In the experiment the recombination rate coefficient for unsubstituted ozone *k* is usually chosen as a reference. Here we try to obtain some insight from a limited set of calculations that include 686 and 868, but no 666. So further we will use the average k_{sym} of 686 and 868 molecules as a reference, since they were available right away from our calculation.

The computed rate coefficients $\varkappa_{sym}$, $\varkappa_A$ and $\varkappa_B$ are listed in Table 6.16, separately for each rotational excitation and for both isotopomers $^{50}O_3$ and $^{52}O_3$.

Table 6.16. Recombination rate coefficients of two isotopomers $^{50}O_3$ and $^{52}O_3$ for typical rotational excitations (*J*, *K*).

(*J*, *K*)	Isotopomer $^{50}O_3$ (686)			Isotopomer $^{52}O_3$ (868)		
	$\varkappa_B$	$\varkappa_{sym}$	$\varkappa_A$	$\varkappa_A$	$\varkappa_{sym}$	$\varkappa_B$
(8, 2)	0.53	0.64	1.20	0.67	0.59	0.68
(8, 4)	0.52	0.82	1.11	0.48	0.77	0.70
(16, 2)	0.65	1.35	2.41	1.15	1.04	1.98
(16, 4)	0.61	1.49	2.72	1.02	0.94	1.83
(16, 8)	0.68	0.99	2.29	0.77	0.98	1.34
(24, 2)	1.54	1.83	1.61	1.37	1.25	1.72
(24, 4)	1.55	1.72	1.62	1.16	1.10	1.60
(24, 8)	0.80	1.27	1.27	0.93	0.94	1.35
(32, 2)	1.23	1.40	1.41	1.29	1.12	1.45
(32, 4)	1.10	1.18	1.19	1.03	1.00	1.60
(32, 8)	0.66	0.69	0.93	0.83	0.78	0.89
(40, 2)	0.64	0.51	0.63	0.55	0.61	0.62
(40, 4)	0.57	0.45	1.13	0.49	0.54	0.58
Average	0.85	1.10	1.50	0.90	0.90	1.26
Experiment[16]	0.92	1.01	1.43	0.92	1.04	1.50
Renormalized	0.87	0.95	1.35	0.87	0.98	1.42

The experimental values, renormalized using the average of k_{sym} for 686 and 868 as reference instead of 666, are given in the last row. The channels A and B are swapped for $^{52}O_3$, because homonuclear and heteronuclear O_2 are exchanged in channels.

The rate coefficients for different rotational excitations (*J*, *K*) may differ significantly. This is due to the quantum character of the process: occasional appearance of just one resonance can significantly affect the rate coefficient $\varkappa$. Nevertheless, the overall pattern stands out: on average, the rate coefficient for channel A (heteronuclear reagent O_2) dominates the rate coefficient for channel B (homonuclear reagent O_2), while the rate coefficient for $\varkappa_{sym}$ is close to $\varkappa_B$. This is ΔZPE-effect.

A good agreement with experiment is demonstrated on Figure 6.10. Though not in the value, but at least in correct direction, the modeled isotope effects agree with experiment quite well, even for the small subset of the rotational states (*J*, *K*) included. The ΔZPE-effect, the slope of dashed green line, is somewhat overestimated for $^{50}O_3$, the ratio $R = \varkappa_A / \varkappa_B$ is 1.55 in the experiment vs. 1.94 in the theory. In contrast, it is underestimated for $^{52}O_3$, 1.63 in the experiment vs. 1.38 in the theory. The situation is opposite for η-effect. For isotopologue $^{50}O_3$, the theory, $\eta = 1.09$, underestimates experiment, $\eta = 1.17$. For isotopologue $^{52}O_3$, the theory, $\eta = 1.18$, overtimes experiment a little, $\eta = 1.16$.

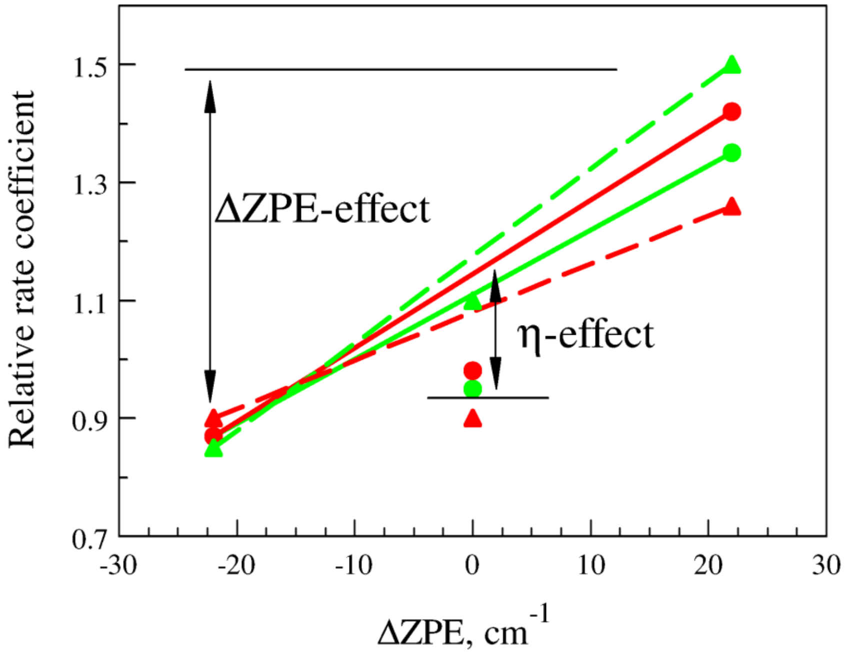

Figure 6.10. Relative rate coefficients as a function of ΔZPE for two isotopologues $^{50}O_3$ (greed data) and $^{52}O_3$ (red data). The experimental data is plotted with solid lines and circles, the computed data is plotted with dashed lines and triangles. The ΔZPE-effect (positive slope of the lines) and the η-effect (lowering of the points at ΔZPE = 0), are in correct direction, the theory agrees with the experiment.

The procedure for numerical estimation of isotopic effects can be formulated using the ranges of hyperangle φ, see Figure 6.11. Basically, the ΔZPE-effect is the difference in the rate coefficient of formation of asymmetric molecule 668 from two different channels: from channel A, defined by ranges $\pi/3 \le \varphi \le 2\pi/3$ and $4\pi/3 \le \varphi \le 5\pi/3$ (top left diagram), and from channel B, defined by $-\pi/3 \le \varphi \le \pi/3$ (top right diagram).

The η-effect shows the difference in the formation of asymmetric molecule 668, defined by $-2\pi/3 \leq \varphi \leq 2\pi/3$ (bottom left diagram) vs. that of symmetric molecule 686, defined by $2\pi/3 \leq \varphi \leq 4\pi/3$ (bottom right panel). The circular diagram will be explained in detail in Section 6.4.4.

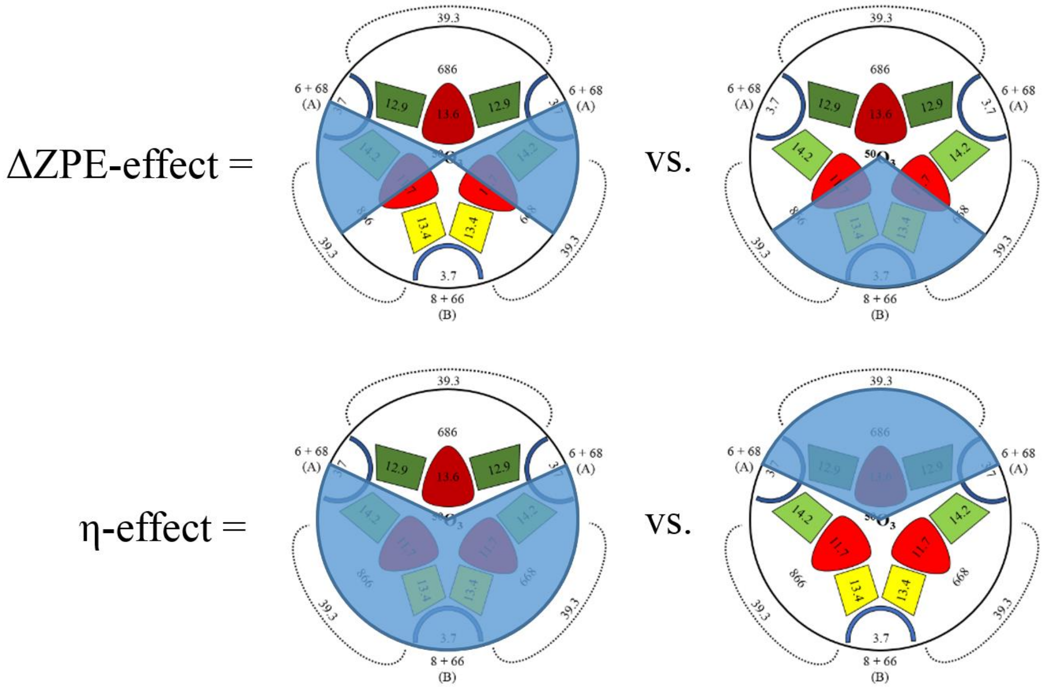

Figure 6.11. Ranges of hyperangle φ (transparent blue sectors) that are used for determination of isotope effects, ΔZPE (top panel) and η-effect (bottom panel). The origin of hyperangle is at the center of channel B. See text for details.

6.4.3. Effect of the resonance widths

What causes these effects? There are at least two possible sources, and the widths Γ of resonance states are one of them. To analyze ΔZPE-effect, widths Γ_A and Γ_B of double well states of asymmetric molecule 668 could be plotted as a function of state energy E above dissociation threshold, see Figure 6.12. However, as seen in the figure, it does not demonstrate any significant difference in width Γ_A and Γ_B. An alternative option is to compute the average values of width Γ_A and Γ_B. For singly substituted ozone with typical $J = 24$ and $K = 2$, we found $<\Gamma_A> = 1.51$ cm^{-1} and $<\Gamma_B> = 1.40$ cm^{-1}. Therefore, isotopomer 668 has a higher tendency to be formed from channel A, rather than B, which is consistent with observed ΔZPE-effect.

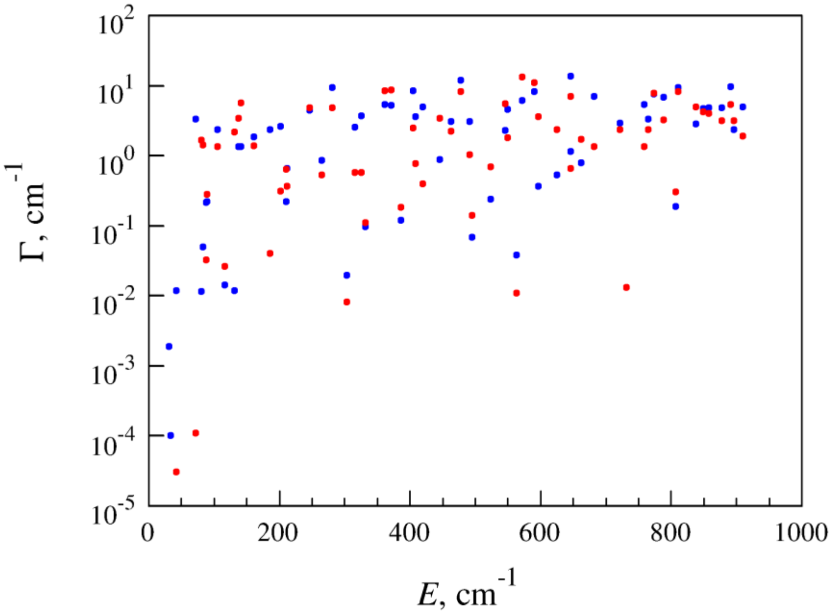

Figure 6.12. Resonance widths Γ_A (blue points) and Γ_B (red points) as a function of state energy E above dissociation threshold. Only double well states of asymmetric molecule 668 are plotted. Rotational excitation is $J = 24$ $K = 2$.

For all 13 rotational excitations, we can perform a simple test, which could give us a better insight on the origin of the anomalous isotope effects. The trick is to assign the same resonance width Γ to all resonances, contributing to the recombination. When we assigned the same total $\Gamma = 1$ cm^{-1}, which is the average width as seen from the distribution of resonance widths in Figure 5.1b, and partial widths $\Gamma_A = \Gamma_B = 0.5$ cm^{-1}, both effects almost disappeared. The ΔZPE-effect dropped from $R = 1.94$ to $R = 0.90$ for isotopologue $^{50}O_3$, and it dropped from 1.38 to 0.93 for isotopologue $^{52}O_3$. The same behavior was observed for η-effect, it decreased from $\eta = 1.09$ to $\eta = 1.05$ for isotopologue ${}^{50}O_3$, and from 1.18 to 1.00 for isotopologue ${}^{52}O_3$. This numerical experiment demonstrates that the possible origin of the ΔZPE-effect are the widths, or lifetimes, or scattering resonances in ozone. This simply reflects the fact that the contributing resonances tend to form (and decay) from the lower channel, making the associated recombination rate coefficient large for that channel. For η-effect, the role of width appears to be the same, however, the effect itself is small, while uncertainty in the relative rate coefficients is still high, due to the small number of the rotational states included.

6.4.4. Effect of the number of states

Another source of isotope effects could be the number of the resonance states in single well and double well. Based on statistical approach, if the molecules (covalent wells) 668 and 686 are computed separately, then due to selection rules all vibrational states are allowed in 668 (C_s) and roughly only half is allowed in 686 (C_{2v}). For three-well calculation, this is also true: per one single well state there are two double well states, see Figure 6.8 earlier. However, for highly excited states, which resonance states of ozone are, this factor is not exact and ultimately is determined by the PES. The higher is the energy, the less localized the states are, similar to what was already discussed on delocalized states in Section 5.3.1.

To get a better insight on the density of states, the probabilities of all states were summed together, but separately in different parts of PES for a typical rotational excitation ($J = 24$ $K = 2$) and plotted on the circular diagram shown in Figure 6.13.

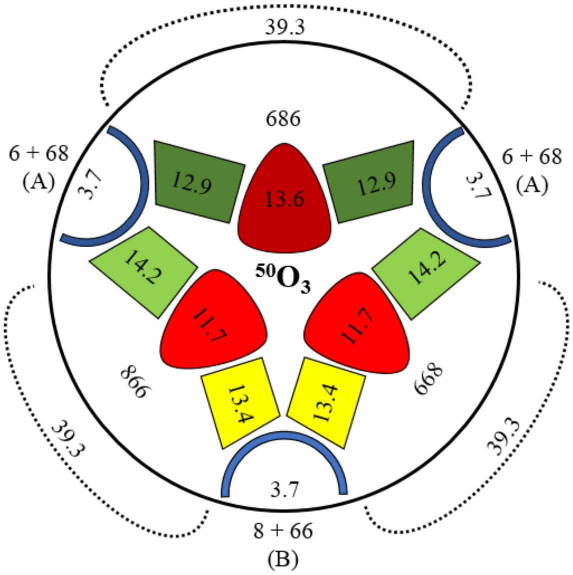

Figure 6.13. Probability distribution of resonance states as a function hyperangle φ for singly substituted ozone $^{50}O_3$ and $J = 24$ $K = 2$. Covalent wells are labeled with 686, 668 and 866 (red smoothed triangles), channels are labeled with letters A and B (blue curves). The van-der-Waals regions are located between wells and channels, total six of them. Van-der-Waals states associated with channel A (green trapezes) do not mix with those in channel B (yellow trapezes).

The resonances are not only localized in the covalent wells, but also delocalized in the van-der-Waals regions and also have some tails. We found that fraction in van-der-Waals wells are pretty much the same as in covalent wells. Also, the total probability in the well and two adjoining van-der-Waals wells is the same, does not matter which covalent well with its van-der-Waals wells is considered. However, the probability can be distributed differently between the covalent well and adjoining van-der-Waals wells. The molecule 686 has 13.6 in covalent region and 12.9 in adjoining van-der-Waals regions, while this is opposite for another molecule, 11.7 in covalent and 13.4 and 14.2 in van-der-Waals well. In this way, the factor of two in the number of states is still valid for these “extended areas”, and is not valid anymore for purely covalent states, for which it is $2 \cdot 11.7 / 13.6 = 1.72$. Interestingly, that particularly for that rotational state, the number of states in the singly substituted ozone plays against resonance width Γ, resulting in a wrong direction of the η-effect, $\eta = 0.86$ (less than one). But, in total, when more rotational states are taken, the effect becomes large then one. The similar diagram for doubly substituted ozone 868 is shown in Figure 6.14. The number of resonance states is almost the factor of two, $2 \cdot 15.0 / 15.2 = 1.97$.

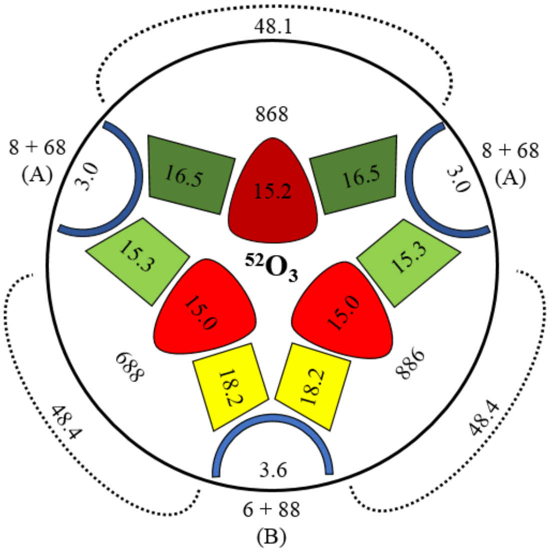

Figure 6.14. Probability distribution of resonance states as a function hyperangle φ for singly substituted ozone $^{52}O_3$ and $J = 24$ $K = 2$. The labels are the same as in Figure 6.13.

The results reported are preliminary, because they were obtained for a small number of rotational states (J, K): only 13 states, meanwhile 95 states were computed in one-well calculation, reported in Chapter 5. The contribution of the chaperon mechanism, which does not exhibit isotope effects,[167] is not taken into account yet, and is expected to reduce the strength of both effects. Also, the stabilization model deserves an extensive review, because in our calculations there are resonances, that have comparable probabilities in both covalent and van-der-Waals regions, while the stabilization models were developed primarily for the resonances localized above covalent well only. We tried two ad-hoc ways to include van-der-Waals states using the same stabilization model used for the states in covalent well and found that the isotope effects change, but not much, at least they were always found to be in the right direction. But again, the stabilization model was built solely for the resonances localized in covalent well and more advanced model is needed.

6.5. Rotation-vibration couplings

The method for calculation of resonances and bound states in ozone, proposed in Chapter 3, describes rotation using symmetric top approximation. Both asymmetric and Coriolis terms are neglected, which makes it possible to decouple calculations with different projections of angular momentum K (different J are automatically decoupled). In other worlds, rotation is incorporated separately: for each particular rotational excitation (J, K) the vibrational spectrum is computed independently, see section 3.2.2. However, if sufficient computational resources are available, then one can include couplings between different K values, what is known as coupled channel or close coupling (CC) approach. Pack and Parker derived matrix elements of CC Hamiltonian for the *prolate* symmetric top with the z axis (projection axis of total angular momentum) lying in the triatomic plane.[60]

In this section, derivation of matrix elements for CC Hamiltonian is reviewed and is applied to other cases, such as the z axis perpendicular to molecule plane, but also to *oblate* symmetric top. Thus, we present the matrix structure resulted from four possible combinations of axis orientations and rotor type together, and discuss with advantages and disadvantages of some cases over others. Similar discussion could be found in the work by Kendrick *et al*.[72] This theory has not been yet implemented in the code, so it should be considered as a possible improvement of the method in future.

In this section, the total rovibrational wave function is expanded in terms of the vibrational functions $\Psi(\rho,\theta,\varphi)$, see Eq. (3.17), and modified rotational Wigner functions of given parity $\hat{D}^{Jp}_{KM}(\alpha,\beta,\gamma)$:

$$\Phi^{(i)}_{JMp} = \sum_{K,n,m} a^{(i)}_{JKnm} f_n(\rho)\Lambda^{n}_{JKm}(\theta,\varphi)\hat{D}^{Jp}_{KM}(\alpha,\beta,\gamma)\,, \tag{6.29}$$

The modified rotational functions $\hat{D}^{Jp}_{KM}(\alpha,\beta,\gamma)$ are normalized sum and difference of usual Wigner functions $D^{J}_{KM}(\alpha,\beta,\gamma)$ and are the same $\varphi_{\pm}$ functions in Section 6.3.1:[60]

$$\hat{D}^{Jp}_{KM}(\alpha,\beta,\gamma) = \left[\frac{2J+1}{16\pi^2(1+\delta_{K0})}\right]^{1/2}\left[D^{J}_{KM}(\alpha,\beta,\gamma) + (-1)^{J+K+p} D^{J}_{-KM}(\alpha,\beta,\gamma)\right] \tag{6.30}$$

Next, we will discuss two possible ways of axes orientation, the matrix elements and matrix structure for prolate and oblate symmetric tops and will present conclusions on application of the rovibrational correction to ozone.

6.5.1. Axes labeling

There are we found two ways of the axes orientation in literature. Table 6.17 shows correspondence between body-fixed (BF) components of the total angular momentum **J** and rotational constants of “fluid” rotor *A*, *B* and *C*. The labeling of angular momentum components for the *z* axis placed in plane follows the convention by Pack and Parker,[60] while for *z*, perpendicular to the plane, Johnson’s way of labeling is given (also adopted by Kendrick).[72,109]

Table 6.17. Correspondence between components of the total angular momentum *J* and rotational constants *A*, *B* and *C* of the fluid rotor in APH coordinates.

z in plane Pack & Parker	*z* ⊥ plane Johnson	Rotational constant
J_x	J_y	$A^{-1} = \mu\rho^2(1+\sin\theta)$
J_y	J_z	$B^{-1} = 2\mu\rho^2\sin^2\theta$
J_z	J_x	$C^{-1} = \mu\rho^2(1-\sin\theta)$

The expressions for angular momentum operator and Coriolis term depend on the axes labeling as well. For *z* in plane:

$$\hat{V}_{rot} = A\hat{J}_x^2 + B\hat{J}_y^2 + C\hat{J}_z^2\,, \tag{6.31}$$

$$\hat{T}_{cor} = 4B\cos\theta\left(i\hbar\frac{\partial}{\partial\varphi}\right)\hat{J}_y\,. \tag{6.32}$$

For *z* ⊥ plane:

$$\hat{V}_{rot} = A\hat{J}_y^2 + B\hat{J}_z^2 + C\hat{J}_x^2\,, \tag{6.33}$$

$$\hat{T}_{cor} = 4B\cos\theta\left(i\hbar\frac{\partial}{\partial\varphi}\right)\hat{J}_z\,. \tag{6.34}$$

In that follows, we will demonstrate that for the case of prolate symmetric top, the choice of *z* in plane appears to be a favorable, due to straightforward matrix structure and smaller off-diagonal blocks. Next, we will show that for the oblate symmetric top, the choice of *z* perpendicular to the molecule plane is more preferred.

6.5.2. Prolate symmetric top

In equilibrium configuration ozone is very close to a prolate-top rotor, see the rotational constants in Section 3.2.2. As ozone dissociates, the associated rotor becomes even more prolate. Thus, prolate symmetric top is a very reasonable approximation for ozone molecule. Then, two rotational constants are close to each other, i.e. $A \sim B$, and both are much smaller than the third one, $\tilde{A} = (A + B) / 2 < C$. The moments of inertia satisfy the following relation (see small pictograms in Figure 6.15):

$$I_x = I_y > I_z \text{ (} z \text{ in plane)} \tag{6.35}$$

$$I_y = I_z > I_x \, (z \perp \text{plane}) \tag{6.36}$$

Once two rotational constants are replaced by their average, the rotational operator $\hat{V}_{rot}$ could be rewritten as a sum of two terms, symmetric $\hat{V}_{sym}$ and asymmetric $\hat{V}_{asym}$. For z in plane:

$$\hat{V}_{sym} = \tilde{A}\hat{J}^2 + (C - \tilde{A})\hat{J}_z^2 , \tag{6.37}$$

$$\hat{V}_{asym} = \frac{A - B}{2}(\hat{J}_x^2 - \hat{J}_y^2) . \tag{6.38}$$

For $z \perp$ plane:

$$\hat{V}_{sym} = \tilde{A}\hat{J}^2 + (C - \tilde{A})\hat{J}_x^2 , \tag{6.39}$$

$$\hat{V}_{asym} = \frac{A - B}{2}(\hat{J}_y^2 - \hat{J}_z^2) . \tag{6.40}$$

These two operators and Coriolis operator $\hat{T}_{cor}$ could be integrated with rovibrational functions in Eq. (6.29) on both sides to obtain matrix elements of rovibrational Hamiltonian, $\left\langle \Phi_{JMp}^{(i)} \middle| \ldots \middle| \Phi_{JMp}^{(i')} \right\rangle$. The vibrational contribution factors out, and one can focus solely on rotational component. In what follows, the vibrational factor is omitted in all equations for convenience. Instead of common label *K* we will use letter Λ for the projection of total angular momentum **J** onto the *z* axis lying in molecule plane (following notation by Pack and Parker[60]), and Ω for projection onto the *z* axis perpendicular to the plane (following Kendrick's notation[72]).

For *z* lying in the plane of the molecule, we obtain the following expressions for the matrix elements of rotational and Coriolis terms (vibrational factor is omitted):

$$V_{sym} = \left[\tilde{A} J(J+1) + (C-\tilde{A})\Lambda^2 \right] \hbar^2 \delta_{\Lambda',\Lambda}, \tag{6.41}$$

$$V_{asym} = \frac{A-B}{2} \hbar^2 U^{Jp}_{\Lambda\Lambda'}, \tag{6.42}$$

$$T_{cor} = 4B\hbar^2 \cos\theta \frac{\partial}{\partial\varphi} W^{Jp}_{\Lambda,\Lambda'}, \tag{6.43}$$

and for *z* ⊥ plane:

$$V_{sym} = \tilde{A}\hbar^2 J(J+1)\delta_{\Omega',\Omega} + (C-\tilde{A})\hbar^2 \left[\frac{J(J+1)-\Omega^2}{2} \delta_{\Omega',\Omega} + \frac{U^{Jp}_{\Omega\Omega'}}{2} \right], \tag{6.44}$$

$$V_{asym} = \frac{A-B}{2}\hbar^2 \left[\left(\frac{J(J+1)-\Omega^2}{2} - \Omega^2 \right) \delta_{\Omega',\Omega} - \frac{U^{Jp}_{\Omega\Omega'}}{2} \right]. \tag{6.45}$$

$$T_{cor} = 4B\hbar^2 \cos\theta \frac{\partial}{\partial\varphi} \Omega \delta_{\Omega',\Omega} \tag{6.46}$$

where we introduced the following matrices (same for Λ and Ω, for brevity denoted here by general quantum number *K*)

$$U^{Jp}_{KK'} = \frac{1}{2}(\lambda_+(J,K)\lambda_+(J,K+1)\delta_{K',K+2}$$
$$+\lambda_-(J,K)\lambda_-(J,K-1)\delta_{K',K-2} + (-1)^{J+K+p}\lambda_-(J,K)\lambda_-(J,K-1)\delta_{K',2-K}) \tag{6.47}$$

$$W^{Jp}_{KK'} = \frac{1}{2}(\lambda_+(J,K)\delta_{K',K+1} - \lambda_-(J,K)\delta_{K',K-1} + (-1)^{J+K+p}\lambda_-(J,K)\delta_{K',1-K}) \tag{6.48}$$

Here $\hat{J}_x$ and $\hat{J}_y$ were represented via operators $\hat{J}_+$ and $\hat{J}_-$

$$\hat{J}_x = (J_+ + J_-)/2, \quad \hat{J}_y = (J_- - J_+)/(2i)\,. \tag{6.49}$$

with eigenvalues depending on J and K as follows:

$$\hat{J}_\pm D^J_{KM} = \lambda_\pm(J,K)\hbar^2 D^J_{K\pm1M} \tag{6.50}$$

$$\lambda_\pm(J,K) = \left[(J \pm K + 1)(J \mp K)\right]^{1/2}. \tag{6.51}$$

In Eqs. (6.41)-(6.49) the Kronecker delta $\delta_{K',K}$ means that corresponding term will appear only in the diagonal block of rovibrational Hamiltonian. In similar fashion, $\delta_{K',K\pm1}$ in expression for $W^{Jp}_{KK'}$ causes first sub-diagonal block to be nonzero. Finally, $U^{Jp}_{KK'}$ appears on second sub-diagonal of the Hamiltonian matrix, and also contributes to the block $K = K' = 1$. As a consequence, symmetric, asymmetric and Coriolis terms contribute to the different blocks of the Hamiltonian matrix and the way it happens depends heavily on axis choice, is it lying in molecule plane or is perpendicular to it.

Figure 6.15 demonstrates Hamiltonian matrix structure depending on the axes orientation for prolate symmetric top. The advantage of z lying in the plane (panel a) is seen right away: the symmetric term contributes solely to diagonal, Coriolis term solely to first sub-diagonals, while asymmetric term to second sub-diagonals, with exception of $K = K' = 1$ block on diagonal. Such matrix structure provides the most straightforward way to decouple different values of Λ: after neglecting both Coriolis and asymmetric terms (both at the same time, as was mentioned by Pack and Parker[60]) the matrix is decomposed into $J + 1$ independent blocks (J for parity $p = -1$) which could be diagonalized independently. This is exactly what we implemented in our method, presented in Chapter 3: the vibrational spectrum was computed separately for each pair of (J, K) with rotational potential added in adiabatic way in the form of Eq. (6.41).

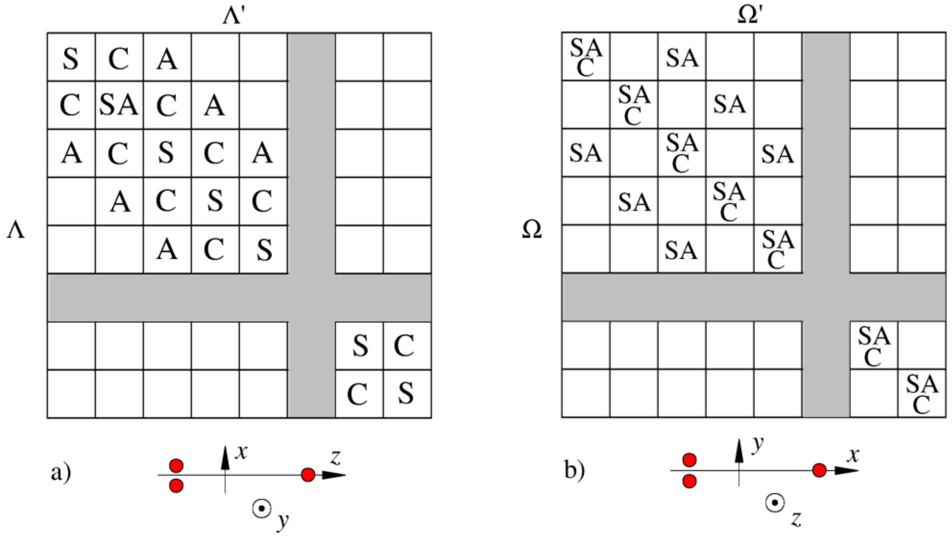

Figure 6.15. Matrix structure of rovibrational Hamiltonian for prolate symmetric top: a) the z axis lying in molecule plane, b) the z axis is perpendicular to the plane. “S” stands for the contribution of symmetric rotational term, “A” stands for the contribution of asymmetric rotational term, while “C” stands for Coriolis contribution. Good quantum numbers Λ and Ω, which are projections of total angular momentum, label matrix blocks.

The values on second sub-diagonal are much smaller for z in plane, compared to the case of z perpendicular to the plane, because $(A - B) / 2 \cdot U^p < (C - A) / 2 \cdot U^p$ due to $A \sim B < C$ for prolate symmetric top. Thus, neglecting second sub-diagonal causes less error for z in plane. When we look at the right panel of Figure 6.15, where the z axis is perpendicular to the molecule plane, we will see that symmetric and asymmetric contributions are mixed, and their separation is not as trivial as on the left panel of the figure. One can see this disadvantage right in Eqs. (6.44) and (6.45): both rotational terms contain $\delta_{\Omega',\Omega}$ and $U^{Jp}_{\Omega\Omega'}$ which result in mixed contributions into both diagonal and second sub-diagonal blocks. One advantage is that the Coriolis term contributes to the diagonal blocks, which means that when all Ω are decoupled, it can be included exactly.

6.5.3. Oblate symmetric top

When two rotational constant are nearly equal, i.e. $A \sim C$ and both are larger than third rotational constant, $\tilde{A} = (A + C) / 2 > B$ then oblate symmetric top approximation can be applied. Example is a triatomic molecule with equilateral equilibrium configuration, such as H_3^+, and three-body dissociation of it (breathing motion). In terms of moments of inertia

$$I_x = I_z < I_y \text{ (} z \text{ in plane)} \tag{6.52}$$

$$I_x = I_y < I_z \text{ (} z \perp \text{ plane)} \tag{6.53}$$

Again, the rotational operator could be split into two terms, symmetric $\hat{V}_{sym}$ and asymmetric $\hat{V}_{asym}$. For z in plane:

$$\hat{V}_{sym} = \tilde{A}\hat{J}^2 + (B - \tilde{A})\hat{J}_y^2, \tag{6.54}$$

$$\hat{V}_{asym} = \frac{C - A}{2}(\hat{J}_z^2 - \hat{J}_x^2)\,. \tag{6.55}$$

For $z \perp$ plane:

$$\hat{V}_{sym} = \tilde{A}\hat{J}^2 + (B - \tilde{A})\hat{J}_z^2, \tag{6.56}$$

$$\hat{V}_{asym} = \frac{C - A}{2}(\hat{J}_x^2 - \hat{J}_y^2)\,. \tag{6.57}$$

Integration of these operators and Coriolis term with rovibrational functions in the form of Eq. (6.29) gives the following matrix elements. For *z* in plane (vibrational factor is omitted):

$$V_{sym} = \tilde{A}\hbar^2 J(J+1)\delta_{\Lambda',\Lambda} + (B-\tilde{A})\hbar^2\left[\frac{J(J+1)-\Lambda^2}{2}\delta_{\Lambda',\Lambda} - \frac{U^{Jp}_{\Lambda\Lambda'}}{2}\right], \qquad (6.58)$$

$$V_{asym} = \frac{C-A}{2}\hbar^2\left[-\left(\frac{J(J+1)-\Lambda^2}{2} - \Lambda^2\right)\delta_{\Lambda',\Lambda} - \frac{U^{Jp}_{\Lambda\Lambda'}}{2}\right], \qquad (6.59)$$

$$T_{cor} = 4B\hbar^2 \cos\theta \frac{\partial}{\partial\varphi} W^{Jp}_{\Lambda\Lambda'}, \qquad (6.60)$$

For *z* ⊥ plane:

$$V_{sym} = \left[\tilde{A}J(J+1) + (B-\tilde{A})\Omega^2\right]\hbar^2\delta_{\Omega',\Omega}, \qquad (6.61)$$

$$V_{asym} = \frac{C-A}{2}\hbar^2 U^{Jp}_{\Omega\Omega'}, \qquad (6.62)$$

$$T_{cor} = 4B\hbar^2 \cos\theta \frac{\partial}{\partial\varphi}\Omega\delta_{\Omega',\Omega}, \qquad (6.63)$$

Figure 6.16 shows the structure of Hamiltonian matrix for the case of oblate symmetric top. The situation is completely opposite to prolate symmetric top: now *z* ⊥ plane results in simple matrix structure, where decoupling can be easily achieved by symmetric top approximation (neglecting the off-diagonal blocks), and, importantly, there is no need to neglect Coriolis coupling. It does not interfere with block structure of the matrix, since appears in the diagonal blocks only. Another advantage of *z*, perpendicular to molecule plane, is that for molecules, which equilibrium configuration is equilateral, for example H_3^+, $\theta = 0$ and $A = C$, so they are automatically symmetric tops and all off-diagonal blocks are zero. For such molecules symmetric top approximation coincides with exact solution. If equilibrium configuration is not equilateral, the *z* axis ⊥ plane is still a good choice: it allows to incorporate Coriolis term exactly, even when all Ω are decoupled. The case of the *z* axis lying in the plane causes mixing of symmetric and asymmetric terms and keeping only diagonal block is not a valid symmetric top approximation anymore.

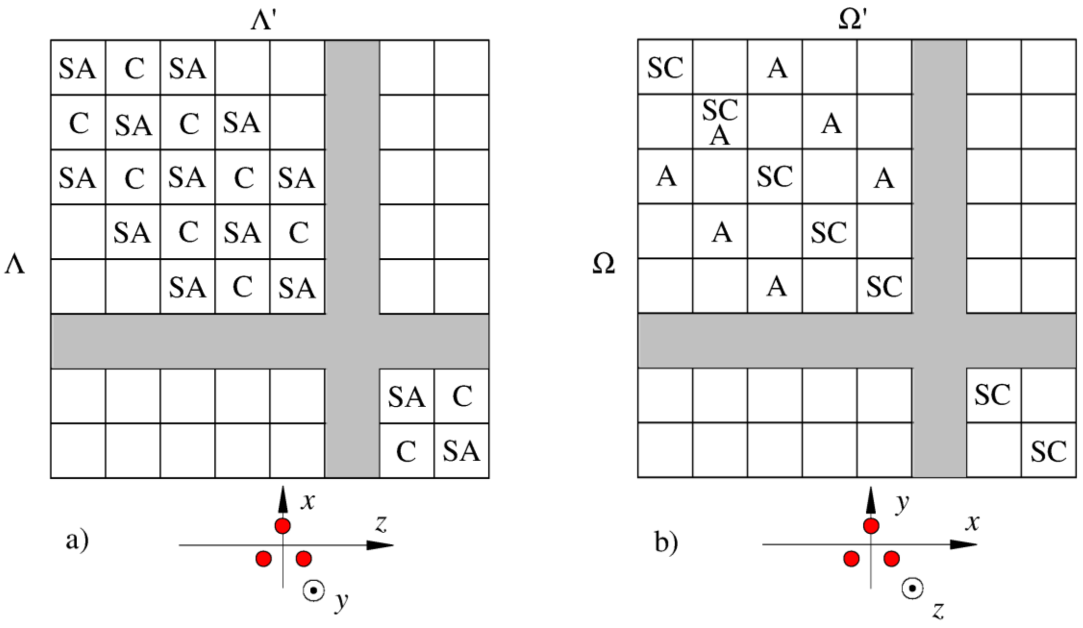

Figure 6.16. Matrix structure of rovibrational Hamiltonian for oblate symmetric top. The meaning of the labels is the same as in Figure 6.15.

6.5.4. Matrix elements and matrix structure

In previous sections, matrix elements for rotational motion were derived with vibrational contribution omitted for transparency. In this section, the complete expressions for matrix elements and complete matrix structure are given, with vibration included. The complete ro-vibrational Hamiltonian operator $\hat{H}$ is split into four components:

$$\hat{H} = \hat{T}_{\rho} + \hat{H}_{a} + \hat{T}_{asym} + \hat{T}_{cor}\,, \tag{6.64}$$

$$\hat{H}_{a} = \hat{T}_{\theta\varphi} + \hat{T}_{sym} + V_{ext} + V_{pot}\,, \tag{6.65}$$

$$\hat{H}_{a}\Lambda^{n}_{JKm}(\theta,\varphi) = \varepsilon^{n}_{JKm}\Lambda^{n}_{JKm}(\theta,\varphi) \tag{6.66}$$

The first operator is kinetic energy operator for hyperradius $\hat{T}_{\rho}$, the second is an operator for two-dimensional angular part $\hat{H}_{a}$, and the last two are asymmetric $\hat{T}_{asym}$ and Coriolis $\hat{T}_{cor}$ terms. The contributions to matrix elements from these four terms, in the case of the *z* axis in the molecular plane ($K = \Lambda$), are as follows:

$$(\hat{T}_{\rho})_{Knm,K'n'm'} = \delta_{KK'} O^{JK}_{nm,n'm'} (\hat{T}_{\rho})_{n,n'}\,, \tag{6.67}$$

$$(\hat{H}_{a})_{Knm,K'n'm'} = \delta_{KK'}\delta_{nn'}\delta_{mm'}\varepsilon^{n}_{JKm}\,, \tag{6.68}$$

$$(\hat{T}_{asym})_{Knm,K'n'm'} = U^{Jp}_{KK'}\delta_{nn'}\left\langle \Lambda^{n}_{JKm} \left| \frac{A_n - B_n}{2} \right| \Lambda^{n}_{JK'm'} \right\rangle \hbar^{2}\,, \tag{6.69}$$

$$(\hat{T}_{cor})_{Knm,K'n'm'} = W^{Jp}_{KK'}\delta_{nn'}\left\langle \Lambda^{n}_{JKm} \left| 4B_n \cos\theta \frac{\partial}{\partial\varphi} \right| \Lambda^{n}_{JK'm'} \right\rangle \hbar^{2}\,. \tag{6.70}$$

Here, matrix *O* is an overlap matrix between two-dimensional eigenvectors Λ^{n}_{JKm} computed for given *J* and *K*, ε^{n}_{JKm} are two-dimensional energies, matrices *U* and *W* are given by Eqs. (6.47) and (6.48), whereas rotational constants A_n and B_n are computed at fixed hyperradius ρ_n.

One can see that indices *K* and *n* are independent, therefore there are at least two ways to construct Hamiltonian matrix, depending on the order of these indices, see Figure 6.17. One way is to have *K* as an outer index and *n* as an inner index. Then, large blocks in the matrix are labeled with index *K*, while small blocks within given large block are labeled with *n*. Rows and columns of a small block are labeled with *m*. Another way to design the matrix is to use index *n* for large blocks and *K* for small blocks. Obviously, both ways result in the same matrix size, however, the first case is more preferable, because it provides a straightforward way for truncation at some particular $K = K_{\max}$. In addition, the large blocks on diagonal are the same matrices that were constructed and used in the uncoupled approach, Chapter 5, so transition to coupled treatment should be easier in this case. Also, all non-zero large blocks are located on diagonal and on first two sub-diagonals, whereas in case with n as an outer index none of large blocks vanish. One can take advantage of such specific matrix structure when solving efficiently for eigenvalues and eigenvectors. Similar analysis can be applied to the z axis perpendicular to the molecular plane.

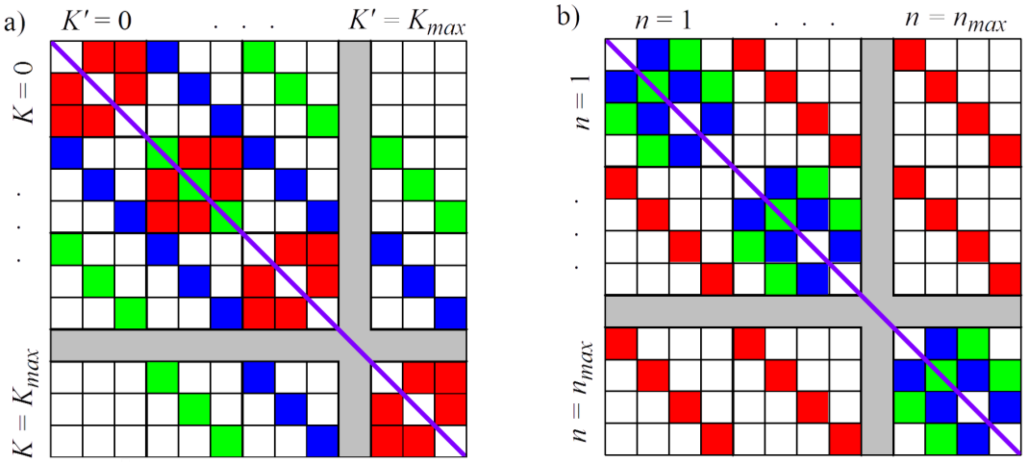

Figure 6.17. Ro-vibration matrix structure where outer index is a) projection K of total angular momentum or b) hyperradius slice number n. Colored blocks represent contributions from: kinetic energy operator T_ρ (red), asymmetric rotational term $\hat{T}_{asym}$(green) and Coriolis term $\hat{T}_{cor}$(blue). Kinetic energy operator T_ρ and eigenvalues of two-dimensional angular Hamiltonian $\hat{H}_a$ contribute to diagonal (magenta line).

6.5.5. Notes on application to ozone

As was mention earlier, the equilibrium configuration of ozone is quite close to the prolate symmetric top. Consequently, to include rotational-vibrational coupling in the Hamiltonian, one can orient the z axis in any of two ways discussed in Section 6.5.1 and construct matrix similar to those in Figure 6.15. In principle, any of four ways discussed in previous sections 6.5.2 and 6.5.3 should work if one does not apply approximations. However, when solution of such huge matrix is not affordable (which is the case), one can solve it approximately, neglecting off-diagonal blocks in Hamiltonian. This will give a smaller error when z is in plane, because then small symmetric term is located solely in diagonal blocks and is not mixed with asymmetric term, as in $z \perp$ plane. Then, eigenvalue decomposition could done separately for each diagonal block.

The exact calculations (including all terms) still may be affordable if two following properties are employed. First of all, if one looks at the matrix structure in Figure 6.15b, one can notice, that even blocks are coupled only with even blocks, while odd with odd, which is also clear from Eqs. (6.44), (6.45) and (6.47). This means that when $z \perp$ plane, then the matrix can be reorganized into two matrices of twice smaller size, one for even values of Ω and another for odd, reducing computational effort in eigenvalue decomposition.

Secondly, for ozone the number of contributing Λ is not large. As was reported in Section 5.3.1, the most contribution to the recombination comes from $\Lambda < 7$, while $J < 38$. One can expect, that for the case of $z \perp$ plane calculations also will require small values of Ω (and separately odd and even values). Taking into account both these facts, incorporation of nonadiabatic couplings might be feasible.

Chapter 7. Conclusion and further research directions

The aim of this dissertation was to develop an accurate model of ozone recombination reaction ($O_2 + O \rightarrow O_3$) and to study anomalous isotope effects in ozone. The modeling of ozone recombination included three steps: calculation of scattering resonances in ozone (energies and lifetimes), the calculation of their stabilization rate coefficients (energy transfer) and combination of those two in the kinetic model for recombination. All steps required the development of new theories and numerically efficient codes.

The largest and most sophisticated part of this work was the calculation of scattering resonances, particular their energies and lifetimes. It was necessary to understand and employ a special kind of internal vibrational coordinate system, APH coordinates (Chapter 2) and application of several techniques and approximations to make such calculation affordable: optimal grid, sequential diagonalization-truncation, complex absorbing potential (Chapter 3) and angular momentum decoupling (Chapter 6). The approach, tested on $J = 0$, allowed to get a detailed information about the upper bound vibrational states close to dissociation threshold, that become scattering resonances for $J > 0$.

The stabilization model within MQCT was reviewed and a numerically efficient frozen-rotor approximation was developed (Chapter 4). This approximation eliminated the artificial transitions (present in the earlier version of MQCT) at the pre- and post-collisional stages, and allowed to reduce the computational cost of scattering calculations by the factor of four. The resultant cross sections are within a factor of 2 to 3 of the accurate values, which may be acceptable for some applications.

Incorporation of lifetimes and energies of scattering resonances into the kinetics allowed to compute the rate coefficients for recombination through the energy-transfer mechanism (Chapter 5). The absolute value of the rate coefficient, together with its temperature and pressure dependences, appeared to be in very good agreement with the experiment. Interestingly, the total recombination rate coefficient was reproduced after the experimentally-estimated contribution of chaperon mechanism was added. Prior to this work, there were only two papers where the rate coefficient was predicted theoretically for the ozone forming reaction, but it was obtained using simpler models.

Then, the method was extended to include three covalent wells, since the treatment of isotopically substituted ozone isotopologues, for example $^{50}O_3$ and $^{52}O_3$, within only one covalent well will be less accurate and not entirely correct. The three-fold symmetry of unsubstituted isotopologue, $^{48}O_3$, is lost in single and double substituted isotopologues. The isotope effects were then studied on a subset of the rotational states and were found to be in the right direction and of the right order of magnitude (Chapter 6). The detailed analysis demonstrated confidently that the resonance width represent the origin of ΔZPE-effect in ozone. The same is true for a weaker η-effect, but one has to keep in mind that it is more sensitive to the accuracy of calculations than ΔZPE-effect, due to smaller magnitude, 20% (η-effect) vs. 60% (ΔZPE-effect).

Building upon this work, we can now undertake the massive calculations, where all rotational expiation will be included. Nevertheless, there are several improvements to this methodology. The symmetric top approximation could appear to be not sufficiently accurate, because the magnitude of the asymmetric rotational term, which was excluded, may affect computed isotope effects. The stabilization also could be improved. It is now obvious, that highly excited rovibrational states, delocalized over the van-der-Waals region, also has to be include in the stabilization study.

In addition, there is a singularity in the Hamiltonian operator for $K = 0$. So far it affected computed rovibrational spectra slightly, but it would be better to apply some technique to avoid at all. Also, Delves coordinate system may be used for description of the wave function in the asymptotic regions, where $\rho \to \infty$. This is an improvement, which may reduce basis sizes and increase accuracy within the same numerical effort.

Overall, the methodology, developed and presented in this dissertation, is universal and could be applied, as a whole or its various components, to many other molecules or processes, where resonances-based mechanism of reaction is possible. For example, to sulfur chemistry, where isotope effects are also observed. But, the method is not restricted to three vibrational degrees of freedom. The underling APH coordinate system is based on Jacobi coordinates, which can be defined for any number of atoms, whereas the sequential diagonalization-truncation is expected to shine with a full power on the systems with larger number of degrees of freedom. Taking into account the growth of computer performance, application of this methodology to such recombination reactions as $S_2 + S_2 \to S_4$ and $S_4 + S_4 \to S_8$ may be affordable in the future.

BIBLIOGRAPHY

(1) Milon, A.; Bulliard, J. L.; Vuilleumier, L.; Danuser, B.; Vernez, D. Estimating the Contribution of Occupational Solar Ultraviolet Exposure to Skin Cancer. *Br. J. Dermatol.* **2014**, *170* (1), 157–164.

(2) Dobson, R. Ozone Depletion Will Bring Big Rise in Number of Cataracts. *BMJ Br. Med. J.* **2005**, *331* (7528), 1292.

(3) Ha, S.-Y.; Joo, H.-M.; Kang, S.-H.; Ahn, I.-Y.; Shin, K.-H. Effect of Ultraviolet Irradiation on the Production and Composition of Fatty Acids in Plankton in a Sub-Antarctic Environment. *J. Oceanogr.* **2014**, *70* (1), 1–10.

(4) Regaudie-de-Gioux, A.; Agustí, S.; Duarte, C. M. UV Sensitivity of Planktonic Net Community Production in Ocean Surface Waters. *J. Geophys. Res. Biogeosciences* **2014**, *119* (5), 929–936.

(5) Mauersberger, K. Measurement of Heavy Ozone in the Stratosphere. *Geophys. Res. Lett.* **1981**, *8* (8), 935–937.

(6) Thiemens, M. H. Nonmass-Dependent Isotopic Fractionation Processes: Mechanisms and Recent Observations in Terrestrial and Extraterrestrial Environments. *Treatise on Geochemistry* **2003**, *4–9*, 1–24.

(7) Thiemens, M. H. History and Applications of Mass-Independent Isotope Effects. *Annu. Rev. Earth Planet. Sci.* **2006**, *34* (1), 217–262.

(8) Thiemens, M. H.; Chakraborty, S.; Dominguez, G. The Physical Chemistry of Mass-Independent Isotope Effects and Their Observation in Nature. *Annu. Rev. Phys. Chem.* **2012**, *63* (1), 155–177.

(9) Thiemens, M. H.; Heidenreich, J. E. The Mass-Independent Fractionation of Oxygen: A Novel Isotope Effect and Its Possible Cosmochemical Implications. *Science* **1983**, *219* (4588), 1073–1075.

(10) Ono, S. Multiple-Sulphur Isotope Biosignatures. *Space Sci. Rev.* **2008**, *135* (1–4), 203–220.

(11) Morton, J.; Barnes, J.; Schueler, B.; Mauersberger, K. Laboratory Studies of Heavy Ozone. *J. Geophys. Res.* **1990**, *95* (D1), 901.

(12) Heidenreich, J. E.; Thiemens, M. H. A Non-mass-dependent Oxygen Isotope Effect in the Production of Ozone from Molecular Oxygen: The Role of Molecular Symmetry in Isotope Chemistry. *J. Chem. Phys.* **1986**, *84* (4), 2129–2136.

(13) Guenther, J.; Krankowsky, D.; Mauersberger, K. Third-Body Dependence of Rate Coefficients for Ozone Formation in Mixtures. *Chem. Phys. Lett.* **2000**, *324* (1–3),

31–36.

(14) Thiemens, M. H. Mass-Independent Isotope Effects in Planetary Atmospheres and the Early Solar System. *Science* **1999**, *283* (5400), 341–345.

(15) Mauersberger, K.; Erbacher, B.; Krankowsky, D.; Guenther, J.; Nickel, R. Ozone Isotope Enrichment: Isotopomer-Specific Rate Ozone Isotope Enrichment: Isotopomer-Specific Rate Coefficients. *Science* **1999**, *283* (5400), 370–372.

(16) Janssen, C.; Guenther, J.; Mauersberger, K.; Krankowsky, D. Kinetic Origin of the Ozone Isotope Effect: A Critical Analysis of Enrichments and Rate Coefficients. *Phys. Chem. Chem. Phys.* **2001**, *3* (21), 4718−4721.

(17) Krankowsky, D.; Mauersberger, K. Heavy Ozone-A Difficult Puzzle to Solve. *Science* **1996**, *274* (5291), 1324–1325.

(18) Anderson, S. M.; Hülsebusch, D.; Mauersberger, K. Surprising Rate Coefficients for Four Isotopic Variants of O+O2+M. *J. Chem. Phys.* **1997**, *107* (14), 5385–5392.

(19) Janssen, C.; Guenther, J.; Krankowsky, D.; Mauersberger, K. Relative Formation Rates of 50O3 and 52O3 in 16O–18O Mixtures. *J. Chem. Phys.* **1999**, *111* (16), 7179–7182.

(20) Gellene, G. I. An Explanation for Symmetry-Induced Isotopic Fractionation in Ozone. *Science* **1996**, *274* (5291), 1344–1346.

(21) Gao, Y. Q.; Marcus, R. A. Strange and Unconventional Isotope Effects in Ozone Formation. *Science* **2001**, *293* (5528), 259–263.

(22) Gao, Y. Q.; Marcus, R. A. On the Theory of the Strange and Unconventional Isotopic Effects in Ozone Formation. *J. Chem. Phys.* **2002**, *116* (1), 137–154.

(23) Gao, Y. Q.; Chen, W.-C.; Marcus, R. A. A Theoretical Study of Ozone Isotopic Effects Using a Modified *Ab Initio* Potential Energy Surface. *J. Chem. Phys.* **2002**, *117* (4), 1536–1543.

(24) Babikov, D.; Kendrick, B. K.; Walker, R. B.; Pack, R. T.; Fleurat-Lesard, P.; Schinke, R. Metastable States of Ozone Calculated on an Accurate Potential Energy Surface. *J. Chem. Phys.* **2003**, *118* (14), 6298–6308.

(25) Babikov, D.; Kendrick, B. K.; Walker, R. B.; Schinke, R.; Pack, R. T. Quantum Origin of an Anomalous Isotope Effect in Ozone Formation. *Chem. Phys. Lett.* **2003**, *372* (5–6), 686–691.

(26) Babikov, D.; Kendrick, B. K.; Walker, R. B.; Pack, R. T.; Fleurat-Lesard, P.; Schinke, R. Formation of Ozone: Metastable States and Anomalous Isotope Effect. *J. Chem. Phys.* **2003**, *119* (5), 2577–2589.

(27) Grebenshchikov, S. Y.; Schinke, R. Towards Quantum Mechanical Description of the Unconventional Mass-Dependent Isotope Effect in Ozone: Resonance Recombination in the Strong Collision Approximation. *J. Chem. Phys.* **2009**, *131* (18), 181103.

(28) Vetoshkin, E.; Babikov, D. Semiclassical Wave Packet Study of Ozone Forming Reaction. *J. Chem. Phys.* **2006**, *125* (2), 24302.

(29) Vetoshkin, E.; Babikov, D. Semiclassical Wave Packet Treatment of Scattering Resonances: Application to the Delta Zero-Point Energy Effect in Recombination Reactions. *Phys. Rev. Lett.* **2007**, *99* (13), 138301.

(30) Vetoshkin, E.; Babikov, D. Semiclassical Wave Packet Study of Anomalous Isotope Effect in Ozone Formation. *J. Chem. Phys.* **2007**, *127* (15), 154312.

(31) Schinke, R.; Fleurat-Lessard, P.; Grebenshchikov, S. Y. Isotope Dependence of the Lifetime of Ozone Complexes Formed in O + O 2 Collisions. *Phys. Chem. Chem. Phys.* **2003**, *5* (10), 1966–1969.

(32) Schinke, R.; Fleurat-Lessard, P. The Effect of Zero-Point Energy Differences on the Isotope Dependence of the Formation of Ozone: A Classical Trajectory Study. *J. Chem. Phys.* **2005**, *122* (9), 94317.

(33) Babikov, D.; Walker, R. B.; Pack, R. T. A Quantum Symmetry Preserving Semiclassical Method. *J. Chem. Phys.* **2002**, *117* (19), 8613–8622.

(34) Pack, R. T.; Walker, R. B. Some Symmetry-Induced Isotope Effects in the Kinetics of Recombination Reactions. *J. Chem. Phys.* **2004**, *121* (2), 800–812.

(35) Ivanov, M. V.; Babikov, D. Mixed Quantum-Classical Theory for the Collisional Energy Transfer and the Rovibrational Energy Flow: Application to Ozone Stabilization. *J. Chem. Phys.* **2011**, *134* (14), 144107.

(36) Hathorn, B. C.; Marcus, R. A. An Intramolecular Theory of the Mass-Independent Isotope Effect for Ozone. I. *J. Chem. Phys.* **1999**, *111* (9), 4087–4100.

(37) Hathorn, B. C.; Marcus, R. A. An Intramolecular Theory of the Mass-Independent Isotope Effect for Ozone. II. Numerical Implementation at Low Pressures Using a Loose Transition State. *J. Chem. Phys.* **2000**, *113* (21), 9497.

(38) Kryvohuz, M.; Marcus, R. A. Coriolis Coupling as a Source of Non-RRKM Effects in Ozone Molecule: Lifetime Statistics of Vibrationally Excited Ozone Molecules. *J. Chem. Phys.* **2010**, *132* (22), 224305.

(39) Charlo, D.; Clary, D. C. Quantum-Mechanical Calculations on Termolecular Association Reactions XY+Z+M→XYZ+M: Application to Ozone Formation. *J. Chem. Phys.* **2002**, *117* (4), 1660–1672.

(40) Charlo, D.; Clary, D. C. Quantum-Mechanical Calculations on Pressure and Temperature Dependence of Three-Body Recombination Reactions: Application to Ozone Formation Rates. *J. Chem. Phys.* **2004**, *120* (6), 2700.

(41) Xie, T.; Bowman, J. M. Quantum Inelastic Scattering Study of Isotope Effects in Ozone Stabilization Dynamics. *Chem. Phys. Lett.* **2005**, *412* (1–3), 131–134.

(42) Ivanov, M. V.; Schinke, R. Vibrational Energy Transfer in Ar–O $_3$ Collisions: Comparison of Rotational Sudden, Breathing Sphere, and Classical Calculations. *Mol. Phys.* **2010**, *108* (3–4), 259–268.

(43) Ivanov, M. V.; Babikov, D. Collisional Stabilization of van Der Waals States of Ozone. *J. Chem. Phys.* **2011**, *134* (17), 174308.

(44) Ivanov, M. V.; Babikov, D. Efficient Quantum-Classical Method for Computing Thermal Rate Constant of Recombination: Application to Ozone Formation. *J. Chem. Phys.* **2012**, *136* (18), 184304.

(45) Ivanov, M. V.; Babikov, D. Forward–backward Propagation in the Mixed Quantum–classical Theory for the Collisional Energy Transfer. *Chem. Phys. Lett.* **2012**, *535*, 173–176.

(46) Jiang, L.; Babikov, D. A Reduced Dimensionality Model of Ozone: Semiclassical Treatment of van Der Waals States. *Chem. Phys. Lett.* **2009**, *474* (4–6), 273–277.

(47) Ivanov, M. V; Babikov, D. On Molecular Origin of Mass-Independent Fractionation of Oxygen Isotopes in the Ozone Forming Recombination Reaction. *Proc. Natl. Acad. Sci. U. S. A.* **2013**, *110* (44), 17708–17713.

(48) Babikov, D.; Mozhayskiy, V. A.; Krylov, A. I. The Photoelectron Spectrum of Elusive Cyclic-N3 and Characterization of the Potential Energy Surface and Vibrational States of the Ion. *J. Chem. Phys.* **2006**, *125* (8), 84306.

(49) Quéméner, G.; Balakrishnan, N.; Kendrick, B. K. Formation of Molecular Oxygen in Ultracold O+OH Collisions. *Phys. Rev. A - At. Mol. Opt. Phys.* **2009**, *79* (2), 22703.

(50) Quéméner, G.; Kendrick, B. K.; Balakrishnan, N. Quantum Dynamics of the H+O2→O+OH Reaction. *J. Chem. Phys.* **2010**, *132* (1), 14302.

(51) Lee, H. S.; Light, J. C. Vibrational Energy Levels of Ozone up to Dissociation Revisited. *J. Chem. Phys.* **2004**, *120* (13), 5859–5862.

(52) Babikov, D. Entrance Channel Localized States in Ozone: Possible Application to Helium Nanodroplet Isolation Spectroscopy. *J. Chem. Phys.* **2003**, *119* (13), 6554.

(53) Kokoouline, V.; Greene, C. H. Unified Theoretical Treatment of Dissociative Recombination of D3h Triatomic Ions: Application to H3+ and D3+. *Phys. Rev. A*

2003, *68* (1), 12703.

(54) Douguet, N.; Kokoouline, V.; Greene, C. H. Theoretical Rate of Dissociative Recombination of HCO+ and DCO+ Ions. *Phys. Rev. A - At. Mol. Opt. Phys.* **2008**, *77* (6), 64703.

(55) Lara, M.; Aguado, A.; Paniagua, M.; Roncero, O. State-to-State Reaction Probabilities Using Bond Coordinates: Application to the Li+HF(v,J) Collision. *J. Chem. Phys.* **2000**, *113* (5), 1781.

(56) Katz, G.; Yamashita, K.; Zeiri, Y.; Kosloff, R. The Fourier Method for Tri-Atomic Systems in the Search for the Optimal Coordinate System. *J. Chem. Phys.* **2002**, *116* (11), 4403.

(57) Semenov, A.; Babikov, D. Mixed Quantum/classical Theory of Rotationally and Vibrationally Inelastic Scattering in Space-Fixed and Body-Fixed Reference Frames. *J. Chem. Phys.* **2013**, *139* (17), 174108.

(58) Sun, Z.; Lin, X.; Lee, S.-Y.; Zhang, D. H. A Reactant-Coordinate-Based Time-Dependent Wave Packet Method for Triatomic State-to-State Reaction Dynamics: Application to the H + O2 Reaction. *J. Phys. Chem. A* **2009**, *113* (16), 4145–4154.

(59) Pack, R. T. Coordinates for an Optimum CS Approximation in Reactive Scattering. *Chem. Phys. Lett.* **1984**, *108*, 333.

(60) Pack, R. T.; Parker, G. A. Quantum Reactive Scattering in Three Dimensions Using Hyperspherical (APH) Coordinates. Theory. *J. Chem. Phys.* **1987**, *87* (7), 3888.

(61) Crawford, J.; Parker, G. A. State-to-State Three-Atom Time-Dependent Reactive Scattering in Hyperspherical Coordinates. *J. Chem. Phys.* **2013**, *138* (5), 54313.

(62) Babikov, D.; Kendrick, B. K. The Infrared Spectrum of Cyclic-N3: Theoretical Prediction. *J. Chem. Phys.* **2010**, *133* (17), 174310.

(63) Kokoouline, V.; Greene, C. H. Photofragmentation of the H3 Molecule, Including Jahn-Teller Coupling Effects. *Phys. Rev. A - At. Mol. Opt. Phys.* **2004**, *69* (3), 032711–1.

(64) Márquez-Mijares, M.; Pérez de Tudela, R.; González-Lezana, T.; Roncero, O.; Miret-Artés, S.; Delgado-Barrio, G.; Villarreal, P.; Baccarelli, I.; Gianturco, F. a.; Rubayo-Soneira, J. A Theoretical Investigation on the Spectrum of the Ar Trimer for High Rotational Excitations. *J. Chem. Phys.* **2009**, *130* (15), 154301.

(65) Suno, H. Hyperspherical Slow Variable Discretization Method for Weakly Bound Triatomic Molecules. *J. Chem. Phys.* **2011**, *134* (6), 64318.

(66) Suno, H. A Theoretical Study of Ne3 Using Hyperspherical Coordinates and a

Slow Variable Discretization Approach. *J. Chem. Phys.* **2011**, *135* (13), 134312.

(67) Ayouz, M.; Dulieu, O.; Robert, J. Resonant States of the H3(–) Molecule and Its Isotopologues D2H– and H2D–. *J. Phys. Chem. A* **2013**, *117* (39), 9941–9949.

(68) Hennig, C.; Schmatz, S. Rotational Effects in Complex-Forming Bimolecular Substitution Reactions: A Quantum-Mechanical Approach. *J. Chem. Phys.* **2009**, *131* (22), 224303.

(69) Pradhan, G. B.; Balakrishnan, N.; Kendrick, B. K. Ultracold Collisions of O(1D) and H2: The Effects of H2 Vibrational Excitation on the Production of Vibrationally and Rotationally Excited OH. *J. Chem. Phys.* **2013**, *138* (16), 164310.

(70) Pradhan, G. B.; Juanes-Marcos, J. C.; Balakrishnan, N.; Kendrick, B. K. Chemical Reaction versus Vibrational Quenching in Low Energy Collisions of Vibrationally Excited OH with O. *J. Chem. Phys.* **2013**, *139* (19), 194305.

(71) Adhikari, S.; Varandas, A. J. C. The Coupled 3D Wave Packet Approach for Triatomic Reactive Scattering in Hyperspherical Coordinates. *Comput. Phys. Commun.* **2013**, *184* (2), 270–283.

(72) Kendrick, B. K.; Pack, R. T.; Walker, R. B.; Hayes, E. F. Hyperspherical Surface Functions for Nonzero Total Angular Momentum. I. Eckart Singularities. *J. Chem. Phys.* **1999**, *110* (14), 6673.

(73) Li, X.; Brue, D. a.; Kendrick, B. K.; Blandon, J. D.; Parker, G. A. Geometric Phase for Collinear Conical Intersections. I. Geometric Phase Angle and Vector Potentials. *J. Chem. Phys.* **2011**, *134* (6), 64108.

(74) Teplukhin, A.; Babikov, D. Interactive Tool for Visualization of Adiabatic Adjustment in APH Coordinates for Computational Studies of Vibrational Motion and Chemical Reactions. *Chem. Phys. Lett.* **2014**, *614*, 99–103.

(75) Rüegg, C. M. Math.NET Numerics https://numerics.mathdotnet.com/ (accessed Feb 1, 2017).

(76) Microsoft. .NET Framework 4.5 https://www.microsoft.com (accessed Feb 1, 2017).

(77) Teplukhin, A. APHDemo http://alextepl.com/aphdemo/ (accessed Feb 1, 2017).

(78) Born, M.; Oppenheimer, R. Zur Quantentheorie Der Molekeln. *Ann. Phys.* **1927**, *389* (20), 457–484.

(79) Wales, D. *Energy Landscapes: Applications to Clusters, Biomolecules and Glasses*; Cambridge University Press, 2003.

(80) Siebert, R.; Schinke, R.; Bittererová, M. Spectroscopy of Ozone at the Dissociation Threshold: Quantum Calculations of Bound and Resonance States on a New Global Potential Energy Surface. *Phys. Chem. Chem. Phys.* **2001**, *3* (10), 1795–1798.

(81) Demtröder, W. Rotations and Vibrations of Polyatomic Molecules. In *Molecular Physics*; Wiley-VCH Verlag GmbH: Weinheim, Germany, 2005; pp 203–236.

(82) Ayouz, M.; Babikov, D. Global Permutationally Invariant Potential Energy Surface for Ozone Forming Reaction. *J. Chem. Phys.* **2013**, *138* (16), 164311.

(83) Babikov, D.; Zhang, P.; Morokuma, K. Cyclic-N3. I. An Accurate Potential Energy Surface for the Ground Doublet Electronic State up to the Energy of the 2A2/2B1 Conical Intersection. *J. Chem. Phys.* **2004**, *121* (14), 6743–6749.

(84) Dawes, R.; Lolur, P.; Li, A.; Jiang, B.; Guo, H. Communication: An Accurate Global Potential Energy Surface for the Ground Electronic State of Ozone. *J. Chem. Phys.* **2013**, *139* (20), 201103.

(85) Ayouz, M.; Babikov, D. Improved Potential Energy Surface of Ozone Constructed Using the Fitting by Permutationally Invariant Polynomial Function. *Adv. Phys. Chem.* **2012**, *2012*, 1–9.

(86) Irikura, K. K. Experimental Vibrational Zero-Point Energies: Diatomic Molecules. *J. Phys. Chem. Ref. Data* **2007**, *36* (2), 389–397.

(87) Lolur, P.; Dawes, R. 3D Printing of Molecular Potential Energy Surface Models. *J. Chem. Educ.* **2014**, *91* (8), 1181–1184.

(88) MathWorks. MATLAB https://www.mathworks.com/ (accessed Feb 1, 2017).

(89) Teplukhin, A.; Ivanov, M.; Babikov, D. Frozen Rotor Approximation in the Mixed Quantum⁄classical Theory for Collisional Energy Transfer: Application to Ozone Stabilization. *J. Chem. Phys.* **2013**, *139* (12), 124301.

(90) Julliard, A. Wine https://www.winehq.org/ (accessed Feb 1, 2017).

(91) Wang, X.; Carter, S.; Bowman, J. M. Pruning the Hamiltonian Matrix in MULTIMODE: Test for C2H4 and Application to CH3NO2 Using a New Ab Initio Potential Energy Surface. *J. Phys. Chem. A* **2015**, *119* (47), 11632–11640.

(92) Wang, Y.; Bowman, J. M. Bend Excitation Is Predicted to Greatly Accelerate Isomerization of Trans-Hydroxymethylene to Formaldehyde in the Deep Tunneling Region. *J. Phys. Chem. Lett.* **2015**, *6* (1), 124–128.

(93) Li, J.; Carter, S.; Bowman, J. M.; Dawes, R.; Xie, D.; Guo, H. High-Level, First-Principles, Full-Dimensional Quantum Calculation of the Ro-Vibrational Spectrum of the Simplest Criegee Intermediate (CH2OO). *J. Phys. Chem. Lett.* **2014**, *5* (13),

2364–2369.

(94) Dawes, R.; Wang, X. G.; Carrington, T. CO Dimer: New Potential Energy Surface and Rovibrational Calculations. *J. Phys. Chem. A* **2013**, *117* (32), 7612–7630.

(95) Jankowski, P.; Murdachaew, G.; Bukowski, R.; Akin-Ojo, O.; Leforestier, C.; Szalewicz, K. Ab Initio Water Pair Potential with Flexible Monomers. *J. Phys. Chem. A* **2015**, *119* (12), 2940–2964.

(96) Li, Y.; Sun, Z.; Jiang, B.; Xie, D.; Dawes, R.; Guo, H. Communication: Rigorous Quantum Dynamics of O + O2 Exchange Reactions on an Ab Initio Potential Energy Surface Substantiate the Negative Temperature Dependence of Rate Coefficients. *J. Chem. Phys.* **2014**, *141* (8), 81102.

(97) Sun, Z.; Yu, D.; Xie, W.; Hou, J.; Dawes, R.; Guo, H. Kinetic Isotope Effect of the 16O + 36O2 and 18O + 32O2 Isotope Exchange Reactions: Dominant Role of Reactive Resonances Revealed by an Accurate Time-Dependent Quantum Wavepacket Study. *J. Chem. Phys.* **2015**, *142* (17), 174312.

(98) Rao, T. R.; Guillon, G.; Mahapatra, S.; Honvault, P. Huge Quantum Symmetry Effect in the O + O2 Exchange Reaction. *J. Phys. Chem. Lett.* **2015**, *6* (4), 633–636.

(99) Rajagopala Rao, T.; Guillon, G.; Mahapatra, S.; Honvault, P. Quantum Dynamics of 16O + 36O2 and 18O + 32O2 Exchange Reactions. *J. Chem. Phys.* **2015**, *142* (17), 174311.

(100) Teplukhin, A.; Babikov, D. A Full-Dimensional Model of Ozone Forming Reaction: The Absolute Value of the Recombination Rate Coefficient, Its Pressure and Temperature Dependencies. *Phys. Chem. Chem. Phys.* **2016**, *18* (28), 19194–19206.

(101) Xie, W.; Liu, L.; Sun, Z.; Guo, H.; Dawes, R. State-to-State Reaction Dynamics of 18O+32O2 Studied by a Time-Dependent Quantum Wavepacket Method. *J. Chem. Phys.* **2015**, *142* (6), 64308.

(102) Blandon, J.; Kokoouline, V. Geometrical Phase Driven Predissociation: Lifetimes of 22A’ Levels of H3. *Phys. Rev. Lett.* **2009**, *102* (14), 143002.

(103) Kendrick, B.; Pack, R. T. Geometric Phase Effects in H+O2 Scattering. I. Surface Function Solutions in the Presence of a Conical Intersection. *J. Chem. Phys.* **1996**, *104* (19), 7475.

(104) Francisco, J. S.; Lyons, J. R.; Williams, I. H. High-Level Ab Initio Studies of the Structure, Vibrational Spectra, and Energetics of S3. *J. Chem. Phys.* **2005**, *123* (5), 54302.

(105) Peterson, K. A.; Lyons, J. R.; Francisco, J. S. An Ab Initio Study of the Low-

Lying Electronic States of S3. *J. Chem. Phys.* **2006**, *125* (8), 84314-084314–084318.

(106) Ma, G. B.; Chen, R. Q.; Guo, H. Quantum Calculations of Highly Excited Vibrational Spectrum of Sulfur Dioxide. I. Eigenenergies and Assignments up to 15,000 Cm(-1). *J. Chem. Phys.* **1999**, *110* (1999), 8408–8416.

(107) Cederbaum, L. S.; Stampfuû, P.; Wenzel, W. Nonadiabatic Wave Packet Dynamics on the Coupled X E 2 B 2 Electronic States of NO 2 Based on New Ab Initio Potential. *Chem. Phys.* **2000**, *259* (2), 211–226.

(108) Huang, X.; Schwenke, D. W.; Tashkun, S. A.; Lee, T. J. An Isotopic-Independent Highly Accurate Potential Energy Surface for CO2 Isotopologues and an Initial 12C16O2 Infrared Line List An Isotopic-Independent Highly Accurate Potential Energy Surface for CO 2 Isotopologues and an Initial 12 C 16 O 2 Infrared Li. *J. Chem. Phys.* **2012**, *136*, 124311.

(109) Johnson, B. R. The Quantum Dynamics of Three Particles in Hyperspherical Coordinates. *J. Chem. Phys.* **1983**, *79* (4), 1916–1925.

(110) Kuppermann, A. A Useful Mapping of Triatomic Potential Energy Surfaces. *Chem. Phys. Lett.* **1975**, *32* (2), 374–375.

(111) Kokoouline, V.; Greene, C. H.; Esry, B. D. Mechanism for the Destruction of H+3 Ions by Electron Impact. *Nature* **2001**, *412*, 891–894.

(112) Yang, B.; Chen, W.; Poirier, B. Rovibrational Bound States of Neon Trimer: Quantum Dynamical Calculation of All Eigenstate Energy Levels and Wavefunctions. *J. Chem. Phys.* **2011**, *135* (9), 94306.

(113) Leitner, D. M.; Doll, J. D.; Whitnell, R. M. Quantum Mechanics of Small Ne, Ar, Kr, and Xe Clusters. *J. Chem. Phys.* **1991**, *94* (10), 6644.

(114) Whitnell, R. M.; Light, J. C. Efficient Pointwise Representations for Vibrational Wave Functions: Eigenfunctions of H+3. *J. Chem. Phys.* **1989**, *90* (3), 1774.

(115) Billing, G. *The Quantum Classical Theory*; Oxford University Press,: New York, 2003.

(116) Bowman, J. M. A Test of an Adiabatic Treatment of Rotation for Vibration/rotation Energies of Polyatomic Molecules. *Chem. Phys. Lett.* **1994**, *217* (1–2), 36–40.

(117) Zou, S. L.; Skokov, S.; Bowman, J. M. Adiabatic Rotation, Centrifugal Sudden, and Exact Calculations of Rotationally Mediated Fermi Resonances in HOCl. *J. Phys. Chem. A* **2001**, *105* (11), 2423–2426.

(118) Light, J. C.; Carrington, T. Discrete-Variable Representations and Their

Utilization. In *Advances in Chemical Physics*; Prigogine, I., Rice, S. A., Eds.; Advances in Chemical Physics; John Wiley & Sons, Inc.: Hoboken, NJ, USA, 2000; Vol. 114, pp 263–310.

(119) Bačić, Z.; Light, J. C. Highly Excited Vibrational Levels of "'floppy'" Triatomic Molecules: A Discrete Variable representation—Distributed Gaussian Basis Approach. *J. Chem. Phys.* **1986**, *85* (8), 4594.

(120) Bačić, Z.; Light, J. C. Accurate Localized and Delocalized Vibrational States of HCN/HNC. *J. Chem. Phys* **1987**, *86*, 3065.

(121) Light, J. C.; Bačić, Z. Adiabatic Approximation and Nonadiabatic Corrections in the Discrete Variable Representation: Highly Excited Vibrational States of Triatomic Molecules. *J. Chem. Phys.* **1987**, *87* (7), 4008–4019.

(122) Tolstikhin, O. I.; Watanabe, S.; Matsuzawa, M. `Slow' Variable Discretization: A Novel Approach for Hamiltonians Allowing Adiabatic Separation of Variables. *J. Phys. B At. Mol. Opt. Phys.* **1996**, *29* (11), L389–L395.

(123) Kokoouline, V.; Masnou-Seeuws, F. Calculation of Loosely Bound Levels for Three-Body Quantum Systems Using Hyperspherical Coordinates with a Mapping Procedure. *Phys. Rev. A - At. Mol. Opt. Phys.* **2006**, *73* (1), 12702.

(124) Kokoouline, V.; Dulieu, O.; Kosloff, R.; Masnou-Seeuws, F. Mapped Fourier Methods for Long-Range Molecules: Application to Perturbations in the Rb2(0u+) Photoassociation Spectrum. *J. Chem. Phys.* **1999**, *110* (20), 9865–9876.

(125) Borisov, A. G. Solution of the Radial Schrödinger Equation in Cylindrical and Spherical Coordinates by Mapped Fourier Transform Algorithms. *J. Chem. Phys.* **2001**, *114* (18), 7770–7777.

(126) Blandon, J.; Kokoouline, V.; Masnou-Seeuws, F. Calculation of Three-Body Resonances Using Slow-Variable Discretization Coupled with a Complex Absorbing Potential. *Phys. Rev. A* **2007**, *75* (4), 42508.

(127) Ayouz, M.; Dulieu, O.; Guérout, R.; Robert, J.; Kokoouline, V. Potential Energy and Dipole Moment Surfaces of H3− Molecule. *J. Chem. Phys.* **2010**, *132* (19), 194309.

(128) Blackford, L. S.; Choi, J.; Cleary, A.; D'Azeuedo, E.; Demmel, J.; Dhillon, I.; Dongarra, J. J.; Hammarling, S.; Henry, G.; Petitet, A.; et al. *ScaLAPACK User's Guide*; Society for Industrial and Applied Mathematics, 1997.

(129) Ndengué, S.; Dawes, R.; Wang, X.-G.; Carrington, T.; Sun, Z.; Guo, H. Calculated Vibrational States of Ozone up to Dissociation. *J. Chem. Phys.* **2016**, *144* (7), 74302.

(130) Grebenshchikov, S. Y.; Schinke, R.; Fleurat-Lessard, P.; Joyeux, M. Van Der

Waals States in Ozone and Their Influence on the Threshold Spectrum of O3(X1A1). I. Bound States. *J. Chem. Phys.* **2003**, *119* (13), 6512–6523.

(131) Siebert, R.; Fleurat-Lessard, P.; Schinke, R.; Bittererová, M.; Farantos, S. C. The Vibrational Energies of Ozone up to the Dissociation Threshold: Dynamics Calculations on an Accurate Potential Energy Surface. *J. Chem. Phys.* **2002**, *116* (22), 9749.

(132) T Pack, R.; Walker, R. B.; Kendrick, B. K. Three-Body Collision Contributions to Recombination and Collision-Induced Dissociation. II. Kinetics. *J. Chem. Phys.* **1998**, *109* (16), 6714.

(133) Pack, R. T. Space-Fixed vs Body-Fixed Axes in Atom-Diatomic Molecule Scattering. Sudden Approximations. *J. Chem. Phys.* **1974**, *60* (2), 633.

(134) Tsien, T. P. Rotationally Inelastic Molecular Scattering. Computational Tests of Some Simple Solutions of the Strong Coupling Problem. *J. Chem. Phys.* **1973**, *59* (10), 5373.

(135) Tsien, T. P.; Pack, R. T. Rotational Excitation in Molecular Collisions. Corrections to a Strong Coupling Approximation. *Chem. Phys. Lett.* **1970**, *6* (5), 400–402.

(136) Tsien, T. P.; Pack, R. . Rotational Excitation in Molecular Collisions. A Many-State Test of the Strong Coupling Approximation. *Chem. Phys. Lett.* **1971**, *8* (6), 579–581.

(137) Sizun, M.; Aguillon, F.; Sidis, V.; Zenevich, V.; Billing, G. D.; Marković, N. Theoretical Investigation of the Ar+(J) + H2 → ArH+ + H Reaction: Semiclassical Coupled Wavepacket Treatment. *Chem. Phys.* **1996**, *209* (2), 327–353.

(138) Aguillon, F.; Sidis, V.; Gauyacq, J. P. Coupled Wave Packets Study of the Dynamics of Dissociative Ion–molecule Charge Exchange. *J. Chem. Phys.* **1991**, *95* (2), 1020–1032.

(139) Billing, G. D. The Semiclassical Treatment of Molecular Roto/vibrational Energy Transfer. *Comput. Phys. Reports* **1984**, *1* (5), 239–296.

(140) Whittier, G. S.; Light, J. C. Quantum/classical Time-Dependent Self-Consistent Field Treatment of Ar+HCO Inelastic and Dissociative Scattering. *J. Chem. Phys.* **1999**, *110* (9), 4280.

(141) Babikov, D.; Aguillon, F.; Sizun, M.; Sidis, V. Fragmentation of Na 2 □ Dimer Ions in Kilo-Electron-Volt Collisions with He: A Coupled Wave-Packet Study 1. **1999**, *59* (1), 330–341.

(142) Qi, J.; Bowman, J. M. The Effect of Rotation on Resonances: Application to HCO. *J. Chem. Phys.* **1996**, *105* (22), 9884.

(143) Qi, J.; Bowman, J. M. Approximations Based on the Adiabatic Treatment of Rotation for Resonances. *J. Chem. Phys.* **1997**, *107* (23), 9960.

(144) Carter, S.; Bowman, J. M. The Adiabatic Rotation Approximation for Rovibrational Energies of Many-Mode Systems: Description and Tests of the Method. *J. Chem. Phys.* **1998**, *108* (11), 4397.

(145) Skokov, S.; Bowman, J. M. Variation of the Resonance Width of HOCl(6vOH) with Total Angular Momentum: Comparison between Ab Initio Theory and Experiment. *J. Chem. Phys.* **1999**, *110* (20), 9789–9792.

(146) Prosmiti, R.; Farantos, S. C. A Periodic Orbit Approach to the Spectroscopy and Dynamics of SO2: C1B2->X1A1. *Mol. Phys.* **1994**, *82* (6), 1213–1232.

(147) Farantos, S. C.; Lin, S. Y.; Guo, H. A Regular Isomerization Path among Chaotic Vibrational States of CH2(a˜1A1). *Chem. Phys. Lett.* **2004**, *399* (1), 260–265.

(148) Farantos, S. C.; Qu, Z. W.; Zhu, H.; Schinke, R. Reaction Paths and Elementary Bifurcations Tracks: The Diabatic 1 B 2-State of Ozone. *Int. J. Bifurc. Chaos* **2006**, *16* (7), 1913–1928.

(149) Lendvay, G.; Schatz, G. C. Choice of Gas Kinetic Rate Coefficients in the Vibrational Relaxation of Highly Excited Polyatomic Molecules. **1992**, *96* (7), 3752–3756.

(150) Lendvay, G.; Schatz, G. C. Comparison of Master Equation and Trajectory Simulation of the Relaxation of an Ensemble of Highly Vibrationally Excited Molecules. *J. Phys. Chem.* **1994**, *98* (26), 6530–6536.

(151) Oref, I.; Tardy, D. C. Energy Transfer in Highly Excited Large Polyatomic Molecules. *Chem. Rev.* **1990**, *90* (8), 1407–1445.

(152) Quack, M.; Troe, J. Unimolecular Reactions and Energy Transfer of Highly Excited Molecules. In *Gas Kinetics and Energy Transfer : Volume 2*; Ashmore, P. G., Donovan, R. J., Eds.; Royal Society of Chemistry, 1977; pp 175–238.

(153) Banks, A. J.; Clary, D. C.; Werner, H. -J. Vibrational Relaxation of N_2 by Collision with He Atoms. *J. Chem. Phys.* **1986**, *84* (7), 3788–3797.

(154) Billing, G. D.; Clary, D. C. Comparison of Semiclassical and Quantum-Mechanical Cross Sections and Rate Constants for CO2(0110) + M → CO2(000O) + M (M = He, Ne). *Chem. Phys. Lett.* **1982**, *90* (1), 27–30.

(155) Mauersberger, K.; Krankowsky, D.; Janssen, C.; Schinke, R. Assessment of the Ozone Isotope Effect. *Adv. Atom. Mol. Opt. Phys.* **2005**, *50*, 1–54.

(156) Schinke, R.; Grebenshchikov, S. Y.; Ivanov, M. V.; Fleurat-Lessard, P. Dynamical Studies of the Ozone Isotope Effect: A Status Report. *Annu. Rev. Phys. Chem.*

2006, *57* (1), 625–661.

(157) Luther, K.; Oum, K.; Troe, J. The Role of the Radical-Complex Mechanism in the Ozone Recombination/dissociation Reaction. *Phys. Chem. Chem. Phys.* **2005**, *7* (14), 2764–2770.

(158) Ivanov, M. V.; Babikov, D. On Stabilization of Scattering Resonances in Recombination Reaction That Forms Ozone. *J. Chem. Phys.* **2016**, *144* (15), 154301.

(159) Balint-Kurti, G. G.; Vibók, Á. Complex Absorbing Potentials in Time Dependent Quantum Dynamics. In *Numerical Grid Methods and Their Application to Schrödinger's Equation*; Cerjan, C., Ed.; Springer Netherlands: Dordrecht, 1993; pp 195–205.

(160) Teplukhin, A.; Babikov, D. Visualization of Potential Energy Function Using an Isoenergy Approach and 3D Prototyping. *J. Chem. Educ.* **2015**, *92* (2), 305–309.

(161) Hippler, H.; Rahn, R.; Troe, J. Temperature and Pressure Dependence of Ozone Formation Rates in the Range 1–1000 Bar and 90–370 K. *J. Chem. Phys.* **1990**, *93* (9), 6560.

(162) Lin, C. L.; Leu, M. T. Temperature and Third-Body Dependence of the Rate Constant for the Reaction O + O2 + M ? O3 + M. *Int. J. Chem. Kinet.* **1982**, *14* (4), 417–434.

(163) Ivanov, M. V.; Grebenshchikov, S. Y.; Schinke, R. Intra- and Intermolecular Energy Transfer in Highly Excited Ozone Complexes. *J. Chem. Phys.* **2004**, *120* (21), 10015–10024.

(164) Ivanov, M. V.; Schinke, R. Temperature Dependent Energy Transfer in Ar–O[sub 3] Collisions. *J. Chem. Phys.* **2005**, *122* (23), 234318.

(165) Atkinson, R.; Baulch, D. L.; Cox, R. A.; Hampson, R. F.; Kerr, J. A.; Troe, J. Evaluated Kinetic and Photochemical Data for Atmospheric Chemistry: Supplement IV. IUPAC Subcommittee on Gas Kinetic Data Evaluation for Atmospheric Chemistry. *J. Phys. Chem. Ref. Data* **1992**, *21* (6), 1125.

(166) Bunker, P. R.; Jensen, P. *The Fundamentals of Molecular Symmetry*; CRC Press: Bristol, UK, 2004.

(167) Ivanov, M. V.; Schinke, R. Recombination of Ozone via the Chaperon Mechanism. *J. Chem. Phys.* **2006**, *124* (10), 104303.

APPENDIX A

Here we show that asymptotically, as $\rho \to \infty$, solution of two-dimensional Schrödinger equation with Hamiltonian operator $\hat{h}_n$ acting on wave function $\Lambda(r, \Theta)$ can be obtained analytically. To recap, the operator $\hat{h} = \hat{T}_{\theta\varphi} + V_{ext} + V_{sym} + V_{pot}$ has four components (omitting index n):

$$\begin{aligned}
\hat{T}_{\theta\phi} &= -\frac{\hbar^2}{2\mu}\cdot\frac{4}{\rho^2}\left(\frac{\partial^2}{\partial\theta^2}+\frac{1}{\sin^2\theta}\frac{\partial^2}{\partial\phi^2}\right);\\
\hat{V}_{ext} &= -\frac{\hbar^2}{2\mu}\cdot\frac{1}{\rho^2}\left(\frac{1}{4}+\frac{4}{\sin^2 2\theta}\right);\\
V_{sym} &= \bar{A}\hbar^2 J(J+1)+(C-\bar{A})\hbar^2 K^2;
\end{aligned} \tag{A1}$$

and the potential energy surface $V_{pot} = V_{pot}(\rho, \theta, \varphi)$. To find the asymptotic form of the operator, it is convenient to transform all four components from the APH coordinates (ρ, θ, φ) to massed-scaled Jacobi coordinates (S, s, Θ) and then consider a limit $S \to \infty$. We start with the following transformation:[60]

$$\begin{aligned}
S &= \frac{\rho}{\sqrt{2}}\left(1+\sin\theta\cos\phi\right)^{1/2},\\
s &= \frac{\rho}{\sqrt{2}}\left(1-\sin\theta\cos\phi\right)^{1/2},\\
\cos\Theta &= \frac{\sin\theta\sin\phi}{\left(1-\sin^2\theta\cos^2\phi\right)^{1/2}}.
\end{aligned} \tag{A2}$$

The first component $\hat{T}_{\theta\varphi}$ transforms as follows:

$$\begin{aligned}
&\frac{4}{\rho^2}\left(\frac{\partial^2}{\partial\theta^2}+\frac{1}{\sin^2\theta}\frac{\partial^2}{\partial\phi^2}\right)=\\
&=\frac{1}{S^2+s^2}\left(s^2\frac{\partial^2}{\partial S^2}-2Ss\frac{\partial^2}{\partial S\partial s}+S^2\frac{\partial^2}{\partial s^2}\right)\\
&-\left(\frac{S^2}{S^2+s^2}+\frac{S^4-s^4}{S^4+s^4-(2Ss\sin\Theta)^2}\right)\frac{1}{S}\frac{\partial}{\partial S}\\
&-\left(\frac{s^2}{S^2+s^2}-\frac{S^4-s^4}{S^4+s^4-(2Ss\sin\Theta)^2}\right)\frac{1}{s}\frac{\partial}{\partial s}\\
&+\frac{S^2+s^2}{(Ss)^2}\frac{\partial^2}{\partial\Theta^2}-\frac{2\sin 2\Theta(S^2+s^2)}{S^4+s^4-(2Ss\sin\Theta)^2}\frac{\partial}{\partial\Theta}
\end{aligned} \tag{A3}$$

The second component $\hat{V}_{ext}$ transforms as follows:

$$\begin{aligned}
&\frac{1}{\rho^2}\left(\frac{1}{4}+\frac{4}{\sin^2 2\theta}\right)=\\
&=\frac{1}{4(S^2+s^2)}+\frac{(S^2+s^2)^3}{(2Ss\sin\Theta)^2(S^4+s^4-(2Ss\sin\Theta)^2)}.
\end{aligned} \tag{A4}$$

In the limit $S \to \infty$, many terms in these two components vanish and their sum approaches the following expression, that depends on s and Θ only:

$$\begin{aligned}
&\left(-\frac{\hbar^2}{2\mu}\right)^{-1}\lim_{S\to\infty}(T_{\theta\phi}+V_{ext})=\frac{\partial^2}{\partial s^2}+\frac{1}{s}\frac{\partial}{\partial s}+\frac{1}{s^2}\frac{\partial^2}{\partial\Theta^2}+\frac{1}{4s^2\sin^2\Theta}=\\
&=\left(\frac{\partial^2}{\partial s^2}+\frac{1}{s}\frac{\partial}{\partial s}-\frac{1}{4s^2}\right)+\frac{1}{s^2}\left(\frac{\partial^2}{\partial\Theta^2}+\frac{1}{4\sin^2\Theta}+\frac{1}{4}\right).
\end{aligned} \tag{A5}$$

A similar expression was reported by Billing.[115] Now we transform to non-scaled Jacobi coordinates that include interatomic distance r (instead of s) and the reduced mass of O_2 (instead that of O_3),

$$\begin{aligned}
&\lim_{S\to\infty}(T_{\theta\phi}+V_{ext})=\left(-\frac{\hbar^2}{2\mu_{O_2}}\right)\left(\frac{\partial^2}{\partial r^2}+\frac{1}{r}\frac{\partial}{\partial r}-\frac{1}{4r^2}\right)\\
&+\left(-\frac{\hbar^2}{2\mu_{O_2}r^2}\right)\left(\frac{\partial^2}{\partial\Theta^2}+\frac{1}{4\sin^2\Theta}+\frac{1}{4}\right)
\end{aligned} \tag{A6}$$

To simplify this part of the operator $\hat{h}$, we transform the initial wave function $\Lambda(r, \Theta)$ to a new wave function $\tilde{\Lambda}(r, \Theta)$,

$$\tilde{\Lambda}(r,\Theta) = \sqrt{\frac{r}{\sin\Theta}}\Lambda(r,\Theta)\,. \tag{A7}$$

This transformation eliminates all terms except the two second derivatives

$$\tilde{h} = -\frac{\hbar^2}{2\mu_{\mathrm{O}_2}}\frac{\partial^2}{\partial r^2} - \frac{\hbar^2}{2\mu_{\mathrm{O}_2} r^2}\frac{1}{\sin\Theta}\frac{\partial}{\partial\Theta}\sin\Theta\frac{\partial}{\partial\Theta}\,. \tag{A8}$$

Finally, we assume asymptotic form of rotational potential $V_{sym} = \hbar^2 K^2 / (2\mu_{\mathrm{O}_2} r^2 \sin^2\Theta)$, as discussed in Sec. 3.2.2, and asymptotic form of potential energy surface, which is simply a potential energy of O_2 fragment, i.e. $V_{pot} \rightarrow V_{O2}(r)$,

$$\tilde{h} = -\frac{\hbar^2}{2\mu_{\mathrm{O}_2}}\frac{\partial^2}{\partial r^2} - \frac{\hbar^2}{2\mu_{\mathrm{O}_2} r^2}\left(\frac{1}{\sin\Theta}\frac{\partial}{\partial\Theta}\sin\Theta\frac{\partial}{\partial\Theta} - \frac{K^2}{\sin^2\Theta}\right) + V_{\mathrm{O}_2}(r)\,. \tag{A9}$$

Now, we approximate the wave function as $\tilde{\Lambda}(r,\Theta) = R(r)\cdot A(\Theta)$ and note that the action of angular operator (in parenthesis) could be expressed using its eigenvalues $j\,(j + 1)$ and associated Legendre polynomials $A(\Theta) = P_j^K(\Theta)$, namely,

$$\left(-\frac{1}{\sin\Theta}\frac{\partial}{\partial\Theta}\sin\Theta\frac{\partial}{\partial\Theta} + \frac{K^2}{\sin^2\Theta}\right)P_j^K(\Theta) = j(j+1)P_j^K(\Theta), \quad j \geq K\,. \tag{A10}$$

This reduces the initial two-dimensional Schrödinger equation to a set of one-dimensional Schrödinger equations $\tilde{h}^j R_v^j(r) = \varepsilon_{v,j} R_v^j(r)$ for vibrational coordinate r and for different values of the angular momentum quantum number j of the diatomic fragment that sets up centrifugal potential of the diatomic product:

$$\tilde{h}^j = -\frac{\hbar^2}{2\mu_{\mathrm{O}_2}}\frac{\partial^2}{\partial r^2} + \frac{j(j+1)\hbar^2}{2\mu_{\mathrm{O}_2} r^2} + V_{\mathrm{O}_2}(r), \quad j \geq K\,. \tag{A11}$$

For a given value of the vibrational quantum number v (for example $v = 0$) energies $\varepsilon_{v,j}$ constitute a *non-degenerate* rotational spectrum $j\,(j + 1)$ of a rigid rotor, that starts with a quantum number $j = K$. If one neglects the effects of potential anharmonicity and centrifugal distortion, then energies $\varepsilon_{v,j}$ could be estimated as

$$\varepsilon_{v,j} \approx \hbar\omega\left(v+\tfrac{1}{2}\right)+\frac{j(j+1)\hbar^2}{2\mu r_0^2}, \quad j \geq K\,. \tag{A12}$$

In this expression, ω and r_0 are vibrational frequency and equilibrium interatomic distance of oxygen molecule, respectively. Indeed, this solution is consistent with density of points in the right most slice in Figure 3.3. Two vibrational levels $v = 0$ and $v = 1$ are easily recognizable, and the spacing between rotational levels in $v = 0$ is increasing with energy. The ground state $v = 0$, $j = 0$ located at $\varepsilon_{0,0} = 791.63$ cm^{-1} above asymptotic limit of the potential energy surface, is forbidden by symmetry. So, the first allowed state is $v = 0$, $j = 1$ with energy $\varepsilon_{0,1} = 794.51$ cm^{-1}.

APPENDIX B

Table B. 1. Vibrational spectrum of ozone $^{48}O_3$ up to 600 cm^{-1} below dissociation threshold

#	E, cm^{-1}	Sym.	#Sym[a]	(v_1,v_2,v_3)	Note[b]	δ^c, cm^{-1}	ΔE^d, cm^{-1}
1	-8618.25	A_1	1	(0,0,0)		-2.40	-0.08
2	-7923.18	A_1	2	(0,1,0)		-1.46	-0.18
3	-7569.60	A_2	1	(0,0,1)		1.92	-0.23
4	-7521.46	A_1	3	(1,0,0)		-0.15	-0.23
5	-7230.82	A_1	4	(0,2,0)		-1.29	-0.28
6	-6890.52	A_2	2	(0,1,1)		2.18	-0.32
7	-6834.13	A_1	5	(1,1,0)		-0.24	-0.33
8	-6549.27	A_1	6	(0,0,2)		1.42	-0.36
9	-6541.49	A_1	7	(0,3,0)		-1.55	-0.37
10	-6506.83	A_2	3	(1,0,1)		3.56	-0.37
11	-6430.20	A_1	8	(2,0,0)		0.89	-0.39
12	-6214.55	A_2	4	(0,2,1)		2.07	-0.41
13	-6149.65	A_1	9	(1,2,0)		-0.95	-0.43
14	-5885.30	A_1	10	(0,1,2)		0.10	-0.45
15	-5855.75	A_1	11	(0,4,0)		-1.71	-0.46
16	-5836.96	A_2	5	(1,1,1)		4.26	-0.46
17	-5751.04	A_1	12	(2,1,0)		0.21	-0.48
18	-5557.57	A_2	6	(0,0,3)		-3.62	-0.48
19	-5542.40	A_2	7	(0,3,1)		2.30	-0.50
20	-5528.25	A_1	13	(1,0,2)		10.17	-0.49
21	-5468.12	A_1	14	(1,3,0)		-2.19	-0.51
22	-5433.76	A_2	8	(2,0,1)		-11.84	-0.51
23	-5349.68	A_1	15	(3,0,0)		5.95	-0.53
24	-5225.41	A_1	16	(0,2,2)		-0.60	-0.53
25	-5174.28	A_1	17	(0,5,0)		-1.07	-0.55
26	-5170.85	A_2	9	(1,2,1)		5.24	-0.54
27	-5074.75	A_1	18	(2,2,0)		-1.08	-0.57
28	-4908.90	A_2	10	(0,1,3)		-6.31	-0.57
29	-4875.99	A_1	19	(1,1,2)		11.80	-0.57
30	-4873.84	A_2	11	(0,4,1)		2.65	-0.59
31	-4790.36	A_1	20	(1,4,0)		-3.13	-0.61
32	-4775.04	A_2	12	(2,1,1)		-8.75	-0.60
33	-4678.13	A_1	21	(3,1,0)		4.12	-0.62
34	-4598.61	A_1	22	(0,0,4)	P35	-9.07	-0.60
35	-4583.73	A_2	13	(1,0,3)	P34	17.68	-0.60
36	-4570.07	A_1	23	(0,3,2)		-0.23	-0.62
37	-4508.97	A_2	14	(1,3,1)		6.98	-0.63
38	-4496.45	A_1	24	(0,6,0)		-0.27	-0.64
39	-4469.09	A_1	25	(2,0,2)	LM	-25.95	-0.63
40	-4401.64	A_1	26	(2,3,0)		-2.66	-0.65
41	-4375.86	A_2	15	(3,0,1)		-18.79	-0.66
42	-4277.88	A_1	27	(4,0,0)		13.00	-0.69
43	-4264.88	A_2	16	(0,2,3)		-7.82	-0.65

44	-4228.64	A_1	28	(1,2,2)		14.87	-0.65
45	-4209.21	A_2	17	(0,5,1)		3.46	-0.67
46	-4120.24	A_2	18	(2,2,1)		-5.23	-0.68
47	-4116.87	A_1	29	(1,5,0)		-3.28	-0.69
48	-4010.16	A_1	30	(3,2,0)		2.38	-0.70
49	-3965.61	A_1	31	(0,1,4)	P50	-12.76	-0.68
50	-3949.50	A_2	19	(1,1,3)	P49	20.67	-0.67
51	-3918.49	A_1	32	(0,4,2)		0.42	-0.70
52	-3852.21	A_2	20	(1,4,1)		10.36	-0.70
53	-3830.14	A_1	33	(2,1,2)	LM	-19.76	-0.71
54	-3821.21	A_1	34	(0,7,0)		-0.36	-0.73
55	-3732.58	A_1	35	(2,4,0)		-3.66	-0.72
56	-3727.72	A_2	21	(3,1,1)		-13.89	-0.73
57	-3680.49	A_2	22	(0,0,5)	P58	-6.85	-0.70
58	-3675.52	A_1	36	(1,0,4)	P57	28.34	-0.70
59	-3625.47	A_2	23	(0,3,3)		-8.19	-0.73
60	-3614.01	A_1	37	(4,1,0)		10.09	-0.77
61	-3586.52	A_1	38	(1,3,2)		20.94	-0.72
62	-3548.30	A_2	24	(0,6,1)		3.35	-0.75
63	-3523.80	A_2	25	(2,0,3)	LM	-29.79	-0.74
64	-3471.15	A_2	26	(2,3,1)		1.52	-0.74
65	-3447.29	A_1	39	(1,6,0)		-6.68	-0.76
66	-3443.95	A_1	40	(3,0,2)		-8.73	-0.76
67	-3349.09	A_1	41	(3,3,0)		-5.81	-0.76
68	-3335.08	A_1	42	(0,2,4)	P70	-31.18	-0.76
69	-3323.82	A_2	27	(4,0,1)		-9.16	-0.79
70	-3320.65	A_2	28	(1,2,3)	P68	28.82	-0.74
71	-3270.97	A_1	43	(0,5,2)		-5.60	-0.77
72	-3215.19	A_1	44	(5,0,0)		20.68	-0.82
73	-3201.13	A_2	29	(1,5,1)		12.79	-0.76
74	-3197.22	A_1	45	(2,2,2)	LM	-1.40	-0.77
75	-3148.10	A_1	46	(0,8,0)		2.64	-0.82
76	-3090.39	A_2	30	(3,2,1)		3.74	-0.77
77	-3069.13	A_1	47	(2,5,0)		-12.20	-0.78
78	-3060.03	A_1	48	(1,1,4)	P79	38.73	-0.76
79	-3059.91	A_2	31	(0,1,5)	P78	-33.07	-0.78
80	-2990.37	A_2	32	(0,4,3)		-21.06	-0.80
81	-2954.79	A_1	49	(4,2,0)		-1.10	-0.82
82	-2949.95	A_1	50	(1,4,2)		24.00	-0.78
83	-2904.08	A_2	33	(2,1,3)	LM	-26.77	-0.81
84	-2890.71	A_2	34	(0,7,1)		2.27	-0.83
85	-2829.61	A_2	35	(2,4,1)		7.92	-0.79
86	-2828.58	A_1	51	(0,0,6)	P87	5.65	-0.79
87	-2807.88	A_2	36	(1,0,5)	P86	53.87	-0.77
88	-2798.69	A_1	52	(3,1,2)	LM	-22.93	-0.81
89	-2782.10	A_1	53	(1,7,0)		-7.05	-0.82
90	-2720.34	A_1	54	(0,3,4)	P91	-29.17	-0.80
91	-2697.42	A_2	37	(1,3,3)	P90	30.65	-0.79
92	-2684.64	A_2	38	(4,1,1)		-8.98	-0.85
93	-2682.77	A_1	55	(3,4,0)		-15.89	-0.83

94	-2627.33	A_1	56	(0,6,2)		-7.31	-0.84
95	-2597.25	A_1	57	(2,0,4)	LM	-69.05	-0.85
96	-2571.88	A_1	58	(2,3,2)	LM	6.61	-0.82
97	-2558.83	A_1	59	(5,1,0)		11.98	-0.88
98	-2556.00	A_2	39	(1,6,1)		17.90	-0.82
99	-2542.67	A_2	40	(3,0,3)		-17.15	-0.85
100	-2477.24	A_1	60	(0,9,0)		-1.10	-0.89
101	-2475.96	A_2	41	(0,2,5)	P102	-14.86	-0.79
102	-2450.71	A_1	61	(1,2,4)	P101	39.87	-0.81
103	-2430.52	A_2	42	(3,3,1)		-14.46	-0.84
104	-2413.63	A_1	62	(4,0,2)		-20.94	-0.89
105	-2412.55	A_1	63	(2,6,0)		-10.24	-0.84
106	-2359.82	A_2	43	(0,5,3)		-24.26	-0.85
107	-2318.96	A_1	64	(1,5,2)		28.67	-0.83
108	-2299.92	A_1	65	(4,3,0)		-6.01	-0.86
109	-2293.98	A_2	44	(2,2,3)	LM	-18.10	-0.85
110	-2280.88	A_2	45	(5,0,1)		-9.66	-0.92
111	-2236.49	A_2	46	(0,8,1)		0.59	-0.89
112	-2236.39	A_1	66	(0,1,6)	P113	1.03	-0.81
113	-2210.92	A_2	47	(1,1,5)	P112	52.79	-0.83
114	-2198.28	A_2	48	(2,5,1)		20.55	-0.83
115	-2178.08	A_1	67	(3,2,2)	LM	-16.47	-0.87
116	-2161.28	A_1	68	(6,0,0)		33.53	-0.94
117	-2121.62	A_1	69	(1,8,0)		-6.68	-0.89
118	-2105.97	A_1	70	(0,4,4)	P119	-30.79	-0.84
119	-2079.32	A_2	49	(1,4,3)	P118	33.61	-0.84
120	-2055.15	A_2	50	(4,2,1)		-3.09	-0.88
121	-2031.14	A_1	71	(3,5,0)		-21.61	-0.88
122	-2013.12	A_1	72	(2,1,4)	LM	-42.45	-0.84
123	-1997.64	A_2	51	(0,0,7)	P125	-18.33	-0.81
124	-1986.86	A_1	73	(0,7,2)		-15.82	-0.90
125	-1968.17	A_1	74	(1,0,6)	P123	49.51	-0.87
126	-1954.94	A_1	75	(2,4,2)	LM	19.38	-0.87
127	-1924.37	A_2	52	(3,1,3)		-10.48	-0.89
128	-1918.29	A_2	53	(1,7,1)		24.65	-0.87
129	-1908.98	A_1	76	(5,2,0)		-2.24	-0.91
130	-1880.63	A_2	54	(0,3,5)	P131	-36.23	-0.83
131	-1847.52	A_1	77	(1,3,4)	P130	34.55	-0.84
132	-1808.97	A_1	78	(0,10,0)		-0.14	-0.96
133	-1800.92	A_2	55	(3,4,1)		-7.34	-0.89
134	-1799.72	A_1	79	(4,1,2)		-1.98	-0.92
135	-1768.38	A_1	80	(2,7,0)		-3.80	-0.89
136	-1733.97	A_2	56	(0,6,3)		-40.42	-0.90
137	-1705.37	A_2	57	(2,0,5)	LM	-103.57	-0.89
138	-1697.27	A_2	58	(2,3,3)	LM	0.59	-0.88
139	-1689.66	A_1	81	(1,6,2)	LM	25.72	-0.90
140	-1673.53	A_1	82	(3,0,4)	LM	-13.27	-0.89
141	-1666.68	A_1	83	(0,2,6)	P144	-18.32	-0.88
142	-1650.53	A_2	59	(5,1,1)		-5.63	-0.94
143	-1644.85	A_1	84	(4,4,0)		-23.70	-0.89

144	-1617.17	A_2	60	(1,2,5)	P141	37.47	-0.87
145	-1586.29	A_2	61	(0,9,1)		-2.28	-0.95
146	-1581.52	A_2	62	(2,6,1)	LM	40.45	-0.88
147	-1559.19	A_1	85	(3,3,2)		-8.78	-0.90
148	-1524.99	A_2	63	(4,0,3)	LM	-27.26	-0.96
149	-1513.54	A_1	86	(6,1,0)		15.34	-0.96
150	-1502.21	A_1	87	(0,5,4)	LM	-48.08	-0.87
151	-1466.87	A_1	88	(1,9,0)		-4.67	-0.95
152	-1466.14	A_2	64	(1,5,3)	LM	27.72	-0.89
153	-1452.39	A_1	89	(1,1,6)	P154	101.75	-0.85
154	-1449.04	A_2	65	(0,1,7)	P153	-8.30	-0.86
155	-1428.33	A_2	66	(4,3,1)		1.48	-0.88
156	-1397.57	A_1	90	(5,0,2)		-7.72	-0.98
157	-1394.13	A_1	91	(3,6,0)	LM	-11.66	-0.94
158	-1368.99	A_1	92	(2,2,4)	LM	-93.01	-0.93
159	-1348.52	A_1	93	(0,8,2)		-23.71	-0.96
160	-1344.93	A_1	94	(2,5,2)	LM	30.79	-0.92
161	-1316.07	A_2	67	(3,2,3)	LM	-15.81	-0.90
162	-1299.96	A_2	68	(0,4,5)	LM	-30.42	-0.86
163	-1290.28	A_2	69	(1,8,1)		36.49	-0.92
164	-1266.80	A_1	95	(5,3,0)		-6.52	-0.94
165	-1251.29	A_1	96	(1,4,4)	LM	34.18	-0.88
166	-1246.79	A_2	70	(6,0,1)		0.88	-1.01
167	-1224.76	A_2	71	(1,0,7)	P168	99.00	-0.83
168	-1224.10	A_1	97	(0,0,8)	P167	-9.78	-0.84
169	-1193.84	A_1	98	(4,2,2)	LM	4.50	-0.93
170	-1179.77	A_2	72	(3,5,1)		2.32	-0.94
171	-1146.17	A_1	99	(1,7,2)	LM	105.95	-0.92
172	-1143.42	A_1	100	(0,11,0)		-7.38	-1.03
173	-1129.51	A_2	73	(1,3,5)	LM	129.53	-0.87
174	-1116.46	A_1	101	(7,0,0)		42.34	-1.04
175	-1113.83	A_2	74	(0,7,3)	LM	-46.24	-0.93
176	-1107.19	A_1	102	(0,3,6)	LM	-7.49	-0.84
177	-1106.55	A_2	75	(2,1,5)	LM	-124.96	-0.93
178	-1068.65	A_1	103	(3,1,4)	LM	-31.33	-0.95
179	-1056.68	A_1	104	(2,8,0)		-66.26	-0.97
180	-1033.67	A_2	76	(5,2,1)		-0.73	-0.95
181	-1026.65	A_2	77	(2,4,3)	LM	-83.67	-0.91
182	-1019.52	A_1	105	(4,5,0)		-18.23	-0.95
183	-985.55	A_2	78	(1,6,3)	LM	124.55	-0.89
184	-944.14	A_1	106	(3,4,2)	LM	-24.66	-0.94
185	-939.94	A_2	79	(0,10,1)		-11.16	-1.01
186	-936.68	A_2	80	(4,1,3)	LM	-16.76	-0.94
187	-918.07	A_1	107	(0,6,4)	LM	-70.42	-0.84
188	-909.42	A_1	108	(1,2,6)	LM	101.77	-0.88
189	-903.14	A_2	81	(0,2,7)	LM	-25.53	-0.85
190	-877.26	A_1	109	(6,2,0)		7.78	-0.97
191	-863.39	A_2	82	(2,7,1)	LM	-59.99	-0.90
192	-858.97	A_1	110	(2,0,6)	LM	-138.48	-0.94
193	-838.09	A_2	83	(3,0,5)	LM	-24.31	-0.93

194	-829.30	A_2	84	(4,4,1)	LM	13.71	-0.95
195	-821.26	A_1	111	(1,10,0)		4.11	-1.01
196	-793.01	A_1	112	(1,5,4)	LM	131.07	-0.93
197	-785.13	A_1	113	(5,1,2)		-11.31	-0.97
198	-777.13	A_1	114	(2,3,4)	LM	-114.97	-0.94
199	-747.23	A_2	85	(0,5,5)	LM	-43.65	-0.83
200	-741.20	A_1	115	(3,7,0)		-32.74	-0.93
201	-720.74	A_2	86	(2,2,5)	LM	45.82	-0.87
202	-711.61	A_1	116	(0,9,2)		-57.50	-1.02
203	-698.86	A_1	117	(0,1,8)	LM	-16.57	-0.87
204	-688.93	A_2	87	(3,3,3)	LM	-60.20	-0.92
205	-676.31	A_2	88	(1,9,1)		42.60	-0.94
206	-665.22	A_1	118	(2,6,2)	LM	-56.60	-0.92
207	-647.71	A_1	119	(4,0,4)	LM	-67.94	-0.99
208	-646.10	A_1	120	(4,3,2)	LM	51.63	-0.98
209	-634.22	A_2	89	(6,1,1)		6.47	-0.96

[a] State number within one symmetry;

[b] Wave function is disturbed by local modes (LM), or paired with state #*n* (P*n*);

[c] Deviation from the Dunham expansion fit of 248 states (see Table I of the main text);

[d] Deviation from result of Ref. 129

APPENDIX C

In this appendix, selection rules for ozone are derived for a different linear combinations of $\varphi_1 = |\, J, K, M\rangle$ and $\varphi_2 = |\, J, -K, M\rangle$, namely

$$\tilde{\varphi}_\pm = (|\, J, K, M\rangle \pm |\, J, -K, M\rangle) \,/\, (2 \cdot (1 + \delta_{K0}))^{1/2}.$$

In contrast to $\varphi_\pm$ used in Section 6.3.1, the linear combinations $\tilde{\varphi}_\pm$ do not have the factor $(-1)^{J+K}$ before φ_2. This form of rotational wave functions was used by Bunker and Jensen.[166] In C_{2v} symmetry group, functions $\tilde{\varphi}_\pm$ generate the following diagonal transformation matrices:

$$M(R^0) = \begin{bmatrix} 1 & 0 \\ 0 & 1 \end{bmatrix} \qquad M(R_x^\pi) = \begin{bmatrix} (-1)^J & 0 \\ 0 & (-1)^{J+1} \end{bmatrix}$$

$$M(R_y^\pi) = \begin{bmatrix} (-1)^{J+K} & 0 \\ 0 & (-1)^{J+K+1} \end{bmatrix} \quad M(R_z^\pi) = \begin{bmatrix} (-1)^K & 0 \\ 0 & (-1)^K \end{bmatrix}$$

Again, two choices of the z axis orientation could be considered. The characters and symmetries of the rotational wave functions $\tilde{\varphi}_\pm$ and $\tilde{\varphi}_0$ for the z axis, chosen to lie in the plane of the molecule, are given in Tables C. 1−C. 3. In this tables, label "e" stands for the even values of rotational quantum number, J or K, whereas label "o" for the odd values.

Table C. 1. Characters and symmetries of the positive combination $\tilde{\varphi}_+$ of the symmetric top wave functions in C_{2v} for the z axis lying in the molecule plane.

J	K	E	(12)	E^*	(12)*	Γ
		R^0	R_x^π	R_y^π	R_z^π	
e	e	1	1	1	1	A_1
e	o	1	1	-1	-1	A_2
o	e	1	-1	-1	1	B_2
o	o	1	-1	1	-1	B_1

Table C. 2. Characters and symmetries of the negative combination $\tilde{\varphi}_-$ of the symmetric top wave functions in C_{2v} for the z axis lying in the molecule plane.

J	K	E	(12)	E^*	$(12)^*$	Γ
		R^0	R_x^π	R_y^π	R_z^π	
e	e	1	-1	-1	1	B_2
e	o	1	-1	1	-1	B_1
o	e	1	1	1	1	A_1
o	o	1	1	-1	-1	A_2

Table C. 3. Characters and symmetries of the symmetric top wave function $\tilde{\varphi}_0$ ($K = 0$) in C_{2v} for the z axis lying in the molecule plane.

J	E	(12)	E^*	$(12)^*$	Γ
	R^0	R_x^π	R_y^π	R_z^π	
e	1	1	1	1	A_1
o	1	-1	-1	1	B_2

For another choice of coordinates system, where the z axis is perpendicular to the molecule plane, the characters and symmetries are listed in Tables C. 4–C. 6.

Table C. 4. Characters and symmetries of the positive combination $\tilde{\varphi}_+$ of the symmetric top wave functions in C_{2v} for the z axis perpendicular to the molecule plane.

J	K	E	(12)	E^*	$(12)^*$	Γ
		R^0	R_y^π	R_z^π	R_x^π	
e	e	1	1	1	1	A_1
e	o	1	-1	-1	1	B_2
o	e	1	-1	1	-1	B_1
o	o	1	1	-1	-1	A_2

Table C. 5. Characters and symmetries of the negative combination $\tilde{\varphi}_-$ of the symmetric top wave functions in C_{2v} for the z axis perpendicular to the molecule plane.

J	K	E	(12)	E^*	$(12)^*$	Γ
		R^0	R_y^π	R_z^π	R_x^π	
e	e	1	-1	1	-1	B_1
e	o	1	1	-1	-1	A_2
o	e	1	1	1	1	A_1
o	o	1	-1	-1	1	B_2

Table C. 6. Characters and symmetries of the symmetric top wave function $\tilde{\varphi}_0$ ($K = 0$) in C_{2v} for the z axis lying in the molecule plane.

J	E	(12)	E*	(12)*	Γ
	R^0	R_y^π	R_z^π	R_x^π	
e	1	1	1	1	A_1
o	1	-1	1	-1	B_1

With known symmetries of the rotational wave functions, the allowed symmetry of vibrational wave functions can be determined. The symmetry of the total rovibrational wave function should be either A_1 or A_2. The matching between rotational and vibrational wave functions is given in Tables C. 7 and C. 8.

Table C. 7. Selection rules in C_{2v} for the z axis lying in the molecule plane.

K	J	Γ_{rot}		Γ_{vib}		Γ_{rv}	
		+	−	+	−	+	−
0	e	A_1		A_1		A_1	
	o	B_2		B_1		A_2	
odd	e	A_2	B_1	A_1	B_1	A_2	A_1
	o	B_1	A_2	B_1	A_1	A_1	A_2
even	e	A_1	B_2	A_1	B_1	A_1	A_2
	o	B_2	A_1	B_1	A_1	A_2	A_1

Table C. 8. Selection rules in C_{2v} for the z axis perpendicular to the molecule plane.

K	J	Γ_{rot}		Γ_{vib}		Γ_{rv}	
		+	−	+	−	+	−
0	e	A_1		A_1		A_1	
	o	B_1		B_1		A_1	
odd	e	B_2	A_2	B_1	A_1	A_2	A_2
	o	A_2	B_2	A_1	B_1	A_2	A_2
even	e	A_1	B_1	A_1	B_1	A_1	A_1
	o	B_1	A_1	B_1	A_1	A_1	A_1

Finally, the allowed vibrational symmetries are plotted as a function of the total angular momentum J, modulus of the projection K and parity p = +/−, see Tables C. 9 and C. 10.

Table C. 9. Symmetry of the allowed vibrational states as a function of total angular momentum *J*, projection *K* and parity *p* of the rotational state. The *z* axis is in the molecule plane.

$K^p \setminus J$	0	1	2	3	4	5
3^+				B_1	A_1	B_1
2^+			A_1	B_1	A_1	B_1
1^+		B_1	A_1	B_1	A_1	B_1
0^+	A_1	B_1	A_1	B_1	A_1	B_1
1^-		A_1	B_1	A_1	B_1	A_1
2^-			B_1	A_1	B_1	A_1
3^-				A_1	B_1	A_1

Table C. 10. Symmetry of the allowed vibrational states as a function of total angular momentum *J*, projection *K* and parity *p* of the rotational state. The *z* axis is perpendicular to the molecule plane.

$K^p \setminus J$	0	1	2	3	4	5
3^+				A_1	B_1	A_1
2^+			A_1	B_1	A_1	B_1
1^+		A_1	B_1	A_1	B_1	A_1
0^+	A_1	B_1	A_1	B_1	A_1	B_1
1^-		B_1	A_1	B_1	A_1	B_1
2^-			B_1	A_1	B_1	A_1
3^-				B_1	A_1	B_1

For asymmetric molecule, C_s symmetry group must be used. Within this group, the total wave function has no symmetry constrains and only the rotational part determines its symmetry. Tables C. 11−C. 13 contain the symmetries of the rotational states for the *z* axis in the molecule plane.

Table C. 11. Characters and symmetries of the positive combination $\tilde{\varphi}_+$ of the symmetric top wave functions in C_s for the *z* axis lying in the molecule plane.

J	K	E	E^*	Γ
		R^0	R_y^π	
e	e	1	1	A'
e	o	1	-1	A''
o	e	1	-1	A''
o	o	1	1	A'

Table C. 12. Characters and symmetries of the negative combination $\tilde{\varphi}_-$ of the symmetric top wave functions in C$_s$ for the *z* axis lying in the molecule plane.

J	K	E	E^*	Γ
		R^0	R_y^π	
e	e	1	-1	A''
e	o	1	1	A'
o	e	1	1	A'
o	o	1	-1	A''

Table C. 13. Characters and symmetries of the symmetric top wave function $\tilde{\varphi}_0$ (K = 0) in C$_s$ for the *z* axis lying in the molecule plane.

J	E	E^*	Γ
	R^0	R_y^π	
e	1	1	A'
o	1	-1	A''

For the *z* axis, perpendicular to the molecule plane, the symmetries of the rotational states do not depend on *J* and can be summarized in only one Table C. 14.

Table C. 14. Characters and symmetries of both positive and negative combinations $\tilde{\varphi}_\pm$ of the symmetric top wave functions in C$_s$ for the *z* axis perpendicular to the molecule plane. K = 0 is also included.

K	E	E^*	Γ
	R^0	R_z^π	
e	1	1	A'
o	1	-1	A''

Again, as was mentioned in Section 6.3.2, the fact that vibrational wave functions exhibit no symmetry, simply means that all computed vibrational states for a given pair of (*J*, *K*) and parity *p* must be retained. The selection rules, derived in this appendix, depend on total angular momentum *J*, whereas those obtained in Section 6.3 do not and therefore are more preferable.